Quantum Fluctuations and Cosmic Inflation

Dissertation

zur Erlangung des Grades eines
Doktors der Naturwissenschaften
dem Fachbereich Physik
der Universität Dortmund

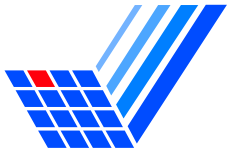

vorgelegt von
Andreas Heinen

April 2005

Abstract

This thesis addresses two topics: the inflationary perturbation spectrum and preheating after hybrid inflation.

Quantum fluctuations in the inflationary universe provide a natural mechanism for the generation of primordial perturbations which seed the formation of cosmic structure. In this thesis we present a semi-analytical, and mathematically controlled, so-called uniform approximation. This approximation can be used for the calculation of scalar and tensor inflationary perturbations. Detailed calculations of the power spectra, the spectral indices and other observables are performed to leading and next-to-leading order in the uniform approximation, respectively. Explicit "slow-roll" assumptions are avoided. A simple extension of the leading order, which is gained from the detailed understanding of the next-to-leading order, leads to excellent accuracy of the uniform approximation, which is demonstrated with several representative examples. The results are compared to standard slow-roll approximations as well as to exact numerical results. The techniques and numerical routines described here allow to calculate primordial perturbation spectra very efficiently with high precision and to constrain some models of inflation.

Furthermore, this thesis provides a detailed analysis of some aspects of preheating after hybrid inflation. In the hybrid model the inflationary expansion is terminated by a phase transition of a symmetry-breaking field. During inflation this symmetry-breaking field is trapped in a false vacuum, becomes dynamically instable and performs a transition to the true vacuum. Herein the important influence of the back-reaction of quantum fluctuations is considered by using a bubble-resummation of the propagators. The problem of renormalization in a system of multiple and coupled fields is explicitly solved. The false vacuum transition after hybrid inflation, along with other physical observables, is analyzed with detailed numerical investigations reliably and the influence of back-reaction of quantum fluctuations is emphasized.

Zusammenfassung

Diese Doktorarbeit behandelt zwei Themengebiete: das inflationäre Störungsspektrum und die Vorerwärmungsphase im Anschluss an die Hybrid-Inflation.

Quantenfluktuationen im inflationären Universum bilden einen natürlichen Mechanismus zur Erzeugung primordialer Störungen, aus denen kosmische Strukturen entstehen. In einem Teil der Arbeit präsentieren wir ein mathematisch kontrolliertes, semi-analytisches Näherungsverfahren zur Berechnung des inflationären Störungsspektrums für skalare und tensorielle Störungen. Detaillierte Berechnungen des Leistungsspektrums, des spektralen Index und anderer Observablen werden durchgeführt, zu führender und nächstführender Ordnung in einer uniformen Approximation sowie mit Fehlerschranken. Diese Berechnungen verzichten auf explizite "slow-roll"-Annahmen. Zusammen mit einer einfach zu implementierenden Erweiterung der führenden Ordnung, welche wir aus dem detaillierten Verständnis nächstführender Ordnungen gewinnen, wird die ausgezeichnete Genauigkeit des Verfahrens uniformer Approximationen anhand verschiedener Beispiele demonstriert. Die Ergebnisse werden mit exakten numerischen Resultaten und der slow-roll-Näherung verglichen. Die vorgestellten Techniken sind zusammen mit den entwickelten Programmen von unmittelbarem Nutzen zur theoretisch präzisen Berechnung von primordialen Störungsspektren sowie der Einschränkung von einigen inflationären Modellen bzw. Modellparametern.

Weiterhin werden einige Aspekte der Vorerwärmungsphase im Anschluss an die Inflation im Rahmen des sogenannten Hybrid-Modells detailliert untersucht. Die inflationäre Expansion endet in diesem Modell mit einem Phasenübergang eines symmetriebrechenden Feldes. Dieses symmetriebrechende Feld ist während der inflationären Phase in einem falschen Vakuumzustand gefangen und vollführt, dynamisch destabilisiert, einen Übergang zum wahren Vakuum. Indem eine Blasen-Resummation der Propagatoren formuliert wird, kann der wichtige Einfluss von Rückwirkungen der Quantenfluktuationen explizit berücksichtigt werden. Das Problem der Renormierung in einem System mit mehreren gekoppelten Kanälen wird gelöst. In detaillierten numerischen Simulationen wird so sehr zuverlässig der Phasenübergang nach der Hybrid-Inflation untersucht und die Bedeutung der Rückwirkungseffekte der Quantenfluktuationen herausgestellt.

Contents

The hum level in the room suddenly increased as several ancillary bass driver units, mounted in sedately carved and varnished cabinet speakers around the room, cut in to give Deep Thought's voice a little more power.

"All I wanted to say," bellowed the computer, "is that my circuits are now irrevocably committed to calculating the answer to the Ultimate Question of Life, the Universe, and Everything." He paused and satisfied himself that he now had everyone's attention, before continuing more quitely. "But the program will take me a little while to run."

Fook glanced impatiently at his watch. "How long?" he said.

"Seven and half million years," said Deep Thought.

Douglas Adams, The Hitchhiker's Guide to the Galaxy

Chapter 1

Introduction

1.1 Cosmological perturbations and the inflationary universe

This thesis is about the physics of the very early Universe. Nevertheless it is appropriate to start with observations of the present Universe, as it turns out that our present Universe contains a wealth of information about its beginning.

It has been found that the distribution of matter on very large astrophysical scales, the so-called large scale structure (LSS), is startlingly homogeneous. Sufficiently large independent volumes of the Universe contain similar mean densities of matter (see, e.g., Ref. [1] for a recent discussion). On smaller astrophysical scales there are inhomogeneities. The galaxies are not randomly distributed. We find them to lie in clusters, bubbles, filaments, walls, and other sheetlike structures. A dominant feature are voids, i.e., there are many regions where we find almost no galaxies (see Figs. 1.1 and 1.2). The superclusters build a network around these voids.

Furthermore, the radiation from the last scattering of primordial photons – released some 400,000 years after the Big Bang – presents itself as an almost uniform background in the microwave range. This cosmic microwave background (CMB) radiation is observable today and can be thought of as a photography of the Big Bang. But also this CMB radiation is not entirely homogeneous. Since the first discovery of tiny fluctuations, by the Cosmic Background Explorer (COBE) satellite experiment [5, 6], a wealth of new data, including the remarkable results from the Wilkinson Microwave Anisotropy Probe (WMAP) [7, 8], have dramatically improved our knowledge about cosmology and the very early Universe [9, 10]. There are tiny anisotropies in the microwave sky, which are of primordial origin (the relevant physics of CMB anisotropies is reviewed, e.g., in Ref. [11]). In terms of numbers the deviation, from an overall homogenous background, is of the order of one part in a 100,000. Fig. 1.3 shows a full sky map of the first-year WMAP data displaying the anisotropies.

One obvious question is where the small anisotropies both in the CMB and in the LSS come from and how the quantitative features may be explained without fine-tuning the

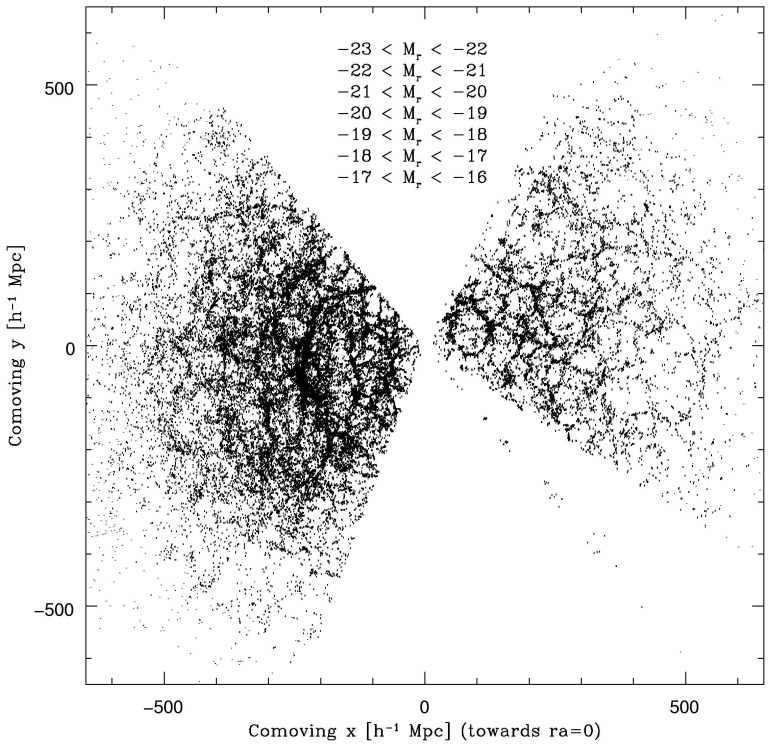

Figure 1.1: Galaxy redshift survey [Sloan Digital Sky Survey (SDSS)] displaying the large scale structure; shown is in comoving coordinates a 5° slice of the equatorial plane containing $\sim$ 70,000 galaxies; each point represents a galaxy; the survey is not complete yet and there are less points in the right part of the plot; taken from the publication of the SDSS collaboration in Ref. [2].

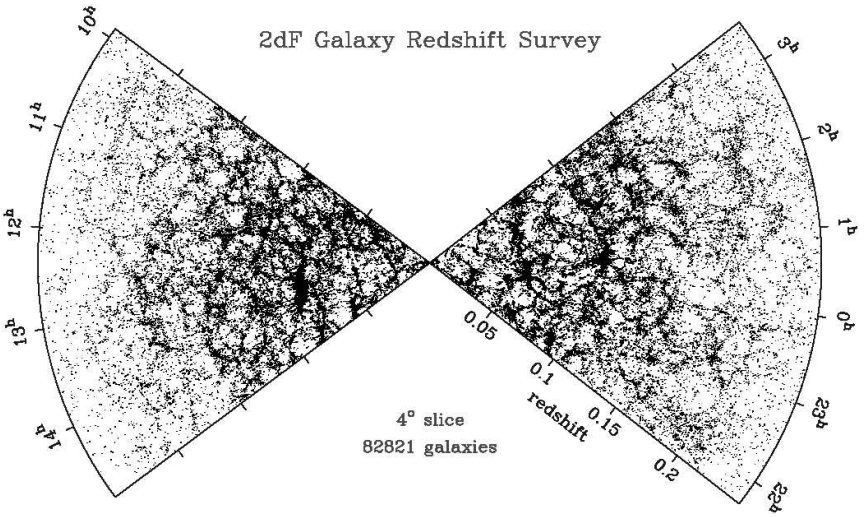

Figure 1.2: 4° slices in northern and southern galactic hemisphere as measured in the 2 degree Field Galaxy Redshift Survey (2dFGRS) containing $\sim$ 80,000 galaxies; the survey is already complete; taken from the review article Ref. [3], see also Ref. [4].

Big Bang initial conditions. Along with these questions the main cosmological puzzles [12, 13, 14] of the standard Big Bang scenario are: (1) Why is the Universe so isotropic and homogeneous on large scales, in spite of the fact that separated regions were causally disconnected? (2) Why is it so flat, i.e. why is it near critical mass density? The first question is known as the horizon problem, the second as the flatness problem. Other questions are: Why is the Universe so large? What is the origin of the Hubble expansion? Why are there so few magnetic monopoles?

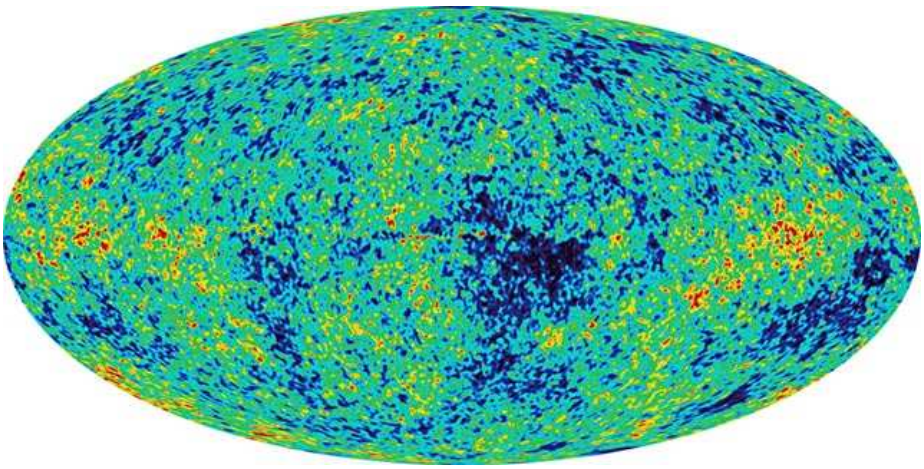

Figure 1.3: Full sky CMB map (internal linear combination map) as published by the WMAP collaboration [7, 15]; colors refer to pixel temperatures in mK and the angular resolution is $\sim 1^{\circ}$; NASA has made the WMAP data available via the LAMBDA archive [16].

Aiming at answering these questions, the *inflationary universe* has been introduced in 1980 by Alan H. Guth [17]. Basically, *inflation* is a phase of rapid exponential expansion driven by vacuum energy which provides a large negative pressure with repulsive gravity. The simplest realization introduces a single scalar background field, called *inflaton* field. During the rapid expansion the Universe has supercooled. Soon after the invention of the inflationary scenario it was realized that quantum fluctuations of the field driving inflation provide a very natural mechanism for the formation of cosmological perturbations [18, 19, 20, 21, 22]. Signatures of such primordial perturbations are present both in the CMB and LSS. In the inflationary universe they have a common origin. Indeed, primordial fluctuations of the inflaton field provide initial seeds that are amplified by the gravitational instability, leading to the formation of structure in our Universe. In this sense quantum fluctuations of subatomic size are blown up to astrophysical scales. The inflationary universe redundantizes many of the required postulates of the standard Big Bang scenario [12, 13, 14].

Although inflation is not a fundamental theory but rather a paradigm, the inflationary universe has been proved extremely successful in order to explain the outstanding cosmological problems and to address them *quantitatively*. Moreover there is no convinc-

ing alternative scenario which is comparably competitive. The finished [23], ongoing [8], and future [24] observations of the CMB via full-sky satellite experiments, high resolution ground based [25, 26, 27, 28] and balloon experiments [29, 30], as well as telescope based large surveys of the sky [31, 32, 33], serve as powerful tools for the understanding of the first moments and the subsequent evolution of our Universe. The satellite experiment PLANCK will be launched in 2007. Its mission is to measure the anisotropies in the CMB radiation over the whole sky "with unprecedented sensitivity and angular resolution" [24]. The source of information provided by PLANCK will allow testing theories of the very early universe at spectacular precision. Cosmology has already entered a new age of precision.[1]

In order to fully utilize the high precision experiments we also need powerful analytical and numerical computation tools, as well as fast, efficient, and reliable computer programs. The analytical and numerical techniques have to cope with the precision requirements of present and future observations. Such theoretical tools are necessary in order to constrain inflation and to analyze cosmological data and thus to finally address the pressing cosmological puzzles quantitatively with the highest possible precision. With very precise and reliable theoretical tools it is then possible to discriminate between particular inflationary models for the first time.

The inflationary fluctuations, primarily, arise from an effectively free scalar field and are hence Gaussian random fields. They are completely characterized by two-point statistics, such as the power spectrum [34]. In the subsequent stages after cosmic inflation the fluctuations have been exposed to various dynamical processes. The physics from the time where light cannot escape the primordial soup until the last scattering of the photons can be encoded in a transfer function for radiation or matter, respectively. Once the Universe becomes transparent for photons in the era of recombination, the CMB radiation is released. The physical processes encoded in the transfer functions have modified the primordial power spectra leading to the power spectra of matter and radiation that we observe today [14].

In this thesis analytical and numerical methods for precision calculations of the primordial power spectra are developed.

We apply the method of uniform approximation [35, 36, 37, 38, 39, 40, 41, 42] to the task of calculating the inflationary fluctuations [43, 44, 45]. We calculate spectra for density and gravitational wave perturbations along with their associated characterizing quantities. Via detailed analytical and numerical calculations the efficiency and precision of the method will be demonstrated and, as a central issue, its error-control discussed. Certainly direct numerical calculations can give answers for the power spectra without further approximations. But powerful analytical or semi-analytical approximations have their own advantages. They provide intuition and understanding of a large class of different models and of the general mechanisms. Provided tight error controls can be met, they are much

[1] Some cosmological quantities like e.g. the baryon density, the total energy density, the age of the Universe, the time of decoupling and the scalar spectral index are already known to a few percent accuracy and will continue to improve in the future. Although the uncertainties in selected quantities in comparison of LSS and CMB data may be slightly bigger ($\sim$20%), it is fair to say that the age of speculations is over.

faster than direct numerical calculations and are thus extremely useful for large parameter studies. Indeed, direct numerical calculations may only be reasonable for spot-checking a small number of parameters or models. In the past, so-called "slow-roll" approximations have been extensively used. The main idea behind the slow-roll approximation is an expansion around the limit of exact scale invariance [14]. However, the expansion made there, being essentially a derivative expansion, is uncontrolled. In addition, simple extensions beyond the leading order in slow-roll parameters are not possible. Some alternative techniques [46] have been suggested but lead to rather involved expressions for the power spectra and spectral indices and, more importantly, are not error-controlled. The ultimate accuracy with which the primordial perturbations must be calculated is of course guided by how accurately the matter and radiation transfer functions can be computed.[2] At present this can be done with an accuracy of the order of 0.1% [51]. As already said, the combination of the primordial power spectrum and the transfer functions leads to power spectra which can be directly compared with observations. One should also keep in mind that beyond a limit of $\sim 0.1\%$ it may no longer be justified to neglect some other effects in the underlying treatment of the cosmological perturbations. The theoretical basis is a perturbed form of Einstein's equations in a spatially flat Friedmann-Robertson-Walker (FRW) universe. Beyond the first-order linearized perturbation theory, the theoretical calculations become very involved, e.g., due to the issue of gauge-invariance. Second-order perturbations typically produce some additional small amount of non-Gaussianity in the perturbation spectra (see, e.g., Ref. [52] and references therein). Presumably it is not meaningful at present to calculate the primordial power spectra with an accuracy much better than $\sim 0.1\%$, i.e., without taking some of the neglected effects into account which may become important when going beyond such accuracy.

We follow a twofold goal when calculating the inflationary perturbation spectra in this thesis. First, error-controlled uniform approximations are presented that are simple to implement and give exquisite accuracy. Second, we utilize some of the findings of the approximate strategy in order to improve the efficiency of a numerical code which is also developed and presented. As a net result the numerical code for calculating the power spectra is expected to be relatively fast.[3] Using several representative examples as well as exactly solvable models we demonstrate that primordial power spectra can be calculated with an accuracy of the order 0.1% (or even better).

1.2 The problem of reheating

Shortly after the introduction of the inflationary universe the problem of *reheating* has been pointed out [54]. After inflation, the Universe is frozen in a state of extremely low entropy without any particles. In contrast, the amount of particles in our present Universe

[2] This is typically done with CMBFAST [47, 48], CAMB [49, 50], or similar Boltzmann codes.

[3] Although other groups [53] may have developed numerical routines for their publications, no code is on the market, so that we cannot check different code speeds at present. We plan to publish our own codes in the future.

is of the order of 10^{90}.

The first obvious question is how particles may have been produced efficiently. When trying to answer this question, the major problems are: (i) there is no fundamental theory for reheating and (ii) the full dynamics with back-reaction of quantum fields are both conceptionally and numerically complex and difficult to solve. The first aspect implies that, as for inflation itself, effective models must be constructed, where successful reheating may further depend on model parameters like masses, vacuum expectation values (if symmetries are spontaneously broken) or coupling constants. The second aspect highlights some of the more technical difficulties of nonequilibrium quantum field theory.

The present picture of reheating can be summarized as follows: Via resonant processes like parametric resonance a large number of particles is produced in a relative short time span (see, e.g., Ref. [55]). Most importantly, space-time expansion can be neglected, allowing us to work in Minkowski space-time. Perturbative processes like the direct decay of the inflaton field are highly suppressed and thus are not efficient in converting the field energy of the inflaton into particles. The reason is that the couplings of the inflaton to other particles or to itself have to be very small.[4] Resonant nonperturbative processes do not require large coupling constants, but instead work for a wide spectrum of parameters. Resonant processes occur while the inflaton field oscillates coherently around the minimum of its potential. The first stage of reheating in which a resonant production of almost all particles contained in the present Universe occurs, is called *preheating*. Parametric resonance in quantum field theory, in the context of preheating or reheating after inflation and also independent of that, has been studied by various authors (see, e.g., Refs. [57, 58, 59, 60, 61, 62, 63]). As long as back-reaction effects are less important, parametric resonance can even be studied within classical field equations. Depending on the model, these equations are of the Mathieu or Lamé type and one can analyze how the system dynamically moves through regions of stability or instability. Narrow or broad resonance regimes (or transitions between them) can be found. Once the system moves away from the resonant regime, the perturbative decay of particles or classical fields is the dominant process. With more and more particles produced, the scattering of these particles, i.e. quanta, becomes important and finally leads to a thermal distribution of particles. The temperature associated with this thermal ensemble is referred to as the reheating temperature $T_{\rm reh}$. Baryogenesis (or leptogenesis) has to take place before thermodynamical equilibrium is established and it is thus very natural to study the appearance of a baryon asymmetry at the stage of reheating [64].

After inflation ends, the Universe gets "warm" and presents itself as a soup of particles, just as postulated in the standard Big Bang scenario. Since there is no guarantee that the initial state was "hot", in the same sense the late entropy-rich Universe is called "hot", the phrase "reheating" should better be understood as "defrosting".

There are different observational constraints on reheating. The reheating temperature,

[4] The amplitude of scalar and tensor perturbation spectra depends on the self-coupling of the inflaton field and is thus fixed by observational constraints [56]. The $\lambda\Phi^4$ model, although under strong observational pressure, requires $\lambda \simeq 10^{-12}$ for instance.

e.g., cannot be too high. Otherwise, too many gravitinos are produced which is in conflict with the abundance of light elements. The decay of many gravitinos after nucleosynthesis would modify the very successful predictions of the standard Big Bang nucleosynthesis (see, e.g., Ref. [65] for some quantitative details). Depending on the model it is also possible that primordial metric perturbations are generated during preheating. Various authors have studied this problem (see e.g., Refs. [66, 67, 68, 69, 70, 71]). Preheating may also imprint a significant amount of non-Gaussianity in the CMB radiation [52, 71].

Thus, for reheating there are many conceptional and observational aspects to discuss; we have named only a few. In this thesis we are primarily interested in the preheating stage, which has a rich dynamical structure by itself. In order to calculate reheating temperatures, we would have to go through the full reheating stage and not just its first moments, namely the preheating stage (see e.g. the discussion in Ref. [62]). The complications of nonequilibrium quantum field theory require some further assumptions and simplifications.

In absence of a fundamental theory we have to consider effective models. Particular types of models are chaotic inflation models [72] with a single scalar inflaton field rolling down in a relatively featureless potential. Inflation ends once the inflaton field expectation value drops below the critical value, where the kinetic energy density of the inflaton field is bigger than its potential energy density. Subsequently the inflaton field oscillates around a minimum value and produces particles (quanta) via resonant processes. These particles interact with each other and are expected to reheat the Universe [57, 62].

In other models the inflaton field couples to a second field that is dynamically unstable and undergoes a phase transition which ends inflation. The second field may be a symmetry-breaking field analogous to the Higgs field postulated in the standard model of particle physics. A phase transition is realized in so-called *hybrid models* of inflation, or *hybrid inflation* for short [73]. The most important feature of hybrid inflation is that the inflaton field is not responsible alone for the particle production and reheating. In the dynamically unstable regime the symmetry breaking field produces lots of particles via spinodal amplification and resonant processes.

In this thesis we will develop analytical and numerical methods which allow to study the effects of quantum back-reaction in the nonequilibrium dynamics of coupled scalar fields [74]. In particular, this requires a nonperturbative approximation scheme and we face many difficulties, usually met in nonequilibrium quantum field theory. Bare propagators have to be resummed in a thermodynamically consistent way. In addition, in quantum field theory we encounter divergences and infinities. Renormalization is thus a central issue [75, 76]. These methods are especially important to understand some aspects of the preheating stage after hybrid inflation [63, 77, 78, 79, 80] with its associated phase transition and quantum dynamics. The phase transition ending inflation there, is a transition from a "false" metastable vacuum to the "true" stable vacuum. It thereby replaces models [63, 81, 82, 83] where a rapid decrease of the energy density is induced by an instantaneous quench. An important goal is the detailed study of this false vacuum transition. The analytical and numerical methods are also useful under more general circumstances. The role of quantum fluctuations and their back-reaction on the classical fields and onto themselves has to be addressed. Compared to previous investigations of other groups [63, 77, 78, 79, 80, 84]

we are able to include the important effects of quantum back-reaction by implementing a summation of bubble diagrams [85]. Because we fully renormalize all divergent equations we completely avoid problems like undesirable and artificial dependences of the physical observables on unphysical cut-off parameters. Without quantum back-reaction the false vacuum transition cannot be studied [86] because numerical simulations break down. We will also study in detail under which circumstances a classical description [87, 88] may be adequate and if some long-range correlations build up [89, 90]. Due to the coupling of two scalar fields the dynamics in hybrid models is very rich and can be complicated.

We still have to neglect re-scattering of quanta and hence our approximation is limited to the early-time dynamics, much before the reheating time scale is reached. Our approximation thus cannot be used to describe the late-time thermalization processes which are ultimatively reheating the Universe. Indeed such a computation of the full reheating dynamics would be extraordinary challenging, both from an analytical and from a numerical point of view. However, since we are mainly interested in the false vacuum transition that happens in the early stage of preheating, the restrictions of our approximation are well justified. Our detailed calculations provide valuable information on the dynamics in systems of coupled scalar fields, as relevant for preheating after hybrid inflation [74].

1.3 Publications

Some aspects of this thesis on inflationary perturbations have already been published or presented at conferences:

1. Salman Habib, Andreas Heinen, Katrin Heitmann, Gerard Jungman and Carmen Molina-Paris,
   Characterizing inflationary perturbations: the uniform approximation,
   Phys. Rev. **D70**, 083507 (2004) [arXiv:astro-ph/0406134].

2. Salman Habib, Andreas Heinen, Katrin Heitmann and Gerard Jungman,
   Inflationary Perturbations and Precision Cosmology, Phys. Rev. **D71**, 043518 (2005), [arXiv:astro-ph/0501130].

3. Andreas Heinen
   The Inflationary Perturbation Spectrum: Numerical and Analytical Calculations,
   Talk given at the 8th Paris Cosmology Colloquium "WMAP and the early Universe", Paris, France, 9-10 December 2004.

Some of the findings on the quantum dynamics in hybrid models have already been published in the following article and conference proceedings:

4. Jürgen Baacke and Andreas Heinen,
   Out-of-equilibrium evolution of quantum fields in the hybrid model with quantum back reaction, Phys. Rev. **D69**, 083523 (2004), [arXiv:hep-ph/0311282].

5. Jürgen Baacke and Andreas Heinen,
   Nonequilibrium dynamics in scalar hybrid models, Proceedings of the 6th Conference on Strong and Electroweak Matter 2004 (SEWM04), Helsinki, Finland, 16-19 June 2004, [arXiv:hep-ph/0407064].

Other studies by the author concerning nonequilibrium quantum field theory in 1+1 dimensional toy models will not be considered here [91, 92, 93].

1.4 Plan of this thesis

The plan of this thesis is as follows. Part I covers the important theoretical background. In Chap. 2 we give an overview on the theory of cosmological perturbations and on inflation. In Chap. 3 different inflationary models are reviewed. In Chap. 4 we briefly summarize conventional slow-roll approximation techniques which are used in this thesis only for comparison.

In Part II the calculation of the *inflationary perturbation spectrum* is presented. In Chap. 5 the method of uniform approximations for inflationary perturbations is developed in great detail. After highlighting some aspects of the numerical implementation in Chap. 6 we present detailed results of extensive numerical calculations in Chap. 7. The Part is finalized by a summary and conclusions of the main findings in Chap. 8.

Part III covers calculations as relevant for the *preheating* stage *after inflation*. In Chap. 9 the application of the technique of effective actions is discussed and a particular resummation scheme is worked out. The set of renormalized dynamical equations for the hybrid model is derived in detail in Chap. 10. The results of large numerical calculations are presented and extensively discussed in Chap. 11. This Part ends with a summary and conclusions of the main findings in Chap. 12.

The thesis is completed by a couple of Appendices covering lists of formula needed, more technical calculations, and some additional aspects.

Part I

Theoretical Background

Chapter 2

Theory of Cosmological Perturbations and of Inflation

In this Chapter we present the theory of linearized gravitational perturbations in an expanding universe. In particular, we focus on cosmologies with fluctuations in a universe with a Friedmann-Robertson-Walker (FRW) background metric. Although the theory of cosmological perturbations is not restricted to the inflationary universe we will focus on the situation where the fluctuations originate from a single, scalar inflaton field. First, we briefly review the relevant cosmological background. Second, the concept of the inflationary universe is presented, along with a discussion of its solution to the main cosmological problems. Third, we summarize the ingredients for a gauge-invariant treatment of classical perturbations. The important aspects of the quantum theory of perturbations are highlighted subsequently. Finally, we explain how to calculate characteristic quantities like the power spectrum and the spectral index.

Gauge-invariant equations for the fluctuations which describe the evolution of cosmological perturbations, will be the central results here. They form the basis from which we derive either approximate or numerical solutions for the perturbation spectra.

The early universe involves many different physical processes. The main target of this Chapter is to show the path to the inflationary perturbation spectrum, rather than to present a self-contained review on the complex theory of cosmological perturbations. For detailed reviews the reader is referred to Refs. [12, 14, 34, 94] (see also Ref. [95] for a review on inflation).

2.1 Background

The background will be a FRW universe with the background line element ds given by

$$\begin{aligned} ds^2 &= g_{\mu\nu}dx^\mu dx^\nu = \left[-dt^2 + a^2(t)\gamma_{ij}(\mathbf{x})dx^i dx^j\right] \\ &= a^2(\eta)\left[-d\eta^2 + \gamma_{ij}(\mathbf{x})dx^i dx^j\right], \end{aligned} \tag{2.1}$$

where

$$\gamma_{ij}(\mathbf{x}) = \delta_{ij}\left[1 + \frac{\mathcal{K}}{4}(x^2 + y^2 + z^2)\right]^{-2}. \tag{2.2}$$

Here $a(t)$ is the scale factor and η is the conformal time given by $a(t)d\eta = dt$. Note that we choose a metric $g^{\mu\nu}$ with the signature $(-1, 1, 1, 1)$. A flat universe corresponds to $\mathcal{K} = 0$, a closed one to $\mathcal{K} = 1$ and an open one to $\mathcal{K} = -1$. These geometries refer to the three-dimensional space corresponding to the hypersurface $\eta = \text{const}$. Greek indices run from 0 to 3 and Latin letters denote spatial indices running from 1 to 3. We also assume that all matter or radiation present can be described by a perfect fluid. The energy-momentum tensor then has the form

$$T_{\mu\nu} = pg_{\mu\nu} + (p + \varrho)u_\mu u_\nu, \tag{2.3}$$

where p is the pressure, u_μ is the velocity vector and ϱ is the energy density, given by the 0-0 component of the conservation law $T^{\mu\nu}{}_{;\nu} = 0$, i.e.

$$\dot{\varrho} = -3H(\varrho + p). \tag{2.4}$$

In Eq. (2.3) possible dissipative terms are neglected. An overdot denotes a derivative with respect to physical time t and H is the Hubble parameter explained below. Einstein's equation is given by

$$R_{\mu\nu} - \frac{1}{2}g_{\mu\nu}R = 8\pi G T_{\mu\nu} - \Lambda g_{\mu\nu}\,, \tag{2.5}$$

where G denotes Newton's constant and we have used the convention $R_{\mu\nu} = R^\sigma_{\mu\sigma\nu} = \Gamma^\sigma_{\mu\nu,\,\sigma} - \Gamma^\sigma_{\sigma\mu,\,\nu} + \Gamma^\sigma_{\mu\nu}\Gamma^\rho_{\sigma\rho} - \Gamma^\sigma_{\rho\mu}\Gamma^\rho_{\sigma\nu}$ and $R = R^\mu_\mu$ [95]. For the discussion presented here a cosmological constant Λ is irrelevant and thus will be omitted by setting $\Lambda = 0$ in the following. From the 0-0 component and the i-i components of the Ricci tensor $R_{\mu\nu}$ we can derive a special solution of Einstein's equations, the Friedmann equations

$$\ddot{a} = -\frac{4\pi}{3}G(\varrho + 3p)a\,, \tag{2.6}$$

$$H^2(t) = \left(\frac{\dot{a}}{a}\right)^2 = \frac{8\pi}{3}G\varrho - \frac{\mathcal{K}}{a^2}\,. \tag{2.7}$$

The Hubble parameter $H = \dot{a}/a$ characterizes the size of the universe since H^{-1} is the Hubble radius. These equations form the basis of the standard Big Bang model.

The observation of a cosmic microwave background supports the idea that the universe has been dominated by radiation at early times ($t \lesssim 10^5$yr). Today the universe is dominated by matter[1]. The equation of state for radiation is given by $p = \frac{1}{3}\varrho$. Neglecting

[1]There is also a dark energy contributing to the total energy density, which may be encapsulated in a non-vanishing cosmological constant Λ [96].

the contribution $\mathcal{K}$ (this is a good approximation for small a) we find in the radiation dominated era

$$a(t) \propto t^{1/2} \quad ; \quad \varrho \propto a^{-4} \qquad \text{(radiation dominated universe)}\,. \tag{2.8}$$

Similarly for a matter dominated universe with $p = 0$

$$a(t) \propto t^{2/3} \quad ; \quad \varrho \propto a^{-3} \qquad \text{(matter dominated universe)}\,. \tag{2.9}$$

The critical density ϱ_c is the density, which would make the universe flat. It is defined by

$$\varrho_c \equiv \frac{3H^2}{8\pi G}. \tag{2.10}$$

The ratio $\Omega_{\rm tot}$ of the total density $\varrho_{\rm tot}$ (including the vacuum energy $\varrho_\Lambda = \frac{\Lambda}{8\pi G}$) and the critical energy density $\Omega_{\rm tot}$ is given by

$$\Omega_{\rm tot} = \frac{\varrho_{\rm tot}}{\varrho_c}\,, \tag{2.11}$$

indicating the geometry of the universe. If $\Omega_{\rm tot} = 1$, we have a flat universe, $\Omega_{\rm tot} > 1$ corresponds to a closed one and $\Omega_{\rm tot} < 1$ to an open universe. The WMAP team [8] gives a value

$$\Omega_{\rm tot} = 1.02 \pm 0.02 \tag{2.12}$$

when first-year WMAP data and data from galaxy clustering are included in the analysis.[2] At present observations are still compatible with all geometries. We will come back to the quantity $\Omega_{\rm tot}$ in the next Section. In the following we will drop the suffix "tot". Unless explicitly stated we will always refer with Ω to the total density.

2.2 The inflationary paradigm

The inflationary universe has been introduced by Alan Guth in 1980 [17] in order to solve some of the outstanding cosmological problems listed below. These problems are fundamental weaknesses of the old Big Bang scenario. Before coming to the problems we sketch the main ideas of the inflationary universe. The fundamental assumption is the existence of a state with negative pressure [17]. As obvious from Eq. (2.6), a negative pressure p produces a repulsive form of gravity, because it leads to an acceleration of the scale factor a, if the pressure term $3p$ dominates over the energy density term ϱ.

The physics of scalar fields makes it easy to construct states of negative pressure. Consider the energy-momentum tensor for a single scalar field ϕ given by

$$T^{\mu\nu} = \partial^\mu\phi\partial^\nu\phi - g^{\mu\nu}\left[\frac{1}{2}\partial^\lambda\phi\partial_\lambda\phi + V(\phi)\right]. \tag{2.13}$$

[2]The fit assumes the so-called ΛCDM model (dark energy plus cold dark matter).

The pressure is given by

$$p = \frac{1}{3}\sum_{i=1}^{3} T_{ii} = \frac{1}{2}\dot{\phi}^2 - \frac{1}{6}(\partial_i\phi)^2 - V(\phi)\,. \tag{2.14}$$

If the dynamics of ϕ is dominated by the potential energy $V(\phi)$ we have a state with negative pressure. The accelerated phase of expansion ends when this is no longer the case, i.e., when the kinetic energy equals the potential energy. The dynamical equation for the inflaton field ϕ is obtained as

$$\ddot{\phi}(t) + 3H(t)\dot{\phi}(t) + \frac{\partial V(\phi)}{\partial\phi} = 0\,. \tag{2.15}$$

The Friedmann equation follows with $\varrho = \frac{1}{2}\dot{\phi}^2 + V(\phi)$

$$H^2(t) = \frac{8\pi G}{3}\left[\frac{1}{2}\dot{\phi}^2(t) + V(\phi)\right]. \tag{2.16}$$

The features of the inflationary universe are most conveniently explained in the view of the well-known cosmological puzzles which we list in the following (see, e.g., Refs. [13, 14, 97, 98]). Some of these aspects are related.

- **The Universe is big.**
  It is of course easy to take the size of our Universe as a matter of fact. In addition, we cannot put its size in any relative context. However, the visible part of our Universe contains the enormous number of $\sim 10^{90}$ particles, i.e., the total entropy is of that order. The obvious question is where this number comes from. This question is also related to the flatness problem. Without a mechanism that can produce such a large number of particles or entropy from nothing, one has to postulate that almost all the particles which our Universe contains, have been there right from the beginning. In contrast to this, the inflationary universe leads to an exponential growth of all scales. During reheating the vacuum energy of the field driving inflation is released, mainly due to decay processes of the inflaton field into its own quanta and other fields or quanta. Starting with a modest entropy it is easier to explain $S \sim 10^{90}$, by exponential multiplication of a small initial number. In his paper Guth suggested $S_p = Z^3 S_0$, where S_p is the present entropy, S_0 is the initial entropy and Z is a (big) numerical factor [17]. The expansion phase during inflation is nonadiabatic, which allows entropy to grow substantially. We will give a value for Z when discussing the flatness problem.

- **The Hubble expansion.**
  During the 1920s and 1930s Edwin Hubble discovered that the Universe is expanding [99]. Galaxies are moving away from each other with a recession velocity $v = H_0 d$, where d is the distance to earth and H_0 is the Hubble constant in the present epoch.

As we have seen, the Hubble constant is part of the Friedmann equations. We may easily take the Hubble expansion for granted. Without inflation the Hubble expansion is one of the postulates of the cosmological model. In the inflationary universe the Hubble expansion is a consequence of states with negative pressure providing repulsive gravity.[3]

- **Homogeneity and isotropy.**
  The Universe is very homogenous on large astrophysical scales. The CMB radiation is also very homogenous. After correcting the motion of the earth around the sun the measured intensity of the CMB radiation is the same in all directions with a precision of one part in 100,000. The CMB radiation was released at a time of $\sim$ 400,000 years after the Big Bang, as the primordial plasma became transparent. The CMB gives thus a view on the Universe at that time, indicating that the uniformity was already established then. One can show that in the standard Big Bang scenario the uniformity would have been established only by processes occurring much faster than the speed of light. This violates causality and so the problem of uniformity at early times is also known as the *horizon problem*. In the inflationary universe the homogeneity is explained by the exponential expansion. The homogeneity was established at the size of quantum fluctuations and has been stretched to become large enough to encompass the whole universe.

- **Flatness.**
  The flatness problem is very startling. In the standard Big Bang scenario there is no explanation why Ω is so close to one. The reason is the following [17]: The Planck time $1/m_{\mathrm{pl}} \approx 5.4 \times 10^{-44}\,\mathrm{s}$ is the typical time scale in which a closed universe reaches its maximum size. An open universe reaches a value ϱ much smaller than the critical density at the order of this time scale. In the standard Big Bang scenario $\Omega \approx 1$ is an unstable equilibrium point. Any tiny deviation from 1 would lead to Ω much bigger or smaller than 1 during expansion, in contrast to the observation of a nearly flat Universe. In terms of numbers one would have to tune the initial value of Ω to 58 decimal places at the Planck time to end up with $\Omega \approx 1$ today. Even at the beginning of nucleosynthesis at $t \approx 1\,\mathrm{s}$ it would have to be tuned to roughly 15 decimal places. Otherwise the universe would never survive the required $\sim 10^{10}$ years. Although it is possible to have such an extreme fine tuning of the initial state, it does not seem very likely. The situation is different in the inflationary universe. There the ratio Ω is driven *towards* one, because

$$\Omega - 1 \propto \exp(-2H_{\mathrm{I}}t), \tag{2.17}$$

[3] One may take up the position that the question of the origin of the Hubble expansion is now replaced by the question where the potential energy of the inflaton field comes from. However, the answer is that the energy is provided by the gravitational field itself. There is no lower bound for the energy of the gravitational field. The total energy can indeed be zero. See, e.g., the comments in Ref. [100] in the context of eternal inflation.

where $H_{\rm I}$ is the value of the Hubble parameter during inflation [97]. As long as the inflationary period is long enough one can start at almost any value of Ω. Coming back to the numerical factor mentioned above one needs $Z \gtrsim 10^{28}$ in order to have a sufficiently flat universe. It is worthwhile to note that inflation does not lead to *exact* flatness, but rather to an universe that is *nearly* flat. (For a suggestion how flatness may be parameterized see e.g., Ref. [101].) Typically inflationary models lead to $|\Omega - 1| \sim 10^{-4}$.

- **Absence of magnetic monopoles.**
  Magnetic monopoles are extremely massive particles that carry a net magnetic charge. Many grand unified theories (GUTs) predict a fairly large number of them, but we do not observe them. If there is, like in the inflationary universe, a phase of exponential expansion which sets in at an energy below the GUT-scale, the density of relic monopoles becomes very low. Basically the inflationary phase dilutes the monopole density to a completely negligible level.

- **Anisotropy of the CMB and LSS.**
  How can structures in the CMB be larger than the horizon? In the standard Big Bang scenario this seems to violate causality. The problem of generating anisotropies in the CMB and the LSS is known as the *causality problem*. In the inflationary universe the situation is different and there is no causality problem. During the stage of an exponential expansion, with vacuum energy dominating, the Hubble radius H^{-1} is roughly constant. Compared to a fixed comoving scale the Hubble radius is shrinking. After inflation the Hubble radius H^{-1} increases more rapidly than a fixed comoving scale. In Fig. 2.1 the situation is sketched schematically. The important aspect of inflationary universe models is that, during the period of inflation, perturbations are generated *inside* the Hubble radius, then leave the horizon and effectively freeze, because they lost causal contact. Eventually they reenter the horizon, since the Hubble radius increases after inflation has ended. With further expansion the fluctuations become perturbations on large astrophysical scales. Thus the perturbations have their origin in quantum fluctuations of the scalar inflaton field. The duration of the inflationary period is what determines the final "size" of the fluctuations.

So far we also did not specify the time scale of inflation. The reason is that it depends on the particular implementation of a successful inflationary model. In order to make definite predictions on the perturbation spectra we have to specify $V(\phi)$ by choosing a particular model. Different classes of inflationary models will be discussed in Chap. 3. However, quite typically the inflationary phase may take place some 10^{-40} s to 10^{-32} s after the initial singularity. During the tiny amount of $\sim 10^{-35}$ s the Universe has enlarged by an enormous factor of $\sim 10^{28}$ (from the size of an elementary particle to the size of a grapefruit). A convenient definition characterizing the expansion is the number of e-foldings defined via

$$a(t) = a_{\rm end} \exp[-N(t)], \tag{2.18}$$

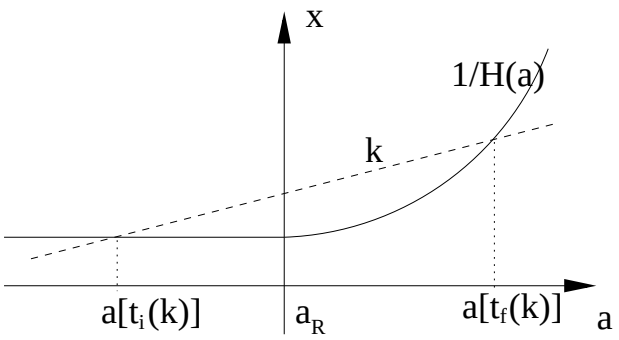

Figure 2.1: Simplified schematic sketch of the evolution of length scales in inflationary universe models; the Hubble radius $1/H$ (solid line) and a perturbation mode with fixed comoving wavenumber k (straight dashed line) are shown as a function of the scale factor a in terms of physical distance x; a_R denotes the scale factor where inflation ends and reheating starts; the scale of the fluctuation leaves the Hubble radius at a time $t = t_i(k)$ and reenters at $t = t_f(k)$.

where $a_{\rm end}$ is the scale factor at the end of inflation. The expansion by a factor of $\sim 10^{26}$ corresponds to $N \approx 60$ e-foldings.

2.3 Gauge invariant treatment of linearized fluctuations – classical perturbations

The FRW universe discussed in the previous Section is not yet realistically, since the matter distribution in our present Universe and the CMB radiation is not entirely homogeneous. We must include perturbations. The full line element ds may be replaced by

$$ds^2 = g^{(0)}_{\mu\nu} dx^\mu dx^\nu + \delta g_{\mu\nu} dx^\mu dx^\nu, \tag{2.19}$$

where $g^{(0)}$ means the unperturbed background part [the FRW universe defined by Eq. (2.1) in our case] and δg describes the perturbations. In general one can distinguish between *scalar*, *vector*, and *tensor* perturbations. Scalar perturbations correspond to density perturbations, vector perturbations to vortical motions in the plasma and tensor perturbations to gravitational waves. Only scalar perturbations are gravitationally instable, meaning that they can provide seeds for structure formation. During expansion vorticity is damped. Moreover, in single-field inflation vector perturbations cannot be produced. Hence, vector perturbations are effectively suppressed. In the following we only consider scalar and tensor perturbations.

The line element may be parameterized by

$$ds^2 = a(\eta)^2 \left[ds_S^2 + ds_T^2\right], \tag{2.20}$$

with

$$ds_S^2 \;=\; -(1+2A)\, d\eta^2 + 2B_{|i}\, d\eta dx^i + \left[(1+2C)\gamma_{ij} + 2E_{|i|j}\right] dx^i dx^j \tag{2.21}$$

and

$$ds_T^2 = h_{ij}dx^i dx^j. \tag{2.22}$$

Scalar perturbations are constructed using the four scalar quantities A, B, C, E. The three-dimensional covariant derivative of a function f with respect to a coordinate i has been denoted by $f_{|i}$. For $\mathcal{K} = 0$, i.e., in a spatially flat universe the covariant derivative will become an ordinary partial derivative. The tensor h_{ij} parameterizing the tensor perturbations is traceless, symmetric and transverse.

A serious complication in the theory of fluctuations around the background of an expanding universe is the freedom of choosing a gauge, i.e., background coordinates [102]. We can introduce two gauge invariant variables Φ_A and Φ_B, the Bardeen potentials

$$\Phi_A = A + (B' + \mathcal{H}B) - (E'' + \mathcal{H}E'), \tag{2.23}$$

$$\Phi_B = C - \frac{1}{3}\Delta^{(3)}E + \mathcal{H}(B - E'). \tag{2.24}$$

Primes denote differentiation with respect to conformal time, $\mathcal{H} = a'/a = aH$ and $\Delta^{(3)}$ denotes the three dimensional spatial Laplacian.

In the longitudinal gauge the perturbed metric becomes

$$ds^2 = a^2(\eta)\left[-(1 + 2\Phi_A)d\eta^2 + (1 + 2\Phi_C)\gamma_{ij}dx^i dx^j\right]. \tag{2.25}$$

This gauge yields a direct physical interpretation for Φ_A and Φ_C. They generalize the Newtonian potential. The longitudinal gauge may be understood as a "conformal Newtonian" gauge. The variables Φ_A and Φ_C are the amplitudes of the metric perturbations in the conformal Newtonian coordinate system. The tensor perturbations, described by h_{ij}, themselves are gauge-invariant.

We also have to introduce matter perturbations. The energy-momentum tensor including first order perturbations is given by

$$T_{\mu\nu} = T^{(0)}_{\mu\nu} + \delta T_{\mu\nu}, \tag{2.26}$$

where $T^{(0)}_{\mu\nu}$ is the unperturbed energy-momentum tensor

$$T^{(0)}_{\mu\nu} = p^{(0)}g^{(0)}_{\mu\nu} + (p^{(0)} + \varrho^{(0)})u^{(0)}_\mu u^{(0)}_\nu, \tag{2.27}$$

corresponding to Eq. (2.3). The perturbation is $\delta T_{\mu\nu}$ given by

$$\delta T^0_0 = \delta\varrho, \tag{2.28}$$

$$\delta T^0_i = a^{-1}(\varrho^{(0)} + p^{(0)})\delta u_i, \tag{2.29}$$

$$\delta T^i_{\ j} = -\delta p\delta^i_{\ j}. \tag{2.30}$$

It is assumed that all quantities are gauge-invariant quantities, constructed analogous to the potentials Φ_A and Φ_C. Note that in the longitudinal gauge the perturbations $\delta\varrho$, δp,

and δu_i immediately correspond to perturbations of the energy density, the pressure, and the velocity field. The perturbations in the pressure δp can be re-expressed in terms of perturbations of the (energy) density $\delta\varrho$ and the entropy per baryon via

$$\delta p = \left(\frac{\partial p}{\partial \varrho}\right)_S \delta\varrho + \left(\frac{\partial p}{\partial S}\right)_\varrho \delta S = c_s^2 \delta\varrho + \tau\delta S\,, \tag{2.31}$$

where c_s has the interpretation of the adiabatic sound speed.[4]

In the case of a vanishing anisotropic stress which is the case for a perfect fluid, the two gauge-invariant parameters Φ_A and Φ_C become identical, i.e., $\Phi \equiv \Phi_A = \Phi_C$ [34]. The perturbed metric becomes

$$ds^2 = a^2(\eta)\left[-(1+2\Phi)d\eta^2 + (1+2\Phi)\gamma_{ij}dx^i dx^j\right]. \tag{2.32}$$

The remaining task is to derive a dynamical equation for Φ. This can be done by combining the components of Einstein's equation with the equation for the pressure perturbation δp, providing a single partial differential equation for the potential Φ (for the derivation see Ref. [34])

$$\Phi'' + 3\mathcal{H}(1+c_s^2)\Phi' - c_s^2\Delta^{(3)}\Phi + [2\mathcal{H}' + (1+3c_s^2)(\mathcal{H}^2 - \mathcal{K})]\Phi = 4\pi G a^2 \tau\delta S\,. \tag{2.33}$$

For purely adiabatic perturbations ($\delta S = 0$) the source term on the right hand side in the above equation vanishes. This will be assumed in the following. With some changes of variables the friction term with Φ' can be eliminated. Let us define w by

$$\Phi \equiv 4\pi G(\varrho^{(0)} + p^{(0)})^{1/2} w = (4\pi G)^{1/2}\left(\frac{\mathcal{H}^2 - \mathcal{H}' + \mathcal{K}}{a^2}\right)^{1/2} w\,. \tag{2.34}$$

After some calculation [34] the equation for w is obtained in the form

$$w'' - c_s^2\Delta^{(3)}w - \frac{\theta''}{\theta}w = 0\,, \tag{2.35}$$

where

$$\theta = \frac{\mathcal{H}}{a}\left[\frac{2}{3}(\mathcal{H}^2 - \mathcal{H}' + \mathcal{K})\right]^{-1/2}. \tag{2.36}$$

A second form of the evolution equation can be obtained by introducing a scalar u, which is defined by the relation

$$\Delta^{(3)}w = -c_s^{-2}\left(\frac{d}{d\eta} + \frac{\theta'}{\theta}\right) c_s u. \tag{2.37}$$

[4]Taking into account radiation (r) and matter (m) components via $\varrho = \varrho_\mathrm{m} + \varrho_\mathrm{m}$ the parameters c_s and τ are obtained as $c_s^2 = \frac{1}{3}(1 + \frac{3}{4}\frac{\varrho_\mathrm{m}}{\varrho_\mathrm{r}})^{-1}$ and $\tau = \frac{c_s^2\varrho_\mathrm{m}}{S}$ [34].

Because of the relation between this definition and the differential operator which appears in the equation for w, it can be shown that u satisfies the evolution equation

$$u'' - c_s^2 \Delta^{(3)} u - \frac{z''}{z} u = 0 \,, \tag{2.38}$$

where

$$z = \frac{a}{c_s \mathcal{H}} \left(\mathcal{H}^2 - \mathcal{H}' + \mathcal{K} \right)^{1/2} \,. \tag{2.39}$$

Eq. (2.38) is the main result of this Section. The gauge-independent variable u is also related to the quantity ζ via $u = z\zeta$. In a comoving gauge ζ takes on the physical meaning of an intrinsic curvature perturbation [103]. The intrinsic curvature perturbation ζ becomes constant for super-horizon modes [104]. It is related to the metric perturbation in a simple way,

$$\Delta^{(3)} \Phi = -(4\pi G)^{1/2} \frac{\mathcal{H}^2 - \mathcal{H}' + \mathcal{K}}{h c_s^2} \left(\frac{u}{z} \right)' \,. \tag{2.40}$$

Recalling that Φ has the interpretation of the Newtonian gravitational potential, this Poisson equation indicates how u/z acts as a source for the potential.

The tensorial perturbations can be derived in a similar way. The corresponding equation for a gauge-invariant quantity v is obtained as

$$v'' - c_s^2 \Delta^{(3)} v - \frac{a''}{a} v = 0 \,. \tag{2.41}$$

If, as in the inflationary scenario, the universe is dominated by a single (relativistic) scalar field, with a background energy-momentum tensor as in Eq. (2.13), the speed of sound is given by $c_s = 1$. Assuming also that the universe is spatially flat ($\mathcal{K} = 0$) the quantity z simplifies to

$$z = \frac{a \dot{\phi}}{H} \,. \tag{2.42}$$

The fluctuations of scalar and tensor modes originate from quantum fluctuations of the underlying matter fields (the inflaton) and of the metric. The dynamical equations for scalar and tensor fluctuations [Eqs. (2.38) and (2.41)] reveal the form of a Klein-Gordon equation with a negative mass squared, given by $-z''/z$ and $-a''/a$, respectively. Having such canonical evolution equations for scalar and density fluctuations allows a straightforward quantization.

2.4 Quantization of the fluctuations

At present a full quantum theory of gravity is not available. However, in the context of linearized fluctuations around the background of an expanding universe, a consistent quantization of cosmological perturbations is possible [34]. This is done by requiring the

usual canonical commutation relations for the fields and their canonical momenta. The gauge-invariant formalism is very useful here, since it only involves physical degrees of freedom. Quantization results in fixing the initial conditions for the fluctuation modes.

At first, the reduced action for scalar perturbations u is given by

$$\int d^4x\sqrt{\gamma}\mathcal{L} = \frac{1}{2}\int d^4x\sqrt{\gamma}\left(u'^2 - \gamma^{ij}u_{,i}u_{,j} + \frac{z''}{z}u^2\right) , \tag{2.43}$$

where γ_{ij} is the metric on background $\eta = \text{const.}$ surfaces and γ is its determinant. There is an analogous action for tensor perturbations.

In the quantum theory the variables u and v become operators and will be denoted by $\hat{u}$ and $\hat{v}$. Without going into detail, we note that the usual canonical commutation relations hold for $\hat{u}$, $\hat{\pi}_u$, $\hat{v}$ and $\hat{\pi}_v$, where the $\hat{\pi}$s denote the canonically conjugate momenta. For a spatially flat universe ($\mathcal{K} = 0$) we can take a basis of plane waves and expand the operator $\hat{u}$ as

$$\hat{u}(\eta, \mathbf{x}) = \int \frac{d^3p}{\sqrt{2\pi}^3}\left[\hat{a}_k u_k(\eta)\exp(i\mathbf{k}\cdot\mathbf{x}) + \hat{a}_k^\dagger u_k^*(\eta)\exp(-i\mathbf{k}\cdot\mathbf{x})\right] . \tag{2.44}$$

The complex amplitude $u_k(\eta)$ satisfies

$$u_k''(\eta) + \left[k^2 - \frac{z''(\eta)}{z(\eta)}\right]u_k(\eta) = 0. \tag{2.45}$$

Solving Eq. (2.45) is the fundamental problem in determining the perturbation spectrum. The corresponding mode equation for tensor perturbations is given by

$$v_k''(\eta) + \left[k^2 - \frac{a''(\eta)}{a(\eta)}\right]v_k(\eta) = 0. \tag{2.46}$$

Since the small fluctuations are Gaussian[5], the perturbation spectrum can be fully characterized by two-point correlation functions, such as the power spectrum defined by

$$\langle 0|\hat{u}(\eta, \mathbf{x})\hat{u}(\eta, \mathbf{x}+\mathbf{r})|0\rangle = \int_0^\infty \frac{dk}{k}\frac{\sin kr}{kr}P_u(\eta, k) . \tag{2.47}$$

2.5 Calculation of the power spectra

Eq. (2.45) and (2.46) have the mathematical form of Schrödinger equations. A simple approach to analytical approximation of Eqs. (2.45) and (2.46) relies on the fact that exact solutions exist in the limits $k^2 \gg |z''/z|$, $|a''/a|$ (short wavelength) and $k^2 \ll |z''/z|$, $|a''/a|$ (long wavelength) or, as will be made more explicit below, as $-k\eta \to \infty$ and $k\eta \to 0^-$. For scalar perturbations,

$$u_k \;\to\; \frac{1}{\sqrt{2k}}e^{-ik\eta} \qquad \left(k^2 \gg |z''/z| ,\ -k\eta \to \infty\right) , \tag{2.48}$$

$$u_k \;\to\; A_k z \qquad \left(k^2 \ll |z''/z| ,\ -k\eta \to 0\right) . \tag{2.49}$$

[5]This is always true in a theory of linear approximations.

Here, the short wavelength solution corresponds to the choice of an adiabatic vacuum for modes on length scales much smaller than the scale set by the curvature. The long wavelength solutions correspond to the growing mode on scales much larger than the Hubble length.

The long wavelength solution for $\zeta_k = u_k/z$ is just the (k-dependent) constant A_k of Eq. (2.49). In order to determine the corresponding power spectrum $P_\zeta(k) \equiv P_S(k)$, the main task is to fix the unknown constant A_k by connecting the two asymptotic solutions. The situation is sketched in Fig. 2.2. The large-k regime lies in region I and the small-k regime lies in region III. The two asymptotic solutions may be connected either by a matching procedure performed in region II, typical of the slow-roll class of approximations (see Chap. 4), or, as performed in Chap. 5, by constructing a global interpolating solution. Once A_k is determined, the power spectrum for ζ_k can be computed in the regime ($k\eta \to 0^-$) of actual interest,

$$P_\zeta(k) = \frac{k^3}{2\pi^2} \left|\zeta_k\right|^2 \ . \tag{2.50}$$

Analogous solutions exist for gravitational wave perturbations and the corresponding power spectrum $P_h(k)$ (h is the amplitude of the two polarizations of gravitational waves).

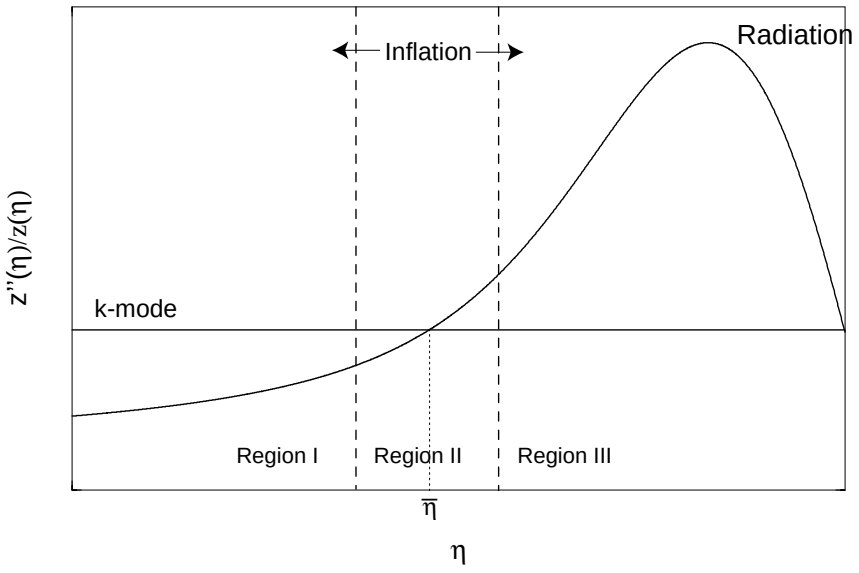

Figure 2.2: Sketch of the potential barrier for density perturbations. The vertical dashed lines delineate the three different regions where the solution for u_k is investigated as explained in the text. $\bar{\eta}$ marks the point where the k-mode enters into the potential barrier, the turning point. Inflation lasts over a wide η-range, extending region II as indicated by the arrows. In the far right of region III radiation dominates.

Solving the mode equations (2.45) and (2.46) for different momenta k, the power spectra

for scalar and tensor perturbations are obtained via

$$P_S(k) = \lim_{k\eta\to 0^-} \frac{k^3}{2\pi^2}\left|\frac{u_k(\eta)}{z(\eta)}\right|^2, \tag{2.51}$$

$$P_T(k) = \lim_{k\eta\to 0^-} \frac{k^3}{2\pi^2}\left|\frac{v_k(\eta)}{a(\eta)}\right|^2, \tag{2.52}$$

where we denote the power spectrum for ζ by P_S and the index S (T) indicates scalar (tensor) perturbations.

The tensor power spectrum is often defined with an additional factor as

$$P_h(k) = 8P_T(k), \tag{2.53}$$

leading to the definition of the tensor to scalar ratio as

$$R(k) = \frac{P_h(k)}{P_\zeta(k)} = \frac{8P_T(k)}{P_S(k)}. \tag{2.54}$$

The generalized spectral indices for the scalar and tensor perturbations are defined to be

$$n_S(k) = 1 + \frac{d\ln P_S(k)}{d\ln k}, \tag{2.55}$$

$$n_T(k) = \frac{d\ln P_T(k)}{d\ln k}. \tag{2.56}$$

Running of the spectral indices is conventionally parameterized by the second logarithmic derivative of the power spectra

$$\alpha_S(k) = \frac{d\ln n_S(k)}{d\ln k}, \tag{2.57}$$

$$\alpha_T(k) = \frac{d\ln n_T(k)}{d\ln k}. \tag{2.58}$$

Chapter 3

Inflationary Models

At present a concrete fundamental theory of everything is not known and there is no fundamental theory for the inflationary universe. Inflation should be understood as a class of theories. The present situation is that we have to rely on effective models. Some of them are introduced ad hoc while others may be motivated from supergravity, string theory or other theories. Each model makes specific predictions. However, there are plenty of models around (see, e.g., Ref. [105] for a comprehensive review on particle physics models of inflation). Some of them are intuitive, while others appear weird to us. We will concentrate on some special classes of models in this Chapter. In general, we distinguish between single-field inflation models, where the background dynamics is dominated by a single scalar field, and multi-field inflation models, where more than one field is dynamically excited. The focus for the remainder of this part we will be on some classes of single-field inflation. We only comment shortly on multi-field inflation (or other exotic scenarios).

3.1 Single-field inflation

Single-field inflation classifies inflationary scenarios in which the background dynamics is dominated by a single scalar background field, the inflaton field ϕ, that evolves in a given potential $V(\phi)$. Other fields may well be present, however they must remain in a frozen state.[1] All simple models have in common that inflation takes place in a part of the potential that is very flat.

The focus in this Section is on chaotic [72], hybrid [73], and power-law inflation [106]. We also investigate potentials with special features that imitate a phase transition. We leave out so-called small-field inflation models where the inflationary phase takes place at a plateau of the potential. This includes, e.g., new inflation [107, 108], natural inflation [109, 110], and other scenarios. In addition we do not comment on the various "inverted" versions, models with running parameters or other modified versions of chaotic or hybrid inflation [105].

[1] Note that we have to reconsider eventually the underlying treatment of linearized fluctuations, if more than one dynamical field is present in the inflationary stage.

3.1.1 Chaotic inflation

Chaotic inflation has been introduced by Andrei Linde in 1983 [72]. In chaotic inflation the inflaton field ϕ is moving towards the origin of its potential. The field amplitude of ϕ during the observable part of its motion is several times larger than $m_{\rm pl}$ (the Planck mass), hence there is no obvious particle physics motivation for chaotic inflation. The inflationary expansion ends once the kinetic energy density of the field driving inflation becomes smaller than its potential energy density. The simplest potential is given by

$$V(\phi) = \frac{1}{2} m^2 \phi^2 \,, \tag{3.1}$$

which has only one parameter, the inflaton mass m. The mass m is constrained by observations to be $m^2 \approx 10^{-12} m_{\rm pl}^2$. Such a potential is compatible with present observations [56, 111]. Higher monomial potentials like

$$V(\phi) = \frac{1}{4} \lambda \phi^4 \,, \tag{3.2}$$

or even

$$V(\phi) = \tilde{\lambda} m_{\rm pl}^{4-p} \phi^p \,, \tag{3.3}$$

with $p/2 \geq 3$ are under strong pressure from recent observations ($p = 4$) or considered as ruled out ($p \geq 5$) [56, 111, 112].

In Fig. 3.1 we display a schematic sketch of a chaotic inflation potential along with the two stages of inflation and reheating. The dashed line symbolizes the value where the kinetic energy of the inflaton field is equal to its potential energy. The inflationary stage is above that line, reheating below it. During reheating the inflaton field oscillates coherently around the minimum of its potential and produces particles via parametric resonance. Note that in the chaotic inflation scenario the inflationary expansion does not start at a metastable point. The terminology "chaotic" refers to the choice of initial conditions. The initial conditions are not known, but it turns out that they are not important [100, 113].

Preheating in chaotic inflation type models has been studied by various authors [55, 57, 58, 60, 114, 115].

3.1.2 Hybrid inflation

Hybrid inflation models incorporate at least two scalar fields. One field is the inflaton field, rolling down in its flat potential, and the other field is a symmetry breaking field that is trapped in a false vacuum state. Hybrid inflation has been introduced by Linde in Ref. [73]. The false vacuum state becomes unstable once the inflaton field reaches a critical value. The symmetry breaking field that ends inflation is practically zero in the inflationary phase, and nonzero only at the end of inflation. Thus, it does not contribute to the perturbation spectrum. Hybrid inflation can be treated as single-field inflation, because the phase transition ending inflation is very rapid and does not leave a signature at

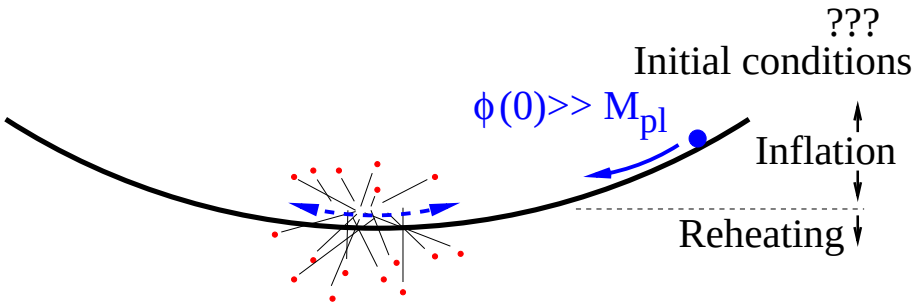

Figure 3.1: Schematic sketch of the stages from inflation to reheating with respect to the inflaton potential of chaotic inflation; during reheating the inflaton field oscillates coherently around the minimum of its potential and produces particles via parametric resonance, as indicated by the small dots and lines.

cosmologically relevant scales. The only relevant contribution from the symmetry breaking field during inflation is false vacuum energy.

The simplest potentials of hybrid inflation contain monomial polynomials of ϕ and a vacuum energy term, i.e.,

$$V(\phi) = V_0 \left[1 + \left(\frac{\phi}{\phi_0}\right)^p\right] . \tag{3.4}$$

Via the parameters ϕ_0 and V_0, hybrid inflation may be embedded at very different energy scales. In particular the field amplitude of the inflaton field may be of the order of $m_{\rm pl}$ or smaller. The reason is that the inflaton field does not necessarily carry the major part of the energy density, which can be provided by V_0.

Hybrid inflation requires additional scalar fields. The question about the origin of all these fields arises. Possible solutions are super-symmetric theories which have a large number of additional fields, the scalar super-partners of the fermions. Since super-symmetry, if it exists, has to be broken in nature, the scalar super-partner of an "ordinary" fermion can be relatively heavy. Hybrid potentials are also "natural" in the context of string theory or super-gravity (see, e.g., Refs. [78, 84, 105, 116, 117]). The most attractive feature of hybrid models is that the inflation field is only responsible for the inflationary expansion, while the symmetry breaking field reheats the universe via particle production and scattering of the produced particles. There is no need to couple the inflaton field directly to other degrees of freedom, unlike in the simpler versions of chaotic inflation.

The standard two-field model

The phase transition ending inflation and preheating *after* hybrid inflation is the main topic of part III of this thesis. For this purpose we choose a particular model for the symmetry breaking sector (for the fields and the coupling between them).

The simplest realization of a hybrid inflation model with two scalar fields as proposed

originally by Linde [73] is defined by the Lagrange density

$$\mathcal{L} = \frac{1}{2}\partial_\mu \Phi \partial^\mu \Phi + \frac{1}{2}\partial_\mu X \partial^\mu X - V(\Phi, X) \;, \tag{3.5}$$

with the hybrid potential

$$V(\Phi, X) = \frac{1}{2}m^2\Phi^2 + \frac{1}{2}g^2\Phi^2 X^2 + \frac{\lambda}{4}(X^2 - v^2)^2 \,. \tag{3.6}$$

For simplicity we have suppressed the dependence of all fields on the space-time arguments $x = (t, \mathbf{x})$. The quantum fields Φ and X, as represented by capital letters, are assumed to have non-vanishing classical expectation values

$$\langle \Phi \rangle = \phi \;, \tag{3.7}$$
$$\langle X \rangle = \chi \,. \tag{3.8}$$

The classical expectation values will also be denoted as the *order parameters* of the fields. We will refer to Φ (or ϕ) as the inflaton field, i.e., the field that couples to gravity, and to X as the symmetry breaking or Higgs field and to χ as its order parameter. The field X mediates the phase transition and is sometimes also dubbed "waterfall" field in the literature. Note that there is no quartic self-coupling present in the inflaton sector.

The shape of the classical hybrid potential $V(\phi, \chi)$ as defined by

$$V(\phi, \chi) = \frac{1}{2}m^2\phi^2 + \frac{1}{2}g^2\phi^2\chi^2 + \frac{\lambda}{4}(\chi^2 - v^2)^2 \,, \tag{3.9}$$

is shown in Fig. 3.2. $V(\phi, \chi)$ follows from the potential $V(\Phi, X)$ by replacing the quantum field operators by their classical expectation values.

Spinodal region

In the χ direction the potential has the form of a double-well close to $\phi \approx 0$ and is symmetric for larger values of ϕ. The critical value is at

$$\phi_\mathrm{c} = \frac{v\sqrt{\lambda}}{g} \,. \tag{3.10}$$

This is precisely the point where the classical mass term for the Higgs field, given by

$$m_\chi^2(\phi) = -\lambda v^2 + g^2\phi^2 \,, \tag{3.11}$$

is zero. Inflation stops, when the system reaches this point [73, 77]. The mass m_χ^2 is negative in the so-called spinodal region with $-\phi_\mathrm{c} < \phi < \phi_\mathrm{c}$ and positive everywhere else. The qualitative picture of this spinodal instability is as follows: In the spinodal region quantum fluctuations are exponentially amplified. The quantum fluctuations lead to corrections to the classical masses. Depending on the relative sizes of classical and

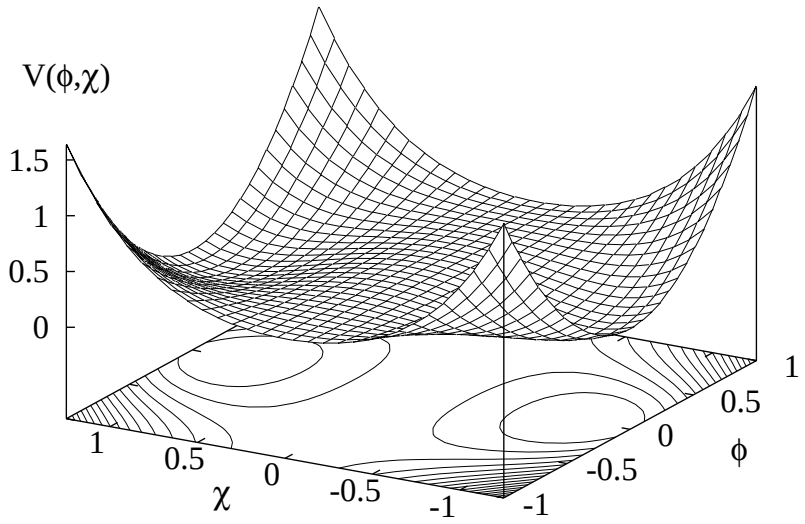

Figure 3.2: Generic shape of a hybrid potential $V(\phi, \chi)$ as a function of the classical fields ϕ and χ; at the base of this plot the contour lines of the potential are shown. Classically the potential has two stable minima located at $\phi = 0$ and $\chi = \pm\lambda v$. The potential is very flat in the ϕ-direction close to $\chi \approx 0$.

quantum contributions from the various fields the process of entering and leaving the spinodal region may be repeated several times in a dynamical evolution. However, via the back-reaction of the quantum fluctuations the dynamically negative masses should finally become positive, which stabilizes the system. The details will depend on the parameters chosen.

In previous investigations quantum fluctuations have been included without back reaction [118], with back reaction in the one-loop approximation [86] and in the Hartree approximation with an ultraviolet (UV) cutoff in a supersymmetric model including axions [78]. The model investigated in Ref. [78] is rather special; it incorporates several scalar degrees of freedom of a non-minimal supersymmetric standard model.

It is important to note that semiclassical one-loop approximations, which miss the back-reaction of the quantum fluctuations onto themselves, do not lead to a stabilization of the system in the spinodal regime. Hence, one cannot describe the false vacuum transition with semiclassical one-loop approximations. We will go beyond such approximations in this thesis.

3.1.3 Power-law inflation

As discussed in the previous Chapter a characteristic feature of the inflationary universe is an accelerated expansion of space-time. In many inflationary models the scale factor a indeed grows exponentially. However, strict exponential growth is not a necessary ingredient of the inflationary paradigm. Abott and Wise [119], Lucchin and Matarrese [106] and

other authors have discussed (shortly after the seminal paper on inflation by Guth [17]) inflationary cosmologies that are characterized by the scale factor growing like

$$a(t) \propto t^p \,, \tag{3.12}$$

where p is a constant greater than one. According to the power-law growth of the scale factor this scenario has been named *power-law inflation*. The starting point may be the inflaton potential defined by [120]

$$V(\phi) = V_0 \exp\left(\sqrt{\frac{2}{p}}\,\phi\right) . \tag{3.13}$$

The attractive feature of power-law inflation is that it is one of the very few analytically tractable models. It provides a useful foil for testing approximations. This feature has maintained its popularity, even though the basic model is not realistic, as inflation never comes to an end. Characteristic of power-law inflation is a constant spectral index. The running of n_S and n_T is zero. In particular the spectral indices for scalar and tensor perturbations are given by

$$n_S = 4 - 2\nu_S \,, \tag{3.14}$$

$$n_T = 3 - 2\nu_T \,, \tag{3.15}$$

with

$$\nu_S = \nu_T = \frac{3}{2} + \frac{1}{p-1} \,. \tag{3.16}$$

Note that $n_T = n_S - 1$. The scale-invariant Harrison-Zeldovich spectrum with $n_S = 1$ corresponds to the choice $p \to \infty$. In that limit power-law inflation also has a quasi-exponential growth of the scale factor $a(t)$.

In Fig. 3.3 we display the dependence of n_S on the power p. Also plotted are the allowed ranges from recent observations of the CMB and LSS.

3.1.4 Potentials with special features

In order to learn something about the possible form of the inflaton potential, as well as about approximation techniques, we can consider artificial potentials, which exhibit special features. These potentials can lead to sharp signatures in the calculated perturbation spectra. The slow-roll approximation may fail [121]. A typical example is a potential with a step [53, 121], defined as

$$V(\phi) = \frac{1}{2} m^2 \phi^2 \left[1 + c \tanh\left(\frac{\phi - \phi_{\rm step}}{d}\right)\right] . \tag{3.17}$$

Depending on the parameters, the calculated spectrum can significantly differ from a scale invariant spectrum. There are oscillations in the power spectrum. Note that the parameters in Eq. (3.17) are already constrained by WMAP, e.g. $c \sim 0.001$ [56].

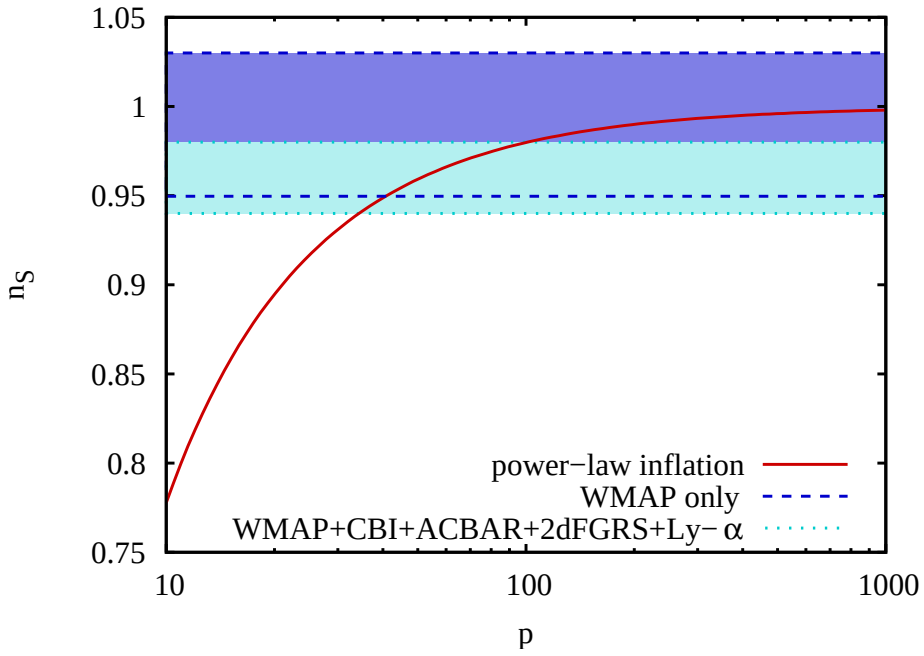

Figure 3.3: Dependence of the scalar spectral index n_S on the power p for power-law inflation (solid line); also shown is the allowed range from observations of the CMB and LSS; the area between the dashed lines corresponds to $n_S = 0.99 \pm 0.04$ (only WMAP data), and the area between the dotted lines to $n_S = 0.96 \pm 0.02$ (WMAP, CBI, ACBAR, 2dFGRS, and Ly-α data); these values are results of power-law fits without running of the spectral index and a ΛCDM cosmology, see Ref. [8]; from present data the Harrison-Zeldovich choice $n_S = 1$ cannot be excluded.

3.2 Multi-field inflation and other exotic scenarios

There are of course many other (more exotic) inflationary scenarios. In a typical grand unified theory the appearance of many scalar degrees of freedom usually cannot be avoided. Supersymmetry, if it exists, provides many scalar degrees of freedom. Also string theories have many scalar fields. Leaving aside completely different scenarios like brane inflation [122, 123] (this cannot be discussed within "ordinary" inflation, i.e., within the context of Chap. 2), the potential driving inflation can be more complex. Potentials with more than one scalar field may lead to multiple inflation, where the individual stages are smoothly connected, so that inflation does not interrupt completely.

Observations of the temperature anisotropies of the CMB by WMAP (first-year data analysis, see Refs. [8, 56]) reveal some statistical anomalies of the data with respect to the fit, which assumes a nearly scale invariant primordial power spectrum. In particular the low quadrupole (also observed by COBE-DRM) has stimulated a lot of speculation [124, 125]. The potential origin of superimposed oscillations, possibly present in the primordial power spectrum, has also been discussed [126, 127]. It should be said that from an observational point of view, all such exotic scenarios do not seem to be required at present. The Universe seems to support very simple ideas [128]. Concerning the low-ℓ phenomena of the temperature anisotropies power spectrum, we have to study and to understand the data in greater detail, e.g., with respect to possible foreground contamination. There is the question, whether the low-ℓ microwave background is cosmic [129].

For these reasons we will focus on single-field inflation in this thesis. Some special single-field inflation potentials can already lead to distinctive features in the primordial power spectrum.

Chapter 4

The Conventional Slow-Roll Approximation

In this Chapter the concept of slow-roll approximation is briefly reviewed. We will list the basic equations, in particular the expressions for the power spectra, the spectral indices, the running of the spectral indices, and the ratio of tensor to scalar perturbations.

We follow the presentation of Stewart and Lyth here [130]. A comprehensive description of the slow-roll approximation may also be found in Ref. [131]. Early investigations, to zero order in the slow-roll parameters, can be found in Refs. [18, 19, 20].

4.1 The method of slow-roll

Conceptionally the slow-roll expansion is an expansion around the limit of exact scale invariance ($n_S = 1$). This can be made clear from the expressions in power-law inflation, where the slow-roll expansion becomes exact if $p \to \infty$ (p is the power with which the scale factor grows in time). The relevant formula will be given in Sec. 5.4. Indeed this observation explains why the slow-roll expansion is expected to work for all models producing a scalar spectral index close to one.

The basis of slow-roll expansions is a set of slow-roll parameters, defined by

$$\epsilon \equiv -\frac{\dot{H}}{H^2} = \frac{1}{2}\left(\frac{\dot{\phi}}{H}\right)^2 , \ \delta_n \equiv \frac{1}{H^n\dot{\phi}}\frac{d^{n+1}\phi}{dt^{n+1}} . \tag{4.1}$$

In terms of ϵ, δ_1 and δ_2 the potential z''/z, appearing in the fluctuation equation for scalar perturbations [Eq. (2.45)], can be written as

$$\frac{z''}{z} = 2a^2H^2\left(1 + \epsilon + \frac{3}{2}\delta_1 + 2\epsilon\delta_1 + \epsilon^2 + \frac{1}{2}\delta_2\right) . \tag{4.2}$$

This expression is still exact. Assuming now that ϵ and δ_1 are constant and small, higher

terms $\delta_{n>1}$ must vanish and the equation for u_k is approximated by

$$u_k''(\eta) + \left(k^2 - \frac{A}{\eta^2}\right) u_k(\eta) = 0\,, \tag{4.3}$$

with

$$A = 2 + 6\epsilon + 3\delta_1 = \text{constant}. \tag{4.4}$$

The solutions to this equation are Hankel functions, i.e., Bessel functions of first and second kind. An analogous equation exists for gravitational waves. The crucial point is that A has to be exactly constant for the solutions to be Bessel functions. When taking into account higher orders of the slow-roll parameters the quantity A is no longer constant. There is thus no natural extension of the slow-roll approximation in terms of Bessel functions. In addition the slow-roll expansion lacks of an error-control theory.

There are some conceptional questions concerning the presentation of Stewart and Lyth [130]. A precisely constant value ϵ would imply $\epsilon = -\delta_1$, while Stewart and Lyth [130] take ϵ and δ_1 to be independently constant at different values. Formally this is impossible. Lidsey et al. discuss this aspect in Ref. [131]. However, the final expressions for the power spectra and spectral indices are not affected.

The precision of slow-roll predictions has been studied in detail in Ref. [132]. Even second order approximations in the slow-roll parameters may not be sufficient in any case. (We will shortly comment on counting the orders in Sec. 4.4.) As said above, the standard slow-roll approximation runs into serious difficulties, once the assumption of ϵ and δ_1 being constant is dropped. Different ways of improving the slow-roll approximation have been suggested, see e.g., Refs. [46, 133, 134, 135]. However, they often lead to rather involved expressions for power spectra and spectral indices and, more importantly, are not error-controlled. Other extensions rely on particular approximations for the behavior of the Hubble radius during inflation [136, 137] and so do not require that ϵ and δ_1 are *independently* small and constant.

It is not impossible though that our Universe is so close to exact scale invariance that any error from slow-roll approximations is subdominant. Further experimental observations of the CMB radiation and of galaxy clustering and redshift surveys will provide an answer in the future.

4.2 Normalized solution

The normalized solution to Eq. (4.3), with the correct asymptotic behavior [see Eq. (2.48)] at small scales, is obtained as

$$u_k(\eta) \;=\; \frac{\sqrt{\pi}}{2} e^{i(\nu+\frac{1}{2})\frac{\pi}{2}} (-\eta)^{1/2} H_\nu^{(1)}(-k\eta)(-\eta)^{1/2}\,, \tag{4.5}$$

where

$$\nu = \frac{3}{2} + 2\epsilon + \delta_1\,. \tag{4.6}$$

To first order in the slow-roll parameters the conformal time is given by

$$\eta = \int^t \frac{dt}{a(t)} \simeq -\frac{1}{aH}\frac{1}{1-\epsilon}\,. \tag{4.7}$$

Inflation ends once $\epsilon > 1$. With help of the above equations the asymptotic solution in the relevant regime $k\eta \to 0^-$ is obtained as

$$u_k(\eta) \to e^{i(\nu-\frac{1}{2})\frac{\pi}{2}} 2^{\nu-\frac{3}{2}} \frac{\Gamma(\nu)}{\Gamma(3/2)} \frac{1}{2k} (-\eta)^{-\nu+1/2}\,. \tag{4.8}$$

4.3 The power spectra

Substituting Eq. (4.8) in the general expression (2.51) the scalar power spectrum, to first order in the slow-roll parameters, reads [130]

$$P_S(k) \;\simeq\; [1 + 2(2 - \ln 2 - b)(2\epsilon + \delta_1) - 2\epsilon]\, \frac{2G}{\pi}\frac{H^4}{\dot\phi^2}\bigg|_{aH=k}\,, \tag{4.9}$$

where b is the Euler-Mascheroni constant, $2 - \ln 2 - b \simeq 0.7296$ and $\ln 2 + b - 1 \simeq 0.2704$. Note that the power spectrum is just rewritten in terms of the values the quantities had when the Hubble radius was crossed ($aH = k$). Nevertheless, it is the asymptotic power spectrum in the limit $k\eta \to 0^-$ or $k/aH \to 0^-$.

Similarly one finds for tensor perturbations [130]

$$P_T(k) \;\simeq\; [1 - 2(\ln 2 + b - 1)\epsilon]\, \frac{2GH^2}{\pi}\bigg|_{aH=k}\,. \tag{4.10}$$

4.4 Spectral indices

The scalar and tensor spectral indices are given by [130]

$$\begin{aligned} n_S(k) \;&\simeq\; 1 - 4\epsilon - 2\delta_1 - 2(1+c)\epsilon^2 + \frac{1}{2}(3-5c)\epsilon\delta_1 \\ &\quad -\frac{1}{2}(3-c)\delta_1^2 + \frac{1}{2}(3-c)\delta_2, \end{aligned} \tag{4.11}$$

$$n_T(k) \;\simeq\; -2\epsilon - (3+c)\epsilon^2 - (1+c)\epsilon\delta_1, \tag{4.12}$$

with $c \simeq 0.08145$. We will refer to these expressions as *second-order* slow-roll results, reflecting the appearance of second-order and squares of first-order slow-roll parameters. The expressions

$$n_S(k) \simeq 1 - 4\epsilon - 2\delta_1 \tag{4.13}$$

and

$$n_T(k) \simeq -2\epsilon \tag{4.14}$$

are the well-known results to *first order* in the slow-roll parameters. Eqs. (4.13) and (4.14) are widely used expressions and will also be compared to corresponding expressions of the uniform approximation.

It is not so obvious how we should count and name the orders in the slow-roll approximation, see, e.g., the discussion in Ref. [131]. We have avoided a terminology like *lowest-order* and *next-to-lowest order*. The latter would correspond to Eqs. (4.9)–(4.12) and, obviously, involves different orders of the slow-roll parameters in the expressions for P_S and n_S.

4.5 Further approximation of the background dynamics

So far all slow-roll expressions have been used without actually approximating the background equation for the inflaton field ϕ. Based on a Taylor expansion in the potential $V(\phi)$ and its derivatives, Liddle and Lyth [138] introduced an approximation for the background equations. This approach (formalized and expanded to higher orders by Liddle, Parsons, and Barrow [139]) leads to a simplification of the slow-roll parameters in the following form:

$$\epsilon = \frac{1}{2}\left(\frac{V'}{V}\right)^2 - \frac{1}{3}\left(\frac{V'}{V}\right)^4 + \frac{1}{3}\frac{V'^2V''}{V^3}, \tag{4.15}$$

$$\delta_1 = \frac{1}{2}\left(\frac{V'}{V}\right)^2 - \frac{V''}{V} - \frac{2}{3}\left(\frac{V'}{V}\right)^4 - \frac{1}{3}\left(\frac{V''}{V}\right)^2 + \frac{4}{3}\frac{V'^2V''}{V^3} + O(V'''). \tag{4.16}$$

Here we have followed the conventions of Stewart and Lyth [130]. Expanding the slow-roll parameters in terms of derivatives of the potential is quite popular in the literature. One reason, presumably, is that one does not have to solve the background equations numerically, which renders the "design" of a potential $V(\phi)$ simpler. Being an asymptotic expansion, this approximation will lead to extra errors, which can become large. We will explicitly demonstrate this when discussing particular models.

Part II

Calculation of the Inflationary Perturbation Spectrum

Chapter 5

The Uniform Approximation

In this Chapter we describe the method of uniform approximation for the calculation of inflationary perturbations, first presented in Ref. [43], and subsequently extended and improved in Refs. [44, 45].

Historically the uniform approximation began with the work of Langer [35, 36, 37, 38, 39, 40] and others, and was followed by notable contributions of Olver [41, 42], which we rely on. The method of uniform approximation employed here can be understood as a "uniformization" of the well-known Wentzel-Kramers-Brillouin (WKB) or Liouville-Green (LG) approximation [140, 141] in the presence of transition points.[1] The WKB approximation has also been applied to the problem of calculating the inflationary perturbation spectrum [127, 142, 143].

Asymptotic expansions of differential equations via approximants in terms of special functions can provide useful insight in problems which can be only numerically addressed. Realistic error bounds for the approximants, as well as for the physical observables derived from them, are of obvious importance for practical calculations.

In Sec. 5.1 we present the method of uniform approximation on the basis of the differential equations for the fluctuations during inflation. Then we turn to the calculation of the power spectra and their characterizing quantities like, e.g., the spectral indices and the ratio of tensor to scalar perturbations. The leading order approximation is presented in Sec. 5.2, the next-to-leading order in Sec. 5.3. We will provide closed expressions to leading and next-to-leading order with corresponding error bounds. In Sec. 5.4 we will investigate power-law inflation which is one of the very few analytically solvable models. In Sec. 5.5 we investigate simplifications of non-local expressions using local expansions. The results for power-law inflation together with the results from local expansions are utilized in Sec. 5.6 in order to calculate estimates of the error bounds, and in Sec. 5.7 in order to find a powerful improvement strategy. Finally, in Sec. 5.8 we comment on further expansions in terms of slow-roll parameters and calculate expressions for the spectral indices that can be compared to the standard slow-roll approximation.

[1] Adiabatic and semiclassical approximations like the WKB approximation have a long history in mathematics and physics. A short history of the uniform approximation can be found in Ref. [42], at the end of Chap. 11.

5.1 The method and general expressions

For our purpose, the key advantages of the uniform approximation are that it does away with WKB-like matching conditions [144], a procedure that fails to indicate the error of the approximation, has controlled error bounds over the entire domain of interest, is systematically improvable, and allows analytic simplifications in special cases of physical interest.

We begin our discussion of the uniform approximation by making the substitution

$$\frac{z''(\eta)}{z(\eta)} \equiv \frac{1}{\eta^2}\mathcal{C}^2(\eta) \tag{5.1}$$

in Eq. (2.45), yielding

$$u_k''(\eta) + \left[k^2 - \frac{\mathcal{C}^2(\eta)}{\eta^2}\right] u_k(\eta) = 0. \tag{5.2}$$

A similar substitution can be made for the case of tensor perturbations.

If, in Eq. (5.2), we make the assumption that $\mathcal{C}$ is constant then an exact solution in terms of Bessel functions is immediate. This is the case for power-law inflation, see Sec. 5.4. The problem is to solve the equation when $\mathcal{C}$ is not constant but slowly varies in time. Our aim is to do this without being forced to state $\mathcal{C}(\eta)$ in any real detail. We will now follow the presentation of Olver [42] and provide a summary of the treatment of uniform approximation for the differential equation of interest (5.2).

The differential equation we wish to solve is of the general form

$$\frac{d^2u(\eta)}{d\eta^2} = \left[b^2 g(\eta) + q(\eta)\right] u(\eta). \tag{5.3}$$

Depending on the behavior of $b^2g(\eta) + q(\eta)$ this equation has different approximating solutions. In the case that $b^2g(\bar{\eta}) + q(\bar{\eta}) = 0$ at the point $\bar{\eta}$, so $\bar{\eta}$ is a turning point, the solution is expressed in terms of Airy functions; if $g(\eta)$ has a pole of order $n \geq 2$ the LG approximation[2] must be employed [42]. In our case the relevant function is $-k^2 + \mathcal{C}^2(\eta)/\eta^2$; we have a turning point which will depend on the explicit form of $g(\eta)$ and a pole of order 2 in the limit $\eta \to 0^-$. Therefore, we have an Airy solution around the turning point which goes over to an LG solution for conformal time approaching zero. As will be shown later, this approximation fits the exact behavior of the solution accurately. For the two approximating solutions (Airy and LG), the convergence criteria are established in the following way. Assume that we have a pole of order $n \geq 2$ at a finite endpoint a_2 and that $g(\eta)$ and $q(\eta)$ are meromorphic functions of the form

$$g(\eta) = \frac{1}{(a_2 - \eta)^2} \sum_{s=0}^{\infty} f_s (a_2 - \eta)^s, \tag{5.4}$$

$$q(\eta) = \frac{1}{(a_2 - \eta)^2} \sum_{s=0}^{\infty} g_s (a_2 - \eta)^s. \tag{5.5}$$

[2]The LG approximation is essentially equivalent to the familiar Wentzel-Kramers-Brillouin (WKB) approximation. More precisely the WKB approximation enforces certain matching conditions [144].

Then the error control function (see Appendix A.1) converges if $g_0 = -1/4$. For a detailed proof of this important fact, see Ref. [42]. For the error control criteria to be satisfied in our case, we must make the choices

$$g(\eta) = \frac{1}{\eta^2}\left[\mathcal{C}^2(\eta) + \frac{1}{4}\right] - k^2 \tag{5.6}$$

$$\equiv \frac{\nu_S^2(\eta)}{\eta^2} - k^2, \tag{5.7}$$

$$q(\eta) = -\frac{1}{4\eta^2}. \tag{5.8}$$

The final form of Eq. (2.45) then becomes

$$u_k''(\eta) = \left\{-k^2 + \frac{1}{\eta^2}\left[\nu_S^2(\eta) - \frac{1}{4}\right]\right\} u_k(\eta)\,, \tag{5.9}$$

where $\nu_S^2 = (z''/z)\eta^2 + 1/4$ and the turning point is at $k^2 = \nu_S^2(\bar{\eta}_S)/\bar{\eta}_S^2$. Note that the turning point $\bar{\eta}_S$ is a given function of k.

In an exactly analogous fashion, the equation for the tensor modes (2.46) is written in the form

$$v_k''(\eta) = \left\{-k^2 + \frac{1}{\eta^2}\left[\nu_T^2(\eta) - \frac{1}{4}\right]\right\} v_k(\eta)\,, \tag{5.10}$$

where $\nu_T^2 = (a''/a)\eta^2 + 1/4$ and the turning point is at $k^2 = \nu_T^2(\bar{\eta}_T)/\bar{\eta}_T^2$.

Unlike the approach of matching solutions through regions I, II, and III in the potential z''/z (see Fig. 2.2) or a''/a, the idea of a uniform approximation is to provide a single approximating solution which converges uniformly in all three regions with a global, finite error bound. The normalization is determined once and for all by simply matching to the exact solution as $k \to \infty$.

To continue, we follow Olver in defining a new independent variable ξ and a new dependent variable U, given by [42]

$$\xi\left(\frac{d\xi}{d\eta}\right)^2 = g(\eta) \tag{5.11}$$

and

$$u = \left(\frac{d\xi}{d\eta}\right)^{-1/2} U. \tag{5.12}$$

In terms of the new variables, Eq. (5.3) becomes

$$\frac{d^2U}{d^2\xi} = \left[b^2\xi + \psi(\xi)\right] U, \tag{5.13}$$

where

$$\psi(\xi) = \left[4g(\eta)g''(\eta) - 5g'^2(\eta)\right]\frac{\xi}{16g^3(\eta)} + \frac{\xi q(\eta)}{g(\eta)} + \frac{5}{16\xi^2}, \tag{5.14}$$

$$\frac{2}{3}\xi^{3/2} = -\int_\eta^{\bar\eta}\sqrt{g(\eta)}d\eta, \quad \eta \geq \bar\eta, \tag{5.15}$$

$$\frac{2}{3}(-\xi)^{3/2} = \int_\eta^{\bar\eta}\sqrt{-g(\eta)}d\eta, \quad \eta \leq \bar\eta. \tag{5.16}$$

Now imagine neglecting $\psi(\xi)$ as a first approximation; then the potential is purely linear in ξ and the solution to the differential equation is given in terms of Airy functions (see Fig. 5.1 for a plot of the Airy functions). In the next order where $\psi(\xi)$ is no longer neglected, the derivation of the solution u becomes more involved. Fortunately, in Ref. [42] the general solution for Eq. (5.3) in the uniform approximation to all orders is derived with error bounds to be

$$u^{(1)}_{2n+1}(b,\xi) = \left[\frac{g(\eta)}{\xi}\right]^{-1/4}\left[\mathrm{Ai}(b^{2/3}\xi)\sum_{s=0}^{n}\frac{A_s(\xi)}{b^{2s}} + \frac{\mathrm{Ai}'(b^{2/3}\xi)}{b^{4/3}}\sum_{s=0}^{n-1}\frac{B_s(\xi)}{b^{2s}} + \epsilon^{(1)}_{2n+1}\right], \tag{5.17}$$

$$u^{(2)}_{2n+1}(b,\xi) = \left[\frac{g(\eta)}{\xi}\right]^{-1/4}\left[\mathrm{Bi}(b^{2/3}\xi)\sum_{s=0}^{n}\frac{A_s(\xi)}{b^{2s}} + \frac{\mathrm{Bi}'(b^{2/3}\xi)}{b^{4/3}}\sum_{s=0}^{n-1}\frac{B_s(\xi)}{b^{2s}} + \epsilon^{(2)}_{2n+1}\right], \tag{5.18}$$

with coefficients defined by an iterative procedure,

$$A_0(\xi) = 1 \quad \text{w.l.o.g.}, \tag{5.19}$$

$$B_s(\xi) = \frac{\pm 1}{2\sqrt{\pm\xi}}\int_0^\xi \left[\psi(v)A_s(v) - A_s''(v)\right]\frac{dv}{\sqrt{\pm v}}, \tag{5.20}$$

$$A_{s+1}(\xi) = -\frac{1}{2}B_s'(\xi) + \frac{1}{2}\int\psi(\xi)B_s(\xi)d\xi\,. \tag{5.21}$$

The upper signs in Eqs. (5.20) and (5.21) are to be taken on the right of the turning point $\bar\eta$, i.e., if $\eta \geq \bar\eta$, and the lower signs on the left of the turning point, equivalent to Eqs. (5.15) and (5.16). The error terms $\epsilon^{(1)}_{2n+1}$ and $\epsilon^{(2)}_{2n+1}$ are discussed in Appendix A.1. In the next and following Sections, we will calculate the leading ($n = 0$) and next-to-leading order ($n = 1$) solution for Eqs. (5.9) and (5.10) with explicit error bounds and derive the corresponding power spectra and spectral indices [44, 45].

(a)

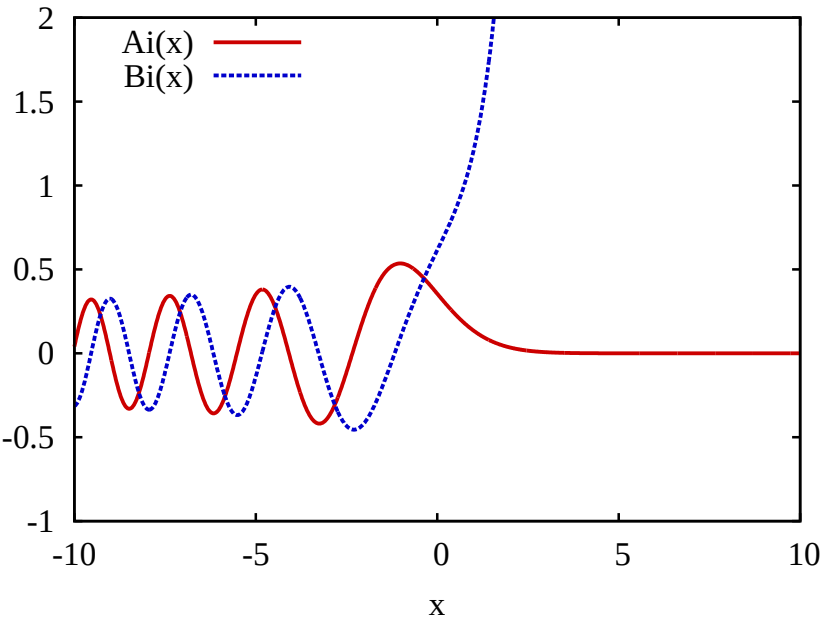

(b)

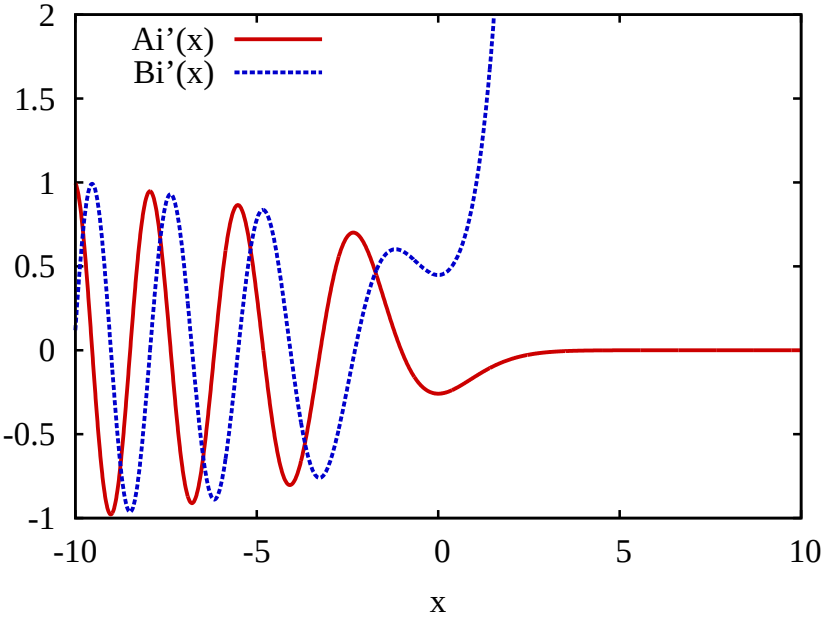

Figure 5.1: Plotted are the Airy functions: (a) Ai(x) (solid line) and Bi(x) (dashed line) (b) Ai$'$(x) (solid line) and Bi$'$(x) (dashed line) where the prime denotes a derivative with respect to x.

5.2 The leading order approximation

We now turn to the specific form of the approximating solutions at leading order.

5.2.1 Normalized solutions with error bounds

Taking $n = 0$ in Eqs. (5.17) and (5.18) we find a solution for $u_k(\eta)$ containing a part valid to the left of the turning point ($\eta \leq \bar{\eta}$) and a part valid to the right of the turning point ($\eta \geq \bar{\eta}$). The unnormalized solutions are

$$u^{(1)}_{k,\lessgtr}(\eta) = u^{(1)}_{k,1,\lessgtr}(\eta)[1+\epsilon^{(1)}_{k,1,\lessgtr}(\eta)], \tag{5.22}$$

$$u^{(2)}_{k,\lessgtr}(\eta) = u^{(2)}_{k,1,\lessgtr}(\eta)[1+\epsilon^{(2)}_{k,1,\lessgtr}(\eta)], \tag{5.23}$$

with

$$u^{(1)}_{k,1,\lessgtr}(\eta) = \left[\frac{f_\lessgtr(k,\eta)}{g_S(k,\eta)}\right]^{1/4} \mathrm{Ai}[f_\lessgtr(k,\eta)]\,, \tag{5.24}$$

$$u^{(2)}_{k,1,\lessgtr}(\eta) = \left[\frac{f_\lessgtr(k,\eta)}{g_S(k,\eta)}\right]^{1/4} \mathrm{Bi}[f_\lessgtr(k,\eta)]\,, \tag{5.25}$$

and

$$f_\lessgtr(k,\eta) = \mp\left\{\pm\frac{3}{2}\int_\eta^{\bar{\eta}_S} d\eta' \left[\mp g_S(k,\eta')\right]^{1/2}\right\}^{2/3}, \tag{5.26}$$

$$g_S(k,\eta) = \frac{\nu_S^2(\eta)}{\eta^2} - k^2\,, \tag{5.27}$$

$$|\epsilon^{(1)}_{k,1,\lessgtr}(\eta)| \leq \frac{1}{\lambda}\frac{M(f_\lessgtr)}{E(f_\lessgtr)\mathrm{Ai}(f_\lessgtr)}\left\{e^{\lambda\mathcal{V}_{\eta,\alpha}(\mathcal{E})}-1\right\}\,, \tag{5.28}$$

$$|\epsilon^{(2)}_{k,1,\lessgtr}(\eta)| \leq \frac{1}{\lambda}\frac{E(f_\lessgtr)M(f_\lessgtr)}{\mathrm{Bi}(f_\lessgtr)}\left\{e^{\lambda\mathcal{V}_{\beta,\eta}(\mathcal{E})}-1\right\}\,. \tag{5.29}$$

The lower index 1 reflects the order of the approximation, the functions with index $<$ are taken on the left of the turning point, and those with the index $>$ are to be taken on the right of the turning point. $M(\eta)$, $N(\eta)$, $\mathcal{V}_{\alpha,\beta}$, and λ are defined in Appendix A.1. An estimate for λ is $\lambda \simeq 1.04$. The error control function $\mathcal{E}(\eta)$ is given by

$$\mathcal{E}(\eta) = -\frac{1}{4}\int d\eta \left\{g_S^{-3/2}\left[g_S'' - \frac{5}{4}\frac{(g_S')^2}{g_S} - \frac{g_S}{\eta^2}\right]\right\} \pm \frac{5}{24|f_\lessgtr|^{3/2}}. \tag{5.30}$$

Inserting the explicit expression for $g_S(k,\eta)$, Eq. (5.27), and integrating by parts leads to

$$\mathcal{E}(\eta) = \frac{\nu_S(\nu_S'\eta-\nu_S)}{(\nu_S^2-k^2\eta^2)^{3/2}} + \int \frac{d\eta}{4\eta\sqrt{\nu_S^2-k^2\eta^2}}\left\{1-\left[\frac{\nu_S(\nu_S'\eta-\nu_S)}{\nu_S^2-k^2\eta^2}\right]^2\right\} \pm \frac{5}{24|f_\lessgtr|^{3/2}}. \tag{5.31}$$

Essentially the error terms $\epsilon^{(1,2)}_{k,1,\lessgtr}(\eta)$ in Eqs. (5.22) and (5.23) encapsulate the contributions to $u^{(1,2)}_{k,1,\lessgtr}(\eta)$ beyond leading-order. The general solution for $u_k(\eta)$ is a linear combination of the two fundamental solutions $u^{(1)}_k(\eta)$ and $u^{(2)}_k(\eta)$, viz.,

$$u_k(\eta) = Au^{(1)}_k(\eta) + Bu^{(2)}_k(\eta), \tag{5.32}$$

independent of the order of the approximation. In order to fix the constants A and B we have to construct a linear combination of $u^{(1)}_k(\eta)$ and $u^{(2)}_k(\eta)$ such that the result has the form $u_k(\eta) = e^{-ik\eta}/\sqrt{2k}$ in the limit $k \to \infty$. In this limit, the domain of interest is region I, far to the left of the turning point. In this case, for well-behaved ν_S, $f_<(k,\eta)$ is large and negative and we can employ the asymptotic forms [145]

$$\begin{aligned} \mathrm{Ai}(-x) &= \frac{1}{\pi^{1/2}x^{1/4}}\cos\left(\frac{2}{3}x^{3/2}\right) - \frac{\pi}{4}, \\ \mathrm{Bi}(-x) &= -\frac{1}{\pi^{1/2}x^{1/4}}\sin\left(\frac{2}{3}x^{3/2}\right) - \frac{\pi}{4}. \end{aligned} \tag{5.33}$$

Making the choices,

$$A = \sqrt{\frac{\pi}{2}}e^{i\frac{\pi}{4}}, \quad B = -i\sqrt{\frac{\pi}{2}}e^{i\frac{\pi}{4}}, \tag{5.34}$$

we find

$$u_{k,1,<}(\eta) = \lim_{-k\eta\to\infty}\frac{C}{\sqrt{2k}}\ \exp\left\{i\frac{3}{2}\left[f_<(k,\eta)\right]^{3/2}\right\}, \tag{5.35}$$

which is the required adiabatic form of the solution at short wavelengths and as $\eta \to -\infty$ (2.5). C is a constant phase factor which is meaningless when computing the power spectrum.

The $\eta \to 0^-$ limit defines the region of interest for calculating power spectra and the associated spectral indices. In this region, the $1/\eta^2$ pole dominates the behavior of the solutions and the Airy solution goes over to the LG solution. The LG form of the solution is more tractable than the Airy form, leading to simple expressions for the spectral indices. We now demonstrate how the Airy solution for small η approaches the LG solution. The linear combination of Eqs. (5.22) and (5.23) in first order with the appropriate normalization is given by

$$u_{k,1,\lessgtr}(\eta) = \sqrt{\frac{\pi}{2}}Cf^{1/4}_{\lessgtr}(k,\eta)g_S^{-1/4}(k,\eta)\left[\mathrm{Ai}(f_{\lessgtr}) - i\mathrm{Bi}(f_{\lessgtr})\right], \tag{5.36}$$

with the error bound

$$|\epsilon_{k,1,\lessgtr}(\eta)| \ \leq\ \frac{\sqrt{2}}{\lambda}\left\{\exp[\lambda\mathcal{V}_{\eta,\alpha}(\mathcal{E})] + \exp[\lambda\mathcal{V}_{\beta,\eta}(\mathcal{E})] - 2\right\} \tag{5.37}$$

derived from Eqs. (5.28), (5.29), (A.3), and (A.5). (The explicit form of the variation of $\mathcal{E}$ will be discussed below.) For small η we are on the right of the turning point; the

argument of the Airy functions, i.e., $f_>(k,\eta)$, becomes large and the Airy functions can be approximated by [145]

$$\mathrm{Ai}(x) = \frac{1}{2\sqrt{\pi}}\, x^{-1/4} \exp\left(-\frac{2}{3}x^{2/3}\right), \tag{5.38}$$

$$\mathrm{Bi}(x) = \frac{1}{\sqrt{\pi}}\, x^{-1/4} \exp\left(\frac{2}{3}x^{2/3}\right), \tag{5.39}$$

which leads to

$$u_{k,1,>}(\eta) = \frac{C}{\sqrt{2}} g_S^{-1/4}(k,\eta) \left[\frac{1}{2}\exp\left\{-\frac{2}{3}\left[f_>(k,\eta)\right]^{3/2}\right\} - i\exp\left\{\frac{2}{3}\left[f_>(k,\eta)\right]^{3/2}\right\}\right]. \tag{5.40}$$

For computing the power spectra in the $k\eta \to 0^-$ limit, only the growing part of the solution is relevant:

$$u_{k,1,>}(\eta) = \lim_{k\eta\to 0^-} -iC\sqrt{\frac{-\eta}{2\nu_S(\eta)}} \exp\left\{\frac{2}{3}\left[f_>(k,\eta)\right]^{3/2}\right\}. \tag{5.41}$$

We now discuss the variation of $\mathcal{E}$. (See Appendix A.1 for a short discussion on the variation of a function in general.) We are interested in the error bound of $u_{k,1}$ over the full domain of interest $-\infty < \eta < 0^-$, which implies $\beta = -\infty$ and $\eta \to 0^-$. In the general case,

$$\mathcal{V}_{-\infty,\eta}(\mathcal{E}) = \sum |\mathcal{E}(\alpha) - \mathcal{E}(\beta)|, \tag{5.42}$$

where the sum is over all individual monotonic subintervals $(\alpha,\beta) \subseteq (-\infty,\eta)$ of $\mathcal{E}$. In the special case of monotonic $\mathcal{E}$ over the full range of η the answer can be given in a simplified form: By inserting the definition of $g_S(k,\eta)$ from Eq. (5.27) into Eq. (5.30) and integrating by parts we find for the variation of the error control function:

$$\mathcal{V}_{-\infty,\eta}(\mathcal{E}) = \left| -\frac{1}{2\nu_S} - \frac{1}{4}\int \frac{d\eta}{\eta\sqrt{\nu_S^2 - k^2\eta^2}} \left\{1 - \left[\frac{\nu_S(\nu_S'\eta - \nu_S)}{\nu_S^2 - k^2\eta^2}\right]^2\right\}\right|, \tag{5.43}$$

where it is understood that η has to be taken in the limit $\eta \to 0^-$.

5.2.2 Power spectra

Once the approximate solutions to Eqs. (2.45) and (2.46) have been found in the manner described above, the relevant power spectra can easily be computed. The definition of the scalar power spectrum is

$$\begin{aligned} P_S(k) &= \lim_{k\eta\to 0^-} \frac{k^3}{2\pi^2}\left|\frac{u_k(\eta)}{z(\eta)}\right|^2 \\ &= \lim_{k\eta\to 0^-} \frac{k^3}{2\pi^2}\left|\frac{u_{k,1,>}(\eta)}{z(\eta)}\right|^2 \left|1 + \epsilon_{k,1,>}(\eta)\right|^2 \\ &= \lim_{k\eta\to 0^-} P_{1,S}(k)\left[1 + \epsilon^P_{k,1,S}(\eta)\right], \end{aligned} \tag{5.44}$$

with

$$\epsilon^{P}_{k,1,S} = 2\mathrm{Re}\,\epsilon_{k,1,>} + |\epsilon_{k,1,>}|^2 \,, \tag{5.45}$$

and $P_{1,S}(k)$ denoting the power spectrum for the scalar perturbations in the leading order approximation. It is understood that all time-dependent quantities are to be evaluated in the limit $\eta \to 0^-$. Substituting the LG expression for u_k from Eq. (5.41), we have

$$P_{1,S}(k) = \lim_{k\eta\to 0^-} \frac{k^3}{4\pi^2}\frac{1}{|z(\eta)|^2}\frac{-\eta}{\nu_S(\eta)} \exp\left\{\frac{4}{3}\left[f_>(k,\eta)\right]^{3/2}\right\}, \tag{5.46}$$

with the error bound for the power spectrum given in Eq. (5.45).

The calculation for the tensor power spectrum follows along the same lines, yielding

$$P_{1,T}(k) = \lim_{k\eta\to 0^-} \frac{k^3}{4\pi^2}\frac{1}{|a(\eta)|^2}\frac{-\eta}{\nu_T(\eta)} \exp\left\{\frac{4}{3}\left[\tilde{f}_>(k,\eta)\right]^{3/2}\right\}, \tag{5.47}$$

with the error being controlled exactly in the same manner as in Eqs. (5.45) and (5.43) with the subscripts $S \to T$ and $\tilde{f}(k,\eta)$ indicating that $g_S(k,\eta)$ in Eq. (5.26) has to be replaced by $g_T(k,\eta)$.

5.2.3 Ratio of tensor to scalar perturbations

The tensor to scalar ratio, $R(k)$, is given by

$$R(k) = \frac{8P_{1,T}(k)}{P_{1,S}(k)}\left(1+\epsilon^{R}_{k,1}\right), \tag{5.48}$$

with the error term

$$\epsilon^{R}_{k,1} = \frac{1+\epsilon^{P}_{k,1,T}}{1+\epsilon^{P}_{k,1,S}} - 1. \tag{5.49}$$

Note that if $\nu_S = \nu_T$ the error is identically zero. In other words, the ratio of tensor to scalar perturbations is exact already at leading order in the uniform approximation if $\nu_S = \nu_T$. We will come back to this point when we discuss power-law inflation where ν is not only constant but also has the same for scalar and tensor perturbations.

5.2.4 Spectral indices

Next we discuss the evaluation of the spectral indices. In general the spectral index for scalar perturbations can be obtained from the power spectrum via Eq. (2.55) and for tensor perturbations via Eq. (2.56). Differentiation of the power spectrum with respect to k is straightforward. It is important to note that the turning point $\bar{\eta}_S$ is a function of k, since $k = -\nu_S(\bar{\eta}_S)/|\bar{\eta}_S|$ where $\nu_S(\bar{\eta}_S)$ is the value of $\nu_S(\eta)$ at the turning point $\eta = \bar{\eta}_S$. Using this relation, we find

$$n_{1,S}(k) = 4 - 2k^2 \lim_{k\eta\to 0^-} \int_{\bar{\eta}_S}^{\eta} \frac{d\eta'}{\sqrt{g_S(k,\eta')}}. \tag{5.50}$$

Following from the discussion above, the error in the spectral index arises only from the k-dependent part of the error in the power spectrum, which vanishes if ν_S is constant. Thus the error in the spectral index is sensitive only to the time variation of ν_S. To estimate this error, the spectral index as written in Eq. (2.55) can be expressed via the leading order power spectrum in the following form:

$$\begin{aligned} n_S(k) &= 1 + \frac{d\ln(P_{1,S} + \epsilon^P_{k,1,S})}{d\ln k} \\ &= 1 + \frac{d\ln P_{1,S}}{d\ln k} + \frac{d\ln(1+\epsilon^P_{k,1,S})}{d\ln k} \qquad (5.51) \\ &\approx 1 + \frac{d\ln P_{1,S}}{d\ln k} + k\frac{d\epsilon^P_{k,1,S}}{dk} \qquad (5.52) \\ &\equiv n_{1,S}(k) + \epsilon^n_{k,1,S}, \qquad (5.53) \end{aligned}$$

with

$$\epsilon^n_{k,1,S} = k\frac{d\epsilon^P_{k,1,S}}{dk}\ . \qquad (5.54)$$

Here we have neglected error terms of order $(\epsilon^P_{k,1,S})^2$.

The above analysis can be carried out for tensor perturbations in an identical fashion, including the error estimation, with the replacement $\nu_S \to \nu_T$. The spectral index for gravitational waves is given by

$$n_{1,T}(k) = 3 - 2k^2 \lim_{k\eta\to 0^-} \int_{\bar\eta_T}^{\eta} \frac{d\eta'}{\sqrt{g_T(k,\eta')}}. \qquad (5.55)$$

5.3 The next-to-leading order approximation

We now turn to the specific form of the solutions at next-to-leading order.

5.3.1 Normalized solutions

To proceed to the next order, we first write the unnormalized solution for u_k, following directly from Eqs. (5.17) and (5.18):

$$\begin{aligned} u^{(1)}_{k,3\lessgtr}(\eta) &= \left[\frac{f_\lessgtr(k,\eta)}{g_S(k,\eta)}\right]^{1/4} \{\mathrm{Ai}[f_\lessgtr(k,\eta)]\,(A_0[f_\lessgtr(k,\eta)] + A_1[f_\lessgtr(k,\eta)]) \\ &\quad + \mathrm{Ai}'[f_\lessgtr(k,\eta)]B_0[f_\lessgtr(k,\eta)]\}\,, \qquad (5.56) \\ u^{(2)}_{k,3\lessgtr}(\eta) &= \left[\frac{f_\lessgtr(k,\eta)}{g_S(k,\eta)}\right]^{1/4} \{\mathrm{Bi}[f_\lessgtr(k,\eta)]\,(A_0[f_\lessgtr(k,\eta)] + A_1[f_\lessgtr(k,\eta)]) \\ &\quad + \mathrm{Bi}'[f_\lessgtr(k,\eta)]B_0[f_\lessgtr(k,\eta)]\}\,, \qquad (5.57) \end{aligned}$$

with

$$A_0[f_{\lessgtr}(k,\eta)] = 1, \tag{5.58}$$

$$B_0[f_{\lessgtr}(k,\eta)] = \frac{\pm 1}{2\sqrt{\pm f_{\lessgtr}(k,\eta)}}\int_0^{f_{\lessgtr}}\frac{\psi(v)}{\sqrt{\pm v}}dv, \tag{5.59}$$

$$A_1[f_{\lessgtr}(k,\eta)] = -\frac{1}{2}B_0'[f_{\lessgtr}(k,\eta)] + \frac{1}{2}\int \psi[f_{\lessgtr}]B_0[f_{\lessgtr}(k,\eta)]d[f_{\lessgtr}(k,\eta)]. \tag{5.60}$$

The error bounds in next-to-leading order are given by [derived from Eqs. (A.1) and (A.2)]:

$$|\epsilon^{(1)}_{k,3,\lessgtr}| \leq 2E^{-1}(f_{\lessgtr})M(f_{\lessgtr})\mathcal{W}_{f_{\lessgtr},\beta}, \tag{5.61}$$

$$|\epsilon^{(2)}_{k,3,\lessgtr}| \leq 2E(f_{\lessgtr})M(f_{\lessgtr})\mathcal{W}_{\alpha,f_{\lessgtr}}, \tag{5.62}$$

with

$$\mathcal{W}_{f_{\lessgtr},\beta} = \exp\left\{2\lambda\mathcal{V}_{f_{\lessgtr},\beta}(|f_{\lessgtr}|^{1/2}B_0)\right\}\mathcal{V}_{f_{\lessgtr},\beta}(|f_{\lessgtr}|^{1/2}B_1), \tag{5.63}$$

$$\mathcal{W}_{\alpha,f_{\lessgtr}} = \exp\left\{2\lambda\mathcal{V}_{\alpha,f_{\lessgtr}}(|f_{\lessgtr}|^{1/2}B_0)\right\}\mathcal{V}_{\alpha,f_{\lessgtr}}(|f_{\lessgtr}|^{1/2}B_1), \tag{5.64}$$

and

$$B_1(f_{\lessgtr}) = \frac{\pm 1}{2\sqrt{\pm f_{\lessgtr}}}\int_0^{f_{\lessgtr}}\frac{dv}{\sqrt{\pm v}}[\psi(v)A_1(v) - A_1''(v)], \tag{5.65}$$

$$A_1''(v) = -\frac{1}{2}B_0'''(v) + \frac{1}{2}[\psi'(v)B_0(v) + \psi(v)B_0'(v)], \tag{5.66}$$

recursively derived from Eqs. (5.20) and (5.21).

As in leading order, the general solution $u_k(\eta)$ is a linear combination of $u_k^{(1)}(\eta)$ and $u_k^{(2)}(\eta)$. Fortunately, we will not have to calculate the normalization again; in the limit $\eta \to -\infty$ the Bunch-Davies vacuum is the exact solution of the differential equation for $u_k(\eta)$, and, in this limit, all corrections from the next-to-leading order terms are subdominant and of no interest.

A further simplification follows from the fact that only the growing solution $u_k^{(2)}(\eta)$ is relevant to determining the power spectrum and spectral index and that we can restrict ourselves to the solution for u_k in the limit $k\eta \to 0^-$. Employing once again the approximation for the Bi-function for large, positive argument, Eq. (5.39), and in addition, the approximation for its derivative,

$$\mathrm{Bi}'(x) = \frac{1}{\sqrt{\pi}}\, x^{1/4}\exp\left(\frac{2}{3}x^{2/3}\right), \tag{5.67}$$

the normalized $u_k(\eta)$ in the relevant regime is

$$u_{k,3,>}(\eta) \stackrel{k\eta\to 0^-}{=} -iC\sqrt{-\frac{\eta}{\pi\nu_S(\eta)}}\exp\left\{\frac{2}{3}\left[f_>(k,\eta)\right]^{3/2}\right\} \times\left\{1-\frac{1}{2}B_0'(f_>)+\sqrt{f_>(k,\eta)}B_0(f_>)+\frac{1}{2}\int\psi(f_>)B_0(f_>)d(f_>)\right\}. \tag{5.68}$$

The error bound is given by

$$|\epsilon_{k,3,>}|\leq 2f_>^{-1/4}\exp\left\{\frac{2}{3}\left[f_>(k,\eta)\right]^{3/2}\right\}\mathcal{W}_{\alpha,f_\leqslant}. \tag{5.69}$$

5.3.2 Power spectra

Analyzing B_0 in detail shows that the derivative B_0' and the integral over ψB_0 are subdominant in the limit $k\eta\to 0^-$. Hence the only term leading to a correction of the power spectrum is B_0 itself. From the general expression (5.44), the power spectrum at next-to-leading order is

$$P_{2,S}(k)\stackrel{k\eta\to 0^-}{=}P_{1,S}(k)\left|1+2\sqrt{f_>(k,\eta)}B_0[f_>(k,\eta)]\right|, \tag{5.70}$$

with $P_{1,S}(k)$ as defined in Eq. (5.46) and

$$B_0(f_>) = \frac{1}{2\sqrt{f_>}}\int_0^{f_>}\frac{\psi(v)}{\sqrt{v}}dv, \tag{5.71}$$

$$\psi(v) = \frac{5}{16v^2}+\frac{v\left(4g_Sg_S''-5g_S'^2\right)}{16g_S^3}-\frac{v}{4\eta^2g_S}. \tag{5.72}$$

The first term in B_0 [after writing out $\psi(v)$ according to Eq. (5.72)] can be integrated immediately. The contribution from the lower integration limit, which appears divergent at a first glance, cancels with contributions from the other terms in the integral. This can be shown by expanding $\psi(v)$ around zero and integrating explicitly. The error bound can be calculated in the same way as in leading order. We find

$$P_S(k)=\lim_{k\eta\to 0^-}\frac{k^3}{2\pi^2}\left|\frac{u_{k,3,>}(\eta)}{z(\eta)}\right|^2\left[1+\epsilon^P_{k,3,S}(\eta)\right], \tag{5.73}$$

with

$$\epsilon^P_{k,3,S}=\frac{2\epsilon_{k,3,>}}{u_{k,3,>}(\eta)}. \tag{5.74}$$

Here we have neglected terms of quadratic order in $\epsilon_{k,3,>}$.

5.3.3 Spectral indices

The spectral index at this order, $n_{2,S}$, as calculated from its definition (2.55), denotes

$$n_{2,S}(k) = n_{1,S}(k) + \lim_{k\eta\to 0^-} \frac{2k}{|1+2\sqrt{f_>}B_0|}\frac{\partial(\sqrt{f_>}B_0)}{\partial k}, \tag{5.75}$$

where $n_{1,S}(k)$ is given by Eq. (5.50). Evaluating the derivative of B_0 with respect to k leads to the following expression for the spectral index:

$$\begin{aligned} n_{2,S}(k) &= n_{1,S}(k) + \frac{2k^2}{2|1+2\sqrt{f_>}B_0|} \\ &\times \left[\int_{\bar\eta_S}^{\eta}\frac{d\eta'}{\sqrt{g_S}}\left(\frac{g_S''}{2g_S^2}-\frac{15g_S'^2}{g_S^3}-\frac{1}{4\eta^2 g_S}\right) - \int_0^{f_>}\frac{dv}{4v^2}\left(\psi(v)-\frac{15}{8v^2}\right)\int_{\bar\eta_S}^{\eta}\frac{d\eta'}{\sqrt{g_S}}\right]. \end{aligned} \tag{5.76}$$

The error estimate for the spectral index can be obtained in a similar way as in leading order, just as for the power spectrum. We find

$$n_S(k) = n_{2,S}(k) + \epsilon^n_{k,3,S}, \tag{5.77}$$

with

$$\epsilon^n_{k,3,S} \approx k\frac{d\epsilon^P_{k,3,S}}{dk}. \tag{5.78}$$

In the case of the errors in next-to-leading order we have to evaluate $\mathcal{W}_{\alpha,f_{\lessgtr}}$ which is defined in Eq. (5.64). This can be done in principle but the result is rather long and complicated. Rather than calculating the integrals explicitly, we will present a simple and powerful improvement strategy in Sec. 5.7, utilizing the general formulae at next-to-leading order without implementing them fully.

Proceeding in the same way as for the scalar perturbations the power spectrum and the spectral index for the tensor perturbations, including error bounds, can be calculated. $P_{2,T}(k)$ can be obtained from Eqs. (5.70)–(5.72) by replacing $P_{1,S}(k)$ with $P_{1,T}(k)$ on the r.h.s. of Eq. (5.70) and replacing $g_S(k,\eta)$ and its derivatives in Eq. (5.72) by $g_T(k,\eta)$ and its derivatives. The spectral index for the tensor perturbations can easily be derived by replacing $n_{1,S}(k)$ and $g_S(k,\eta)$ and its derivatives in Eq. (5.76) on the right hand side by $n_{1,T}(k)$ and $g_T(k,\eta)$ and its derivatives.

5.4 Analytical solutions for power-law inflation

In order to demonstrate the accuracy of our approximation we now investigate power-law inflation, where ν_S and ν_T are constant. Power-law inflation, as defined by the potential $V(\phi) = V_0\exp(\sqrt{2/p}\ \phi)$, is one of the few classes of exactly solvable models. Both the dynamical background equations as well as the equations for the fluctuation modes can be solved analytically. Exact expressions for the power spectra have been given, e.g., by Stewart and Lyth [146]. (See also the discussion in Ref. [131].)

We will restrict the discussion first to scalar perturbations. Tensor perturbations can be treated in the same way replacing $\nu_S \to \nu_T$. The equation for the scalar modes u_k [Eq. (5.9)] simplifies to a Bessel equation of the form

$$u_k''(\eta) = \left[-k^2 + \frac{1}{\eta^2}\left(\nu_S^2 - \frac{1}{4}\right)\right] u_k(\eta)\,, \tag{5.79}$$

where

$$\nu_S = \nu_T = \frac{3}{2} + \frac{1}{p-1}\,. \tag{5.80}$$

The conformal time follows from the exact expression

$$\eta = -\frac{1}{aH}\frac{1}{(1/p-1)}\,. \tag{5.81}$$

The normalized solution with the correct asymptotic behavior at small scales ($k\eta \to -\infty$) is given by

$$u_k(\eta) \;=\; \frac{\sqrt{\pi}}{2}(-\eta)^{1/2} H^{(1)}_{\nu_S}(-k\eta)\,, \tag{5.82}$$

where $H^{(1)}_{\nu_S}$ is the Hankel function of the first kind of order ν_S [146]. Note that the solutions are only exact up to a (meaningless) phase factor. In Eq. (5.82) we have dropped a phase factor $e^{i(\nu_S+1/2)\pi/2}$, which is included in the expressions of Lyth and Stewart. The solution in Eq. (5.82) has the advantage that in the limit $k\eta \to 0^-$ the two orthogonal solutions reproduce the e^x and e^{-x} asymptotic of the uniform approximation. This will facilitate the direct comparison of the various numerical, analytical or approximate results.[3]

Inserting the solution in Eq. (5.82) in the general expression (5.44) and calculating the limit $k\eta \to 0^-$ provides the exact power spectrum

$$P_S^{\rm ex}(k) \;=\; \frac{2^{2\nu_S-2}}{2\pi^3}\Gamma^2(\nu_S)(-k\eta)^{1-2\nu_S}k^2\left(\frac{H}{a\dot\phi}\right)^2\Bigg|_{k=aH} \tag{5.83}$$

$$\;=\; \frac{2^{2\nu_S-2}}{\pi^2}e^{-2\nu_S}\nu_S^{2\nu_S-1}(-k\eta)^{1-2\nu_S}k^2\left(1+\frac{1}{6\nu_S}+\frac{1}{72\nu_S^2}+\cdots\right)\left(\frac{H}{a\dot\phi}\right)^2\Bigg|_{k=aH}\,, \tag{5.84}$$

where we have used Stirling's formula to replace the Γ function. Note that the power spectrum is rewritten in terms of the values the quantities had when the Hubble radius was crossed ($k/aH \to 0$). This is a subtle point, see, e.g., the discussion of Eq. (5.83) in

[3] Solutions very similar to the one in Eq. (5.82) have been found for the slow-roll approximation, see Sec. 4.2. Note that in Chap. 4 the quantity ν has been approximated to first order in the slow-roll parameters. While for power-law inflation both definitions agree exactly, the same is not true in general.

Ref. [131]. Since the k-dependence is explicit in Eq. (5.83), the scalar spectral index is easily found from Eq. (2.55)

$$n_S = 4 - 2\nu_S \,. \tag{5.85}$$

For power-law inflation the tensor power spectrum and the tensor spectral index are given by

$$P_T^{\rm ex}(k) = \frac{2}{p} P_S^{\rm ex}(k) \,, \tag{5.86}$$

$$n_T = 3 - 2\nu_T \,. \tag{5.87}$$

Next we turn to the corresponding expressions in the uniform approximation. The general expression for the power spectrum in leading and next-to-leading order in the uniform approximation is given by Eq. (5.46) and Eq. (5.70), respectively. For constant ν_S, the integrals which appear in these expressions can be solved analytically, leading to the results

$$P_S^{(1)}(k) = \frac{2^{2\nu_S-2}}{\pi^2} e^{-2\nu_S} \nu_S^{2\nu_S-1} (-k\eta)^{1-2\nu_S} k^2 \left(\frac{H}{a\dot{\phi}}\right)^2 \Bigg|_{k=aH} , \tag{5.88}$$

$$P_S^{(2)}(k) = \frac{2^{2\nu_S-2}}{\pi^2} e^{-2\nu_S} \nu_S^{2\nu_S-1} (-k\eta)^{1-2\nu_S} k^2 \left(1 + \frac{1}{6\nu_S}\right) \left(\frac{H}{a\dot{\phi}}\right)^2 \Bigg|_{k=aH} . \tag{5.89}$$

Comparison of these results with the exact power spectrum in Eq. (5.84) reveals a nice feature of the uniform approximation for the special case of power-law inflation: Improving the uniform approximation order by order leads to matching corrections to the Γ-function in powers of inverse ν.

A more rigorous analysis of the errors in the uniform approximation along the lines explained in Sec. 5.2 and 5.3 shows that the leading order solution is bounded by the absolute value of the relative error

$$|\epsilon_{>,1,2}| \leq \sqrt{2} \left(\frac{1}{6\nu_S} + \frac{\lambda}{72\nu_S^2} + \cdots \right) , \tag{5.90}$$

where $\lambda \simeq 1.04$ [42]. The error in the power spectrum given in Eq. (5.88) falls comfortably within the bound.

Similarly, we can exactly solve the integrals in the expressions for the spectral indices in leading and next-to-leading order, Eqs. (5.50) and (5.76). We find that the spectral index in leading order is already exact

$$n_S^{(1)} = n_S^{(2)} = 4 - 2\nu_S . \tag{5.91}$$

This is an important result demonstrating the high accuracy of the uniform approximation already at leading order. There are no higher order corrections to be expected since the corrections to the power spectrum in second order, Eq. (5.89), are k-independent. We

can also evaluate the error bound for the spectral index from Eq. (5.54) for constant ν as a cross-check: Consistent with obtaining the exact value of n_S, we find that the error vanishes.

Next, we give the corresponding expressions in the slow-roll approximation. Traditionally, results for slow-roll inflation are calculated at $k = aH$ (see Sec. 4.3). Following this choice, the result for power-law inflation is [46]

$$P_S^{SR}(k) = \frac{H^4}{4\pi^2\dot{\phi}^2}\left[1 - \frac{2}{p}(c+1) + \frac{2}{p^2}\left(c^2 + c - \frac{5}{2} + \frac{\pi^2}{4}\right)\right]. \tag{5.92}$$

The scalar spectral index is given by

$$n_S^{SR} = 1 - \frac{2}{p} - \frac{2}{p^2}. \tag{5.93}$$

Apparently, in the limit of exact scale invariance ($n_S = 1$, which is the case for $p \to \infty$) the slow-roll result for n_S becomes exact.

Before proceeding, we note that for power-law inflation $\nu = \nu_S = \nu_T$ can take values between 1.5 and 2.5 for $p \to \infty$ and $p = 2$, respectively. In Fig. 5.2 we display the relative error of the power spectrum in the uniform approximation to leading-order (LO), next-to-leading order (NLO) and to next-to-next-to-leading order (NNLO) as a function of ν. The relative errors are $\sim$10% at LO, $\sim$0.5% at NLO and $\sim$0.1% at NNLO, respectively. The error of the power spectrum in the uniform approximation does not change dramatically as a function of ν. This robustness of the error control is a key feature of the uniform approximation.

Slow-roll is known to be inaccurate for small values of p [132]. We therefore pick $p = 2$ as a test case—equivalent to $\nu_S = 5/2$. The slow-roll result for the scalar power-spectrum to first order in the slow-roll parameters has an error of almost 30% [44], while the leading-order uniform approximation has an error of roughly 7% (see Fig. 5.2). The slow-roll result to second order in the slow-roll parameters is still inaccurate to 9%, which is worse than the result from the uniform approximation at leading order. The uniform approximation at next-to-leading order has the remarkably small error of only 0.2% (see Fig. 5.2). This is a very encouraging result.

In addition we can compare the spectral index for power-law inflation. For the case $p = 2$, the slow-roll approximation clearly does not lead to a good answer, as the exact result is $n_S = -1$ while the slow-roll answer is $n_S = -0.5$ (second-order result). Of course $p = 2$ does not represent a realistic model for inflation. At higher values of p the slow-roll answer improves dramatically. The amplitude of the power spectrum in slow-roll approximation also enhances rapidly for larger values of p. It becomes exact only for $p \to \infty$. In Fig. 5.3 we display the relative error of n_S in the slow-roll approximation to first and second order in the slow-roll parameters which corresponds to the first and second inverse powers in p [see Eq. (5.93)]. At $p \approx 10$ the result to second order in the slow-roll parameters is smaller than $\sim 0.1\%$. Note that this result holds only for power-law inflation with no running of the spectral index. The uniform approximation for n_S is exact already at leading-order, independent of the choice of the power p.

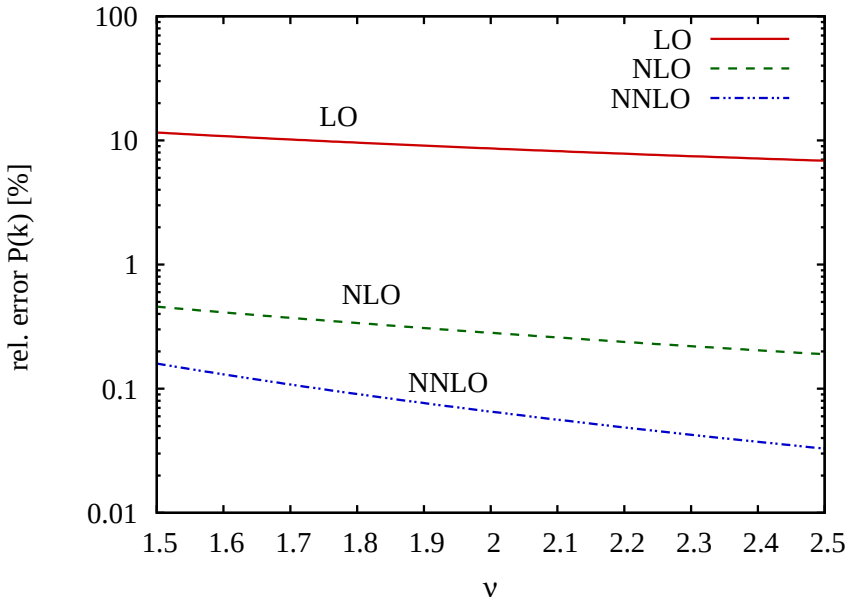

Figure 5.2: Relative error (in percent) of the power spectrum for the uniform approximation to leading order (LO, solid line), next-to-leading order (NLO, dashed line) and next-to-next-to-leading order (NNLO, dashed-dotted line) as a function of the parameter ν; the LO gives an accuracy $\sim 10\%$, the NLO $\sim 0.5\%$ and the NNLO $\sim 0.1\%$. Note that for power-law inflation the errors are k-independent, i.e., the power spectra are inaccurate by a simple global normalization factor.

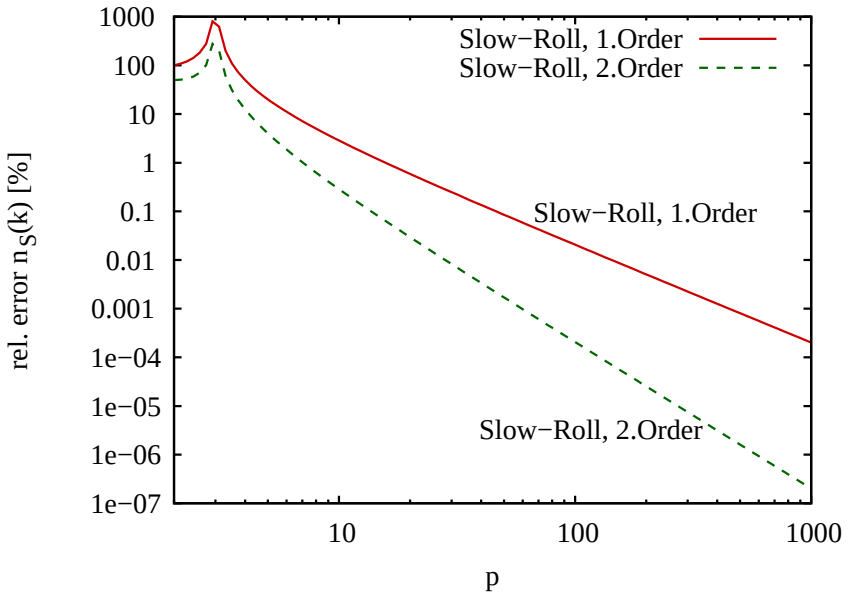

Figure 5.3: Relative error (in percent) of the scalar spectral index n_S for the slow-roll approximation to first (solid line) and second order (dashed line) in the slow-roll parameters as a function of the power p in power-law inflation; the slow-roll approximation becomes exact for $p \to \infty$; the uniform approximation is exact already at leading-order, independent of the choice of the power p.

As we will show in Sec. 5.7 the results for power-law inflation are very useful in order to improve the accuracy of the leading-order uniform approximation in the case of time-dependent ν.

5.5 Local approximations: Expansion around the turning points

After we have discussed the $\nu = \text{const.}$ case in detail, we now turn back to the general case of time dependent ν_S and ν_T.

The results for the power spectra and the spectral indices to leading and next-to-leading order in the uniform approximation are non-local expressions. In order to compare them with conventional slow-roll results it is desirable to have local expressions for some physical quantities of interest. Moreover, local approximations will turn out to be very useful simplifying the calculation of the error control functions and improving accuracy of the leading order expressions (see Sec. 5.6 and 5.7). Again the analysis is identical for the scalar and tensor cases so we address the scalar case first.

We note that the leading-order power spectra in the uniform approximation involve integrals of the form [see, e.g., Eq. (5.46)]

$$I_1(k) = \int_{\bar{\eta}_S}^{\eta} d\eta \sqrt{g_S(k,\eta)} = \int_{\bar{\eta}_S}^{\eta} d\eta \sqrt{\frac{\nu_S^2(\eta)}{\eta^2} - k^2}\,. \tag{5.94}$$

The leading order expressions for the spectral indices involve integrals with a square-root singularity at the turning point $\bar{\eta}_S$, i.e., [see, e.g., Eq. (5.50)]

$$I_{-1}(k) = \int_{\bar{\eta}_S}^{\eta} \frac{d\eta}{\sqrt{g_S(k,\eta)}} = \int_{\bar{\eta}_S}^{\eta} \frac{d\eta}{\sqrt{\frac{\nu_S^2(\eta)}{\eta^2} - k^2}}\,. \tag{5.95}$$

Similar integrals appear in the case of tensor perturbations, with ν_S replaced by ν_T. In the relevant limit $k\eta \to 0^-$, where the perturbation spectra are calculated, the integrals are dominated by the pole term $1/\eta^2$ under the square root. The integrand in the integral I_{-1} vanishes indeed linearity in this limit. In addition, for many inflationary models ν_S is also slowly varying with time. It is therefore justified to expand ν_S in a Taylor series. Including terms up to second order derivatives, $\nu_S(\eta)$ reads

$$\nu_S^2(\eta) = \bar{\nu}_S^2 + 2\bar{\nu}_S\bar{\nu}_S'\,(\eta - \bar{\eta}_S) + (\bar{\nu}_S'^2 + \bar{\nu}_S''\bar{\nu}_S)(\eta - \bar{\eta}_S)^2 + \mathcal{O}[(\nu - \bar{\nu}_S)^3]\,. \tag{5.96}$$

The bar indicates that the quantities are evaluated at the turning point $\bar{\eta}$, defined by $k\bar{\eta} = -\nu(\bar{\eta})$. The turning point is k-dependent and so is, e.g., $\bar{\nu}_S$. If in Eq. (5.96) only the first term of the Taylor series is included, the terminology *ultra-local* (approximation) will be used.

With the expansion in Eq. (5.96) the integrals in Eqs. (5.94) and (5.95) can be solved exactly. Solutions from the ultra-local part of a local expansion of ν_S correspond to the

results from the case of power-law inflation, with ν_S replaced by $\bar{\nu}_S$ and analogously ν_T replaced by $\bar{\nu}_S$.

As an example we now calculate the scalar spectral index at leading order in the uniform approximation as given by Eq. (5.50). To second order in derivatives we find

$$n_S(k) \simeq 4 - 2\bar{\nu}_S \left\{ 1 - \frac{\bar{\nu}'_S}{\bar{\nu}_S}\bar{\eta}_S \left(1 - \frac{\pi}{2}\right) + \frac{\bar{\eta}_S^2}{2}\left[\frac{\bar{\nu}'^2_S}{\bar{\nu}_S^2}(2-\pi) + \frac{\bar{\nu}''_S}{\bar{\nu}_S}(1-\pi)\right]\right\} . \quad (5.97)$$

This is a simplification of the non-local result. For the tensor spectral index we find analogously

$$n_T(k) \simeq 3 - 2\bar{\nu}_T \left\{ 1 - \frac{\bar{\nu}'_T}{\bar{\nu}_T}\bar{\eta}_T \left(1 - \frac{\pi}{2}\right) + \frac{\bar{\eta}_T^2}{2}\left[\frac{\bar{\nu}'^2_T}{\bar{\nu}_T^2}(2-\pi) + \frac{\bar{\nu}''_T}{\bar{\nu}_T}(1-\pi)\right]\right\} . \quad (5.98)$$

Using simple test functions with a mild variation of the potential ν, we have verified that it is adequate (at the one percent level) to keep terms up to second order derivatives. The accuracy of such simplified leading-order results will also be checked numerically with several representative examples in Chap. 7.

5.6 Estimate of the leading-order error bound

Although we can calculate (in principle) the error bound for the power spectra from the general expressions in Eqs. (5.28) and (5.30), it is convenient to have simpler estimates for the errors.

We begin by considering the case of constant ν, where the k-independent error bound for the power spectrum in leading order of the uniform approximation is found by substituting Eq. (5.90) in Eq. (5.45)

$$|\epsilon_1^P| \leq 2\sqrt{2}\left(\frac{1}{6\nu} + \frac{\lambda}{72\nu^2} + \frac{1}{36\sqrt{2}\nu^2} + \cdots\right) , \quad (5.99)$$

the generic ν denoting either of ν_S or ν_T. This bound is rigorous and useful, though the prefactor is not optimally sharp for the case of constant ν.

Suppose now that $\nu(\eta)$ varies slowly with time. Fix k and consider the value of $\nu(\eta)$ at the turning point $\bar{\eta}(k)$, defined by $k\bar{\eta} = -\nu(\bar{\eta})$. Given the slow variation of $\nu(\eta)$, this value $\bar{\nu}(k)$ is a slowly varying function of k. By expanding the expression for the error control function of Eq. (5.30) locally around the turning point as in the previous Section, we obtain what is effectively a derivative expansion of the error term. The leading term in this expansion, which is free of derivatives, has the same form as the expression above for constant ν, though it now carries the mild k-dependence of the variable-ν case,

$$|\epsilon_{k,1}^P| \lesssim 2\sqrt{2}\left[\frac{1}{6\bar{\nu}(k)} + \frac{\lambda}{72\bar{\nu}^2(k)} + \frac{1}{36\sqrt{2}\bar{\nu}^2(k)} + \cdots\right] . \quad (5.100)$$

This bound is not meant to be rigorous, since higher order terms in the derivative expansion are not included. However, it is effective and useful in the case of slowly varying $\nu(\eta)$.

Before proceeding, we make a few observations on the nature of the error terms. In the case of constant ν, i.e., for power-law inflation, we have seen that the spectral index is exact already at leading order of the uniform approximation. All higher orders lead to a k-independent amplitude correction for the power spectrum. Because $\nu_S = \nu_T$ in the constant ν case, the ratio of tensor to scalar perturbations is also exact.

5.7 A simple and powerful improvement of the leading order

The next-to-leading order results for u_k and v_k and the corresponding power spectra and spectral indices contain several integrals over η, which are tedious to evaluate [see, e.g., Eqs. (5.70) and (5.76)]. In contrast, the results at next-to-leading order for the case of constant ν turned out to be very simple. In essence, higher order terms in the uniform approximation generate a prefactor which occurs in the Stirling series for $\Gamma(\nu)$ [147]. In particular

$$\Gamma^2(\nu) = \frac{1}{2\pi} e^{-2\nu} \nu^{2\nu-1} \left(1 + \frac{1}{6\nu} + \frac{1}{72\nu^2} - \frac{31}{6480\nu^3} - \frac{139}{155520\nu^4} + \dots\right) \quad (5.101)$$

$$\equiv \frac{1}{2\pi} e^{-2\nu} \nu^{2\nu-1} [\Gamma^*(\nu)]^2 \quad (5.102)$$

with

$$\Gamma^*(\nu) \equiv 1 + \frac{1}{12\nu} + \frac{1}{288\nu^2} - \frac{139}{51840\nu^3} + \cdots . \quad (5.103)$$

We know this prefactor a-priori to be present in the case of constant ν (see Sec. 5.4). The all-orders prefactor $[\Gamma^*(\nu)]^2$ improves the normalization of the power spectrum dramatically. The first and second term represent the leading order and next-to-leading order corrections, respectively.

The natural question arises as to whether or not it is possible to utilize these results to improve the leading order expressions without recourse to full computation of the sub-leading approximations.

For most viable inflationary models, ν varies slowly and corrections from the derivatives of ν are sub-dominant. The full next-to-leading order machinery may not be required if ν is sufficiently well-behaved. In this Section we implement this idea and derive improved leading-order results for the power spectra. Note that, at leading order, the spectral index is exact for constant ν. Thus, the main improvement is to be expected in the amplitude of the power spectrum.

First, we make two important observations: (i) The next-to-leading order expression for the power spectrum [see, e.g, Eq. (5.70)] has the form of a multiplicative correction to the leading order power spectrum and (ii) the correction factor involves a non-local integral expression.

For the case of constant ν this correction factor reduces at next-to-leading order to the k-independent normalization correction, as given by the first two terms in Eq. (5.103).

For time-dependent and slowly varying $\nu(\eta)$, the error bound for the power spectrum is in fact dominated by an amplitude prefactor which has only a subdominant contribution to the spectral index. This can be understood as follows. Suppose that we split the scattering potential in the form

$$\nu^2(\eta) - \frac{1}{4} = \bar{\nu}^2 - \frac{1}{4} + \nu^2(\eta) - \bar{\nu}^2, \tag{5.104}$$

and choose the η-independent but k-dependent constant $\bar{\nu}(k)$ to be the value of $\nu(\eta)$ at the turning point. This splitting allows us to identify two separate contributions to the total error term for the power spectrum,

$$\epsilon_{k,1}^P = \bar{\epsilon} + \tilde{\epsilon}. \tag{5.105}$$

The term $\bar{\epsilon}$ arises solely from the ultra-local contribution in the derivative expansion of ν, and by explicit calculation it is known to be of the form

$$\begin{aligned} \bar{\epsilon} &= [\Gamma^*(\bar{\nu})]^2 - 1 \\ &= \frac{1}{6\bar{\nu}(k)} + \frac{1}{72\bar{\nu}^2(k)} - \frac{31}{6480\bar{\nu}^3(k)} - \frac{139}{155520\bar{\nu}^4(k)} + \cdots . \end{aligned} \tag{5.106}$$

We do not have to calculate the error term $\bar{\epsilon}$ with the ultra-local approximation $\nu(S) \simeq \bar{\nu}$ explicitly, since this is the same as for constant ν with ν replaced by $\bar{\nu}(k)$, i.e., Eq. (5.103) can be used immediately. The remaining error term $\tilde{\epsilon}$ satisfies an integral equation of the form considered by Olver [42], with a reduced inhomogeneity; explicit calculation leads to the rigorous bound

$$|\tilde{\epsilon}| \leq \frac{\mathcal{V}(\mathcal{E} - \bar{\mathcal{E}})}{\mathcal{V}(\bar{\mathcal{E}})} \left[1 + \mathcal{O}(|\bar{\epsilon}|)\right] |\bar{\epsilon}| \,. \tag{5.107}$$

Here $\mathcal{E}$ is the full error control function, $\bar{\mathcal{E}}$ is the error control function for the case of constant $\nu = \bar{\nu}(k)$, and $\mathcal{V}(\cdot)$ indicates total variation as defined in Appendix A.1.

In the generic case of slowly varying $\nu(\eta)$ this expression clearly shows that $\tilde{\epsilon}$ is significantly reduced in comparison to $\bar{\epsilon}$. Therefore we are motivated to absorb the ultra-local contributions from higher order corrections into the power spectrum, leading to an improved leading-order expression

$$\tilde{P}_1(k) = P_1(k)[\Gamma^*(\bar{\nu})]^2. \tag{5.108}$$

This improvement applies to both the scalar and tensor power spectra, with $\nu_S(\eta)$ and $\nu_T(\eta)$ respectively. Since typical values of $\nu \sim 2$ occur for both scalar and tensor fluctuations, the terms on the right hand side of Eq. (5.108) correspond to amplitude corrections of order 10%, 0.35%, 0.06%, and 0.006%, respectively (see Fig. 5.2). These can be viewed primarily as local normalization corrections.

To complete the discussion, we can obtain a non-rigorous estimate for the size of $\tilde{\epsilon}$, again using a derivative expansion in $\mathcal{E}$ to isolate the leading local contributions. In this

expansion, the leading derivative-free terms in $\mathcal{E}-\bar{\mathcal{E}}$ must cancel, and therefore the leading term is proportional to the first derivative of $\nu(\eta)$. We find

$$\begin{aligned} |\tilde{\epsilon}| &\lesssim \frac{3}{2}\left|\frac{\bar{\nu}'}{k}\right|\left[1+\mathcal{O}(|\bar{\epsilon}|)\right]|\bar{\epsilon}| \\ &\lesssim \frac{1}{4\bar{\nu}(k)}\left|\frac{d\ln\bar{\nu}(k)}{d\ln k}\right|\left[1+\mathcal{O}\left(\frac{1}{\bar{\nu}(k)}\right)\right], \end{aligned} \tag{5.109}$$

where we have used the chain rule to write the derivative in terms of a derivative of $\bar{\nu}(k)$ with respect to k and have used the explicit form for $\bar{\epsilon}(k)$ [45]. It is understood that this is not a rigorous inequality, since we have neglected the higher order terms in the derivative expansion, but it is well-motivated and useful for slowly-varying $\nu(\eta)$. This error estimate determines the order to which the local corrections (5.108) should be taken into account. For instance, when ν is slowly varying, most of the error can be compensated using Eq. (5.108). Examples will be specified in Chap. 7, where we explicitly demonstrate the success of this improvement procedure. As is to be expected, the ratio $R(k)$ is much less sensitive to the normalization error compared to the amplitude of the power spectrum. For this quantity, the error is well estimated by Eq. (5.109).

5.8 Slow-roll redux

It is possible to simplify the approximate expressions for the spectral indices[4], as presented in Sec. 5.5, one step further by expanding them in terms of slow-roll parameters ϵ and δ_i. Obtaining expressions from the local approximants for n_S and n_T [Eqs. (5.97) and (5.98)] is straightforward: we simply expand ν_S, ν_T, and their derivatives in terms of slow-roll parameters. A crucial point to keep in mind is the value of k in terms of which the results are stated. In the slow-roll expansion the evaluation of the slow-roll parameters is traditionally given at horizon crossing, $-k\eta \to 1$, a somewhat arbitrary choice due to the uncontrolled nature of the approximation. As shown in detail in by Steward in Ref. [133] calculating the slow-roll parameters at a convenient time close to horizon crossing leads to small finite corrections in power spectra and spectral indices. In our case, the natural expansion point is the turning point, therefore a truly direct comparison with slow-roll results, such as those of Ref. [46], is rather complicated.

The starting point is an expression which connects the conformal time η with the slow-roll parameters [131]

$$\eta \simeq -\frac{1}{aH}\left[1+\epsilon+3\epsilon^2+2\epsilon\delta_1+15\epsilon^3+20\epsilon^2\delta_1+2\epsilon\delta_1^2+2\epsilon\delta_2+\cdots\right]. \tag{5.110}$$

It follows from Eq. (5.110) that to first order in the slow-roll parameters, $\eta \simeq -(1+\epsilon)/aH$ [this expression can be compared to Eq. (4.7)]. Using Eq. (5.110) and for scalar

[4]Obtaining expressions for the power spectra is also possible. The results from the improved leading-order uniform approximation should be used in order to do this.

perturbations

$$\nu_S^2 = \frac{z''}{z}\eta^2 + \frac{1}{4}, \tag{5.111}$$

and the expression for z''/z given in Eq. (4.2), we can write $\bar{\nu}_S$, $\bar{\nu}_S'\bar{\eta}_S$ and $\bar{\nu}_S''\bar{\eta}_S^2$ in terms of ϵ and δ_n. We find for the different contributions to second order in the slow-roll parameters[5]:

$$\bar{\nu}_S = \frac{3}{2} + 2\bar{\epsilon} + \bar{\delta}_1 + \frac{16}{3}\bar{\epsilon}^2 + \frac{14}{3}\bar{\epsilon}\bar{\delta}_1 - \frac{1}{3}\bar{\delta}_1^2 + \frac{1}{3}\bar{\delta}_2 + \mathcal{O}(\bar{\epsilon}^3), \tag{5.112}$$

$$\bar{\eta}_S\bar{\nu}_S' = -4\bar{\epsilon} - 5\bar{\epsilon}\bar{\delta}_1 + \bar{\delta}_1^2 - \bar{\delta}_2 + \mathcal{O}(\bar{\epsilon}^3), \tag{5.113}$$

$$\bar{\eta}_S^2\bar{\nu}_S'' = 4\bar{\epsilon}^2 + 5\bar{\epsilon}\bar{\delta}_1 - \bar{\delta}_1^2 + \bar{\delta}_2 + \mathcal{O}(\bar{\epsilon}^3)\,. \tag{5.114}$$

As before, the bar indicates that the slow-roll parameters are to be calculated at the turning point, and $\mathcal{O}(\bar{\epsilon}^3)$ represents all slow-roll terms of third order and higher. Finally, inserting Eqs. (5.112)-(5.114) into the local expression for the scalar spectral index (5.97) allows us to write the spectral index in terms of slow-roll parameters:

$$\begin{aligned} n_S(k) \simeq\ & 1 - 4\bar{\epsilon} - 2\bar{\delta}_1 - 8\bar{\epsilon}^2\left(\frac{17}{6} - \pi\right) - 10\bar{\epsilon}\bar{\delta}_1\left(\frac{73}{30} - \pi\right) \\ & + 2(\bar{\delta}_1^2 - \bar{\delta}_2)\left(\frac{11}{6} - \pi\right)\,. \end{aligned} \tag{5.115}$$

Thus, starting from the non-local expression for the scalar spectral index given by the leading-order uniform approximation [Eq. (5.50)], we have arrived at a local expression for n_S in terms of slow-roll parameters by employing two expansions: First we expanded the integrand in the expression for the spectral index in a derivative expansion in $\bar{\nu}_S$, to solve the integral in Eq. (5.50). Then we further expanded the result in slow-roll parameters. However, the two expansions are not independent; had we decided to stop the expansion in derivatives in ν_S after the first term we would not have obtained the second order slow-roll contributions from the expansion of the second derivative of ν_S. If one wants results quoted to some order in slow-roll parameters, this requires going up to a finite order in derivatives of $\bar{\nu}_S$; however, written in this way, it is *a priori* not obvious which expansion is the dominant one—either the expansion in derivatives of $\bar{\nu}_S$ or the expansion in slow-roll parameters. In the absence of further information regarding ν_S itself, the question cannot be answered satisfactorily. This demonstrates one of the inherent difficulties of deriving higher order expressions for the spectral index via Taylor expansions without having a well-defined error bound.

The analogous result in the slow-roll approximation [Eq. (4.11)] agrees to first order in the slow-roll parameters [Eq. (4.13)]. The forms of the higher order contributions are apparently different due to the difference in evaluation points and the different approximations employed. However, both results should be treated with some caution: (i) Without an error control theory, it is not clear that inclusion of higher order terms actually improves

[5] In Ref. [44] we have given the expression including third-order terms.

the accuracy of the result (convergence is not guaranteed since the Taylor expansion leads only to an asymptotic expansion); (ii) the evaluation point of the slow-roll parameters leads to an uncertainty in the calculation—if one really wants results accurate to the per cent level, this uncertainty is important. In order to obtain results with high accuracy, error controlled approximations are necessary.

For completeness we also give the equivalent result for the tensor spectral index, derived from a slow-roll expansion of the local result, Eq. (5.98). We find

$$n_T(k) \simeq -2\bar{\epsilon} - \left(\frac{34}{3} - 3\pi\right)\bar{\epsilon}^2 - \left(\frac{28}{3} - 3\pi\right)\bar{\epsilon}\bar{\delta}_1 \,, \tag{5.116}$$

where we have used

$$\frac{a''}{a} = 2a^2H^2\left(1 - \frac{1}{2}\epsilon\right). \tag{5.117}$$

As for the scalar spectral index, the result agrees with Eq. (4.12) to first order in the slow-roll parameters.

Chapter 6

Numerical Implementation

In this Chapter we describe the numerical implementation of the exact mode-by-mode integration and the uniform approximation and its simplifications. Some additional technical details can be found in Appendix A.2. Since the uniform approximation is useful both in setting initial conditions for the exact numerical solution, and as a complete semi-analytic method in its own right, we discuss it first below (Sec. 6.1). The exact mode-by-mode integration follows in Sec. 6.2. A dedicated test of power-law inflation poses as a benchmark for testing the accuracy of the various numerical implementations. Important results are presented in Sec. 6.3.

6.1 Leading-order uniform approximation: Numerical issues

6.1.1 Preliminaries

We begin by addressing some technical points and introducing conventions. Since the conformal time is defined only up to a constant, we set it to zero at the end of inflation. If the given model does not have a natural end to inflation this point is somewhat arbitrary and we set η to zero typically a number of e-folds after the highest mode of interest freezes out.

The power spectrum and the spectral index are to be calculated in the limit $k\eta \to 0^-$, so that the LG approximation can be used. To avoid accumulation of numerical error, however, these quantities should not be calculated directly in this limit. Since the freeze-out happens soon after the turning point is crossed, the computation is carried out some e-folds after the turning point for each respective mode, but well before the end of inflation. The linear combination of both solutions to the mode equations, in terms of Ai- and Bi-functions, is then completely dominated by the exponentially growing part. We found that carrying out the computations four or five e-folds after the respective turning point provided sufficient accuracy.

In the computations described below, the Ai- and Bi-functions were calculated with the algorithm given in Ref. [148].

6.1.2 The mode solutions

The full solutions $u_{k,1,>}(\eta)$ and $u_{k,1,<}(\eta)$ are not needed for the calculation of the power spectrum and the spectral index. Nevertheless, it is useful to calculate some of them for selected momenta k in order to compare the leading order uniform solutions to the exact numerical solutions found from a mode-by-mode integration of the differential equations. For $\eta < \bar{\eta}$ we can calculate the integrals appearing in $f_<(k,\eta)$, as defined in Eq. (5.26) numerically via

$$\int_{\eta}^{\bar{\eta}} d\eta' \sqrt{g(k,\eta')} = \left(\int_{\eta}^{\eta_\mathrm{i}} + \int_{\eta_\mathrm{i}}^{\bar{\eta}} \right) d\eta' \sqrt{g(k,\eta')}, \tag{6.1}$$

where η_i is an initial value of the conformal time. In the actual numerical routine we therefore have to know the second integral before we can calculate the uniform solutions left of the turning point: This is achieved by an additional run of the integrator for the background equations.

6.1.3 Power spectra and spectral indices

The power spectra for scalar and tensor perturbations in leading order of the uniform approximation are given by Eqs. (5.46) and (5.47). The integrals are calculated using a trapezoidal rule with non-equidistant discretization in conformal time. As mentioned above, we avoid calculating the spectra numerically in the limit $k\eta \to 0^-$, but instead do so some 4-5 e-folds after the turning point. In the case of power-law inflation analytical results are available for the leading order contributions to the power spectra (see Sec. 5.4). We have checked that the power spectra numerically calculated from Eqs. (5.46) and (5.47) are in agreement with these analytic results (see Sec. 6.3 for more details).

The spectral indices in the uniform approximation may be calculated either by numerically differentiating the power spectra, or by using the formulae in Eqs. (5.50) and (5.55). In Appendix A.2.2 we describe how to deal with the inverse square root singularities appearing in the integrals to be performed in the second case.

6.2 Mode-by-mode numerical integration

6.2.1 Initial conditions and mode functions

In order to numerically calculate the mode functions, we must satisfy the initial condition requirement, i.e., in the limit $k\eta \to -\infty$,

$$u_k(\eta) \longrightarrow \frac{1}{\sqrt{2k}} e^{-ik\eta}. \tag{6.2}$$

Two difficulties in imposing this formal initial condition immediately arise. First, in any numerical solution, the calculation must begin at a finite initial time, thus for modes with small enough values of k, the condition $k\eta \to -\infty$ may not be fulfilled. Second, for modes at larger k values, there are very many oscillations before the turning point is reached, naively requiring very fine time steps if the entire temporal range must be handled numerically.

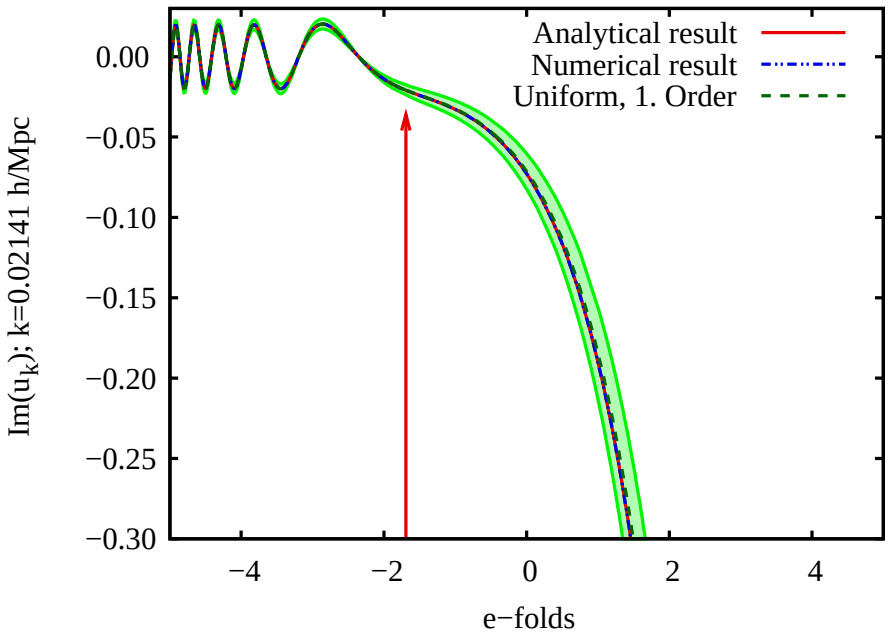

Figure 6.1: Imaginary (growing) part of the scalar mode function for a power-law model with $p = 11$ for the mode $k = 0.0214\,h\,\mathrm{Mpc}^{-1}$. The solid red line is the exact analytical solution, the dashed-dotted blue line the result from the numerical solution of the exact equations, and the dashed green line the uniform approximation to leading order; the results of analytical and uniform approximation calculations are almost on top of each other. The arrow shows the turning point and the green band is the estimated error bound for the leading order uniform approximation.

To circumvent these problems, we use the uniform approximation to set initial conditions in a regime where it is exponentially accurate. For each mode, we take as initial condition the uniform approximation result at roughly 20 zeros, i.e., 10 oscillations, before the turning point for that mode. The number of zeros from a given time to the turning point can be estimated by $n\pi \approx k[\bar{\eta}(k) - \eta]$. As shown below, this initialization procedure suppresses numerical errors, especially in the high-k regime where the precision of the power spectrum and the spectral index is improved without taking smaller time steps. In addition, only a smaller number of "active" modes, i.e., the modes that are within some 20 zeros before the turning point and not yet frozen out, need be considered at any time. In the regime of small k, we first note that as inflation has to start somewhere in practical numerical calculations, this introduces a lowest value for k, defined by the criterion that

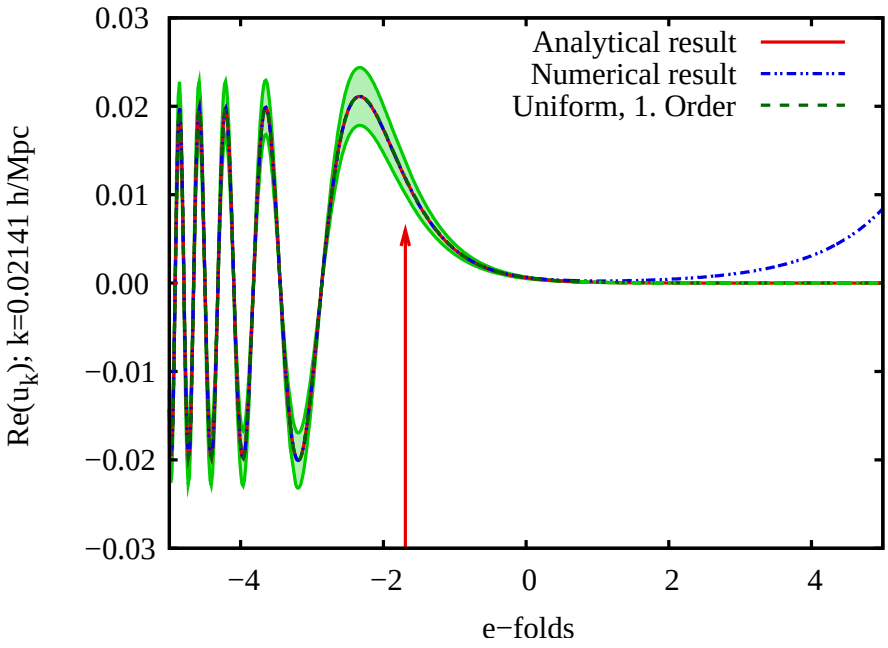

Figure 6.2: Real (damped) part of the scalar mode function for a power-law model following Fig. 6.1; we made no attempt of fine-tuning the meaningless initial phase of the numerical solution so that we observe a slight rise of the numerical solution around 2 e-folds here; the absolute value is not affected (Fig. 6.3).

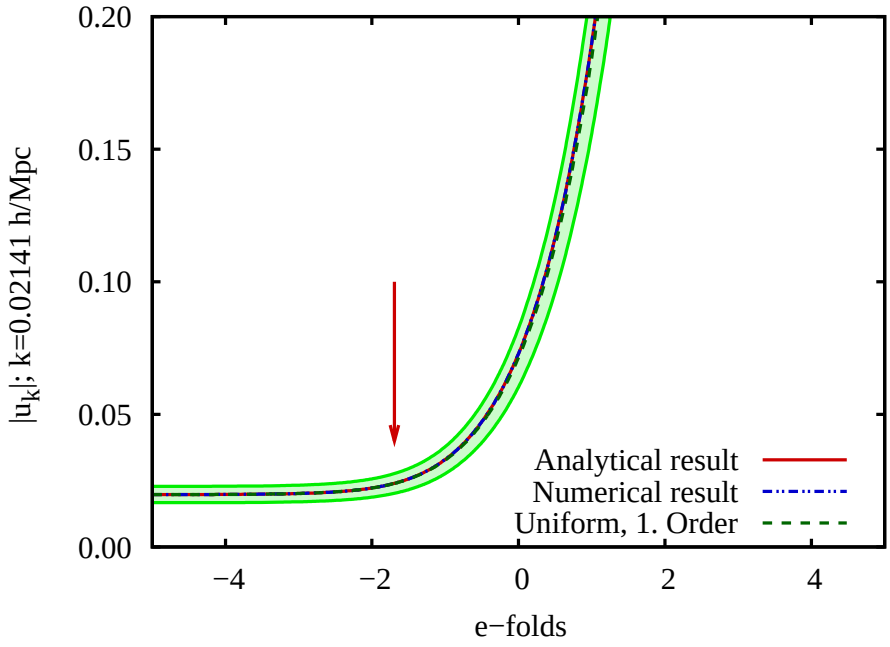

Figure 6.3: The absolute value of the scalar mode function for a power-law model following Fig. 6.1.

the mode should be well inside the Hubble length. As the initial conditions for inflation are unknown, we will assume (i) that inflation began well before the 55-65 e-folds necessary to solve the flatness and horizon problems, and (ii) by the time our calculations are to be performed, Eq. (6.2) applies. By isolating how initial conditions are defined from possible early-time artifacts, our method of implementing initial conditions also leads to substantial improvement in the low-k regime as well.

In Figs. 6.1, 6.2, and 6.3 we display the (growing) imaginary part, (damped) real part and absolute value of u_k for a mode with $k = 0.0214\,h\,\mathrm{Mpc}^{-1}$ for a power-law inflation model. As can be seen in all cases, the uniform approximation at leading order and the numerical results are very close. The error in the absolute value $|u_k|$ (relevant to the power spectrum) from the mode-by-mode integration is shown in Fig. 6.4. The numerical error is less than 1 part in 10^5. To check the accuracy of the solution of the background equations, the numerical deviations from the expected pure constant values for ν, ϵ, and δ_1 are shown in Fig. 6.5; the errors are comfortably below one part per million. Detailed quantitative results are given in the following Section.

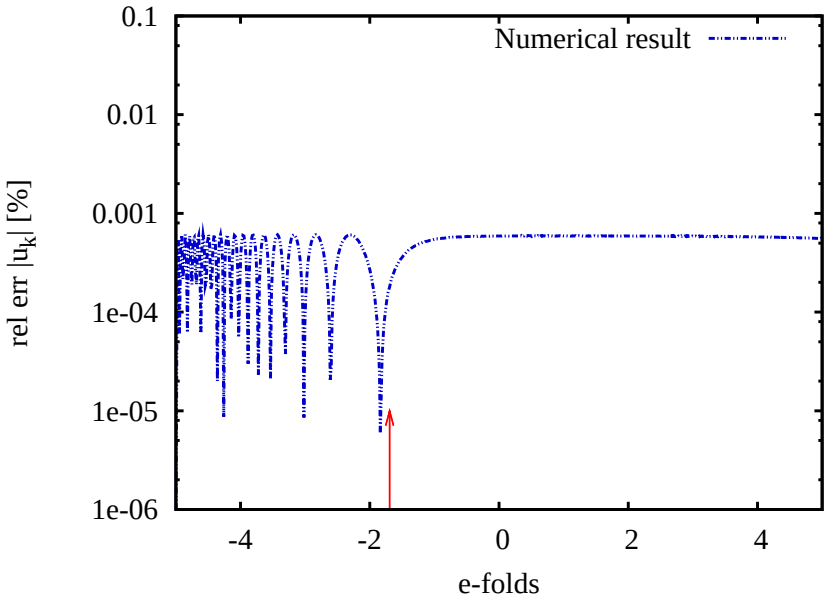

Figure 6.4: Relative error of $|u_k|$ shown in Fig. 6.3 for the numerical calculation (blue line). The arrow shows the turning point for the mode.

6.2.2 Power spectra and spectral indices

For the case of scalar perturbations the modes freeze out once the power spectrum $P_S(k,\eta)$, as defined in Eq. (2.51), becomes constant as a function of conformal time, i.e., when $P'_S(k,\eta_{\rm freeze}) \simeq 0$ at a numerically determined freeze-out time $\eta_{\rm freeze}$. We found that it

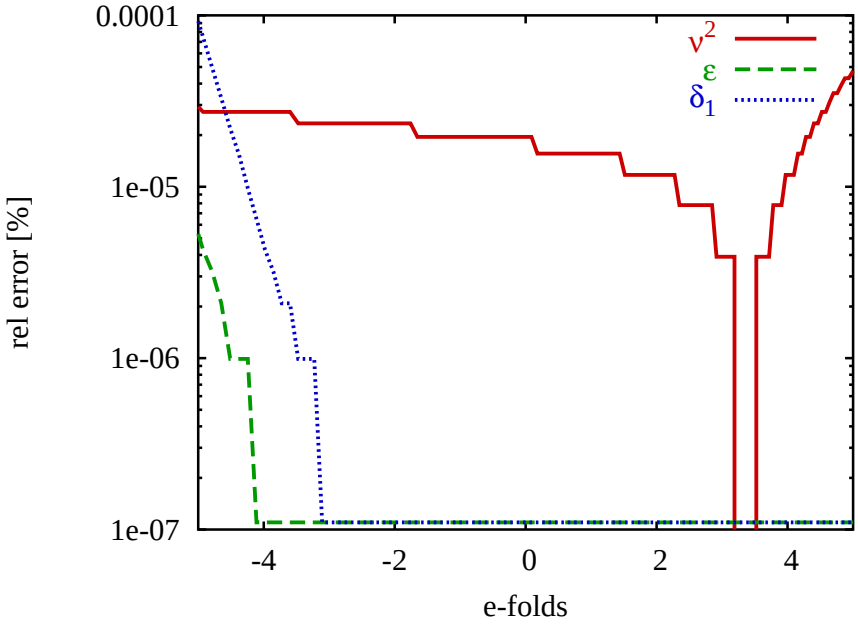

Figure 6.5: Relative errors of ν, ϵ, and δ_1; model parameters are as specified in Fig. 6.1.

is numerically robust to track the time derivative of $P_S(k,\eta)$ to determine this freeze-out. The same situation holds for the tensor perturbations and $P_T(k,\eta)$ as defined in Eq. (2.52).

Once the power spectra have been obtained, the spectral indices for scalar and tensor perturbations are found by evaluating the derivatives of the power spectra with respect to k, as defined in Eqs. (2.55) and (2.56). The derivatives are computed numerically with non-equidistant momentum discretization due to the momentum readjustment described in Appendix A.2.1. We take three discretization points and approximate the derivative by a non-symmetric second-order rule. In the numerical evaluation of the derivatives, for every individual k we use two very close neighboring points with $\Delta \ln k \approx 0.01$–$0.02$ over the entire k-range considered.

6.3 Tests for power-law inflation

As one of the few analytically tractable models, power-law inflation [106, 120] provides a useful foil for testing approximations. This feature has maintained its popularity, even though the basic model is not realistic, as inflation never comes to an end.

We compared detailed results from the uniform approximation in leading and next-to-leading order with slow-roll and exact results in Sec. 5.4.

Here, we use the power-law model for testing the accuracy of our numerical implementations of the exact mode equations, as well as the uniform and slow-roll approximations. The spectral indices are constant, therefore the running of the spectral index—which measures the k-dependence of n_S and n_T—vanishes. In addition, the ratio $R(k) = 16/p$ of the

Table 6.1: Numerical precision tests in the power-law case with $p = 11$ at $k_* = 0.06875\,h\,\mathrm{Mpc}^{-1} = 0.0495\ \mathrm{Mpc}^{-1}$ ($h = 0.72 \pm 0.05$; the WMAP pivot scale is at $0.05\ \mathrm{Mpc}^{-1}$, see Ref. [8]) in the various approximations.

Approximation	$R(k_*)$	$n_S(k_*)$	$\alpha_S(k_*)$	$n_T(k_*)$	$\alpha_T(k_*)$
Analytical	1.454545	0.8	0	-0.2	0
Numerical[a]	1.454544	0.79998	$< 10^{-7}$	-0.20002	$< 10^{-7}$
Uniform, 1. order[b]	1.454541	0.79992	0.00001	-0.20008	0.00001
Local approx., 0. order[b]	–	0.80000	$< 10^{-7}$	-0.20000	$< 10^{-7}$
Local approx., 1. order[b]	–	0.79999	$< 10^{-6}$	-0.20001	$< 10^{-6}$
Uniform, Slow-Roll redux[c]	–	0.80165	$< 10^{-7}$	-0.19835	$< 10^{-7}$
Slow-Roll, 1. order[d]	1.454545	0.81818	$< 10^{-7}$	-0.18182	$< 10^{-7}$
Slow-Roll, 2. order[e]	–	0.80165	$< 10^{-7}$	-0.19835	$< 10^{-7}$

[a]Mode-by-mode integration.
[b]Already exact in that order.
[c]See Eqs. (5.115) and (5.116).
[d]Expected results: $n_S = 1 - 2/p$ and $n_T = -2/p$.
[e]Expected results: $n_S = 1 - 2/p - 2/p^2$ and $n_T = -2/p - 2/p^2$.

power spectra is constant. Instead of showing our results graphically—all curves would be almost indistinguishable by eye—we summarize our findings in Tab. 6.1. We quote the results for $R(k)$, the spectral indices, and their running α_S and α_T at the WMAP pivot scale $k_* = 0.0495\ \mathrm{Mpc}^{-1}$ [8]. We have picked the power $p = 11$, which is of course much too small to be considered a realistic inflationary model, but is perfectly acceptable for illustrative purposes. In the uniform approximation there is an explicit expression for the spectral indices n_S and n_T, while the tensor to scalar ratio $R(k)$ is calculated via the amplitudes of the power spectra. In the purely numerical computation, the spectral index is obtained by taking numerical derivatives of the power spectrum as described earlier.

The error in the exact numerical determination of the ratio of the power spectra $R_*(k)$ is smaller than 1 part in 10^6, while the numerical error in the implementation of the uniform approximation is slightly larger (3 parts in 10^6). In the case of power-law inflation, the spectral indices do not accurately reproduce the expected analytic results, though they do reproduce the expected slow-roll results to $1/p$-order with the slow-roll parameters being constant in time (in this case, $\epsilon = -\delta_1 = 1/p$ and $\delta_2 = 2/p^2$). This provides a check on the integration of the background equations, but contains no further useful information.

For the scalar spectral index $n_S(k_*)$ we find a relative error in the exact numerical calculation of 0.0025% while for the uniform approximation the relative error is roughly 0.01%. Again, no error in the numerical implementation of the slow-roll approximation is detected. The situation for the tensor spectral index $n_T(k_*)$ is similar. The numerical errors in the uniform approximation for the spectral indices are slightly larger than for the

exact numerical mode-by-mode approach due to the numerical integration of a function with an inverse square root singularity. The results for $\alpha_S(k_*)$ and $\alpha_T(k_*)$ are very close to zero in all cases.

In addition, we tested our improvement strategy for the uniform approximation which should work perfectly in the case of power-law inflation since ν is constant. We found a relative error for $P_S(k)$ of 0.15% if we include corrections up to $1/\nu^2$, of 0.025% including corrections up to $1/\nu^3$, and of 0.01% if we include corrections up to $1/\nu^4$ following Eq. (5.108). The corrections are slightly worse than anticipated but consistent with the small error of 0.01% in the numerical implementation of the uniform approximation.

Chapter 7

Results from Numerical Calculations

7.1 Chaotic inflation

7.1.1 Quadratic potential $V(\phi) = m^2\phi^2/2$

The simplest chaotic model is that for a free scalar field with mass m. In this model, normalizing the amplitude of the scalar power spectrum to the WMAP fit, as described in Appendix A.2.3, is equivalent to fixing $m^2 = (1.89 \pm 0.21) \times 10^{-12}/8\pi G$. The initial value for the inflaton field is given by $\phi(0) = 16.8/\sqrt{8\pi G}$ with a small initial velocity of $\dot{\phi}(0) = -0.1/\sqrt{8\pi G}/\mathrm{s}$. These parameters ensure that the inflationary phase lasts long enough to provide a realistic model, i.e., it leads to 57.655 e-folds after the $k = 0.0495\,\mathrm{Mpc}^{-1}$ mode crosses the Hubble length.

First, we analyze the results for the power spectra $P_S(k)$ and $P_T(k)$, plotted in Figs. 7.1(a) and 7.1(b). The exact numerical results for the power spectra as defined in Eqs. (2.51) and (2.52) are shown in red (solid line), the results from the leading-order uniform approximation given in Eqs. (5.46) and (5.47) are shown in green (dashed line), the first order slow-roll results as defined in Eqs. (4.9) and (4.10) are shown in blue (dashed-dotted line), and the improved uniform approximation results [to second-order in the sense of Eq. (5.108) for the scalar perturbations] are shown in purple (dotted line). The light green band displays our estimate of the error bound for the leading-order uniform approximation as given in Eq. (5.100). The estimate error for the improved uniform approximation in leading order [see Eq. (5.109)] is so close to the result itself that the error band is not visible in this plot. We will use these color and linestyle assignments for the remainder of the Chapter.

The exact numerical results, the improved leading-order uniform approximation, and the slow-roll approximation are almost indistinguishable by eye in Fig. 7.1. The leading-order uniform approximation deviates in the amplitude from the exact numerical result by $\sim 10\%$ as expected. The improvement strategy performs just as predicted by Eq. (5.108): the second-order correction reduces the error to $\sim 0.1\%$ while the fourth-order reduces it further to $\sim 0.01\%$, for both scalar and tensor perturbations. This consistently good behavior is due to the fact that ν is varying slowly. Note that the improvement strategy should be carried out to roughly match the error estimate given by Eq. (5.109)—fourth-

Table 7.1: Determination of the characteristic quantities for the $\frac{1}{2}m^2\phi^2$ chaotic inflation model at $k_* = 0.06875\,h\,\mathrm{Mpc}^{-1} = (0.0495 \pm 0.0034)\ \mathrm{Mpc}^{-1}$ ($h = 0.72 \pm 0.05$; the WMAP pivot scale is at $k = 0.05\ \mathrm{Mpc}^{-1}$, see Ref [8]) in the various approximations; parameters: $m^2 = (1.89 \pm 0.21) \times 10^{-12}/8\pi G$, $\phi(0) = 16.8/\sqrt{8\pi G}$, $\dot{\phi}(0) = -0.1/\sqrt{8\pi G}$/s leading to 57.655 e-folds of inflation after horizon crossing of k=0.0495 Mpc^{-1}.

Approximation	$R(k_*)$	$n_S(k_*)$	$\alpha_S(k_*)$	$n_T(k_*)$	$\alpha_T(k_*)$
Numerical[a]	0.13749	0.96507	-0.00064	-0.01765	-0.01779
Uniform, 1. order	0.13740(14)	0.96505(3)	-0.00064	-0.01768(1)	-0.01773
Uniform, imp. 1. order[b]	0.13749(0)	0.96507(0)	-0.00064	-0.01765(0)	-0.01773
Local approx., 0. order[c]	–	0.96465	-0.00066	-0.01786	-0.01799
Local approx., 1. order[c]	–	0.96501	-0.00064	-0.01761	-0.01770
Uniform, slow-roll redux[d]	–	0.96566	-0.00062	-0.01757	-0.01768
Slow-Roll, 1. order[e]	0.13752	0.96523	-0.00063	-0.01741	-0.01755
Slow-Roll, 2. order[e]	–	0.96507	-0.00064	-0.01764	-0.01779

[a]Mode-by-mode integration.
[b]The improvement here is to second order in powers of $1/\nu$, cf. Eq. (5.108)
[c]See Eqs. (5.97) and (5.98).
[d]See Eqs. (5.115) and (5.116).
[e]See Eqs. (4.11) and (4.12).

order in this instance; beyond this point the error is dominated by other contributions.

Next we investigate the scalar and tensor spectral indices as functions of k. The results are displayed in Figs. 7.2a and 7.2b. The shaded band represents the error estimate for the leading order of the uniform approximation [see Eq. (5.54), calculated with the estimate in Eq. (5.106)]. The error estimate for the scalar spectral index is of the order $\sim 0.002\%$, therefore of the same order as the discrepancy to the numerical result. Note that the improved scalar and tensor spectral index calculations agree completely with the numerical results in Tab. 7.1. The deviation of the slow-roll approximation for the scalar spectral index in first order from the exact numerical result is also very small, roughly $\sim 0.02\%$. As stated before this is not surprising: the slow-roll approximation is expected to work well for this type of model, where the slow-roll parameters ϵ and δ_1 are very small and almost constant. However, the tensor spectral index has an error of more than 1%.

In Fig. 7.3 the ratio $R(k)$ of tensor to scalar perturbations as defined in Eq. (2.54) is shown. The corresponding relative errors of the uniform approximation, of the slow-roll approximation, and of the improved uniform approximation are presented in Fig. 7.4. In Fig. 7.3 the lines representing the different approximations are practically indistinguishable by eye. In contrast to the relative errors in the power spectra ($\sim 10\%$ without improvement and $\sim 0.01\%$ with fourth-order improvement), the relative error in the tensor to scalar ratio $R(k)$ is already smaller than $\sim 0.07\%$ (dashed line in Fig. 7.4) without the improvement, and smaller than $\sim 0.001\%$, i.e., practically exact, with second-order improvement (solid line in Fig. 7.4) (cf. Sec. 5.7). There is no point in improving further since the result has already reached the estimated error threshold (5.109) beyond which improvement becomes incomplete. This behavior is a general feature of the approximation when the inflation model leads to a slowly varying $\nu(\eta)$.

Finally, we have listed the ratio of tensor to scalar perturbations, the scalar and spectral spectral index, and their running in the various approximations or simplified approximations, in Tab. 7.1. All quantities are again evaluated at $k_* = 0.0495\ \mathrm{Mpc}^{-1}$. Error estimates for the uniform approximation are indicated by the numbers in brackets. For chaotic inflation the running of the spectral indices, $\alpha_S(k)$ and $\alpha_T(k)$ is non-zero. Note that the running of the tensor spectral index is roughly one order of magnitude bigger than the running of the scalar spectral index.

7.1.2 Quartic potential $V(\phi) = \lambda\phi^4/4$

In the quartic model—relative to the quadratic potential—higher derivatives of the potential exist. Consequently, the slow-roll results in this case are expected to have a bigger error. In comparison to the quadratic case, for the model considered below, the errors are worse for the scalar spectral index ($\sim 0.02\%$ versus $\sim 0.1\%$) and comparable for the case of the tensor spectral index ($\sim 2\%$). In contrast, the uniform approximation still provides an accuracy of a fraction of a percent. Although the slow-roll expansion for this model can be improved to second-order with notably better results. This behavior exhibits the general tendency of the slow-roll expansion if terms arising from higher order derivatives of the potential are significant. In terms of observational viability, the ϕ^4-model is under

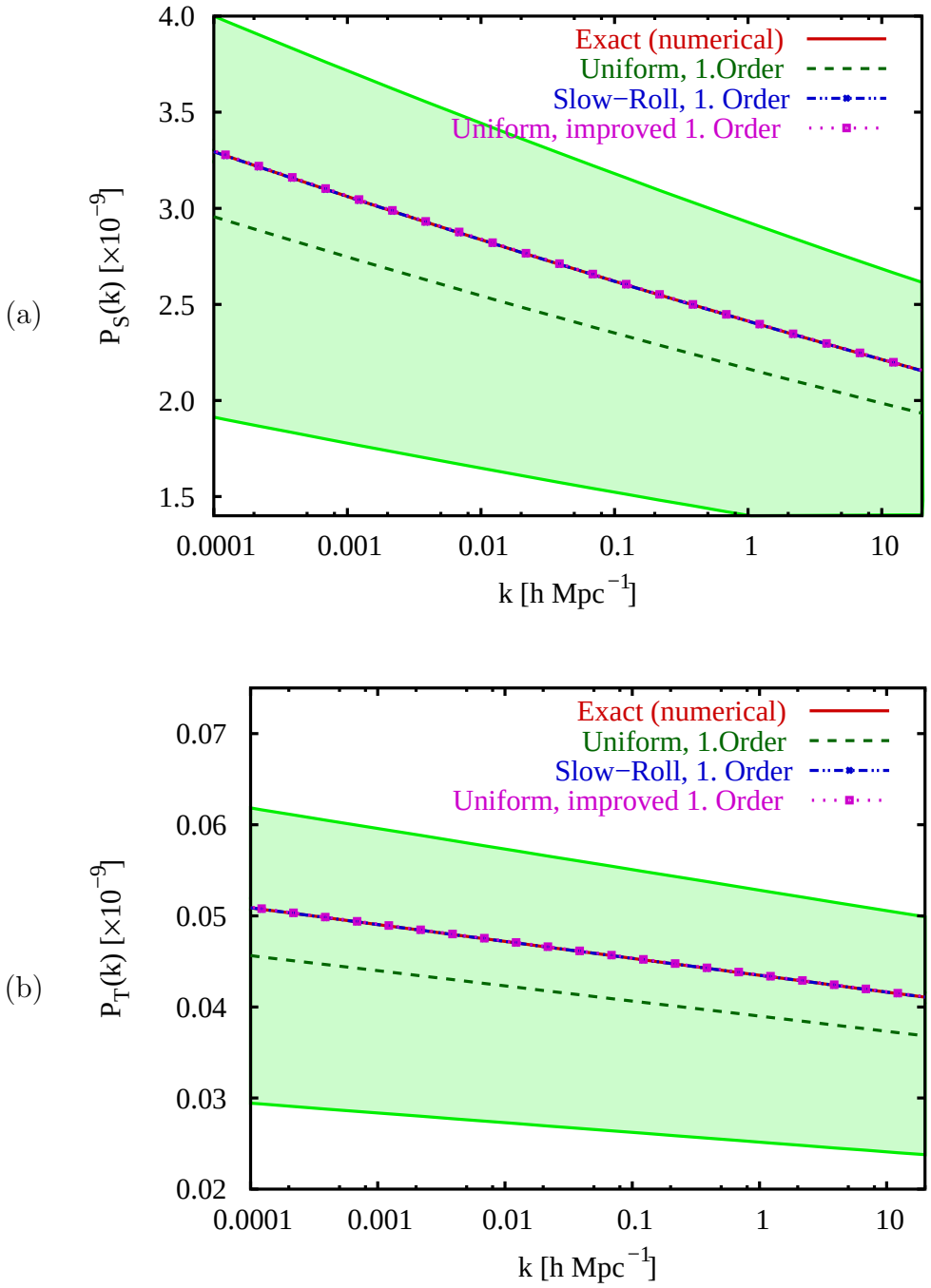

Figure 7.1: (a) Scalar power spectrum $P_S(k)$ and (b) tensor power spectrum $P_T(k)$ for a chaotic $\frac{1}{2}m^2\phi^2$-model, parameters as specified in Tab. 7.1. Solid red line: exact numerical results, dashed green line: uniform approximation, dashed-dotted blue line: slow-roll; dotted purple line: second-order improved uniform approximation [cf. Eq. (5.108)]; the green band is the estimate for the error bound for the uniform approximation, Eq. (5.100). The exact results and the results from the improved uniform and slow-roll approximation are visually on top of each other. The error estimate for the improved uniform approximation, Eq. (5.109), is so small as to be indistinguishable from the result itself.

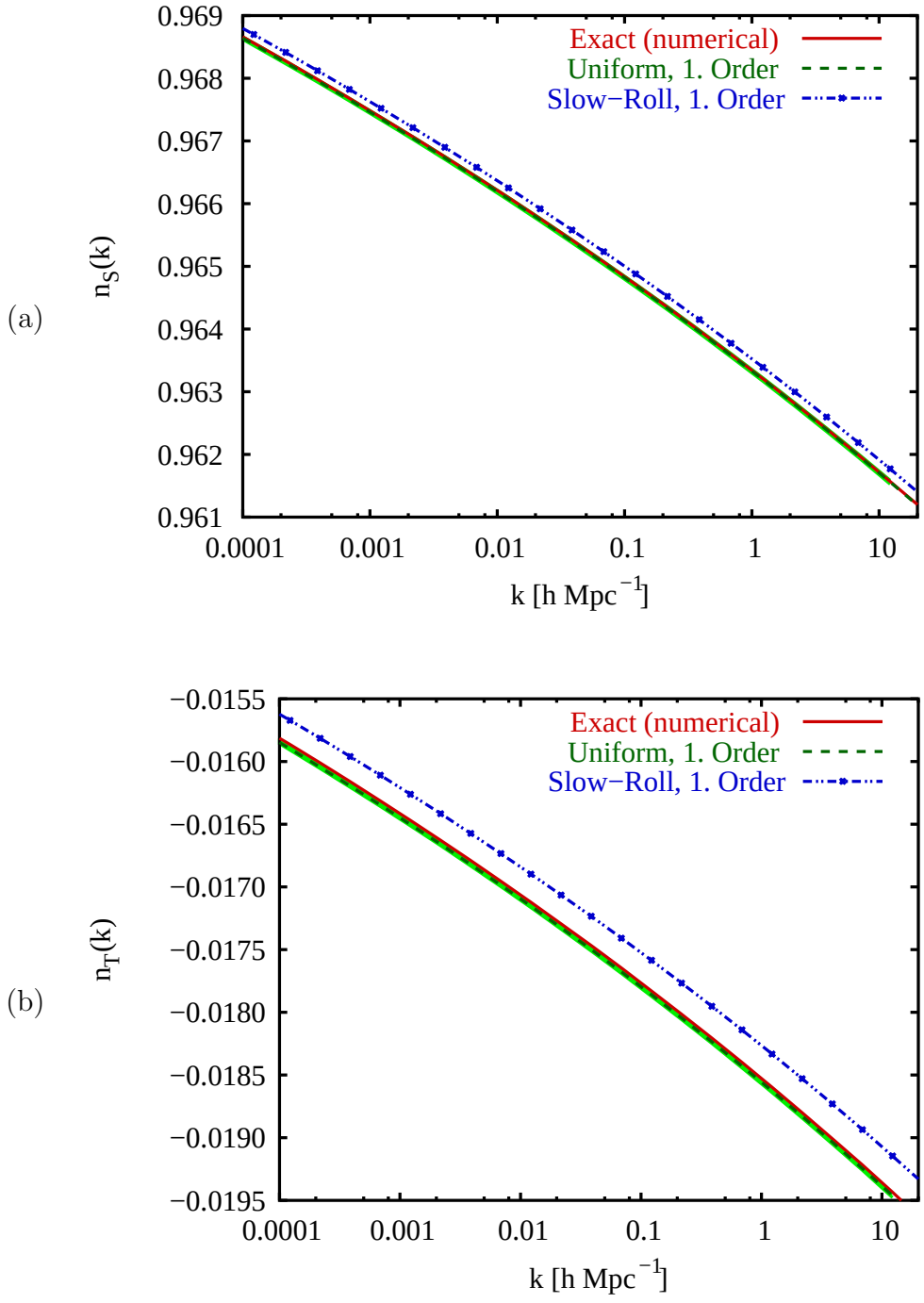

Figure 7.2: (a) Scalar spectral index $n_S(k)$ and (b) tensor spectral index $n_T(k)$ for a chaotic $\frac{1}{2}m^2\phi^2$-model, parameters as specified in Tab. 7.1. Solid red line: exact numerical results, dashed green line: uniform approximation, dashed-dotted blue line: slow-roll; the green band is the error estimate for the uniform approximation. Unlike the case for the power spectrum, accurate results for the uniform approximation are obtained without recourse to the improvement procedure specified by Eq. (5.108).

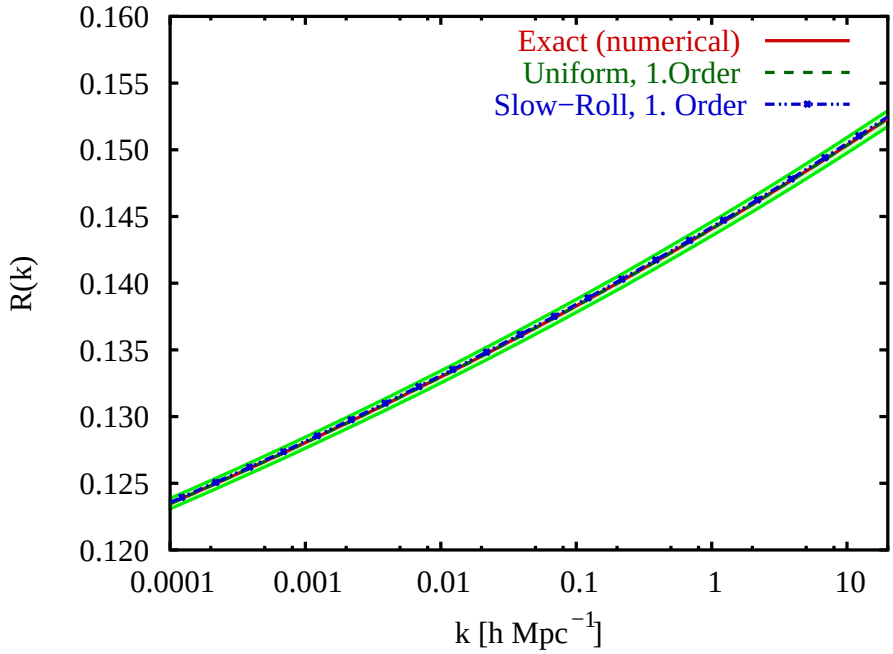

Figure 7.3: Tensor to scalar ratio $R(k)$ for a chaotic $\frac{1}{2}m^2\phi^2$-model; parameters as specified in Tab. 7.1. All three lines lie practically on top of each other; see Fig. 7.4 for the relative errors.

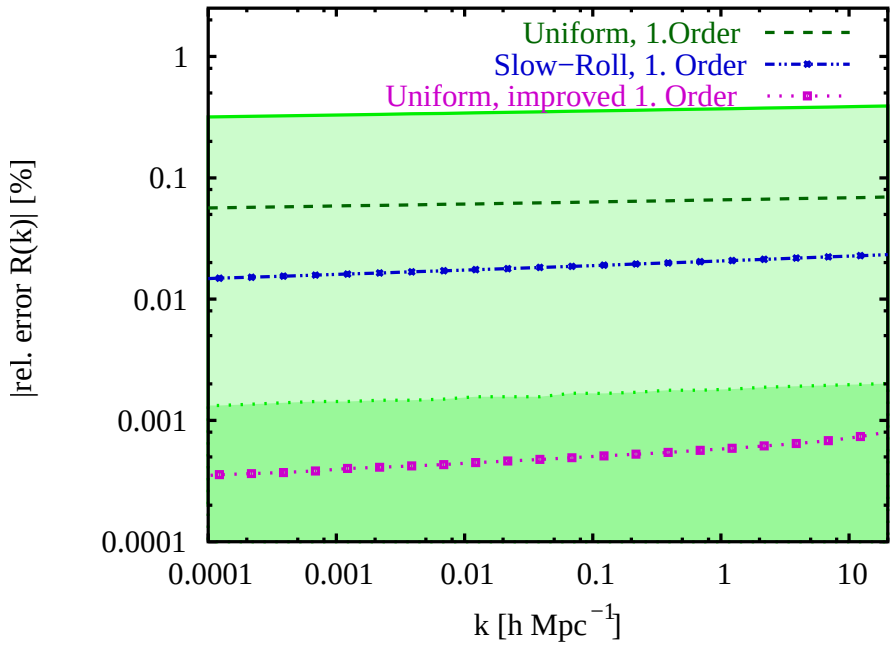

Figure 7.4: Relative error of the tensor to scalar ratio $R(k)$ for a chaotic $\frac{1}{2}m^2\phi^2$-model; parameters as specified in Tab. 7.1. Here the dotted purple line denotes the (second-order) improved leading-order of the uniform approximation; the green error band is the error estimate for the first order uniform approximation, the dark green band is the error estimate for the improved leading-order result.

strong pressure from combined analysis of the WMAP CMB anisotropy data and data from galaxy clustering (see e.g., Refs. [56, 111, 112]).

The results for the spectral indices are displayed in Figs. 7.5(a) and 7.5(b). As in the previous example the leading-order uniform approximation is very close to the exact numerical result. However, the first-order slow-roll result does not match as closely as for the quadratic potential. As done earlier for the ϕ^2-model, we have listed various characteristic quantities in Tab. 7.2.

Table 7.2: Determination of the characteristic quantities for the $\frac{1}{4}\lambda\phi^4$ chaotic inflation model at $k_* = 0.06875\,h\,\mathrm{Mpc}^{-1} = (0.0495 \pm 0.0034)\ \mathrm{Mpc}^{-1}$ ($h = 0.72 \pm 0.05$; the WMAP pivot scale is at 0.05 Mpc^{-1}, see Ref [8]) in the various approximations; parameters: $\lambda = (1.75 \pm 0.19) \times 10^{-13}$, $\phi(0) = 24/\sqrt{8\pi G}$, $\dot{\phi}(0) = -1/\sqrt{8\pi G}$/s, leading to 60.579 e-folds of inflation horizon crossing of k=0.05/Mpc.

Approximation	$R(k_*)$	$n_S(k_*)$	$\alpha_S(k_*)$	$n_T(k_*)$	$\alpha_T(k_*)$
Numerical[a]	0.25963	0.94999	-0.00090	-0.03356	-0.01705
Uniform, 1. order	0.25948(113)	0.94990(3)	-0.00089	-0.03367(2)	-0.01694
Uniform, imp. 1. order[b]	0.25964(0)	0.94999(0)	-0.00089	-0.03356(0)	-0.01703
Local approx., 0. order[c]	–	0.94942	-0.00092	-0.03395	-0.01726
Local approx., 1. order[c]	–	0.94991	-0.00090	-0.03340	-0.01697
Uniform, slow-roll redux[d]	–	0.95081	-0.00087	-0.03368	-0.01706
Slow-Roll, 1. order[e]	0.25969	0.95077	-0.00087	-0.03285	-0.01669
Slow-Roll, 2. order[e]	–	0.95001	-0.00089	-0.03354	-0.01703

[a]Mode-by-mode integration.
[b]The improvement here is to second order in powers of $1/\nu$, cf. Eq. (5.108)
[c]See Eqs. (5.97) and (5.98).
[d]See Eqs. (5.115) and (5.116).
[e]See Eqs. (4.11) and (4.12).

7.2 Inflationary model with a $\mathcal{C}^2$ potential function

As a next example we investigate a toy model with a continuous potential function with continuous first and second derivatives and a jump in the third derivative at a specific value of ϕ. Generally speaking, dynamical changes in the potential of the field driving inflation can be induced by couplings to other degrees of freedom. For example, in hybrid models a phase transition is used to terminate inflation. If a dynamical transition happens at cosmologically relevant scales, i.e., well before the end of inflation, it leaves a clear signature in the power spectra and spectral indices. Such a transition may be naturally realized in multi-field models of inflation (see, e.g., Ref. [127]). Other examples are steps

(a)

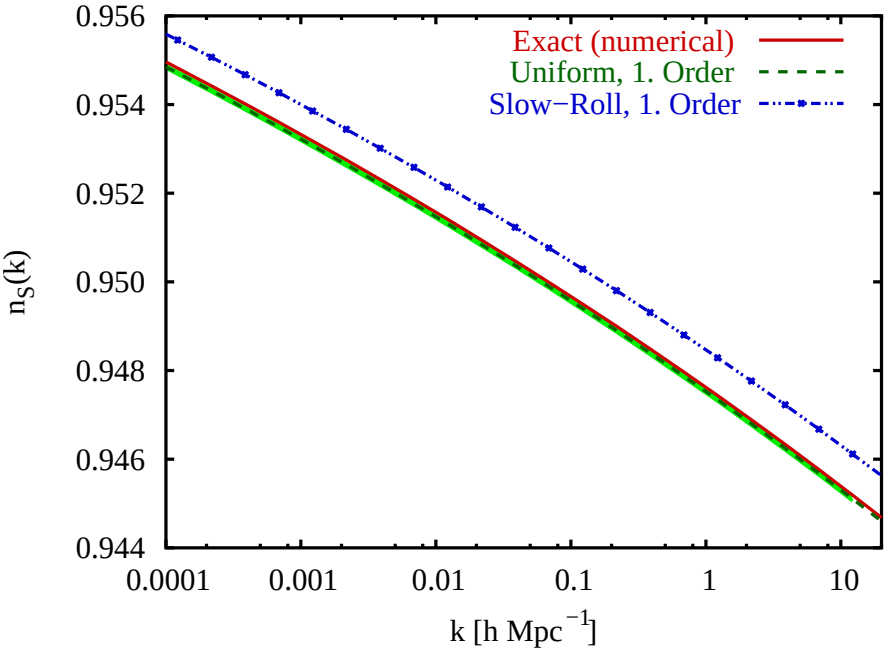

(b)

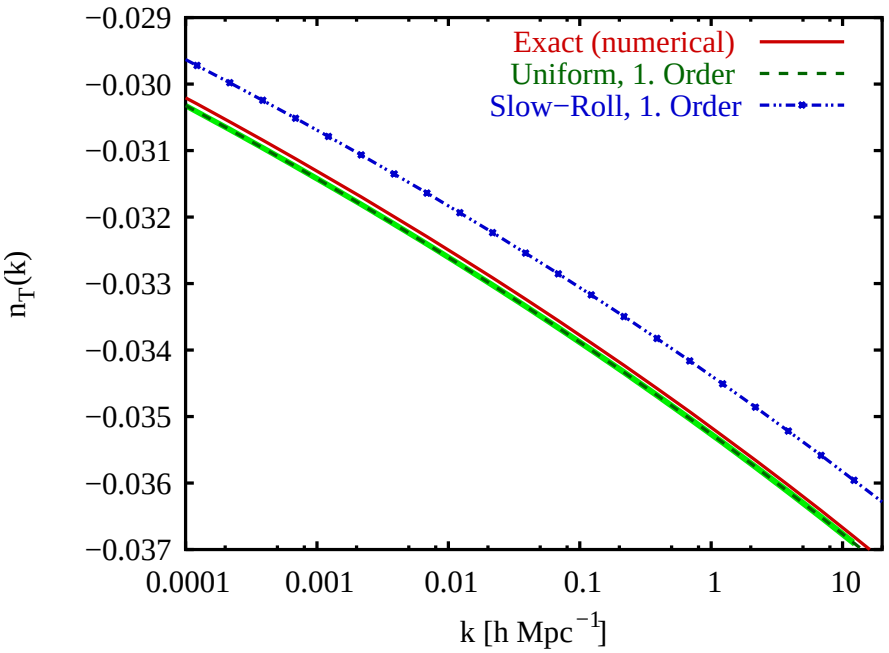

Figure 7.5: (a) Scalar spectral index $n_S(k)$ and (b) tensor spectral index $n_T(k)$ for the quartic potential potential $\lambda\phi^4$, parameters as specified in Tab. 7.2. Solid red line: exact numerical results, dashed green line: uniform approximation, dashed-dotted blue line: slow-roll; the green band is the error estimate for the uniform approximation.

in the potential (Sec. 3.1.4, Ref. [121, 53]), leading to oscillations in the primordial power spectra and spectral indices. In such models ν^2 cannot be considered as a constant, but can display sudden changes. Rather than taking one of such potentials we consider here a toy potential that is smoother in the sense that oscillations in ν^2 or z''/z are avoided:

$$V_>(\phi) = \frac{1}{4}m^2\phi_*^2(\alpha-1) + \frac{2}{3}m^2\phi_*(1-\alpha)\phi + \frac{1}{2}\alpha m^2\phi^2 + \frac{1}{12\phi_*^2}m^2(1-\alpha)\phi^4, \quad (7.1)$$

$$V_<(\phi) = \frac{1}{2}m^2\phi^2, \quad (7.2)$$

where $V(\phi) = V_>(\phi)$ for $\phi > \phi_*$ and $V(\phi) = V_<(\phi)$ for $\phi < \phi_*$. The potential is constructed in such a way that $V_>(\phi_*) = V_<(\phi_*)$, $V_>'(\phi_*) = V_<'(\phi_*)$ and $V_>''(\phi_*) = V_<''(\phi_*)$ but $V_>'''(\phi_*) \neq V_<'''(\phi_*)$. Thus there is a finite jump in the third derivative of the potential.

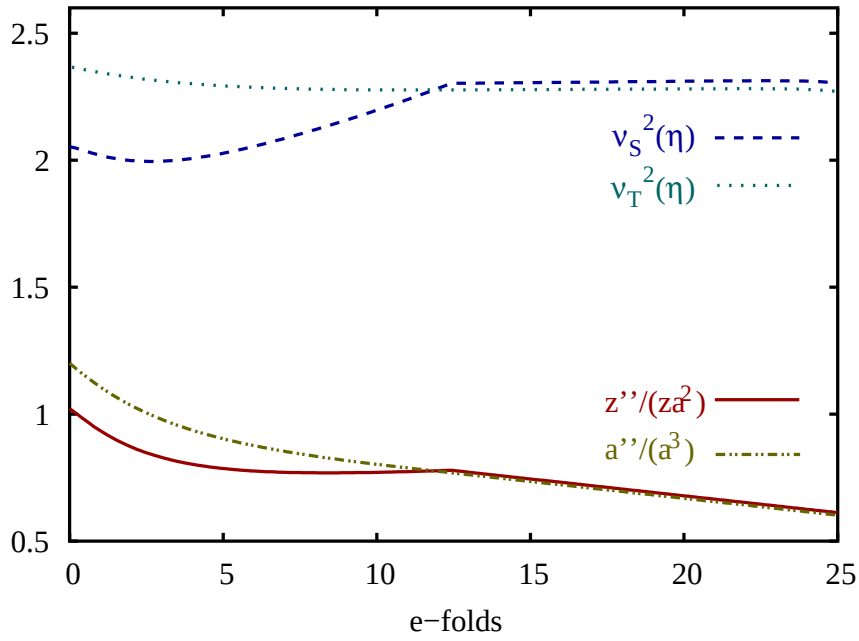

Figure 7.6: $z''/(za^2)$ and ν_S^2 and a''/a^3 and ν_T for the C^2-potential; the point ϕ_* is reached at $N \approx 12.4$. The beginning in time of the numerical calculation is at $N = 0$. The inflationary attractor is reached at $N \simeq 1.8$, checked by varying $\dot{\phi}(0)$ and determining at which e-fold the ϕ behavior becomes independent of the initial velocities. The quantities a''/a^3 and ν_T, relevant for tensor perturbations, are much smoother than the corresponding quantities z''/za^2 and ν_S for the scalar perturbations, leading to smaller errors in the approximations as discussed in the text.

We present numerical results with parameters chosen specifically to demonstrate the general effect of a more rapidly changing ν. During the evolution in this potential the parameters ϵ and δ_i are not constant (not even approximately); δ_1 cannot be considered small when the inflaton field fulfills $\phi > \phi_*$ (with the parameters below, $|\delta_1|$ can be as large as 0.14).

(a)

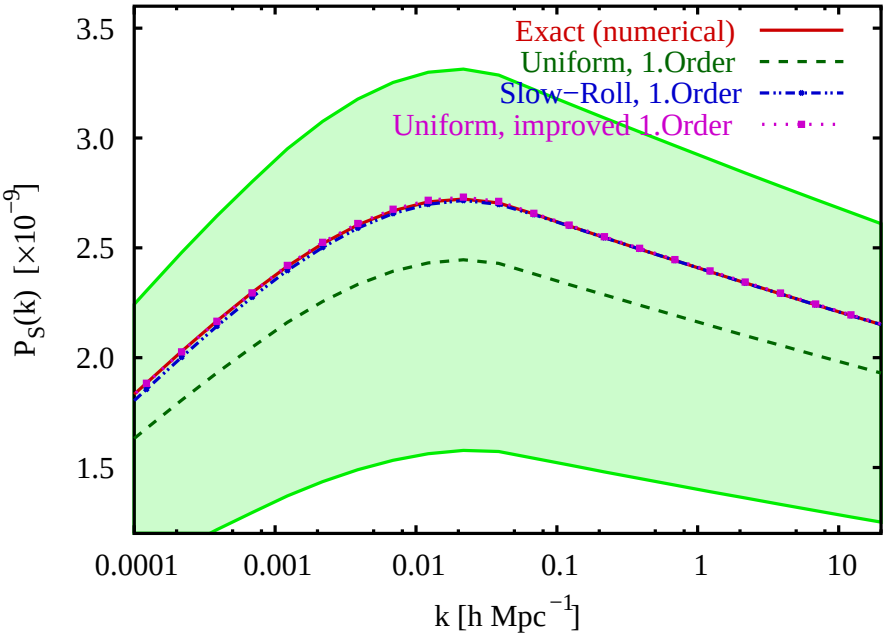

(b)

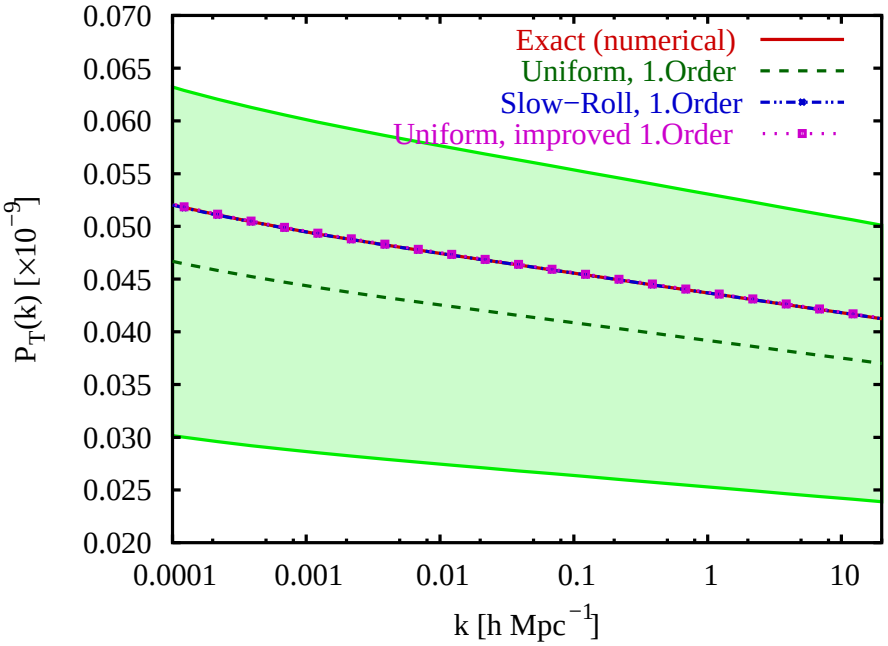

Figure 7.7: (a) Scalar power spectrum $P_S(k)$ and (b) tensor power spectrum $P_T(k)$ for the C^2-potential in Eqs. (7.1) and (7.2); parameters: $\alpha = -100$, $m^2 = (1.90 \pm 0.21) \times 10^{-12}/8\pi G$, $\phi_* = 15.2/\sqrt{8\pi G}$, $\phi(0) = 17.5/\sqrt{8\pi G}$, $\dot{\phi}(0) = -0.2/\sqrt{8\pi G}$/s. Solid red line: exact numerical results, dashed green line: uniform approximation, dashed-dotted blue line: slow-roll; the green band is the estimate for the error bound for the (unimproved) uniform approximation. Again, the exact results and the results from the improved uniform and slow-roll approximation are on top of each other.

(a)

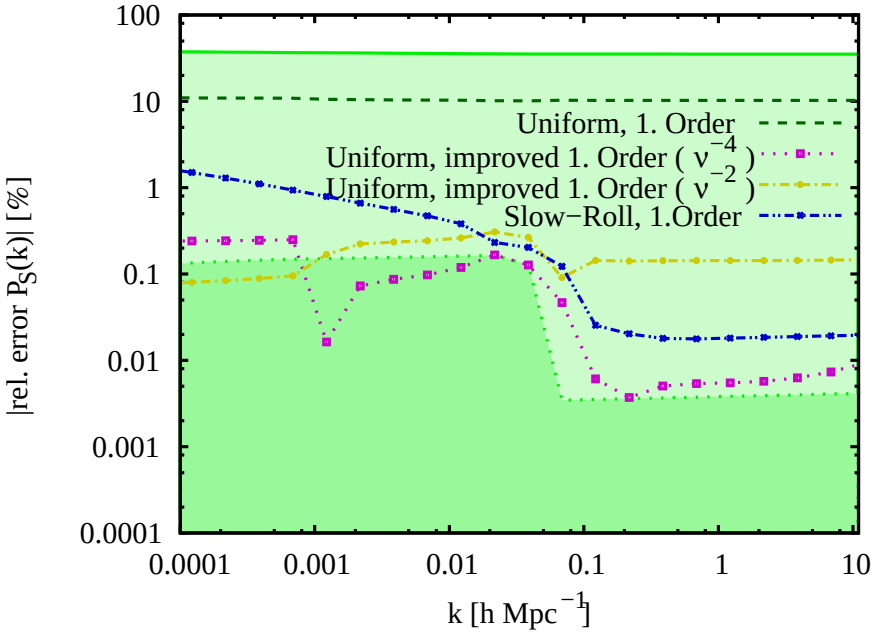

(b)

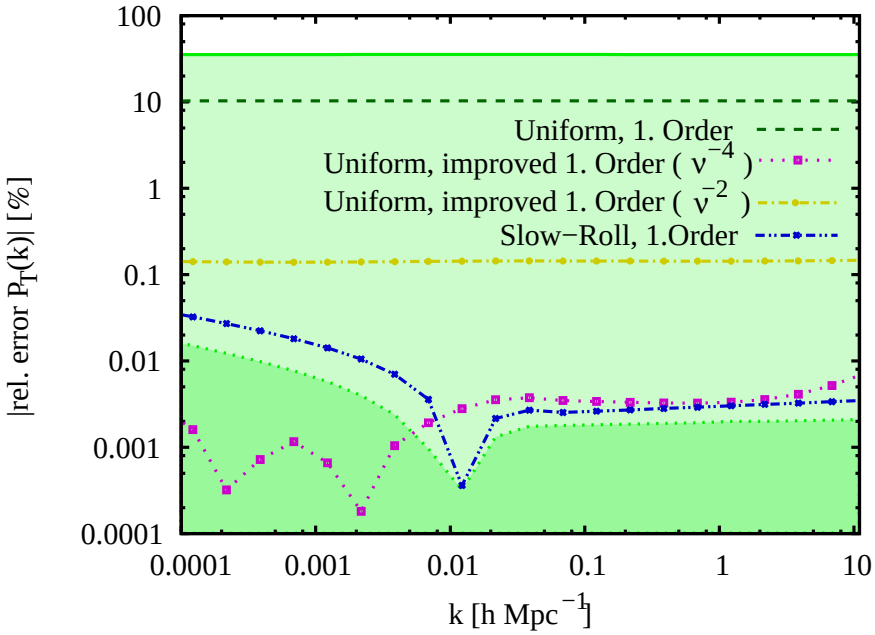

Figure 7.8: (a) Relative errors for the scalar power spectrum $P_S(k)$ and (b) tensor power spectrum $P_T(k)$ for the C^2-potential, Eqs. (7.1) and (7.2). In both cases, the light green band denotes the estimated error bound for the leading-order uniform approximation (5.100) and the dark green band denotes the best estimated error for the improvement procedure (5.108). The results are nicely consistent with these estimates showing where the second-order improvement can be enhanced by going to higher order, and also where it cannot.

The parameters chosen to specify the model are: $\alpha = -100$, $m^2 = (1.90 \pm 0.21) \times 10^{-12}/8\pi G$, $\phi_* = 15.2/\sqrt{8\pi G}$, $\phi(0) = 17.5/\sqrt{8\pi G}$, $\dot{\phi}(0) = -0.2/\sqrt{8\pi G}$/s. With this choice of parameters the number of e-folds is 57.320, counted from $k_* = 0.0495\,\mathrm{Mpc}^{-1}$.

The relevant time-dependent terms ν_S^2 and $z''/(za^2)$ in the scalar mode equation and ν_T^2 and a''/a^3 in the tensor mode equation are displayed in Fig. 7.6 as a function of expansion e-folds (z''/z and a''/a have been divided by a^2 to filter out the exponential growth of the scale factor). The point ϕ_* is reached at $N \approx 12.4$ (note that in this plot $N = 0$ defines the beginning of the numerical calculation). Due to the jump in the third derivative both quantities for the scalar perturbations display a kink at this point. The qualitative behavior is also different on either side of the kink. While z''/z has a kink, a''/a is completely well-behaved. Note that z''/z, as e.g., expressed in Eq. (4.2) as an exact expression in terms of the slow-roll parameters, is more sensitive to higher derivatives of the potential than a''/a [cf. Eq. (5.117)]. Thus we can expect the effects of the change in the potential at $\phi = \phi_*$ to be amplified in the scalar power spectrum relative to the tensor power spectrum.

The results for the scalar and tensor power spectrum are displayed in Fig. 7.7. With the same conventions as in Fig. 7.1, the different approximations (leading- and improved leading-order of the uniform approximation and the slow-roll approximation) are compared to the exact numerical results. The scalar power spectrum [see Fig. 7.7(a)] shows a significant deviation from a power-law shape. Up to $k \approx 0.025\,h\,\mathrm{Mpc}^{-1}$ the spectrum rises, reaches a maximum and falls off for larger k. As in the previous examples, the leading order of the uniform approximation has an amplitude error of roughly 10% with respect to the exact numerical results. The (second-order) improved leading-order uniform approximation, however, lies almost on top of the numerical results. Remarkably, although the shape deviates from a simple power-law behavior quite significantly, the improvement strategy is still effective.

The relative errors are shown in Figs. 7.8(a) and 7.8(b). The error behavior divides into two regimes, to the left and the right of $k \sim 0.05\,h\,\mathrm{Mpc}^{-1}$. The behavior to the right is that of a ϕ^2-model [cf. Eq. (7.1)] while the behavior to the left is that of a polynomial potential with linear, quadratic, and quartic terms (7.2). Note that the error estimate from Eq. (5.109) changes sharply across this divide, by more than an order of magnitude, from $\sim 0.1\%$ to $\sim 0.005\%$. To the left, this error estimate shows that there is no point in attempting a correction beyond second-order using Eq. (5.108), consistent with the results shown for second and fourth-order corrected spectra. To the right, the smallness of the error estimate is consistent with the improved quality of the fourth-order results. Results for the tensor spectrum are qualitatively similar. As expected, the uniform approximation improves on the slow-roll result to the left of $k \sim 0.05\,h\,\mathrm{Mpc}^{-1}$, since the slow-roll assumptions are violated in this region.

The spectral indices are displayed in Figs. 7.9(a) and 7.9(b). The potential z''/z (see Fig. 7.6) leads to a blue scalar spectrum for smaller momenta and a red scalar spectrum for larger momenta [Fig. 7.9(a)]. For the spectral index the uniform approximation in leading order is remarkably close to the exact numerical result, more or less independent of k. It only deviates slightly at $k \approx 0.04\,h\,\mathrm{Mpc}^{-1}$ for the scalar spectral index. In Fig. 7.10 the relative errors of the uniform approximation and the slow-roll approximation

(a)

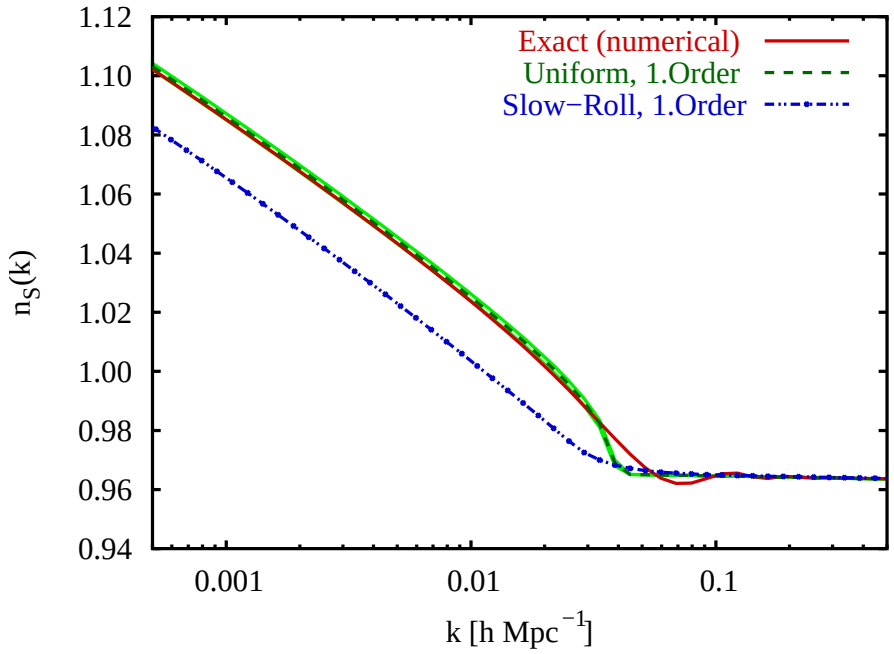

(b)

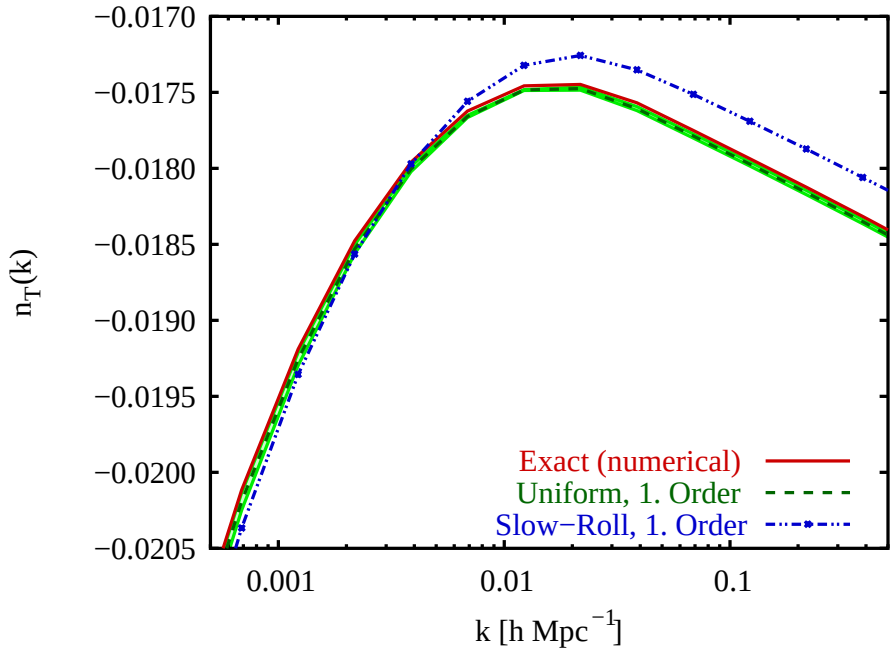

Figure 7.9: (a) Scalar spectral index $n_S(k)$ and (b) tensor spectral index $n_T(k)$ for the C^2-potential in Eqs. (7.1) and (7.2) in the region around the kink; parameters specified as in Fig. 7.7. Solid red line: exact numerical results, dashed green line: uniform approximation, dashed-dotted blue line: slow-roll; the green band is the error estimate for the uniform approximation.

are displayed. Away from the transition k-value, the relative error is smaller than $\sim 0.2\%$ for the scalar spectral index and smaller than $\sim 0.5\%$ for the tensor spectral index. The slow-roll approximation, by comparison, deviates by $\sim 2\%$ from the exact numerical results.

In all the computations so far, the background equations were not approximated to obtain $H(t)$ and $\phi(t)$ and its derivatives, but were solved numerically. For the model in Eqs. (7.1) and (7.2), we have calculated the spectral indices in the slow-roll approximation also with the additional approximation for the background equations in Eqs. (4.15) and (4.16) (see Sec. 4.5). The degradation in the relative error is shown in Fig. 7.10.

The ratio $R(k)$ of tensor to scalar perturbations is depicted in Fig. 7.11, while the corresponding relative errors for the different approximations are shown in Fig. 7.12. The uniform and the slow-roll approximation are both quite close ($\sim 1\%$ error) to the exact numerical result, even though the variations in $R(k)$ are not small. Following Sec. 5.7 the accuracy of the leading-order uniform approximation for the ratio $R(k)$ can be improved using Eq. (5.108) and the corresponding equation for tensor perturbations. We have not displayed this improved ratio in Fig. 7.11, since it would be almost indistinguishable from the exact numerical result. However, Fig. 7.12 shows that the relative error of the (second-order) improved leading order of the uniform approximation is smaller than $\sim 0.3\%$ over the whole k range, consistent with the error estimate (5.109).

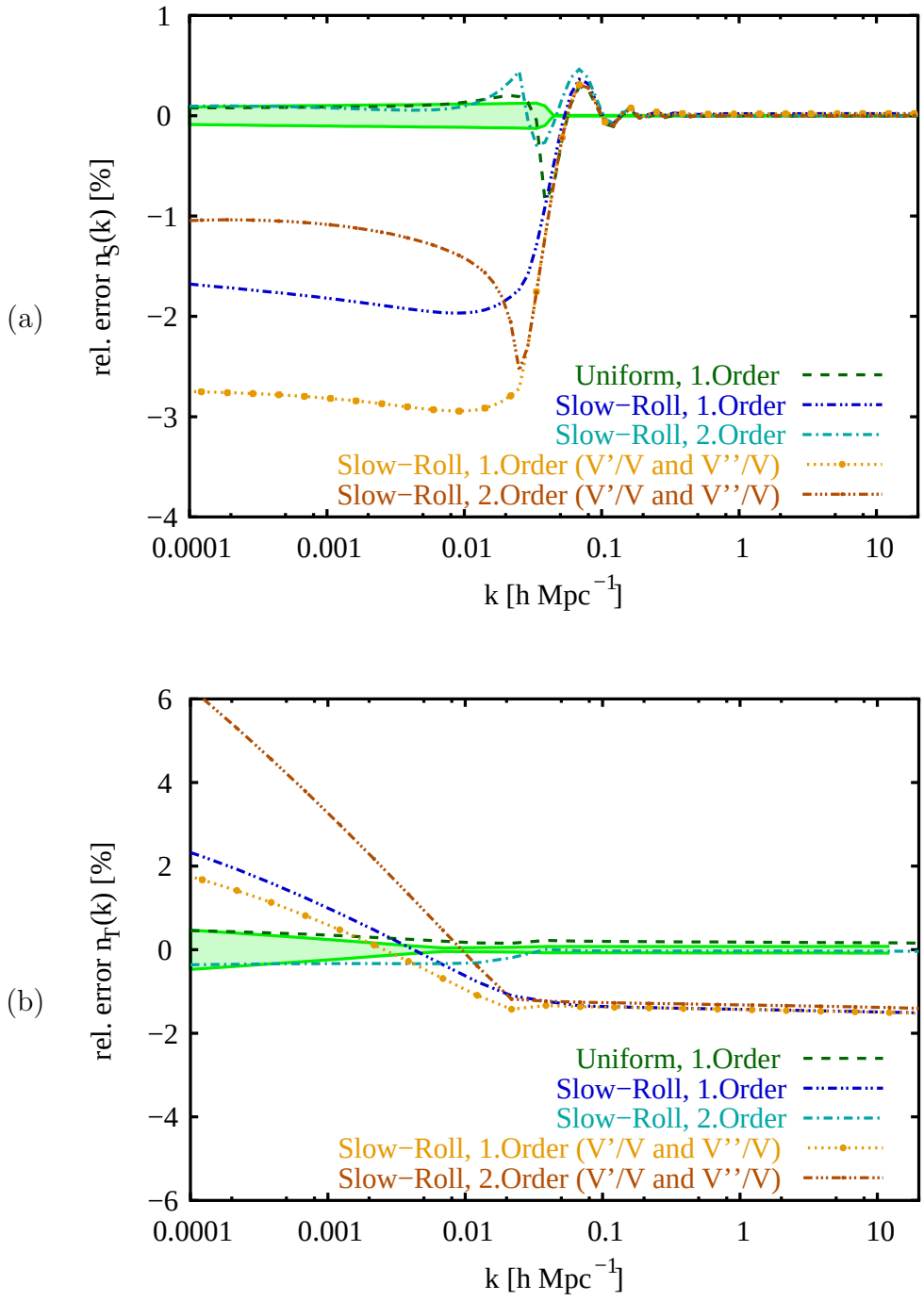

Figure 7.10: Relative error of the (a) scalar and (b) tensor spectral index [see Figs. 7.9(a) and 7.9(b)] for the C^2-potential in Eqs. (7.1) and (7.2). The green band is the error estimate for the uniform approximation. In addition to the uniform and the slow-roll approximation we also show the slow-roll approximation including higher order derivatives of $V(\phi)$ [see Eqs. (4.15) and (4.16)]. Light brown dotted line: first-order slow-roll, dark brown dashed-dotted line: second-order slow-roll.

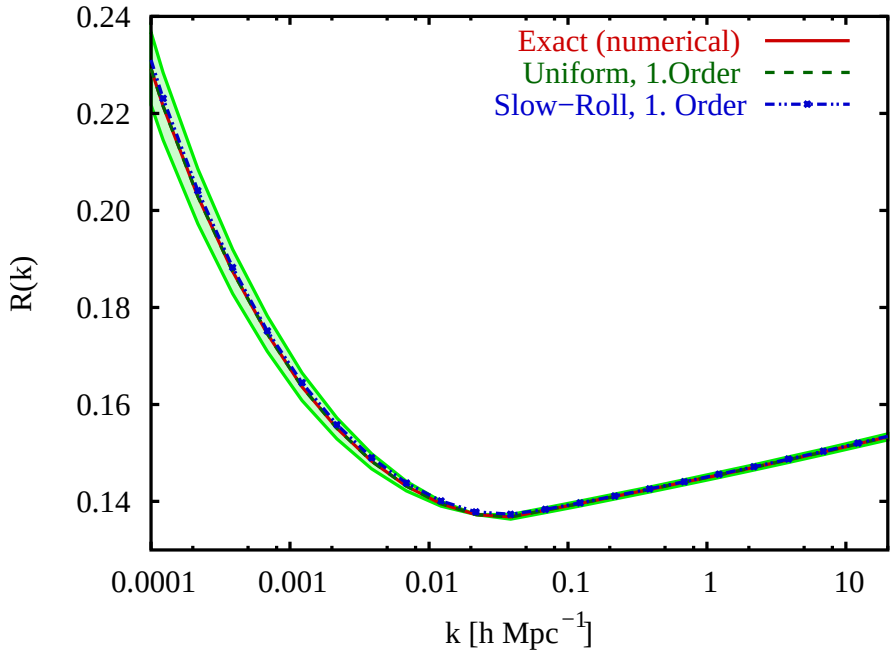

Figure 7.11: Ratio $R(k)$ of tensor to scalar perturbations for the C^2-potential in Eqs. (7.1) and (7.2); the green band is the error estimate for the uniform approximation to leading order; the relative difference between all three approximations is below 2% (see Fig. 7.12), making it difficult to distinguish the curves.

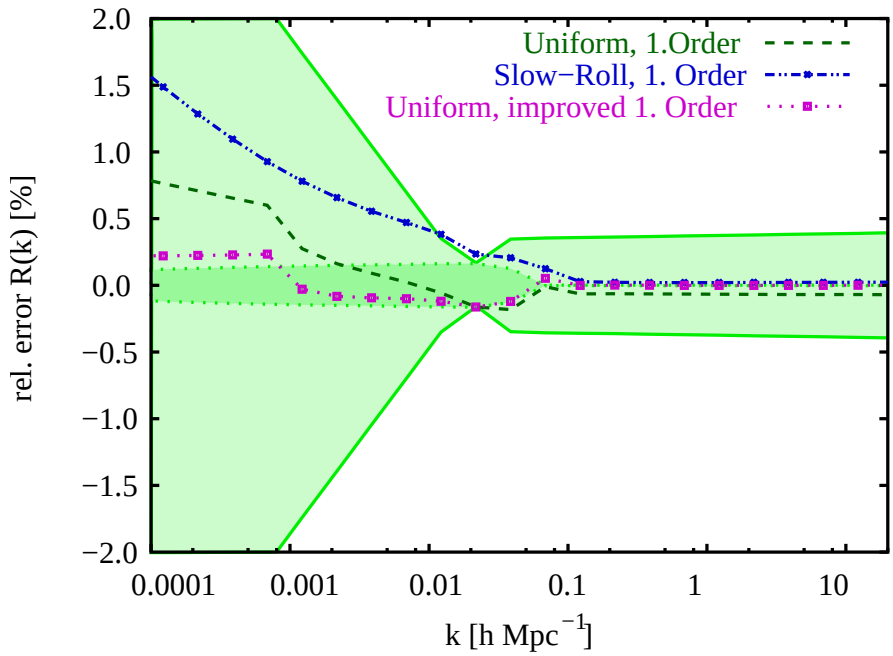

Figure 7.12: Relative error for the ratio $R(k)$ (ratio of tensor to scalar perturbations) for the C^2-potential in Eqs. (7.1) and (7.2); the green band is the error estimate for the uniform approximation to leading order, the dark green band is the estimate for the improved leading order.

Chapter 8

Conclusions of Part II

We have presented the method of uniform approximation as an excellent technique for calculating the inflationary perturbation spectra [43, 44, 45]. A key feature of the method is the existence of a robust error-control theory [42]. Error control, which is missing in the slow-roll approximation and also in WKB approximations [142, 143], is a crucial advantage for practical calculations. We have presented closed expressions for the power spectra, spectral indices and other quantities of interest, to leading and next-to-leading order in the uniform approximation, and with corresponding error bounds.

At leading order in the uniform approximation, we showed how to implement a useful approximate error bound for the power spectrum and the spectral indices. We demonstrated that the leading-order results in this approximation can be easily improved for well-behaved ν_S and ν_T using previously obtained results for the case of constant ν (power-law inflation). In addition, we provided an error estimate for the power spectra obtained from the improved leading-order. The improvement strategy and the error estimates are based on our knowledge of the ultra-local corrections from the next-to-leading order uniform approximation results. The estimates are much tighter than the general leading-order error bounds from the uniform approximation. We have discussed further simplifications of the non-local integral expressions appearing in the uniform approximation, in terms of a derivative expansion combined with an expansion in terms of slow-roll parameters. The inherent danger of uncontrolled approximations has been pointed out.

In addition to semi-analytic calculations in the uniform approximation, we have also implemented an efficient and accurate method for exact mode-by-mode integration utilizing results from the uniform approximation to set up the initial conditions. Such an initialization procedure is very convenient in numerical calculations, since it avoids the time-integration over fast oscillating functions, thus improving both precision and speed of numerical calculations.

The uniform approximation was numerically investigated in detail and compared to exact mode-by-mode results. Our numerical and semi-analytic results for the power spectra and spectral indices agree within 0.1%. Thus, the primordial power spectra can be determined at the same level of accuracy as the transfer functions [51]. We have also compared the results for the power spectra, the corresponding spectral indices and their running

to standard slow-roll approximations, with a view to understanding and controlling the various sources of errors.

We have analyzed in detail different classes of inflationary models: power-law models, chaotic models, and a model with a $\mathcal{C}^2$-potential. We used the power-law model, for which exact analytical results exist, to demonstrate the accuracy of our numerical implementations of the exact mode-by-mode integration, the uniform approximation, and the slow-roll approximation. The deviation of the analytic and numerical results was in general very small, around 1 part in 10^6. Two almost scale-free chaotic inflationary models were chosen as representatives for common slow-roll models: For these models the slow-roll approximation was very good. As a final example, we constructed a $\mathcal{C}^2$-potential which had two dynamical phases patched together in a relatively smooth manner. In the first phase, where ν changes more rapidly than in the second phase, the uniform approximation was much more accurate than the slow-roll approximation, while in the second phase both approximations produced very good results with small errors.

Up-coming high-precision CMB measurements [24, 26, 27, 28, 30] will provide data to constrain the zoo of inflation models [105]. An accurate and fast code for calculating primordial power spectra, spectral indices, and their running will be crucial to this analysis. We have developed and tested a code for calculating the primordial perturbation spectra. The next step is to develop an interface to connect the code to Boltzmann solvers [47, 48, 49, 50] in order to generate the different C_ls, which characterize the anisotropies, directly. The fine structure of the observations of the CMB and LSS holds much of the information about the inflationary epoch, and the new high-precision methods will expose this information.

In addition, it is possible to use the code to test the robustness of the information obtained on the inflationary equation of state from the measured power spectrum by the recently introduced non-parametric reconstruction program [149] and other parametric reconstruction techniques [131].

A deeper understanding of inflation can shed light on the nature of dark energy [96, 150], since there may be a profound link between inflation and the late-time acceleration of the expansion of the Universe which is the signal of dark energy (see Refs. [151, 152, 153, 154] for some very recent discussions). The two complementary approaches of forward predictions and non-parametric reconstruction can provide new precision probes of the first moments of our Universe.

Part III

Preheating after Hybrid Inflation

Chapter 9

Nonperturbative Approximations

In this Chapter a nonperturbative approximation technique for nonequilibrium quantum field theory is presented. First, we give an overview on nonequilibrium quantum field theory and various approximation techniques. Next, we introduce a fairly general Lagrangian for scalar fields. Then, relevant types of Feynman diagrams are introduced. Finally, we turn to a special effective action approach which we will use in order to derive renormalized equations of motion for the classical fields and their quantum fluctuations.

9.1 Nonequilibrium quantum field theory

Nonequilibrium quantum field theory means the study of initial value problems in quantum field theory. The initial state is most of the cases *very far away* from thermal equilibrium. The very early universe was in such a state and preheating is essentially a problem of nonequilibrium (quantum) field theory.

In almost any quantum field theory the departure from thermal equilibrium leads to major complications. Resonance processes can be important, dynamical instabilities can occur, the fields may develop exponentially large values or effective coupling constants may become very large. Standard perturbation theory breaks down in any of these situations. Lattice calculations, i.e., ab initio calculations starting from a discretized action and using statistical methods for the path integral, are not applicable. Within nonequilibrium quantum field theory we cannot work with an imaginary time, unlike in classical field theories or in thermal equilibrium. However, the situation is not hopeless. Over the last decades powerful approximations have been developed. These approximations have to rely on a nonperturbative resummation of perturbative Feynman diagrams. They contain arbitrary high orders of the coupling parameters and propagators. The so-called *resummation* of an infinitely large class of perturbative Feynman diagrams leads to self-consistent Schwinger-Dyson equations, also known and widely used in other contexts (see, e.g., Ref. [155]).

Most importantly, reasonable approximations are constrained by the requirements:

1. They have to be nonperturbative.
2. There should be thermodynamical consistency $\Leftrightarrow$ total energy must be conserved.
3. Renormalizability should be guaranteed.
4. The time evolution should not be secular.

Usually these requirements are not independent of each other.

The first requirement is fulfilled if the equations of motion for the quantum part are self-consistent, i.e., the equations for the propagators are Schwinger-Dyson equations. However, not every Schwinger-Dyson equation is thermodynamically consistent. Thermodynamical consistency is easily achieved by using a variation principle, i.e., if all relevant equations are derived by a functional variation of the same effective action, the resulting set of equations is thermodynamically consistent (see, e.g., Ref. [156]). Within nonequilibrium quantum field theory thermodynamical consistency is related to the conservation of the total energy. The third aspect from the list above means that we should not violate the renormalizability of the original theory when developing an approximation. Unlike in standard perturbation theory we usually cannot fix the counterterms order by order perturbatively. This effectively makes the procedure of renormalization much more involved. We need a full hierarchy of perturbative counterterms. Only very recently several authors have carefully studied the issue of renormalization [157, 158, 159, 160, 161]. Finally, the last requirement of having a secular-free evolution further constrains the possibilities of finding appropriate approximations.

It turns out that the requirements listed above are fulfilled by so-called N-particle irreducible (NPI) effective actions, where $N \geq 2$ in order to guarantee a non-secular time evolution. Also dynamical renormalization group techniques have been used (see, e.g., Refs. [162, 163]).

Besides all these aspects, directly addressing the approximation, the dynamics itself have to be causal. The time evolution of out-of-equilibrium systems in quantum field theory is described within the closed-time-path (CTP) or Schwinger-Keldysh formalism [164, 165] (see also Ref. [166, 167]). In addition we have to choose a proper initial state so that the usual canonical commutation relations for the creation and annihilation operators of the quantum fields are satisfied. This is done by taking a Fock basis at the initial time $t = 0$.

Another—more pragmatic—requirement that has not been mentioned so far, is the efficiency of the numerical implementation due to computational limitations. The past numerical calculations have been limited very often by insufficient computer power. Along with the development of computation power, nonequilibrium quantum field theory improved tremendously, after seminal publications in the 1980's [168, 169, 170], mainly in the last decade [76, 89, 115, 171, 172, 173, 174, 175, 176, 177]. The well-known one-loop, Hartree and large-N approximations can be based on the two-particle irreducible (2PI) formalism [178, 179, 180]. This formalism has also been used beyond mean field approaches

[181, 182, 183, 184, 185, 186]. A subclass of the 2PI formalism is the so-called two-particle point-irreducible (2PPI) formalism [85, 91, 92, 187, 188]. The various leading-order approximations of the 2PI and 2PPI effective action are identical. The latter scheme has advantages with respect to some technical issues of renormalization [157, 158, 159, 160, 161] and we will use the 2PPI formalism here when deriving renormalized equations of motion.

Although leading-order approximations, like the Hartree or large-N approximation, can give useful insight into the out-of-equilibrium dynamics of quantum fields at early times, they miss the important scattering of quanta which ultimatively lead to reheating.[1] Thus, using leading-order type approximations we can only address the preheating stage in which scattering processes are believed to be almost unimportant. Here we are mainly interested in the transition from the false vacuum to the true vacuum, i.e., the first moments of preheating after inflation. Using a leading-order approximation scheme is thus adequate. Calculations in systems with coupled scalar fields are already difficult, both analytically and numerically [86, 191]. The main complication is due to the renormalization of the coupled fields in the presence of quantum back-reaction. In the past, other groups have either completely neglected the back-reaction of the quanta onto themselves [80, 84, 86] or they have used simple cut-off schemes [78] which may exhibit a dangerous dependence on the cut-off parameters chosen and therefore can lead to unphysical artefacts. We are able to explicitly renormalize the equations of motion with quantum back-reaction being present. We are using a resummation scheme of one-loop bubble diagrams that is generalized from the equilibrium case to the more general nonequilibrium situation. The strategy is similar to the one in Ref. [192], used for the O(N) model, but goes beyond it, mainly due to the non-diagonalizable coupling of the fields. It should be stressed that it is not immediately obvious how renormalization of theories, like the one discussed here, proceeds. The basic Lagrangian has no continuous symmetries and in the way it is constructed one of the field has a quartic self-coupling while the other field does not. With the strategy to be presented here there remain no ambiguities.

9.2 Lagrange density

A general Lagrange density for a N component field $\mathbf{\Phi} = (\Phi_1, \ldots, \Phi_N)$ is given by

$$\mathcal{L}(x) = \frac{1}{2}\partial_\mu \Phi^i(x)\partial^\mu \Phi^i(x) - V(x) \;, \tag{9.1}$$

$$V(x) = \frac{1}{2}m^2_{ij}\Phi^i(x)\Phi^j(x) + \frac{1}{4!}\lambda_{ijkl}\Phi^i(x)\Phi^j(x)\Phi^k(x)\Phi^l(x) \;, \tag{9.2}$$

where a summation over i, j, k, l is understood and we have introduced a coupling constant matrix (λ_{ijkl}) and a mass matrix (m^2_{ij}).

[1] When using 2PI resummation techniques, thermalization has been demonstrated for simple low dimensional systems or using lattice regularization techniques [181, 185, 186, 189]. If the quantum fields are spatially inhomogeneous thermalization has also been observed [190].

The classical expectation values (order parameters) of the fields Φ^i are defined as

$$\left\langle \Phi^i(x) \right\rangle = \phi^i(x)\,. \tag{9.3}$$

Depending on the values of the coupling constants λ_{ijkl} and the mass parameters m^2_{ij} the Lagrangian in Eq. (9.1) includes chaotic inflation, hybrid inflation as well as small-field inflation models. We will develop and present a particular approximation for the nonequilibrium dynamics in the hybrid model on the basis of this more general Lagrangian.

9.3 Reducible and irreducible Feynman diagrams

Within relativistic quantum field theory effective actions are conveniently expressed with the help of N-particle irreducible Feynman diagrams. We define: A diagram that does not fall apart if N (arbitrary) propagator lines are cut is called *N-particle irreducible*. A diagram is connected if there are no isolated interaction vertices. We will mostly refer to 2PI (two-particle irreducible) effective actions or diagrams. In general a meaningful maximum value for N is given by the interaction vertices of interest.

A diagram that does not fall apart if two propagator lines *meeting at the same point* are cut is called *two-particle point-irreducible* (2PPI). Both sets of diagrams (2PPI and 2PI) are of course infinitely large. Yet there are two-particle reducible (2PR) diagrams which are not two-particle point-reducible (2PPR).

In Fig. 9.1(a) we display an example for a diagram that is both 2PR and 2PPR. The solid lines in this figure represent the propagators, while dashed lines denote a coupling to an external classical field. On the vertex at the bottom of this diagram two propagator lines meet. If we cut these lines the diagram is disconnected. The diagram in Fig. 9.1(b) is still 2PR but 2PPI. We can cut two arbitrary lines that meet at the same point and the diagram does not fall apart. Each interaction vertex in Fig. 9.1(b) has three propagator lines. In other words, a diagram is 2PPI if each interaction vertex is reached by at least three propagator lines, while such a condition is not sufficient for characterizing 2PI diagrams. Finally, the diagram shown in Fig. 9.1(c) is both 2PI and 2PPI. We can cut any of the lines and the diagram remains connected. The difference between reducible and irreducible diagrams will be essential for the construction of an effective action as well as for the discussions on resummation and renormalization.

9.4 The 2PPI resummation scheme

The 2PPI resummation scheme has been originally developed for finite temperature quantum field theory by Verschelde and Collaborators [85, 187, 188, 193, 194]. In order to generalize the scheme to the nonequilibrium situation we use a strategy similar to the one in [192], there used for the O(N) model. We have to extent the calculations further due to non-diagonalizable coupling of the fields and we have to establish a more rigorous connection between effective counter terms and the standard counter term Lagrangian [85].

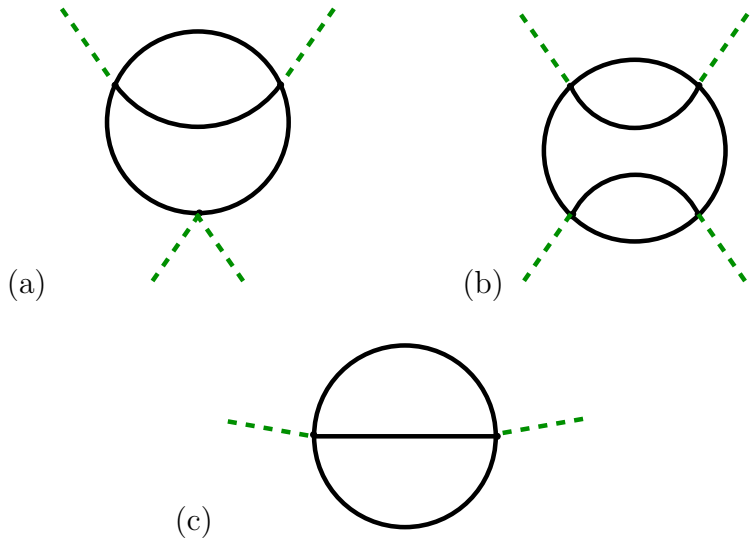

Figure 9.1: Different reducible and irreducible diagrams. The solid lines denote propagators, the dashed lines represent a coupling to an external classical field. (a) This diagram is both 2PR and 2PPR. Such diagrams are thus implicitly contained in the various effective actions. (b) This ladder-type diagram is 2PR but 2PPI. In 2PI effective actions such diagrams are implicitly contained, while in the 2PPI scheme we would have to them explicitly into account. (c) This sunset-type diagram is both 2PI and 2PPI. Such diagrams are not implicitly contained in the effective actions.

Compared to the O(N) case there is no continuous global symmetry assumed, therefore renormalization proceeds slightly different.

9.4.1 Effective action

The basic quantities in the 2PPI resummation scheme are the mean fields ϕ^i and local propagator insertions Δ_{ij}. The local insertions in the propagator are resummed via a Schwinger-Dyson or *gap equation*. The Green's function G fulfills the local equation

$$(G^{-1})_{ij}(x,x') = i\left[\Box\delta_{ij} + \mathcal{M}^2_{ij}(x)\right]\delta^{(D)}(x-x')\ , \tag{9.4}$$

where $\mathcal{M}^2_{ij}$ is a variational mass parameter explained below and G^{-1} denotes the inverse propagator. In the context of nonequilibrium quantum field theory, Eq. (9.4) represents the dynamical equation for the quantum fluctuations. Via the resummation the mass parameter $\mathcal{M}^2_{ij}$ depends on G and ϕ. Compared to the 2PI (or more general NPI) schemes the non-local self-energy is reduced to a local self-energy. The most important feature in the 2PPI scheme—also known from the LO in a $1/N$ expansion—is that the dynamical equation for the propagator G is only an ordinary differential equation rather than a partial differential equation. This greatly simplifies numerical computations. We will elaborate on the shortcomings of this approach when discussing the results in Sec. 11.

The 2PPI effective action for the general potential in Eq. (9.2) can be written as (see, e.g., Ref. [85, 193])

$$\Gamma[\phi^i, \Delta^{ij}] \;=\; S[\phi^i] + \Gamma^{\rm 2PPI}[\phi^i, \mathcal{M}^2_{ij}] + \frac{1}{8}\lambda_{ijkl}\int d^D x \Delta^{ij}(x)\Delta^{kl}(x)\,, \tag{9.5}$$

where D is the number of space-time dimensions and the relation between Δ_{ij} and $\mathcal{M}^2_{ij}$ is given by

$$\Delta^{ij}(x) \;=\; -2\frac{\delta\Gamma^{\rm 2PPI}}{\delta\mathcal{M}^2_{ij}(x)}\,. \tag{9.6}$$

The term proportional to an integral over $\Delta^{ij}(x)\Delta^{kl}(x)$ in Eq. (9.5) corrects the double counting of bubble graphs.

The masses $\mathcal{M}^2_{ij}(x)$ have to fulfill the so-called gap equations

$$\mathcal{M}^2_{ij}(x) \;=\; m^2_{ij} + \frac{1}{2}\lambda_{ijkl}\left[\phi^k(x)\phi^l(x) + \Delta^{kl}(x)\right]\,. \tag{9.7}$$

The term $\Gamma^{\rm 2PPI}[\phi^i, \mathcal{M}^2_{ij}]$ denotes the infinite sum over all 2PPI diagrams.

The classical action $S[\phi^i]$ is given by

$$S[\phi^i] \;=\; \int d^D x \left[\frac{1}{2}\partial_\mu\phi^i(x)\partial^\mu\phi^i(x) - \frac{1}{2}m^2_{ij}\phi^i(x)\phi^j(x) + \frac{1}{4!}\lambda_{ijkl}\phi^i(x)\phi^j(x)\phi^k(x)\phi^l(x)\right]\,. \tag{9.8}$$

9.4.2 Mode functions

In the following we will assume spatially homogeneous fields. The classical fields then obey $\phi^i(t,x) \equiv \phi^i(t)$ and the Green's functions can be expressed via their Fourier components

$$G_{ij}(t,t';\mathbf{x},\mathbf{x}') = \int \frac{d^{D-1}p}{(2\pi)^{D-1}} e^{i\mathbf{p}\cdot(\mathbf{x}-\mathbf{x}')} G_{ij}(t,t';\mathbf{p})\,. \tag{9.9}$$

Since the 2PPI formalism resums *local* self energy insertions in the Green's function, $G_{ij}(t,t';\mathbf{p})$ can be rewritten in terms of mode functions $f_i(t;\mathbf{p})$ and $f_j(t';\mathbf{p})$, leading to a diagonal Wronskian matrix. The Green's function reads

$$G_{ij}(t,t';\mathbf{p}) \;=\; \sum_{\alpha=1}^{2}\frac{1}{2\omega_\alpha}\left[f_i^\alpha(t;p)f_j^{*\,\alpha}(t';p)\Theta(t-t') + f_i^\alpha(t';p)f_j^{*\,\alpha}(t;p)\Theta(t'-t)\right]\,, \tag{9.10}$$

where the mode functions satisfy

$$\ddot{f}_i^\alpha(t;p) + \left[\mathbf{p}^2\delta_{ij} + \mathcal{M}^2_{ij}(t)\right] f_j^\alpha(t;p) = 0\,. \tag{9.11}$$

The fundamental solutions of this system of coupled differential equations will be labeled with Greek letters $(\alpha, \beta, \ldots)$. Hence, there are $2i$ different complex mode functions.

In Eq. (9.10) we have introduced the quantities ω_α defined as

$$\omega_\alpha = \sqrt{\mathbf{p}^2 + m^2_{0,\,\alpha}}\,. \tag{9.12}$$

They will be explained below, as they depend on the initial conditions via the initial masses $m^2_{0,\,\alpha}$.

The decomposition of G in mode functions is very useful, both numerically and analytically. The major numerical simplification compared to the 2PI or NPI schemes is that we have to solve only ordinary differential equations. We reduce the storage requirements by a factorization of functions of two time arguments in two functions with one time argument. In contrast to 2PI schemes this feature remains beyond leading order in a loop expansion or in a $1/N$ expansion. For the analytical calculations we directly benefit from the achievements of expansions of the mode functions as been previously developed in various other models (see, e.g., Ref. [76, 177, 191]). Such expansions allow a clear separation of divergent and finite parts in the propagator insertions and thus simplify renormalization. The remaining task in this work is the generalization to nonequilibrium quantum field theory in the presence of non-diagonalizable couplings and back-reaction of the quantum fields.

9.4.3 Loop expansion

The infinite sum of two-particle point-irreducible diagrams in Γ^{2PPI} can be truncated in several ways. If the original Lagrangian consisting of N fields is invariant under global $\mathrm{O}(N)$ transformations[2], one may use $1/N$ expansion techniques. The leading order in a $1/N$ expansion is also called large-N. As long as N is not small, higher order corrections are comfortably suppressed by inverse powers of N.

Since we cannot assume an $\mathrm{O}(N)$ symmetry in general—the hybrid model does not have it—, we will discuss a loop expansion here. The loop expansion can be denoted as

$$\Gamma^{\mathrm{2PPI}} = \sum_{\ell=1}^{\infty} \Gamma^{(\ell)} = \Gamma^{(1)} + \Gamma^{(2)} + \ldots\,, \tag{9.13}$$

where the index $\ell = 1, 2, \ldots$ corresponds to the number of loops in a 2PPI diagram. The control parameter in a loop expansion is $\hbar$. [3]

The dots in the last equation indicate all contributions beyond the two-loop order. The fluctuation integrals Δ_{ij} are expanded in an analogous way as

$$\Delta_{ij}(t) = \Delta^{(1)}_{ij}(t) + \Delta^{(2)}_{ij}(t) + \ldots\,. \tag{9.14}$$

The one-loop order in the 2PPI loop expansion is equivalent to the Hartree approximation, as already stated above.

[2] The Lagrangian in Eq. (9.1) is $\mathrm{O}(N)$ invariant if all masses and coupling constants are equal.

[3] Note that higher loop diagrams also involve smaller symmetry factors and higher powers in $1/(2\pi)^3$.

Zero-loop—classical approximation

To zero-loop order we discard the term $\Gamma^{\rm 2PPI}$ completely, which leads to $\Delta_{ij} = 0$ and $\delta\Gamma^{\rm 2PPI}/\delta\phi_i = 0$. In this approximation there are no quantum fluctuations at all included.

One-loop—Hartree type approximation

The one-loop approximation is identical to what we might call *Hartree approximation*. Since a Hartree type factorization has not been the starting point here, it would be better to speak about one-loop bubble-resummations in our case.

The sum of all 2PPI diagrams is truncated at $\Gamma^{\rm 2PPI} \approx \Gamma^{(1)}$ with (see the diagram in Fig. 9.2)

$$\Gamma^{(1)}[\mathcal{M}^2_{ij}] = \frac{i}{2}{\rm Tr}\ln\left[\mathcal{G}^{-1}\right] \ . \tag{9.15}$$

We have introduced a matrix

$$\mathcal{G} = (G_{ij})_{i,j=1,\ldots N} \ . \tag{9.16}$$

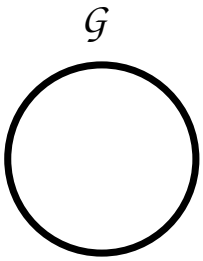

Figure 9.2: One-loop bubble diagram representing leading-order approximation that may also be called Hartree approximation. The line denotes a propagator $\mathcal{G}$ as given by Eq. (9.16).

The functional derivative of $\Gamma^{(1)}$ with respect to $\mathcal{M}^2_{ij}$ gives the tadpole insertions

$$\Delta^{(1)}_{ij}(t) = \frac{1}{2}\int\frac{d^{D-1}p}{(2\pi)^{D-1}}\Big[G_{ij}(t,t;\mathbf{p}) + G_{ji}(t,t;\mathbf{p})\Big] \tag{9.17}$$

$$= \sum_{\alpha=1}^{2}\int\frac{d^{D-1}p}{(2\pi)^{D-1}}\frac{1}{2\omega_\alpha}{\rm Re}\left[f^\alpha_i(t;p)f^{\alpha\,*}_j(t;p)\right] \ . \tag{9.18}$$

The momentum integrations in the quantities $\Delta^{(1)}$ are divergent and thus have to be renormalized properly. We will discuss this issue in the next section.

Two-loop—sunset diagrams

The only two-loop diagram appearing is the sunset diagram displayed in Fig. 9.3. This sunset graph leads to time integrations over the past of classical and quantum fields ("memory integrations") and introduces scattering of the quanta. While it would be interesting to study how this next-to-leading order diagram affects the dynamics studied here, this is far beyond the scope of this work.

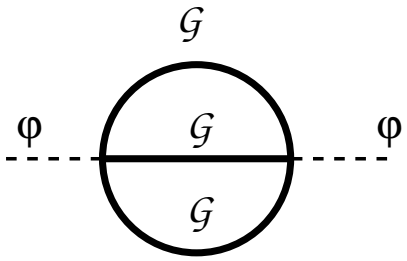

Figure 9.3: Two-loop sunset diagram; the solid lines denote the propagator $\mathcal{G}$, the dashed lines the classical fields $\varphi = (\phi_1, \ldots, \phi_N)$; this diagram is the first contribution that introduces scattering of the quanta.

9.4.4 Renormalization of the 2PPI effective action

We will introduce *effective* counterterms that render the renormalization procedure simple and efficient. It is important to connect such effective counterterms to the counterterms in the original formulation of the 2PPI scheme, since the latter ones follow from a standard counterterm Lagrangian (see Ref. [85, 187, 188, 193]).

In order to renormalize the general Lagrange density for the model in Eq. (9.1) we include a counterterm $\delta\mathcal{L}$

$$\mathcal{L} = \frac{1}{2}\partial_\mu\Phi^i\partial^\mu\Phi^i - \frac{1}{2}m_{ij}^2\Phi^i\Phi^j - \frac{1}{4}\lambda_{ijkl}\Phi^i\Phi^j\Phi^k\Phi^l + \delta\mathcal{L}\,. \tag{9.19}$$

We have omitted here the space-time dependence of all fields. As in standard perturbation theory the counterterm Lagrangian $\delta\mathcal{L}$ is given by

$$\delta\mathcal{L} = \frac{1}{2}\delta Z_{ij}\partial^\mu\Phi^i\partial^\mu\Phi^j - \frac{1}{2}\delta m_{ij}^2\Phi^i\Phi^j - \frac{1}{4}\delta\lambda_{ijkl}\Phi^i\Phi^j\Phi^k\Phi^l\,. \tag{9.20}$$

The gap equation for the renormalized effective mass $\mathcal{M}^2_{\mathrm{R},ij}$ with mass and coupling constant counterterms is given by

$$\mathcal{M}^2_{\mathrm{R},ij} = m_{ij}^2 + \delta m_{ij}^2 + \frac{1}{2}\left(\lambda_{ijkl} + \delta\lambda_{ijkl}\right)\left(\phi^k\phi^l + \Delta^{kl}\right)\,. \tag{9.21}$$

Verschelde [85] has demonstrated by diagrammatical counting that in the 2PPI scheme the following relations for the renormalization constants hold, if we take a *mass independent*

renormalization scheme[4]

$$(\delta m^2)^{ij} = \delta Z_m^{ij;kl} m_{kl}^2 \,, \tag{9.22}$$

$$\delta\lambda^{ij;kl} = \lambda^{ij}{}_{pq} \delta Z_m^{pq;kl} \,, \tag{9.23}$$

$$\delta Z_m^{ij;kl} = \lambda^{ij}{}_{pq} \delta\zeta^{pq;kl} \,. \tag{9.24}$$

Moreover, at the level of the effective action all renormalization constants may be derived from a single vacuum counterterm

$$\delta E_{\rm vac} = \frac{1}{2}\mathcal{M}_{ij}^2 \mathcal{M}_{kl}^2 \, \delta\zeta^{ij;kl} \,. \tag{9.25}$$

With the help of the identities in Eqs. (9.22)–(9.24) the gap equations read

$$\begin{aligned} \mathcal{M}_{{\rm R},\,ij}^2 &= m_{ij}^2 + \frac{1}{2}\lambda_{ijkl}\left(\phi^k\phi^l + \Delta^{kl}\right) + \lambda_{ijpq}\,\delta\zeta^{pq;kl} m_{kl}^2 \\ &\quad + \frac{1}{2}\lambda_{ijpq}\lambda^{pqrs}\,\delta\zeta_{rs;kl}\left(\phi^k\phi^l + \Delta^{kl}\right) \qquad (9.26) \\ &\equiv m_{ij}^2 + \frac{1}{2}\lambda_{ijkl}\left(\phi^k\phi^l + \Delta_{\rm R}^{kl}\right) \,, \qquad (9.27) \end{aligned}$$

with

$$\lambda_{ijkl}\Delta_{\rm R}^{kl} = \lambda_{ijkl}\Delta^{kl} + 2\lambda_{ijpq}\delta\zeta^{pq;kl} m_{kl}^2 + \frac{1}{2}\lambda_{ijpq}\lambda^{pqrs}\,\delta\zeta_{rs;kl}\left(\phi^k\phi^l + \Delta^{kl}\right) \,. \tag{9.28}$$

Once the propagator Δ^{ij} is renormalized the gap equations for the masses $\mathcal{M}_{ij}^2$ become finite. In the one-loop 2PPI approximation, i.e., when $\Delta_{ij} = \Delta_{ij}^{(1)}$, the equations for the classical fields ϕ^i are finite as well. No wave function renormalization is needed.

Although wave function renormalization is indeed not a major complication in the 2PPI scheme, we have restricted the discussion of renormalization to leading order here, since we do not aim to go beyond leading order in the numerical calculations either.

Summarizing renormalization in the 2PPI scheme, we simply have to renormalize the propagator insertion Δ_R and all equations of motion will be finite. In the context of nonequilibrium quantum field theory this implies the separation of the divergent parts from the finite parts in a time-dependent quantity. Moreover, the independence of the counterterms on the details of the initial conditions has to be proven.

[4]E.g., minimal subtraction (MS) or a modified minimal subtraction ($\overline{\rm MS}$)

Chapter 10

Renormalized Equations

In this Chapter the renormalized equations of motion are derived. First, the initial conditions and the way of fixing the vacuum have to be discussed. Then we present a method of isolating the divergencies in all equations. Once the divergencies have been regularized—which is done using standard dimensional regularization—all dynamical equations can be renormalized. After renormalization all equations are explicitly finite and thus can be directly used in numerical simulations without further assumptions.

We have introduced a very general effective action for N scalar fields in the previous Chapter. This has been necessary in order to take advantage of existing expressions of the 2PPI resummation scheme [85]. The standard hybrid potential in Eq. (3.6) follows from Eq. (9.2) for the case $N = 2$ with the identifications

$$\begin{aligned}
\Phi_1 &= \Phi\,, && (10.1)\\
\Phi_2 &= X\,, && (10.2)\\
m_{11}^2 &= m^2\,, && (10.3)\\
m_{22}^2 &= -\lambda v^2\,, && (10.4)\\
m_{12}^2 &= m_{21}^2 = 0\,, && (10.5)\\
\lambda_{2222} &= 6\lambda\,, && (10.6)\\
\lambda_{\mathrm{Perm}(1122)} &= 2g^2\,, && (10.7)\\
\lambda_{1111} &= \lambda_{1112} = \ldots = \lambda_{2221} = 0\,. && (10.8)
\end{aligned}$$

10.1 Initial conditions

The choice of initial conditions is similar to the one in Ref. [86]. We will take a Gaussian initial density matrix with non-vanishing initial values $\phi(t = 0)$ and $\chi(t = 0)$ for the classical field amplitudes. For the renormalization of the equations of motion we need a properly quantized system at the initial time. In order to satisfy the usual canonical commutation relations for the creation and annihilation operators of the quantum fields, we choose a Fock space basis at $t = 0$. The basic quanta are defined by diagonalizing the

mass matrix at $t = 0$ and by choosing canonical initial conditions (see below) for the mode functions (see, e.g., Refs. [76, 86, 177, 195]).

We define the initial masses $m_{0,\alpha}$ as the eigenvalues of the initial mass matrix $\mathcal{M}_{ij}(0)$, i.e., by the equation

$$m^2_{0,\,\alpha} f^\alpha_i(0;p) - \mathcal{M}^2_{ij}(0) f^\alpha_j(0;p) \;=\; 0\,. \tag{10.9}$$

The eigenvalues are given by

$$m^2_{0,\,\alpha} \;=\; \frac{1}{2}\left\{\mathcal{M}^2_{\phi\phi}(0) + \mathcal{M}^2_{\chi\chi}(0) \pm \sqrt{\left[\mathcal{M}^2_{\phi\phi}(0) - \mathcal{M}^2_{\chi\chi}(0)\right]^2 + 4\mathcal{M}^4_{\phi\chi}(0)}\right\}. \tag{10.10}$$

We denote the corresponding eigenvectors by $O_{i\alpha}$, where the index α refers to the eigenvalue, and the Latin indices to the components. The canonical initial conditions at $t = 0$ for the mode functions are

$$f^\alpha_i(0;p) \;=\; O_{i\alpha}\,, \tag{10.11}$$
$$\dot{f}^\alpha_i(0;p) \;=\; -i\omega_\alpha O_{i\alpha} = -i\omega_\alpha f^\alpha_i(0;p)\,. \tag{10.12}$$

The Wronskian matrix of these mode functions is then given by

$$W(f^\alpha_i, f^\beta_i) \;=\; [f^{\alpha,\,*}_i(0;p)\dot{f}^\beta_i(0;p) - \dot{f}^{\alpha,\,*}_i(0;p) f^\beta_i(0;p)] \tag{10.13}$$
$$\;=\; -i[(\omega_\alpha + \omega_\beta) O_{i\alpha} O_{i\beta}]\,. \tag{10.14}$$

As the eigenvectors are orthogonal this matrix is diagonal. Choosing the normalization

$$O_{i\alpha} O_{i\beta} = \delta_{\alpha\beta}\,, \tag{10.15}$$

the Wronskian matrix becomes

$$W(f^\alpha_i, f^\beta_i)_{\alpha,\beta=1,2} \;=\; -2i \begin{pmatrix} \omega_1 & 0 \\ 0 & \omega_2 \end{pmatrix}. \tag{10.16}$$

If $\mathcal{M}^2_{\chi\chi}(0) > \mathcal{M}^2_{\phi\phi}(0)$ we can fix the matrix O as

$$O \;=\; \begin{pmatrix} \cos\vartheta & \sin\vartheta \\ -\sin\vartheta & \cos\vartheta \end{pmatrix}, \tag{10.17}$$

$$\tan\vartheta \;=\; \frac{1}{2\mathcal{M}^2_{\phi\chi}(0)}\left\{\mathcal{M}^2_{\chi\chi}(0) - \mathcal{M}^2_{\phi\phi}(0) + \sqrt{\left[\mathcal{M}^2_{\chi\chi}(0) - \mathcal{M}^2_{\phi\phi}(0)\right]^2 + 4\mathcal{M}^4_{\phi\chi}(0)}\right\}. \tag{10.18}$$

For the opposite case $\mathcal{M}^2_{\chi\chi}(0) < \mathcal{M}^2_{\phi\phi}(0)$ we should interchange $m^2_{0,\,1}$ with $m^2_{0,\,2}$ and switch $\vartheta \to -\vartheta$. Indeed this is important for the numerical implementation. We need three initial parameters and may either choose $\{m^2_{0,\,1}, m^2_{0,\,1}, \tan\vartheta\}$ or $\{\mathcal{M}^2_{\phi\phi}(0), \mathcal{M}^2_{\chi\chi}(0), \mathcal{M}^2_{\phi\chi}(0)\}$ as the set of equations that we numerically iterate.

10.2 Isolation of the divergencies

From now on we will restrict the discussion to the one-loop bubble-resummation with $\Gamma^{\rm 2PPI} \approx \Gamma^{(1)}$ and thus

$$\Delta_{ij}(t) = \Delta_{ij}^{(1)}(t) \; , \tag{10.19}$$

where the propagator insertions $\Delta_{ij}^{(1)}(t)$ [see Eq. (9.17)] contain the divergent loop integrals.

It is important to separate divergent pieces from the finite ones. The divergent pieces are not of physical interest. Moreover, we will isolate the divergences in such a way that standard regularization techniques like dimensional regularization can be used.

A strategy for the isolation of the divergences via the perturbative expansion of the mode functions in terms of partial integrations has been described in Refs. [76, 191]. We have summarized what we need in Appendix B.2.

In dimensional regularization with the abbreviation

$$L_\epsilon = \frac{2}{\epsilon} - \gamma + \ln 4\pi \tag{10.20}$$

we have, using Eq. (B.16) and Eqs. (B.1),(B.4)

$$\begin{aligned}
\Delta_{ij}^{(1)}(t) &= \frac{1}{2}\int \frac{d^{D-1}p}{(2\pi)^{D-1}} \Big[G_{ij}(t,t;\mathbf{p}) + G_{ji}(t,t;\mathbf{p}) \Big] \\
&= -\sum_\alpha \Bigg[\frac{m_{0,\,\alpha}^2}{16\pi^2}\bigg(L_\epsilon - \ln\frac{m_{0,\,\alpha}^2}{\mu^2} + 1 \bigg) O_{i\alpha}O_{j\alpha} + \frac{1}{16\pi^2}\bigg(L_\epsilon - \ln\frac{m_{0,\,\alpha}^2}{\mu^2} + 1 \bigg) \\
&\quad + \frac{1}{16\pi^2}\sum_\beta \bigg(\frac{m_{0,\,\beta}^2}{m_{0,\,\alpha}^2 - m_{0,\,\beta}^2} \ln\frac{m_{0,\,\beta}^2}{m_{0,\,\alpha}^2} \bigg) O_{i\alpha}O_{j\beta}O_{l\beta}O_{k\alpha}\mathcal{V}_{kl}(t) \Bigg] \quad + \ldots \\
&= -\frac{1}{16\pi^2}\left[L_\epsilon + 1 \right] \mathcal{M}_{ij}^2(t) + \sum_\alpha \frac{m_{0,\,\alpha}^2}{16\pi^2} O_{i\alpha}O_{j\alpha} \ln\frac{m_{0,\,\alpha}^2}{\mu^2} \\
&\quad + \frac{1}{16\pi^2}\sum_{\alpha,\beta} O_{i\alpha}O_{j\beta}O_{l\beta}O_{k\alpha}\mathcal{V}_{kl}(t) \bigg(\ln\frac{m_{0,\,\alpha}^2}{\mu^2} - \frac{m_{0,\,\beta}^2}{m_{0,\,\alpha}^2 - m_{0,\,\beta}^2} \ln\frac{m_{0,\,\beta}^2}{m_{0,\,\alpha}^2} \bigg) \\
&\quad + \ldots \; ,
\end{aligned} \tag{10.21}$$

where $\sum_\alpha O_{i\alpha}O_{j\alpha}m_{0,\,\alpha}^2 = \mathcal{M}_{ij}^2(0)$ has been used. The new parameter μ appearing in Eq. (10.21) is the renormalization scale[1] and the potential $\mathcal{V}_{ij}(t)$ is defined as

$$\mathcal{V}_{ij}(t) \;=\; \mathcal{M}_{ij}^2(t) - \mathcal{M}_{ij}^2(0) \, . \tag{10.22}$$

[1] We will take $\mu = \lambda v$ which is the only natural mass scale present. Usually a renormalization scale dependence is not studied in the context of nonequilibrium quantum field theory.

We can define the finite part of $\Delta^{(1)}_{ij}$ by a subtraction as [see Eq. (B.16)]

$$\Delta^{(1)}_{ij,\,\mathrm{fin}}(t) = \int \frac{d^{D-1}p}{(2\pi)^{D-1}} \sum_{\alpha,\beta} \frac{1}{2\omega_\alpha} \Big\{ \mathrm{Re}\left[f^\alpha_i(t;p) f^{\alpha,\,*}_j(t;p)\right] \delta_{\alpha\beta} - O_{i\alpha}O_{j\alpha}\delta_{\alpha\beta} + \frac{1}{\omega_\beta(\omega_\alpha+\omega_\beta)} O_{i\alpha}O_{j\beta}O_{l\beta}O_{k\alpha}\mathcal{V}_{kl}(t) \Big\} . \tag{10.23}$$

The momentum integrations in this expression are convergent, because the subtracted terms cancel exactly the divergent parts (see Appendix B.2). There are still some finite contributions from the divergent part of $\Delta^{(1)}_{ij}$ [see. Eq. (10.21)]. These parts are important and removing them is not allowed because of the dependence on the initial conditions. In order to simplify the notation it is useful to define the following quantities

$$C^0_{ij} = \frac{1}{16\pi^2} \sum_\alpha O_{i\alpha}O_{j\alpha} m^2_{0,\,\alpha} \ln \frac{m^2_{0,\,\alpha}}{\mu^2} , \tag{10.24}$$

$$C^{k\ell}_{ij} = \frac{1}{16\pi^2} \sum_{\alpha,\beta} O_{i\alpha}O_{j\beta}O_{k\alpha}O_{\ell\beta} \left(\ln \frac{m^2_{0,\,\alpha}}{\mu^2} - \frac{m^2_{0,\,\beta}}{m^2_{0,\,\alpha} - m^2_{0,\,\beta}} \ln \frac{m^2_{0,\,\beta}}{m^2_{0,\,\alpha}} \right) , \tag{10.25}$$

and

$$C^1_{ij} := C^{11}_{ij} , \quad C^2_{ij} := C^{22}_{ij} , \quad C^3_{ij} := C^{12}_{ij} + C^{21}_{ji} . \tag{10.26}$$

The constants C^0_{ij} are important for the renormalization of the initial conditions, because they appear without the quantity $\mathcal{V}(t)$ that is zero at $t = 0$. Note that all constants C^k_{ij} contain only the three quantities related to the initial conditions.

The full one-loop bubble-resummed insertion $\Delta^{(1)}_{ij}$ takes a simple form given by

$$\begin{aligned} \Delta^{(1)}_{ij}(t) = {} & \Delta^{(1)}_{ij,\mathrm{fin}}(t) - \frac{1}{16\pi^2}\left[L_\epsilon + 1\right] \mathcal{M}^2_{ij}(t) + C^0_{ij} \\ & + C^1_{ij}\left[\mathcal{M}^2_{\phi\phi}(t) - \mathcal{M}^2_{\phi\phi}(0)\right] + C^2_{ij}\left[\mathcal{M}^2_{\chi\chi}(t) - \mathcal{M}^2_{\chi\chi}(0)\right] \\ & + C^3_{ij}\left[\mathcal{M}^2_{\phi\chi}(t) - \mathcal{M}^2_{\phi\chi}(0)\right] . \end{aligned} \tag{10.27}$$

The divergent part of $\Delta^{(1)}_{ij}$ can be defined as

$$\Delta^{(1)}_{ij,\mathrm{div}}(t) = -\frac{1}{16\pi^2}\left[L_\epsilon + 1\right] \mathcal{M}^2_{ij}(t) . \tag{10.28}$$

Note that $\Delta^{(1)}_{ij,\mathrm{div}}(t)$ is directly proportional to $\mathcal{M}^2_{ij}$, i.e., with a *uniform factor* for all combinations of i and j. In particular $\Delta^{(1)}_{ij,\mathrm{div}}(t)$ is independent of the masses $m^2_{0,\,\alpha}$ and the matrix O_{ij} and thereby of the initial conditions. However, the different finite parts depend on the initial conditions via the constants C^n_{ij} and involve all components of the effective mass matrix $\mathcal{M}^2_{ij}$. The independence of the divergent pieces on the initial conditions is analogous to the independence on the temperature in the context of finite temperature

quantum field theory. The fact that the divergent term is proportional to $\mathcal{M}_{ij}(t)$, a term that is time-dependent, does *not* mean that we need time-dependent counterterms, but simply reflects the fact that effectively the resummation scheme has to treat the bare part and the counterterm part of the original Lagrangian on equal footing. Counterterms are likewise resummed. In the next section we will see that the counterterms are not simply perturbative.

10.3 Renormalized effective action with suitable effective counterterms

First, we write down the unrenormalized effective action. With the help of the identifications in Eq. (10.1)–(10.8) the 2PPI effective action for the hybrid potential in Eq. (3.6) reads

$$\begin{aligned}\Gamma[\phi,\chi,\Delta^{(1)}_{\phi\phi},\Delta^{(1)}_{\phi\chi},\Delta^{(1)}_{\chi\chi}] &= S[\phi,\chi]+\Gamma^{(1)}\left[\mathcal{M}^2_{\phi\phi},\mathcal{M}^2_{\phi\chi},\mathcal{M}^2_{\chi\chi}\right]\\ &\quad+\frac{g^2}{2}\int d^Dx\left\{\Delta^{(1)}_{\phi\phi}(x)\Delta^{(1)}_{\chi\chi}(x)+2[\Delta^{(1)}_{\phi\chi}(x)]^2\right\}\\ &\quad+\frac{3\lambda}{4}\int d^Dx[\Delta^{(1)}_{\chi\chi}(x)]^2\,. \end{aligned} \tag{10.29}$$

The unrenormalized gap equations for the masses $\mathcal{M}^2$ are given by

$$\mathcal{M}^2_{\phi\phi}(x) = m^2+g^2\left[\chi^2(x)+\Delta^{(1)}_{\chi\chi}(x)\right]\,, \tag{10.30}$$

$$\mathcal{M}^2_{\chi\chi}(x) = -\lambda v^2+3\lambda\left[\chi^2(x)+\Delta^{(1)}_{\chi\chi}(x)\right]+g^2\left[\phi^2(x)+\Delta^{(1)}_{\phi\phi}(x)\right]\,, \tag{10.31}$$

$$\mathcal{M}^2_{\phi\chi}(x) = 2g^2\left[\phi(x)\chi(x)+\Delta^{(1)}_{\phi\chi}(x)\right]=\mathcal{M}^2_{\chi\phi}(x)\,. \tag{10.32}$$

Inverting the gap equations leads to

$$\Delta^{(1)}_{\phi\phi}(x) = \frac{1}{g^2}\left\{\mathcal{M}^2_{\chi\chi}(x)+\lambda v^2-\frac{3\lambda}{g^2}\left[\mathcal{M}^2_{\phi\phi}(x)-m^2\right]\right\}-\phi^2(x)\,, \tag{10.33}$$

$$\Delta^{(1)}_{\chi\chi}(x) = \frac{1}{g^2}\left[\mathcal{M}^2_{\phi\phi}(x)-m^2\right]-\chi^2(x)\,, \tag{10.34}$$

$$\Delta^{(1)}_{\phi\chi}(x) = \frac{1}{2g^2}\mathcal{M}^2_{\phi\chi}(x)-\phi(x)\chi(x)=\Delta^{(1)}_{\chi\phi}(x)\,. \tag{10.35}$$

The unrenormalized effective action can therefore be expressed without the Δs, i.e.,

$$\begin{aligned}\Gamma\left[\phi,\chi,\mathcal{M}^2_{\phi\phi},\mathcal{M}^2_{\chi\chi},\mathcal{M}^2_{\phi\chi}\right] &= \int d^Dx\Big\{\frac{1}{2}\partial_\mu\phi(x)\partial^\mu\phi(x)+\frac{1}{2}\partial_\mu\chi(x)\partial^\mu\chi(x)\\ &-\frac{1}{2}\mathcal{M}^2_{\phi\phi}(x)\phi^2(x)+g^2\phi^2(x)\chi^2(x)-\frac{1}{2}\mathcal{M}^2_{\chi\chi}(x)\chi^2(x)\\ &+\frac{\lambda}{2}\chi^4(x)-\frac{\lambda}{4}v^4-\mathcal{M}^2_{\phi\chi}(x)\phi(x)\chi(x)-\frac{3\lambda}{4g^4}\left[\mathcal{M}^2_{\phi\phi}(x)-m^2\right]^2\\ &+\frac{1}{2g^2}\left[\mathcal{M}^2_{\phi\phi}(x)-m^2\right]\left[\mathcal{M}^2_{\chi\chi}(x)+\lambda v^2\right]+\frac{1}{4g^2}\left[\mathcal{M}^2_{\phi\chi}(x)\right]^2\Big\}\\ &+\Gamma^{(1)}\left[\mathcal{M}^2_{\phi\phi},\mathcal{M}^2_{\phi\chi},\mathcal{M}^2_{\chi\chi}\right]. \qquad (10.36)\end{aligned}$$

In the previous subsection we were able to isolate the divergent parts in Eq. (10.27). The divergences were found to be proportional to the effective masses $\mathcal{M}^2_{ij}$.

In order to calculate the renormalized effective action it is convenient to define effective mass counter terms. As elucidated in Sec. 9.4.4 all counterterms needed can be derived from a single vacuum counter term involving the variational masses times a divergent constant [see Eq. (9.25)]. More precisely, the 2PPI formalism establishes a one-to-one mapping between effective counterterms that are useful on the level of effective actions and the standard counterterm Lagrangian.

Let us define a vacuum energy counterterm of the general form

$$\delta\mathcal{M}^4 = \delta\xi_{\phi\phi}\left(\mathcal{M}^2_{\phi\phi}\right)^2+\delta\xi_{\chi\chi}\left(\mathcal{M}^2_{\chi\chi}\right)^2+2\,\delta\xi_{\phi\chi}\left(\mathcal{M}^2_{\phi\chi}\right)^2. \qquad (10.37)$$

With the proper choice of the constants $\delta\xi$—to be fixed in the following—the effective action in Eq. (10.36) becomes renormalized, i.e.,

$$\Gamma_R\left[\phi,\chi,\mathcal{M}^2_{\phi\phi},\mathcal{M}^2_{\chi\chi},\mathcal{M}^2_{\phi\chi}\right]=\Gamma\left[\phi,\chi,\mathcal{M}^2_{\phi\phi},\mathcal{M}^2_{\chi\chi},\mathcal{M}^2_{\phi\chi}\right]+\delta\mathcal{M}^4. \qquad (10.38)$$

With the introduced effective mass counterterms the renormalized gap equations take the form

$$\begin{aligned}\mathcal{M}^2_{\mathrm{R},\,\phi\phi}(t) &= m^2+g^2\left[\chi^2(t)+\Delta^{(1)}_{\chi\chi}(t)\right]-4g^2\,\delta\xi_{\chi\chi}\mathcal{M}^2_{\mathrm{R},\chi\chi}(t), \qquad (10.39)\\ \mathcal{M}^2_{\mathrm{R},\,\chi\chi}(t) &= -\lambda v^2+g^2\left[\phi^2(t)+\Delta^{(1)}_{\phi\phi}(t)\right]+3\lambda\left[\chi^2(t)+\Delta^{(1)}_{\chi\chi}(t)\right]\\ &\quad -4g^2\,\delta\xi_{\phi\phi}\mathcal{M}^2_{\mathrm{R},\,\phi\phi}(t)-12\lambda\,\delta\xi_{\chi\chi}\mathcal{M}^2_{\mathrm{R},\,\chi\chi}(t), \qquad (10.40)\\ \mathcal{M}^2_{\mathrm{R},\,\phi\chi}(t) &= 2g^2\left[\phi(t)\chi(t)+\Delta^{(1)}_{\phi\chi}(t)\right]-8g^2\,\delta\xi_{\phi\chi}\mathcal{M}^2_{\mathrm{R},\,\phi\chi}(t). \qquad (10.41)\end{aligned}$$

Even if we did not know expressions for the divergent part of $\Delta^{(1)}_{ij}$ we would immediately conclude that any possible divergence has to be proportional to the effective masses, precisely what has been found in Eq. (10.28). The gap equations become finite if we fix the constants $\delta\xi$ to be

$$\begin{aligned}\delta\xi_{\phi\phi}=\delta\xi_{\chi\chi}=\delta\xi_{\phi\chi} &= -\frac{1}{64\pi^2}\left[L_\epsilon+1\right] \qquad (10.42)\\ &= -\frac{1}{64\pi^2}\left(\frac{2}{\epsilon}-\gamma+1+\ln 4\pi\right). \qquad (10.43)\end{aligned}$$

This choice of $\delta\xi$ corresponds to a $\overline{\text{MS}}$ prescription. In particular, the renormalization scheme is mass independent. We will write down the final set of gap equations in the next section.

It should also be noted that we could easily calculate the nonperturbatively fixed standard counterterms δm^2, δv^2, δg^2 and $\delta\lambda$ explicitly, insofar the renormalized gap equations just form a coupled system of equations. However, we think that this would not be very enlightening, because the final expressions would be quite lengthy. Moreover, they are not needed explicitly.

10.4 Equations of motion and gap equations

In summary we have to solve in the Hartree approximation the following renormalized equations of motion numerically. The classical equations of motion are given by

$$\begin{aligned} 0 &= \ddot{\phi}(t) + \mathcal{M}^2_{\mathrm{R},\,\phi\phi}(t)\phi(t) + \mathcal{M}^2_{\mathrm{R},\,\phi\chi}(t)\chi(t) - 2g^2\chi^2(t)\phi(t)\;, && (10.44)\\ 0 &= \ddot{\chi}(t) + \mathcal{M}^2_{\mathrm{R},\,\chi\chi}(t)\chi(t) + \mathcal{M}^2_{\mathrm{R},\,\phi\chi}(t)\phi(t) - 2\lambda\chi^3(t) - 2g^2\phi^2(t)\chi(t)\;, && (10.45)\end{aligned}$$

while the equations for the mode functions denote explicitly

$$\begin{aligned} 0 &= \ddot{f}^\alpha_\phi(t;p) + \mathbf{p}^2 f^\alpha_\phi(t;p) + \mathcal{M}^2_{\mathrm{R},\,\phi\phi}(t) f^\alpha_\phi(t;p) + \mathcal{M}^2_{\mathrm{R},\,\phi\chi}(t) f^\alpha_\chi(t;p)\,, && (10.46)\\ 0 &= \ddot{f}^\alpha_\chi(t;p) + \mathbf{p}^2 f^\alpha_\chi(t;p) + \mathcal{M}^2_{\mathrm{R},\,\chi\chi}(t) f^\alpha_\chi(t;p) + \mathcal{M}^2_{\mathrm{R},\,\phi\chi}(t) f^\alpha_\phi(t;p)\,. && (10.47)\end{aligned}$$

In addition we have to solve, at each time step, the 3×3 system of renormalized gap equations given by

$$\begin{aligned} \mathcal{M}^2_{\mathrm{R},\,\phi\phi}(t) &= m^2 + g^2\left[\chi^2(t) + \Delta_{\chi\chi,\mathrm{fin}}(t)\right] + g^2 C^0_{\chi\chi}\\ &\quad + g^2 C^1_{\chi\chi}\left[\mathcal{M}^2_{\mathrm{R},\,\phi\phi}(t) - \mathcal{M}^2_{\mathrm{R},\,\phi\phi}(0)\right] + g^2 C^2_{\chi\chi}\left[\mathcal{M}^2_{\mathrm{R},\,\chi\chi}(t) - \mathcal{M}^2_{\mathrm{R},\,\chi\chi}(0)\right]\\ &\quad + g^2 C^3_{\chi\chi}\left[\mathcal{M}^2_{\mathrm{R},\,\phi\chi}(t) - \mathcal{M}^2_{\mathrm{R},\,\phi\chi}(0)\right]\;, && (10.48)\\ \mathcal{M}^2_{\mathrm{R},\,\chi\chi}(t) &= -\lambda v^2 + g^2\left[\phi^2(t) + \Delta_{\phi\phi,\mathrm{fin}}(t)\right] + g^2 C^0_{\phi\phi} + 3\lambda\left[\chi^2(t) + \Delta_{\chi\chi,\mathrm{fin}}(t)\right] + 3\lambda C^0_{\chi\chi}\\ &\quad + g^2 C^1_{\phi\phi}\left[\mathcal{M}^2_{\mathrm{R},\,\phi\phi}(t) - \mathcal{M}^2_{\mathrm{R},\,\phi\phi}(0)\right] + g^2 C^2_{\phi\phi}\left[\mathcal{M}^2_{\mathrm{R},\,\chi\chi}(t) - \mathcal{M}^2_{\mathrm{R},\,\chi\chi}(0)\right]\\ &\quad + g^2 C^3_{\phi\phi}\left[\mathcal{M}^2_{\mathrm{R},\,\phi\chi}(t) - \mathcal{M}^2_{\mathrm{R},\,\phi\chi}(0)\right] + 3\lambda C^1_{\chi\chi}\left[\mathcal{M}^2_{\mathrm{R},\,\phi\phi}(t) - \mathcal{M}^2_{\mathrm{R},\,\phi\phi}(0)\right] && (10.49)\\ &\quad + 3\lambda C^2_{\chi\chi}\left[\mathcal{M}^2_{\mathrm{R},\,\chi\chi}(t) - \mathcal{M}^2_{\mathrm{R},\,\chi\chi}(0)\right] + 3\lambda C^3_{\chi\chi}\left[\mathcal{M}^2_{\mathrm{R},\,\phi\chi}(t) - \mathcal{M}^2_{\mathrm{R},\,\phi\chi}(0)\right]\;,\\ \mathcal{M}^2_{\mathrm{R},\,\phi\chi}(t) &= 2g^2\left[\phi(t)\chi(t) + \Delta_{\phi\chi,\mathrm{fin}}(t)\right] + 2g^2 C^0_{\phi\chi}\\ &\quad + 2g^2 C^1_{\phi\chi}\left[\mathcal{M}^2_{\mathrm{R},\,\phi\phi}(t) - \mathcal{M}^2_{\mathrm{R},\,\phi\phi}(0)\right] + 2g^2 C^2_{\phi\chi}\left[\mathcal{M}^2_{\mathrm{R},\,\chi\chi}(t) - \mathcal{M}^2_{\mathrm{R},\,\chi\chi}(0)\right]\\ &\quad + 2g^2 C^3_{\phi\chi}\left[\mathcal{M}^2_{\mathrm{R},\,\phi\chi}(t) - \mathcal{M}^2_{\mathrm{R},\,\phi\chi}(0)\right]\;. && (10.50)\end{aligned}$$

This system of linear equations is similar to the 2×2 system appearing in the $O(N)$-model in the Hartree approximation [192]. However, the coefficient matrix can be diagonalized with a time independent rotation matrix, because it is time independent itself. Such a rotation matrix is indeed analogous to the factor $\mathcal{C} = (1 + \frac{\lambda}{16\pi^2}\ln\frac{m^2}{m_0^2})^{-1}$ in the renormalization of the $O(N)$-model in the large-N approximation [177]. Since the resulting rotation

matrix is a rather lengthy expression and is not of practical use, we do not write it down here explicitly. In sum, the presence of a rotation matrix or a factor $\mathcal{C}$ reflects the non-perturbative resummation of counterterms and coupling constants. Infinitely high orders of the coupling constants contribute. This can be seen by expanding the matrix order by order in the coupling constants.

10.5 Renormalized energy

The 2PPI resummation scheme guarantees that the total energy is conserved. As a cross-check for the numerical implementation it is thus helpful to have a finite expression for the energy. Within the one-loop bubble-resummation the contributions to the energy introduce logarithmic, quadratic and quartic divergences. These divergences have to be compensated by the already fixed counterterms (Sec. 10.37). We have to find the proper subtraction terms rendering the energy density finite and we have to calculate the finite pieces.

The zero-loop contribution to the energy is found from all terms except $\Gamma^{(1)}$ which contains the loops. This contribution is denoted by $E^{(0)}$ and is given by

$$\begin{aligned} E^{(0)}(t) &= \frac{1}{2}\dot{\phi}^2(t) + \frac{1}{2}\mathcal{M}^2_{\phi\phi}(t)\phi^2(t) - g^2\phi^2(t)\chi^2(t) + \frac{1}{2}\dot{\chi}^2(t) + \frac{1}{2}\mathcal{M}^2_{\chi\chi}(t)\chi^2(t) \\ &\quad -\frac{\lambda}{2}\chi^4(t) + \frac{\lambda}{4}v^4 + \mathcal{M}^2_{\phi\chi}(t)\phi(t)\chi(t) - \frac{1}{4g^2}\left[\mathcal{M}^2_{\phi\chi}(t)\right]^2 \\ &\quad +\frac{3\lambda}{4g^4}\left[\mathcal{M}^2_{\phi\phi}(t) - m^2\right]^2 - \frac{1}{2g^2}\left[\mathcal{M}^2_{\phi\phi}(t) - m^2\right]\left[\mathcal{M}^2_{\chi\chi}(t) + \lambda v^2\right] . \end{aligned} \tag{10.51}$$

The contribution of the one-loop bubble graphs (see Fig. 9.2) to the energy is defined by the relation

$$\frac{dE^{(1)}(t)}{dt} = -\frac{\delta\Gamma^{(1)}[\mathcal{M}^2_{\phi\phi}, \mathcal{M}^2_{\chi\chi}, \mathcal{M}^2_{\phi\chi}]}{\delta\mathcal{M}^2_{ij}(t)}\frac{d\mathcal{M}^2_{ij}(t)}{dt} \tag{10.52}$$

$$= \frac{1}{2}\int\frac{d^{D-1}p}{(2\pi)^{D-1}}G_{ij}(t,t;\mathbf{p})\frac{d\mathcal{M}^2_{ij}(t)}{dt} . \tag{10.53}$$

This equation can be integrated explicitly if we use the equations of motion for the mode functions $f^\alpha_i(t;p)$, yielding

$$\begin{aligned} E^{(1)}(t) &= \frac{1}{2}\int\frac{d^{D-1}p}{(2\pi)^{D-1}}\sum_\alpha\frac{1}{2\omega_\alpha}\Big\{\dot{f}^\alpha_\phi(t;p)\dot{f}^{\alpha\,*}_\phi(t;p) + \dot{f}^\alpha_\chi(t;p)\dot{f}^{\alpha\,*}_\chi(t;p) \\ &\quad + \left[\mathbf{p}^2 + \mathcal{M}^2_{\phi\phi}(t)\right] f^\alpha_\phi(t;p)f^{\alpha\,*}_\phi(t;p) + \left[\mathbf{p}^2 + \mathcal{M}^2_{\chi\chi}(t)\right] f^\alpha_\chi(t;p)f^{\alpha\,*}_\chi(t;p) \\ &\quad +2\mathcal{M}^2_{\phi\chi}(t)\mathrm{Re}\left[f^\alpha_\phi(t;p)f^{\alpha\,*}_\chi(t;p)\right]\Big\} . \end{aligned} \tag{10.54}$$

If the effective masses are identified by the *renormalized* effective masses, then the zero-loop contribution to the energy [see Eq. (10.51)] is automatically renormalized.

In the following we use the rotated potential $\widetilde{\mathcal{V}}$ defined as

$$\begin{aligned}\widetilde{\mathcal{V}}_{\alpha\beta}(t) &= O_{k\alpha}\mathcal{V}_{kl}(t)O_{l\beta} && (10.55)\\ &= O_{1\alpha}O_{1\beta}\mathcal{V}_{\phi\phi}(t) + O_{2\alpha}O_{2\beta}\mathcal{V}_{\chi\chi}(t) + (O_{1\alpha}O_{2\beta} + O_{2\alpha}O_{1\beta})\mathcal{V}_{\phi\chi}(t)\,. && (10.56)\end{aligned}$$

According to the expansion of the mode functions in Appendix B.2 the divergent part of the one-loop contribution from the bubble graphs to the quantum energy is given by [see Eq. (B.27)]

$$E^{(1),\,\mathrm{div}}(t) = \frac{1}{2}\int\frac{d^{D-1}p}{(2\pi)^{D-1}}\sum_\alpha\frac{1}{2\omega_\alpha}\left[2\omega_\alpha^2 + \widetilde{\mathcal{V}}_{\alpha\alpha}(t) - \sum_\beta\frac{1}{2\omega_\beta(\omega_\alpha+\omega_\beta)}\widetilde{\mathcal{V}}_{\alpha\beta}(t)\widetilde{\mathcal{V}}_{\alpha\beta}(t)\right]. \tag{10.57}$$

The first term is quartically divergent. Its renormalization corresponds to a renormalization of the cosmological constant Λ. Since we do not couple to gravity here, it is therefore somewhat arbitrary and can be omitted.

If the divergent parts are evaluated in dimensional regularization [using Eqs. (B.1), (B.4) and (B.8)] the full one-loop contribution in Eq. (10.54) denotes

$$\begin{aligned}E^{(1)}(t) &= E^{(1)}_{\mathrm{fin}}(t) + \sum_\alpha\frac{m_{0,\,\alpha}^4}{64\pi^2}\left[L_\epsilon - \ln\frac{m_{0,\,\alpha}^2}{\mu^2} + \frac{3}{2}\right] - \sum_\alpha\frac{m_{0,\,\alpha}^2}{32\pi^2}\widetilde{\mathcal{V}}_{\alpha\alpha}(t)\left[L_\epsilon - \ln\frac{m_{0,\,\alpha}^2}{\mu^2} + 1\right]\\ &\quad - \sum_{\alpha,\,\beta}\frac{1}{64\pi^2}\widetilde{\mathcal{V}}_{\alpha\beta}(t)\widetilde{\mathcal{V}}_{\alpha\beta}(t)\left[L_\epsilon - \ln\frac{m_{0,\,\alpha}^2}{\mu^2} + 1 + \frac{m_{0,\,\beta}^2}{m_{0,\,\alpha}^2 - m_{0,\,\beta}^2}\ln\frac{m_{0,\,\beta}^2}{m_{0,\,\alpha}^2}\right], \qquad (10.58)\end{aligned}$$

where the finite part has been defined as

$$\begin{aligned}E^{(1)}_{\mathrm{fin}}(t) &= \frac{1}{2}\int\frac{d^{D-1}p}{(2\pi)^{D-1}}\sum_\alpha\frac{1}{2\omega_\alpha}\Big\{\dot f^\alpha_\phi(t;p)\dot f^{\alpha\,*}_\phi(t;p) + \dot f^\alpha_\chi(t;p)\dot f^{\alpha\,*}_\chi(t;p)\\ &\quad + \left[\mathbf{p}^2 + \mathcal{M}^2_{\phi\phi}(t)\right] f^\alpha_\phi(t;p) f^{\alpha\,*}_\phi(t;p) + \left[\mathbf{p}^2 + \mathcal{M}^2_{\chi\chi}(t)\right] f^\alpha_\chi(t;p) f^{\alpha\,*}_\chi(t;p)\\ &\quad + 2\mathcal{M}^2_{\phi\chi}(t)\mathrm{Re}\left[f^\alpha_\phi(t;p) f^{\alpha\,*}_\chi(t;p)\right]\\ &\quad - 2\omega_\alpha^2 - \widetilde{\mathcal{V}}_{\alpha\alpha}(t) + \sum_\beta\frac{1}{2\omega_\beta(\omega_\alpha+\omega_\beta)}\widetilde{\mathcal{V}}_{\alpha\beta}(t)\widetilde{\mathcal{V}}_{\alpha\beta}(t)\Big\}. \qquad (10.59)\end{aligned}$$

From the definition of $m^2_{0,\,\alpha}$ and $\widetilde{\mathcal{V}}_{\alpha\beta}(t)$ we can prove the identity

$$\sum_\alpha\left[m_{0,\,\alpha}^4 - 2m_{0,\,\alpha}^2\widetilde{\mathcal{V}}_{\alpha\alpha}(t) - \sum_\beta\widetilde{\mathcal{V}}_{\alpha\beta}(t)\widetilde{\mathcal{V}}_{\alpha\beta}(t)\right] = -\mathcal{M}^2_{ij}(t)\mathcal{M}^2_{ij}(t)\,, \tag{10.60}$$

so that the divergent part becomes very simple. The full fluctuation energy $E^{(1)}$ is then

given by

$$\begin{aligned} E^{(1)}(t) &= E^{(1)}_{\rm fin}(t) - \frac{1}{64\pi^2}\left[L_\epsilon + 1\right]\mathcal{M}^2_{ij}(t)\mathcal{M}^2_{ij}(t) \\ &\quad + \sum_\alpha \frac{m^4_{0,\,\alpha}}{64\pi^2}\left[-\ln\frac{m^2_{0,\,\alpha}}{\mu^2} + \frac{1}{2}\right] + \sum_\alpha \frac{m^2_{0,\,\alpha}}{32\pi^2}\widetilde{\mathcal{V}}_{\alpha\alpha}(t)\ln\frac{m^2_{0,\,\alpha}}{\mu^2} \\ &\quad + \sum_{\alpha,\beta}\frac{1}{64\pi^2}\widetilde{\mathcal{V}}_{\alpha\beta}(t)\widetilde{\mathcal{V}}_{\alpha\beta}(t)\left[\ln\frac{m^2_{0,\,\alpha}}{\mu^2} - \frac{m^2_{0,\,\beta}}{m^2_{0,\,\alpha}-m^2_{0,\,\beta}}\ln\frac{m^2_{0,\,\beta}}{m^2_{0,\,\alpha}}\right]. \end{aligned} \tag{10.61}$$

The divergent part of $E^{(1)}$ is proportional to $\mathcal{M}^2_{ij}\mathcal{M}^2_{ij} = \mathcal{M}^4_{\phi\phi} + \mathcal{M}^4_{\chi\chi} + 2\mathcal{M}^4_{\phi\chi}$, i.e., the counterterm in Eq. (10.37), as expected.

Finally, the renormalized total energy is given by

$$E_{\rm tot} = E^{(0)}(t) + E^{(1)}(t) - \delta\mathcal{M}^4 \tag{10.62}$$

$$\begin{aligned} &= E^{(0)}(t) + E^{(1)}_{\rm fin}(t) + \sum_\alpha \frac{m^4_{0,\,\alpha}}{64\pi^2}\left[-\ln\frac{m^2_{0,\,\alpha}}{\mu^2} + \frac{1}{2}\right] + \sum_\alpha \frac{m^2_{0,\,\alpha}}{32\pi^2}\widetilde{\mathcal{V}}_{\alpha\alpha}(t)\ln\frac{m^2_{0,\,\alpha}}{\mu^2} \\ &\quad + \sum_{\alpha,\beta}\frac{1}{64\pi^2}\widetilde{\mathcal{V}}_{\alpha\beta}(t)\widetilde{\mathcal{V}}_{\alpha\beta}(t)\left[\ln\frac{m^2_{0,\,\alpha}}{\mu^2} - \frac{m^2_{0,\,\beta}}{m^2_{0,\,\alpha}-m^2_{0,\,\beta}}\ln\frac{m^2_{0,\,\beta}}{m^2_{0,\,\alpha}}\right]. \end{aligned} \tag{10.63}$$

The renormalized energy has a negative sign, because we have added the counterterm $\delta\mathcal{M}^4$ to the effective action Γ, i.e., $\Gamma_{\rm R} = \Gamma + \delta\mathcal{M}^4$.

Chapter 11

Results from Numerical Simulations

In this Chapter we present in detail the results from numerical simulations, to investigate the main features of the dynamics in hybrid models. It turns out that the dynamics is very rich. We highlight only a few features which we believe are most relevant in the context of preheating.

In Sec. 11.1 we give some details on the numerical implementation and demonstrate that numerical errors are well under control. Sec. 11.2 is an overview on the time evolution of the classical fields and fluctuation integrals in dependence of the parameters chosen. In Sec. 11.3 we show typical phase-space trajectories that indicate chaotic dynamics. The late time behavior of the quantities characterizing the phase transition is further analyzed in Sec. 11.4. In Sec. 11.5 we present the momentum spectra. Possible long-range spatial correlations between fluctuations are studied in Sec. 11.6. Finally, decoherence is addressed in Sec. 11.7.

11.1 Numerical implementation

At the initial time of the simulation we have to fix the vacuum state. This is done by solving the set of nonlinear equations defining the initial masses $m^2_{0,\alpha}$ and the mixing angle $\tan\vartheta$ using a standard relaxation method.

The equations of motion are given in Eqs. (10.44)–(10.47). Since we only have to solve ordinary differential equations, we can pick one of the very robust integrators. We take a fourth-order standard Runge-Kutta integrator, because such integrators offer a very good compromise between precision and speed. In most simulations we use a time discretization $\Delta t = 0.0003$. The 3×3 system of linear equations for the renormalized variational masses $\mathcal{M}^2_{\mathrm{R},ij}$ [see Eqs. (10.48)–(10.50)] is solved with Cramer's rule.

The analytical calculations are very involved and mistakes would show up immediately in the numerical results. The accuracy of the numerical computations is monitored in two ways: (1) by verifying that the Wronskian is constant and (2) by verifying that the total energy is conserved. We can easily verify that the total energy, as given in Eq. (10.63), is analytically conserved, therefore it is a powerful crosscheck, to see if the numerically

calculated energy is also conserved. In Fig. 11.1 we display a plot of the relative error for a typical simulation. The total energy is found to be numerically conserved to $\sim 0.1\%$ in all simulations. Due to the limitations in the accuracy of the integration of the equations of motion we cannot expect that the numerically calculated energy is exactly constant.

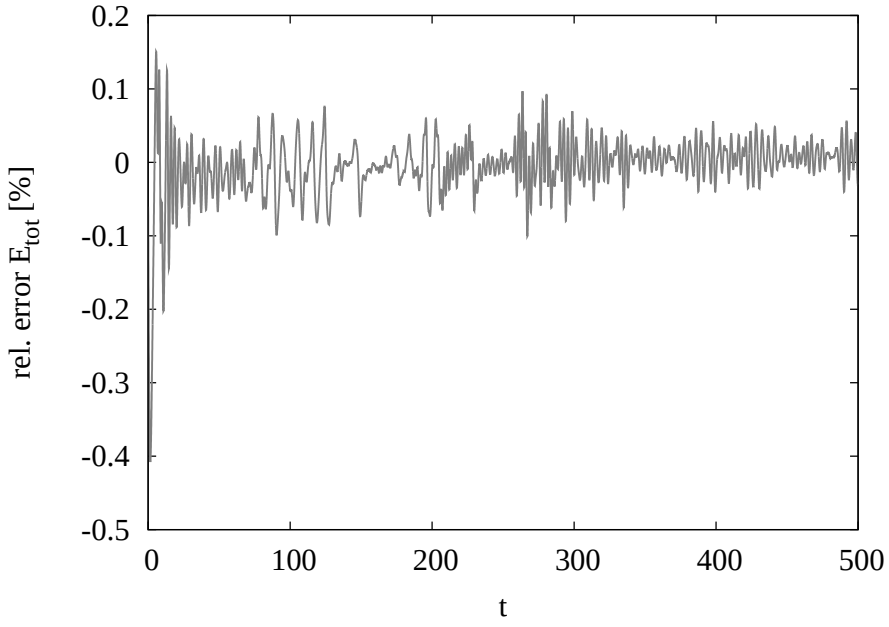

Figure 11.1: Relative error of the total energy for a typical simulation; due to limitations in the accuracy of the integration of the equations of motion, small fluctuations of order $\sim 0.1\%$ can be observed; the relative error is larger at initial time due to the initial singularity [196].

Next, we comment on the numerical implementation of the momentum integrations. First, we have to discretize the momentum space. We have chosen a non-equidistant discretization, in particular we take smaller steps for smaller momenta and larger steps for larger momenta. We use a pragmatic momentum cut-off $p_{\max} = 12$ and $n_p = 300$ independent momenta for the convergent fluctuation integrals in Eqs. (10.23) and (10.59), which are calculated without further assumptions. We may extent the mode expansion given in Eq. (B.9) further by using higher order functions, formally written as

$$f_i^{\alpha}(t;p) = e^{-i\omega_\alpha t}\left[O_{i\alpha} + h_i^{(1),\,\alpha}(t;p) + h_i^{(2),\,\alpha}(t;p) + h_i^{\overline{(2)},\,\alpha}(t;p)\right] . \tag{11.1}$$

Such a decomposition of the mode functions up to terms of second derivative order [with respect to the potential $\mathcal{V}_{ij}(t)$] can be used to keep the momentum integrals completely free from subtraction terms (see, e.g., Ref. [76]). However, we observe that the subtraction used in Eq. (10.23) leads to stable results and is sufficient for calculating the momentum integrals numerically in our case. In Fig. 11.2 we display the important part of the integrand

in Eq. (10.23) as a function of p at a fixed time, i.e., the kernel $[\mathrm{Re}f_i^\alpha(t,p)f_j^\alpha(t,p) - \mathrm{sub}]/2\omega_\alpha$, where "sub" denotes the subtraction terms in Eq. (10.23). In the high p-regime this integration kernel has to fall of like $1/p^5$.[1] In Fig. 11.2 one can see that indeed for $p \gtrsim 1$ all lines become parallel to the straight dotted line that represents a function $h(p) = 1/p^5$. This proves that the subtraction terms are of the correct form and lead to renormalized propagators. Moreover, it is indeed justified to choose $p_{\max} = 12$ for the numerical integrations. The value of the integration kernel at $p_{\max} = 12$ is then small enough ($\sim 10^{-5}$) so that the remainder of the integral from $p_{\max}$ to infinity can be neglected. Again we stress the fact that the loop integrals are finite after renormalization and that such a pragmatic momentum cut-off is only chosen for numerical convenience.

Note that the energy is more divergent than the propagator insertions, in particular the degree of divergence is four compared to two. A priori, we expect the propagator insertions to be much better calculated than the energy density. We have checked that the accuracy of the total energy improves, if the time discretization Δt is lowered.

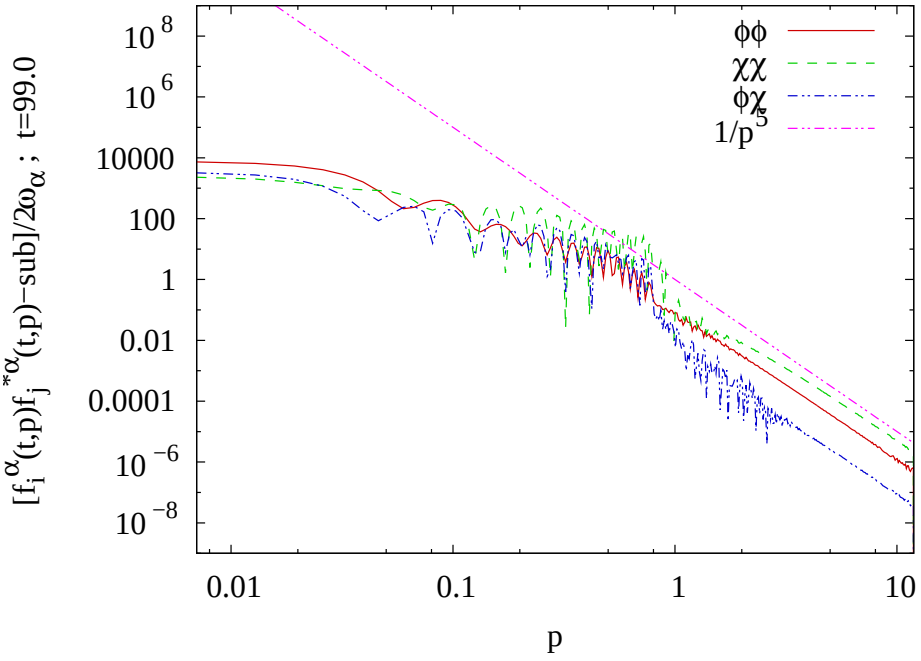

Figure 11.2: The subtracted mode functions $[\mathrm{Re}f_i^\alpha(t,p)f_j^\alpha(t,p) - \mathrm{sub}]/2\omega_\alpha$ are displayed on a logarithmic scale as a function of the momentum p with $ij = \phi\phi$ (red solid line), $ij = \chi\chi$ (green dashed line) and $ij = \phi\chi$ (blue dotted line); for high p the subtracted mode functions are proportional to $1/p^5$ as indicated by the straight line, demonstrating the convergence of the momentum integrals.

[1] The kernel is multiplied by $d^3p = 4\pi p^2 dp$. Propagator structures in quantum field theory require an inverse power $1/p^2 \sim dp/p^3 \sim d^3p/p^5$.

11.2 Dynamical evolution and dependence on the parameters

The basic conception in the hybrid model is an efficient energy transfer from the inflaton to the Higgs degree of freedom mediated by a phase transition and the associated spinodal regime. It is then a question how these expectations are realized.

We are mainly interested in the following questions:

1. On which time scales and in which form does the energy transfer between the inflaton and symmetry breaking (Higgs) fields take place?

2. Is it possible to conclude on the structure of the effective Higgs potential after this energy transfer? Though the system does not go right away into a thermal equilibrium phase, the behavior at intermediate and late times can be thought as reflecting the shape of an effective Higgs potential, with a symmetric or broken symmetry structure.

3. Do the spectra for the different quantum modes reflect the mechanism of particle production?

4. To which extent is the transition to a classical description justified (in a certain momentum range)?

The answers to these questions obviously depend on the parameters chosen for the simulations.

In the absence of a fundamental theory hybrid models are taken as effective models for the preheating stage at the end of cosmic inflation. The mass parameters m^2 and v^2 and the coupling constants g and λ are then constrained by the observations of the various CMB experiments (see, e.g., Refs. [197, 56, 198, 111] for constraints of inflation from first year WMAP data). In particular the anisotropies of the correlations of temperature fluctuations in the CMB imply

$$m^2 \simeq 10^{-12} m_{\rm pl}^2 \,, \tag{11.2}$$

if $v^2 = 0$, i.e., for a plain $m^2\phi^2$ chaotic inflation model. A larger inflaton mass would overestimate the amplitude of scalar (density) perturbations in the CMB. More generally, for nonzero v, the inflaton mass m has to be chosen very small [73],

$$m^2 \ll g^2 v^2 \,. \tag{11.3}$$

This relation implies that the potential in the ϕ direction close to $\chi \approx 0$ is very flat.

Indeed when treating the period *after* inflation the inflaton mass m^2 can be neglected entirely (see also the discussion in [79]); we have chosen $m^2 = 0$ in the numerical simulations throughout. As discussed in [73] the couplings λ and g^2 can vary over a wide range, depending on the specific preheating scenario. This is interrelated with the particular choice of the mass scale v which is chosen to be 1 in the numerical simulations. Since

we restrict the discussion to Minkowski space-time its absolute physical value is irrelevant here. Of course this choice enters into the time, momentum, and energy scales.

As a concrete phenomenological model preheating after hybrid inflation can be embedded at least at two manifestly different energy scales. For electroweak preheating [77, 80, 199, 200, 201], the symmetry breaking field mimics the standard Higgs sector of the standard model, while ignoring contributions from the gauge and fermion fields. Of course we would have to generalize the symmetry breaking field to be a complex doublet in order to represent the SU(2) symmetry breaking Higgs sector. The vacuum expectation value v in this case would be chosen equal to 246 GeV. The classical Higgs mass is $m_\chi^2 = \lambda v^2$. If the phase transition at the end of inflation takes place at the scale of a Grand Unified Theory (GUT), the symmetry breaking field could be, e.g., a very heavy sneutrino, i.e., the scalar super-partner of one of the light neutrinos. The reheating in such a scenario would come from the decay of this heavy sneutrino. We will not restrict our study to one of these two scenarios in the following.

In order to study the influence of the coupling strength g^2 and the self-coupling λ on both the classical and quantum components of the Higgs and the inflaton fields we have performed simulations with $m^2 = 0$, $v^2 = 1$, $\lambda = 1$ fixed, while g^2 is equal to 2λ, 0.1λ and 0.01λ (see Figs. 11.3, 11.4 and 11.5) and for $g^2 = 2\lambda$ with a smaller coupling $\lambda = 0.1$ and $\lambda = 0.01$. The renormalization scale will be fixed as $\mu^2 = \lambda v^2$. In Tab. 11.1 we have listed the different sets of parameters. With these parameter choices we include the different scenarios studied by other authors [63, 77, 79, 80, 83]. In addition to the mass and coupling parameters we have to specify initial amplitudes (and initial velocities) for the classical fields. We have chosen $\chi(0) = 10^{-7}$, i.e., a very small value for the initial amplitude of the classical Higgs field, in order to trigger the "spontaneous" symmetry breaking. The initial amplitude for the inflaton field has been fixed for the simulations in Figs. 11.3–11.5 to $\phi(0) = 1.697\,\phi_c = 1.2$. With this choice of the initial amplitude there is a short phase of slow-rolling of the inflaton field until the spinodal regime is entered.

Table 11.1: Sets of parameters used

Set #	g^2/λ	λ	m^2	v^2
1	2	1	0	1
2	2	0.1	0	1
3	2	0.01	0	1
4	0.1	1	0	1
5	0.01	1	0	1

In Figs. 11.3–11.5 we display the time evolution of the classical fields $\phi(t)$ and $\chi(t)$, of the variational masses $\mathcal{M}^2_{\phi\phi}(t)$, $\mathcal{M}^2_{\chi\chi}(t)$ and $\mathcal{M}^2_{\phi\chi}(t)$ and of the fluctuation integrals $\Delta^{(1)}_{\phi\phi}(t)$, $\Delta^{(1)}_{\chi\chi}(t)$, and $\Delta^{(1)}_{\phi\chi}(t)$. We observe that in all three cases the Higgs field $\chi(t)$ oscillates around

a nonzero value at later times (see the dashed line in Figs. 11.3a–11.5a), while the inflaton field oscillates around zero (solid lines in Figs. 11.3a–11.5a).

We have identified three time regimes in the simulations that we want to investigate further in the following. The regimes are described as follows:

(I) Initial period, end of slow-roll. Here $\mathcal{M}^2_{\chi\chi}(t) > 0$. A phase of featureless rolling of the inflaton field after the main period of inflation. Quantum fluctuations are almost negligible.

(II) Early times, spinodal regime, $\mathcal{M}^2_{\chi\chi}(t) < 0$ or oscillating several times around zero. Spinodal amplification of Higgs quantum fluctuations and exponential growth of $\chi(t)$.

(III) Intermediate and late times, $\mathcal{M}^2_{\chi\chi}(t) > 0$ and oscillations of the classical fields. Excitation of inflaton and mixed quantum fluctuations, parametric resonance bands in all momentum spectra.

The first period (I) is easy to identify in Figs. 11.3–11.5: only the inflaton decreases with time in smooth way while the Higgs mean field is still practically zero.

In the early time period (II) the inflaton field passes through zero once or several times, depending on the coupling g^2, see Figs. 11.3–11.5. The period is identified by an increase of $|\chi(t)|$ and ends once $\chi(t)$ begins to oscillate in a regular way. A closer analysis shows that the amplitude of the classical Higgs field growths exponentially. In Fig. 11.6 we display the absolute value $|\chi(t)|$ on a logarithmic scale, for simulations with $g^2 = 2\lambda$, $\lambda = 1$, $m^2 = 0$, $v^2 = 1$, and $\chi(0) = 10^{-7}$ fixed, while the initial amplitude of the inflaton field, $\phi(0)$, is varied from 1.2 to 1.8. The exponential growth sets in when $\phi(t)$ becomes smaller than the critical value ϕ_c [see Eq. (3.10)] and stops when $\chi(t)$ reaches the turning point which is at $|\chi(t)| \approx 1$. There does not seem to be a systematic trend for the dependence of the period of growth on $\phi(0)$.

The regime (II) can be very short. For the simulation with a small coupling $g^2 = 0.01\lambda$ the transition to the broken symmetry phase can take place within a single oscillation of the inflaton field (see Fig. 11.5a).

The intermediate and late time period (III) is characterized by oscillations of both the inflaton and the Higgs field, with essentially constant period and amplitude (see, e.g., Fig. 11.5a). The Higgs mean field may oscillate around a nonzero value, related to a broken symmetry minimum of an effective potential (see below) or around $\chi = 0$, to be identified with symmetry restoration. (This will be further analyzed in Sec. 11.4.) We immediately observe in Figs. 11.3–11.5 that in region (III) the field amplitudes of the classical fields (ϕ and χ) and also the amplitudes of the various fluctuation integrals ($\Delta_{\phi\phi}$, $\Delta_{\chi\chi}$, and $\Delta_{\phi\chi}$) remain almost constant as a function of time. Thus, effective dissipative dynamics and further production of quanta does not take place. This is different from investigations without back-reaction of the quanta onto themselves [86] (see also the discussion in Secs. 11.5 and 11.7).

The rich dynamics in the hybrid model is due to the mixing of the coupled fields. In

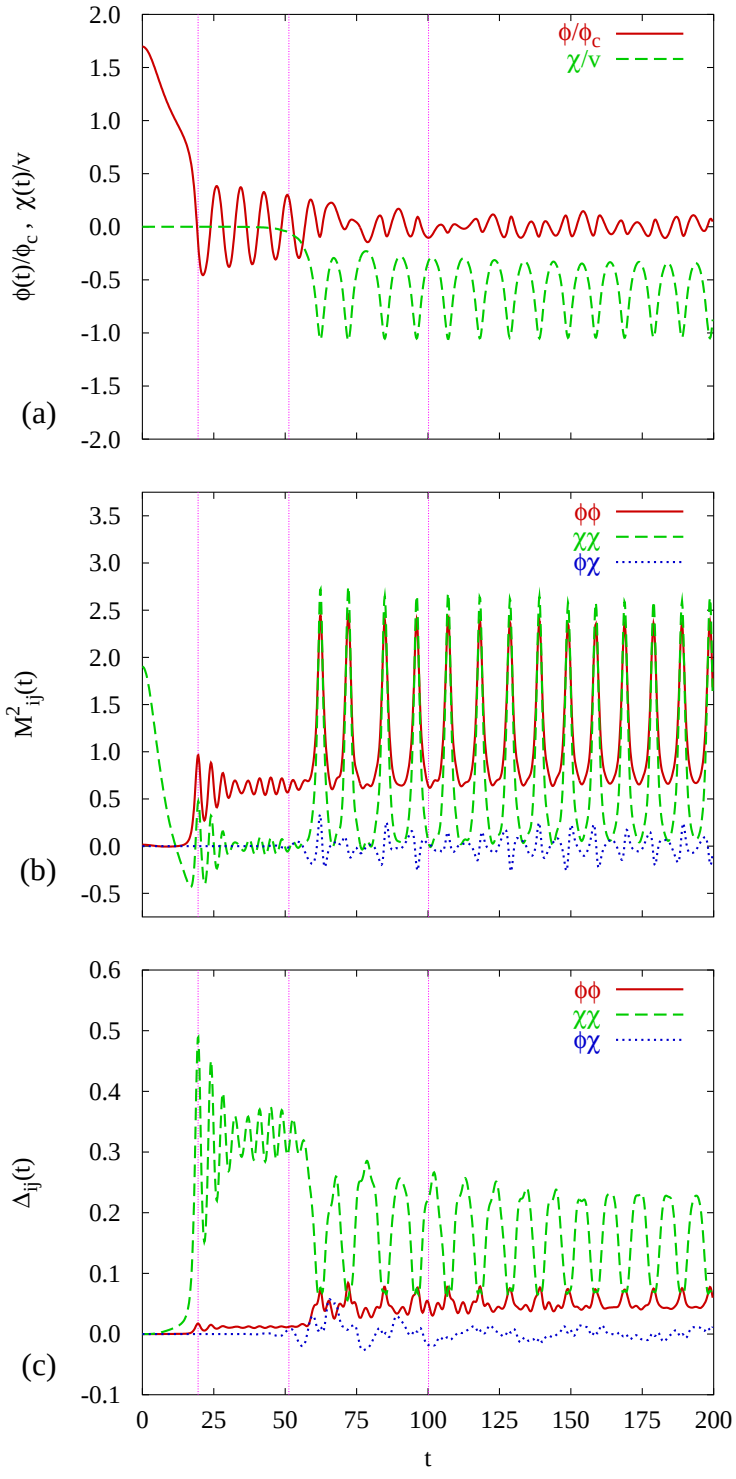

Figure 11.3: Time evolution for the simulation with $g^2 = 2\lambda$. Initial values: $\phi(0) = 1.2$ and $\chi(0) = 1.0 \times 10^{-7}$; other parameters: $m^2 = 0$, $\lambda = 1$, $v^2 = 1$; we plot as a function of time (a) the classical fields $\phi(t)/\phi_c$ (red solid line) and $\chi(t)/v$ (green dashed line), (b) the effective masses $\mathcal{M}^2_{ij}(t)$ with $ij = \phi\phi$ (red solid line), $ij = \chi\chi$ (green dashed line) and $ij = \phi\chi$ (blue dotted line) (c) the fluctuation integrals $\Delta_{ij}(t)$ with $ij = \phi\phi$ (red solid line), $ij = \chi\chi$ (green dashed line) and $ij = \phi\chi$ (blue dotted line); the vertical dotted lines indicate the times where t is equal to 19.5, 51.3, and 100.2 (see also Sec. 11.5).

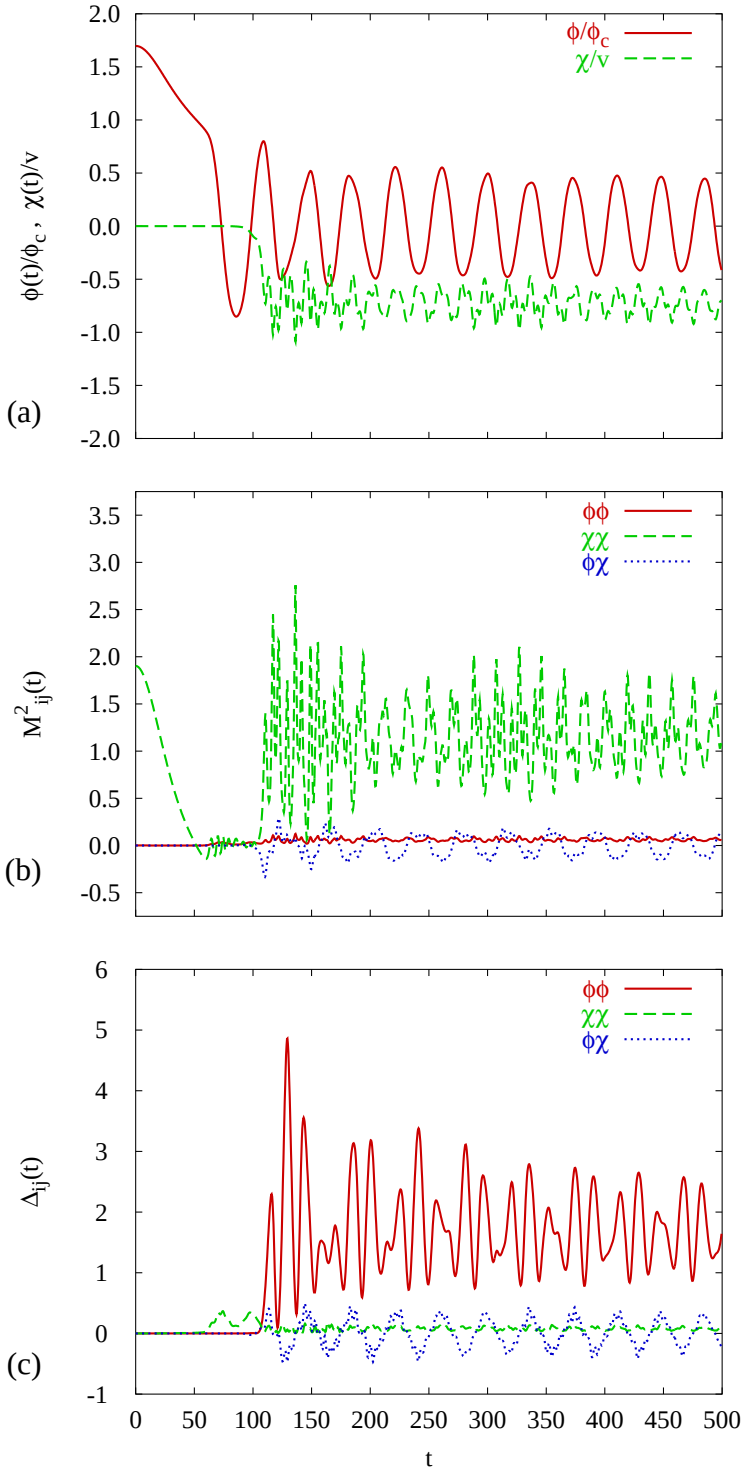

Figure 11.4: The same as Fig. 11.3 but for $g^2 = 0.1\lambda$; note that the time axis has a different range.

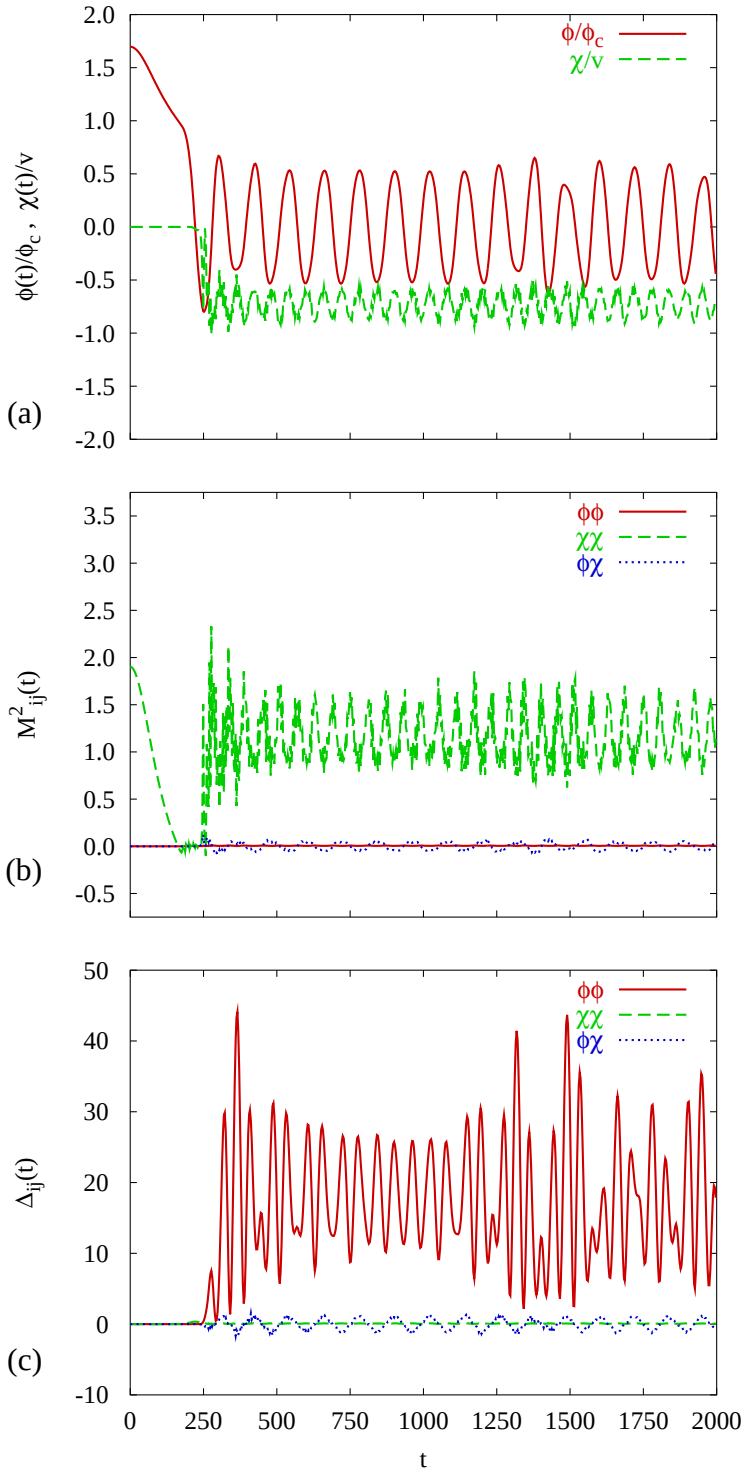

Figure 11.5: The same as Fig. 11.3 but for $g^2 = 0.01\lambda$. The transition of the symmetry breaking field χ from the metastable vacuum is completed within less than one oscillation of the inflaton field ϕ; note that the time axis has a different range.

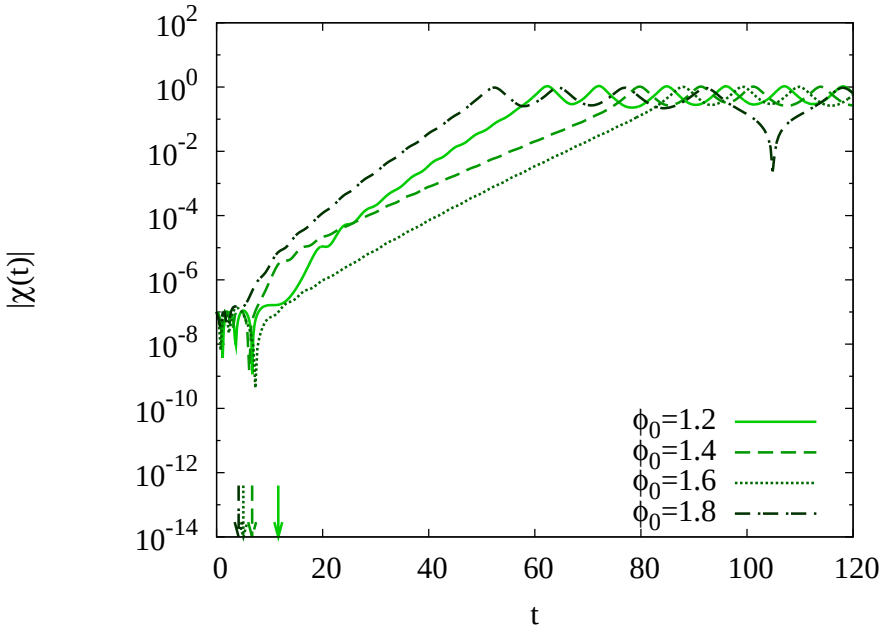

Figure 11.6: Time evolution of the absolute value $|\chi(t)|$ for simulations with the parameters $g^2 = 2\lambda$, $m^2 = 0$, $v^2 = 1$, and $\lambda = 1$ and four different initial values $\phi(0)$ equal to 1.2 (solid line), 1.4 (dashed line), 1.6 (dotted line) and 1.8 (dashed-dotted line); the corresponding arrows pointing at the t-axis indicate the time when $\phi(t)$ drops below ϕ_c.

order to quantify the mixing we define a time-dependent mixing angle as

$$\tan\vartheta(t) \;=\; \frac{1}{2\mathcal{M}^2_{\phi\chi}(t)}\left\{\mathcal{M}^2_{\chi\chi}(t)-\mathcal{M}^2_{\phi\phi}(t)+\sqrt{\left[\mathcal{M}^2_{\chi\chi}(t)-\mathcal{M}^2_{\phi\phi}(t)\right]^2+4\mathcal{M}^4_{\phi\chi}(t)}\right\}. \tag{11.4}$$

In Fig. 11.7 we plot $\vartheta(t)$ for the simulation in Fig. 11.3. We observe that there are many oscillations around zero. Obviously the mixing of the field changes drastically with time. The bigger spikes are due to zeros in $\mathcal{M}^2_{\phi\chi}(t)$.

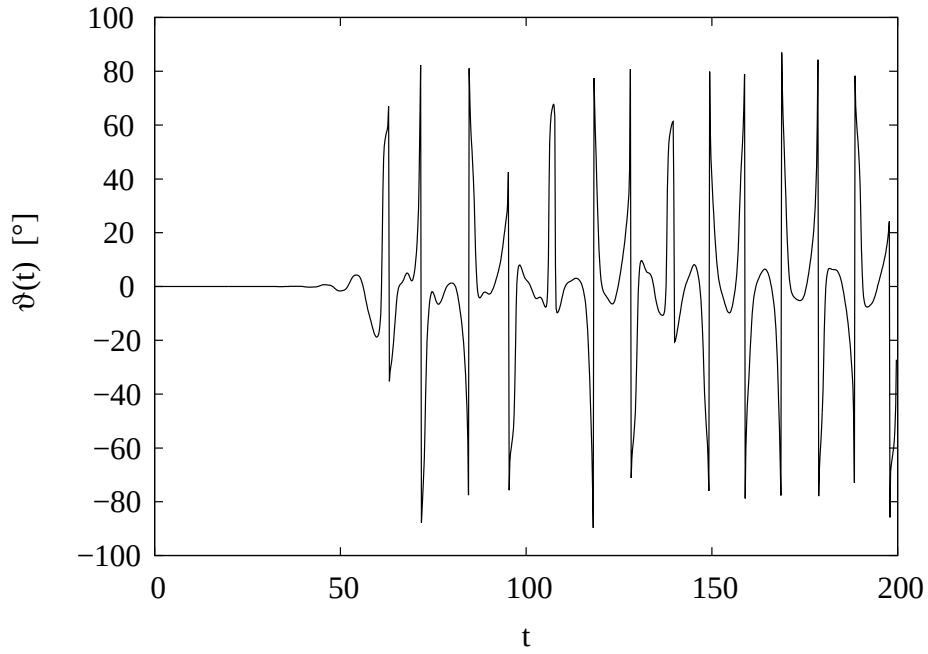

Figure 11.7: Time dependent mixing angle $\vartheta(t)$ (in degree) as defined by Eq. (11.4) for the simulation in Fig. 11.3; for $t \lesssim 50$ the mixing is roughly zero but increases for later times; obviously there is a continuous exchange of energy between the coupled fields.

We have also run simulations with smaller values of the Higgs self-coupling constant λ, namely $\lambda = 0.1$ and $\lambda = 0.01$ and compared them to the case where $\lambda = 1$ (we have fixed $g^2 = 2\lambda$ in these cases). As long as the Higgs field is trapped in a metastable phase the coupling constant λ is unimportant. Once the spinodal regime is entered there are still a couple of oscillations of the inflaton field ϕ until the Higgs field χ reaches its maximum value for the first time. We note that this number of oscillations goes slightly down from ~ 5 for $\lambda = 1$ to ~ 1 for $\lambda = 0.01$. However, there is a quite complex dependence on the other parameters too and it is not the goal of this thesis to explore the full parameter space in detail. Rather we will take the exemplary value $\lambda = 1$ in most cases and focus on some observables which can be of physical interest.

11.3 Phase-space trajectories

The dynamics of the classical fields and their respective quantum fluctuations is rather complicated, mainly due to the coupling of the fields. The reason for complex dynamical behavior of the system is that the field amplitudes of the various fields can be of the same order.

In Fig. 11.8 and Fig. 11.9 the phase-space trajectory $\{\phi(t), \chi(t)\}$ is shown for two simulations with identical parameters $m^2 = 0$, $v = 1$, $g^2 = 2\lambda$, $\lambda = 1$, and $\chi(0) = 1 \times 10^{-7}$ but slightly different initial energy densities. For the simulation in Fig. 11.8 we have chosen $\phi(0) = 1.9$ and for Fig. 11.9 $\phi(0) = 2.1$. We have also plotted contour lines for the corresponding classical potential as defined in Eq. (3.9). We immediately observe that the classical fields $\phi(t)$ and $\chi(t)$ do not lie on a simple phase-space trajectory in neither of these two examples. Moreover, for the simulation in Fig. 11.8 there seems to be an attractor at $\phi \approx 0$ and $\chi \approx 0.6$, while for the simulation in Fig 11.9 the attractor is suspected at $\phi \approx \chi \approx 0$. We will analyze in detail in Sec. 11.4 how the dynamics and late time behavior is affected by the initial energy density [via different values of $\phi(0)$].

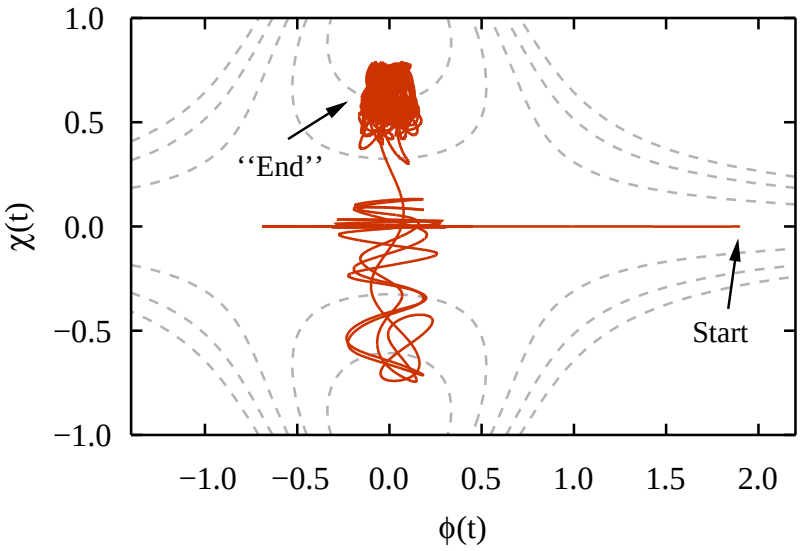

Figure 11.8: The solid line represents the phase-space trajectory of the classical fields $\phi(t)$ and $\chi(t)$ for a simulation with $\phi(0) = 1.9$ (other parameters as in Fig. 11.3); the dashed lines represent contour lines of the classical potential (see Fig. 3.2). The dynamics appears to be rather chaotic, however, finally the field χ oscillates around a nontrivial minimum indicating spontaneous symmetry breaking; note that the quantum fluctuations shift the position of the minimum.

Various authors have also studied the complex dynamics in hybrid models by calculating Lyaponov exponents (or similar quantities) and found some hints for chaotic dynamics [202, 203].

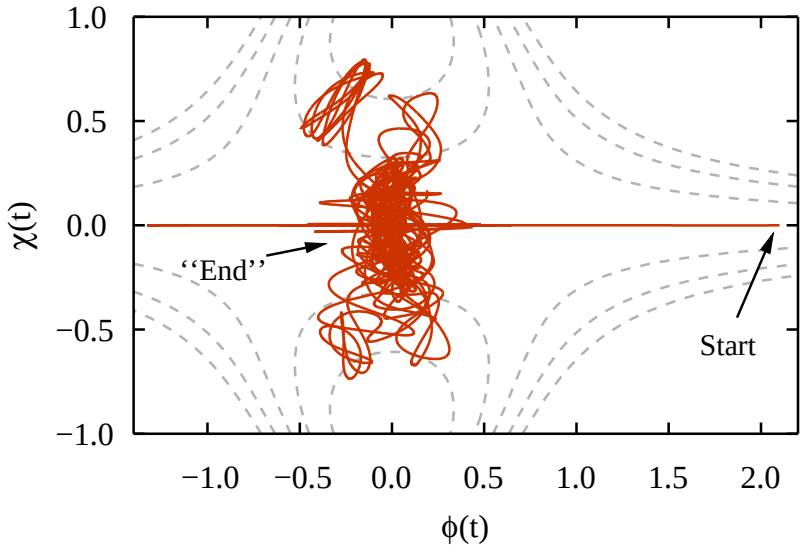

Figure 11.9: The same as Fig. 11.8 but for $\phi(0) = 2.1$; at later time the fields oscillate around the trivial minimum indicating symmetry restoration.

11.4 Late time averages—Phase transition

The amplitudes of the classical fields ϕ and χ decrease very slowly, if at all, at late times, i.e., once they have started to oscillate in a kind of effective potential. Though we make no attempt to reconstruct such a potential in detail, the oscillations allow to conclude on the minimum and the range of such an effective potential for both the Higgs and inflaton fields. In this sense we can speak of a symmetric or broken symmetry phase for the Higgs field, if the minimum of its effective potential is at $\chi = 0$ and $\chi \neq 0$, respectively. We associate this minimum with the time average of the Higgs field at late times. The shape of the effective potential depends here on the energy density (in place of the temperature) and therefore on the initial value of the inflaton field. The question of spontaneous symmetry breaking and of the point of the phase transition reduces therefore to finding the dependence of $\chi(t \to \infty)$ on the initial value $\phi(0)$.

In order to study this issue we have performed a series of simulations where we have varied the initial amplitude $\phi(0)$ while keeping all the other parameters fixed. In Fig. 11.10 the time evolution of $\chi(t)$ for simulations with $\phi(0) = 1.9$, 2.0 and 2.1 is displayed. The other parameters are $g^2 = 2\lambda$, $\lambda = 1$, $v = 1$, $m = 0$ and $\chi(0) = 10^{-7}$.

A first inspection suggests that there is a phase transition between $\phi(0) = 2.0$ and $\phi(0) = 2.1$, as for the latter simulation the field χ oscillates around zero. From the simulation with $\phi(0) = 2.0$ in Fig. 11.10 it becomes apparent that the field χ can jump several times from one "minimum" to the other if $\phi(0)$ is close to the critical point of the phase transition. This is typical for a first-order phase transition and has been observed in the scalar $O(N)$ model in the Hartree approximation as well [192].

In Fig. 11.11 we display the time averages $|\overline{\chi}(\infty)|$ and $\overline{\mathcal{M}^2}_{\chi\chi}(\infty)$ as a function of the

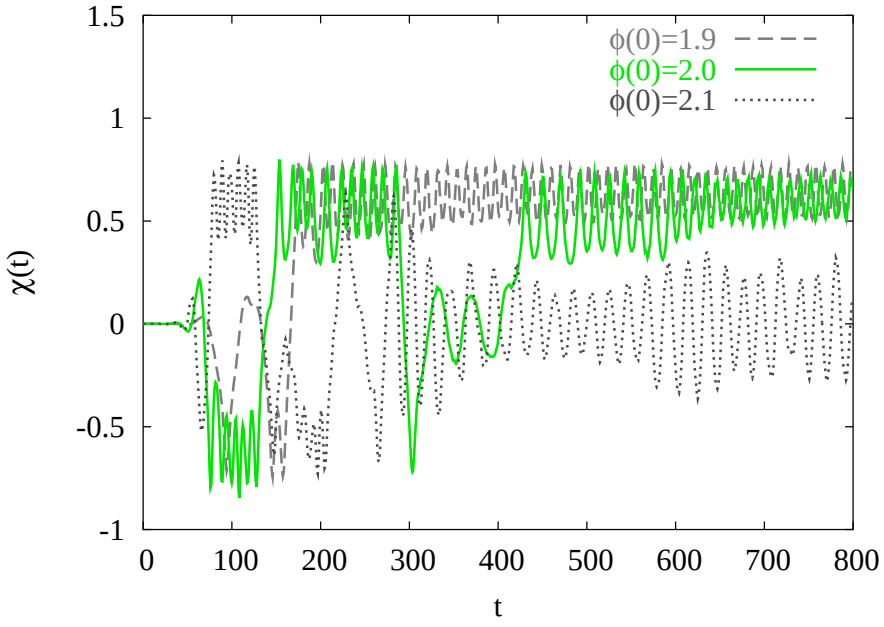

Figure 11.10: Time evolution of $\chi(t)$ with parameters as in Fig. 11.6 but for the initial values $\phi(0)$ equal to 1.9 (dashed line), 2.0 (green solid line) and 2.1 (dotted line).

initial amplitude $\phi(0)$. The other parameters are fixed to $g^2 = 2\lambda$, $\lambda = 1$, $v = 1$, $m = 0$ and $\chi(0) = 10^{-7}$.

A first-order phase transition is signaled by a non-continuous drop of the minimum value $|\overline{\chi}(\infty)|$ and the effective mass $\mathcal{M}^2_{\chi\chi}$ from finite (positive) values to zero. This indeed is the case and we can extract a value for this drop as $\phi_{\rm drop} \approx 2.011 \approx 2.844\,\phi_{\rm c}$, where $\phi_{\rm c}$ denotes the critical value as defined in Eq. (3.10). Close to $\phi_{\rm drop}$ the Higgs field may jump several times from one minimum to zero as it already does for $\phi = 2.0$ (see the solid line in Fig. 11.10). Since we have neglected space-time expansion in our analysis, we should also be careful when interpreting such a result with respect to the mechanism how inflation terminates in the hybrid model. Moreover, the details of this phase transition depend on the parameters. In Fig. 11.12 we display a corresponding plot of the averaged values $|\overline{\chi}(\infty)|$ and $\overline{\mathcal{M}^2}_{\chi\chi}(\infty)$ for simulations with $g^2 = 0.01$. The phase transition is suspected roughly at $\phi_{\rm drop} \approx 28.5 = 2.85\,\phi_{\rm c}$. Note that we have to go to much later times if the coupling constant g^2 is small.

11.5 Momentum spectra

Using the amplitudes $f^\alpha_j(t,p)$ we can define various "power spectra". One of those is the integrand of the fluctuation integrals $\Delta_{ij}(t)$, i.e., the tadpole contributions. We have already introduced the kernel

$$G_{ij}(t,t,\mathbf{p}) = \langle \tilde{\Phi}^*_i(t,\mathbf{p})\tilde{\Phi}(t,\mathbf{p})\rangle/V\,, \tag{11.5}$$

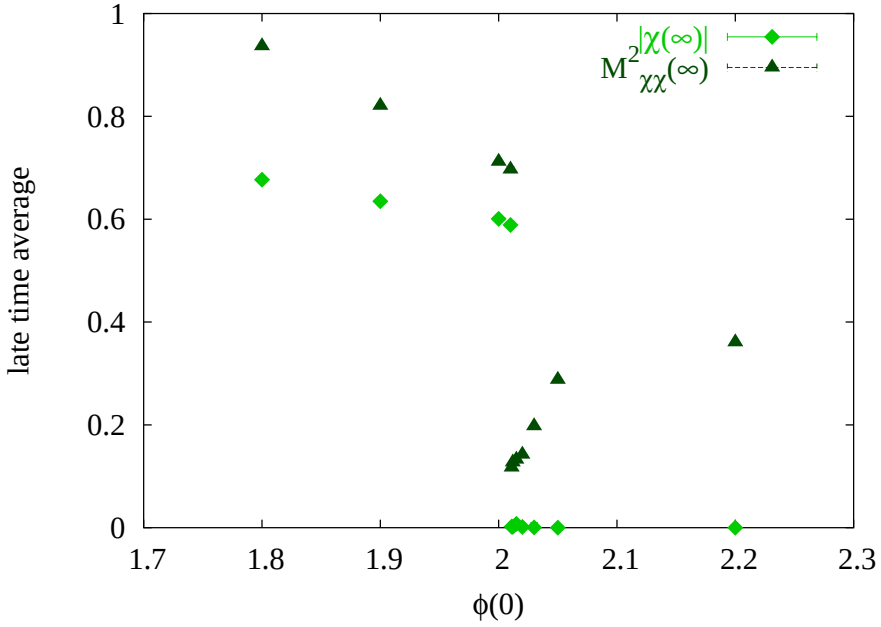

Figure 11.11: The late-time absolute value $|\chi(\infty)|$ (diamonds) and the late time effective mass $\mathcal{M}^2_{\chi\chi}(\infty)$ (triangles) averaged at times $t \approx 1000$ as a function of the initial amplitude $\phi(0)$ for simulations with $g^2 = 2\lambda$; each single pair of dots is the result of a full simulation; other parameters as in Fig. 11.3.

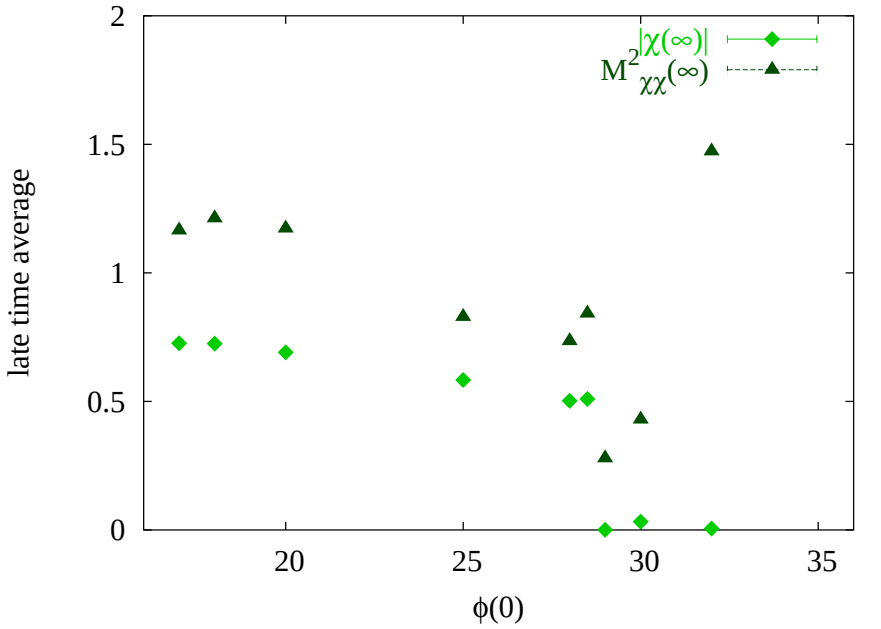

Figure 11.12: The same as Fig. 11.11 but for $g^2 = 0.01\lambda$; other parameters as in Fig. 11.5.

in terms of which we define the power spectrum of the fluctuation amplitudes

$$\frac{P_{ij}(t,p)}{p} = G_{ij}(t,t,\mathbf{p})\frac{p^2}{2\pi^2} \tag{11.6}$$

by including the momentum phase space factor.

In Fig. 11.13 we display the momentum spectra of all fluctuations for the simulation in Fig. 11.3. The plots show the absolute values in the $p-t$ plane as gray-scaled maps. White points correspond to zero, black points to the maximum value in each case. The three time regimes described in Sec. 11.2 are clearly visible here. Regime (I) ranges from $t = 0$ to $t \approx 20$, and is followed by regime (II) up to $t \approx 60$. Finally, regime (III) ranges from $t \approx 60$ to the end of the simulation. In Fig. 11.14 we display the same spectra at selected times t equal to 19.5, 51.3, and 100.2. These time steps are indicated in Fig. 11.3 by vertical dashed lines and in Fig. 11.13 by small arrows.

We have subtracted the free field part and the first order perturbative part of this kernel, both for Fig. 11.13 and Fig. 11.14, analog to the right hand side of Eq. (10.23). The free field part rises linearly with momentum; for $p = 2$, the maximal value used in our plots, has typical values of 0.05 and would be visible. It makes the tadpole integrals divergent; as discussed above, in our computations this divergence is absorbed by dimensional regularization and renormalization.

At early and intermediate times the Higgs fluctuations dominate. The inflaton and mixed fluctuation spectra only appear in the late-time regime, however, they are subdominant even there. At early times, $t \lesssim 20$ the Higgs spectrum is generated by negative squared masses as in tachyonic preheating or quench scenarios. In Ref. [80] it was found that the peak in the momentum spectrum $pP_{\chi\chi}(t,p)$ can be fitted by a Gaussian; we similarly find, at $t = 19.5$, a spectrum

$$pP_{\chi\chi}(t,p) \simeq A \exp\left[-B(|\mathbf{p}| - C)^2\right] \tag{11.7}$$

with

$$A = 0.4482 \pm 0.0038\,, \tag{11.8}$$
$$B = 36.1115 \pm 0.7131\,, \tag{11.9}$$
$$C = 0.307995 \pm 0.001168\,. \tag{11.10}$$

At intermediate times the smooth peak broadens and decays into spikes, typical of parametric resonance. Parametric resonance also dominates the shape of the spectra at late times. As the period and amplitude of oscillation change very slowly, the width of the spectrum remains almost constant.

11.6 Correlation functions

Many authors have studied spatial correlation functions in the presence of spontaneous symmetry breaking (see, e.g., Refs. [89, 90]).

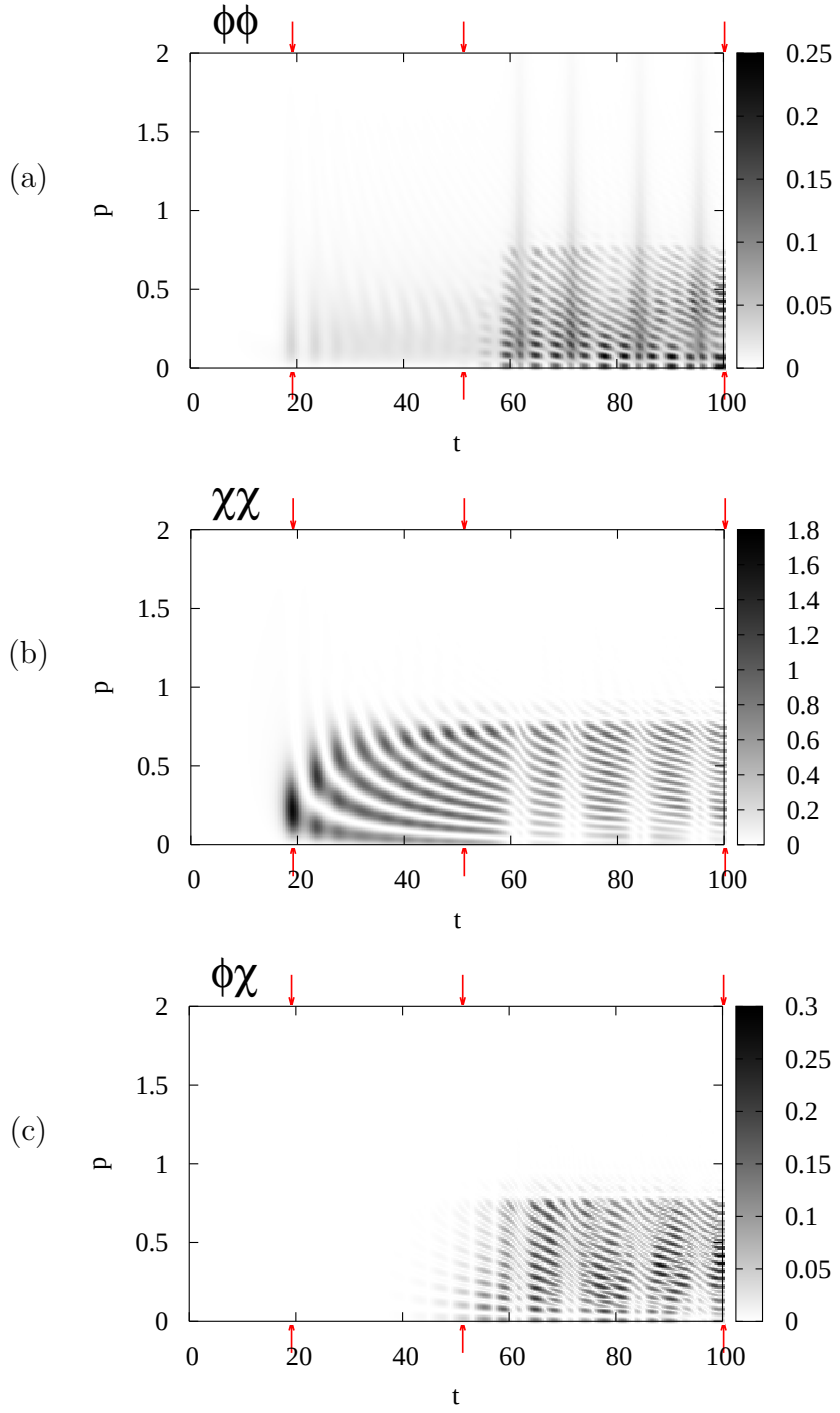

Figure 11.13: Momentum spectra $G_{ij}(t,t;\mathbf{p})p^2/(2\pi^2)$ for the simulation in Fig. 11.3. The x-axis shows the time t and the y-axis the momentum p. The absolute values $|G_{ij}(t,t;\mathbf{p})|p^2/(2\pi^2)$ are visualized by a gray-scale ranging from white for zero to black in each case. Displayed are: (a) the inflaton fluctuations $ij = \phi\phi$, (b) Higgs fluctuations $ij = \chi\chi$, (c) mixed fluctuations $ij = \phi\chi$. The small arrows pointing on the x-axis indicate the times $t = 19.5$, $t = 51.3$ and $t = 100.2$ (see also Fig. 11.14).

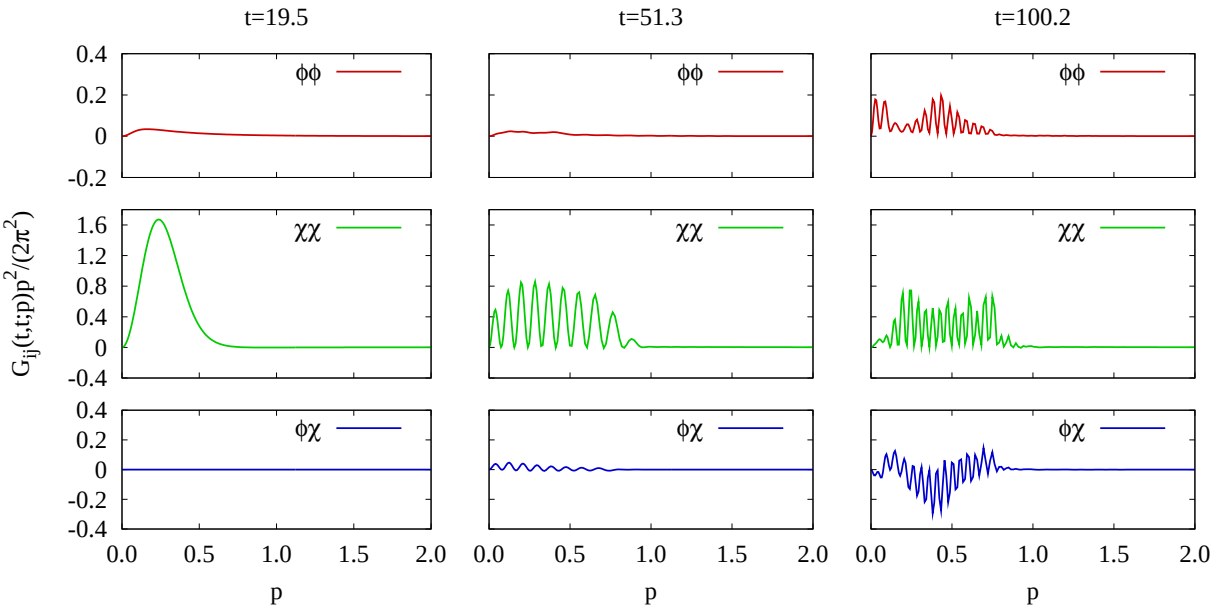

Figure 11.14: Momentum spectra $G_{ij}(t,t;\mathbf{p})p^2/(2\pi^2)$ for the simulation in Fig. 11.3 at the times $t = 19.5$ (left), $t = 51.3$ (middle) and $t = 100.2$ (right).

We define the correlation function between the different fluctuations as

$$C_{ij}(r,t) = \int \frac{d^3p}{(2\pi)^3} e^{i\mathbf{p}\cdot\mathbf{x}} G_{ij}(t,t;\mathbf{p}) \tag{11.11}$$

$$= \int \frac{d^3p}{(2\pi)^3} e^{i\mathbf{p}\cdot\mathbf{x}} \sum_\alpha \frac{1}{2\omega_\alpha} \mathrm{Re}\left[f_i^\alpha(t,\mathbf{p}) f_j^{*\alpha}(t,\mathbf{p})\right]$$

$$= \frac{1}{2\pi^2 r} \int_0^\infty dp\, p \sin(pr) \sum_\alpha \frac{1}{2\omega_\alpha} \mathrm{Re}\left[f_i^\alpha(t,\mathbf{p}) f_j^{*\alpha}(t,\mathbf{p})\right] . \tag{11.12}$$

We consider here the correlations of the Higgs fluctuations ($i = j = 2$), which are displayed in Fig. 11.15. We observe the correlations to be mainly positive and propagating with $\Delta r = 2\Delta t$, as also found in the large-N approximation [90]. The propagation with twice the speed of light can be related to the fact that the quantum fluctuations are correlated by the mean fields whose influence propagates in opposite space directions. Usually this is corroborated by a strong decrease of such correlations when the mean field amplitude goes to zero [192].

11.7 Decoherence

One of the important questions is the justification of using classical instead of quantum dynamics. In the context of nonequilibrium quantum field theory this has been discussed in Refs. [87, 88, 204] and applied to the hybrid model in Refs. [84, 80]. We use here the

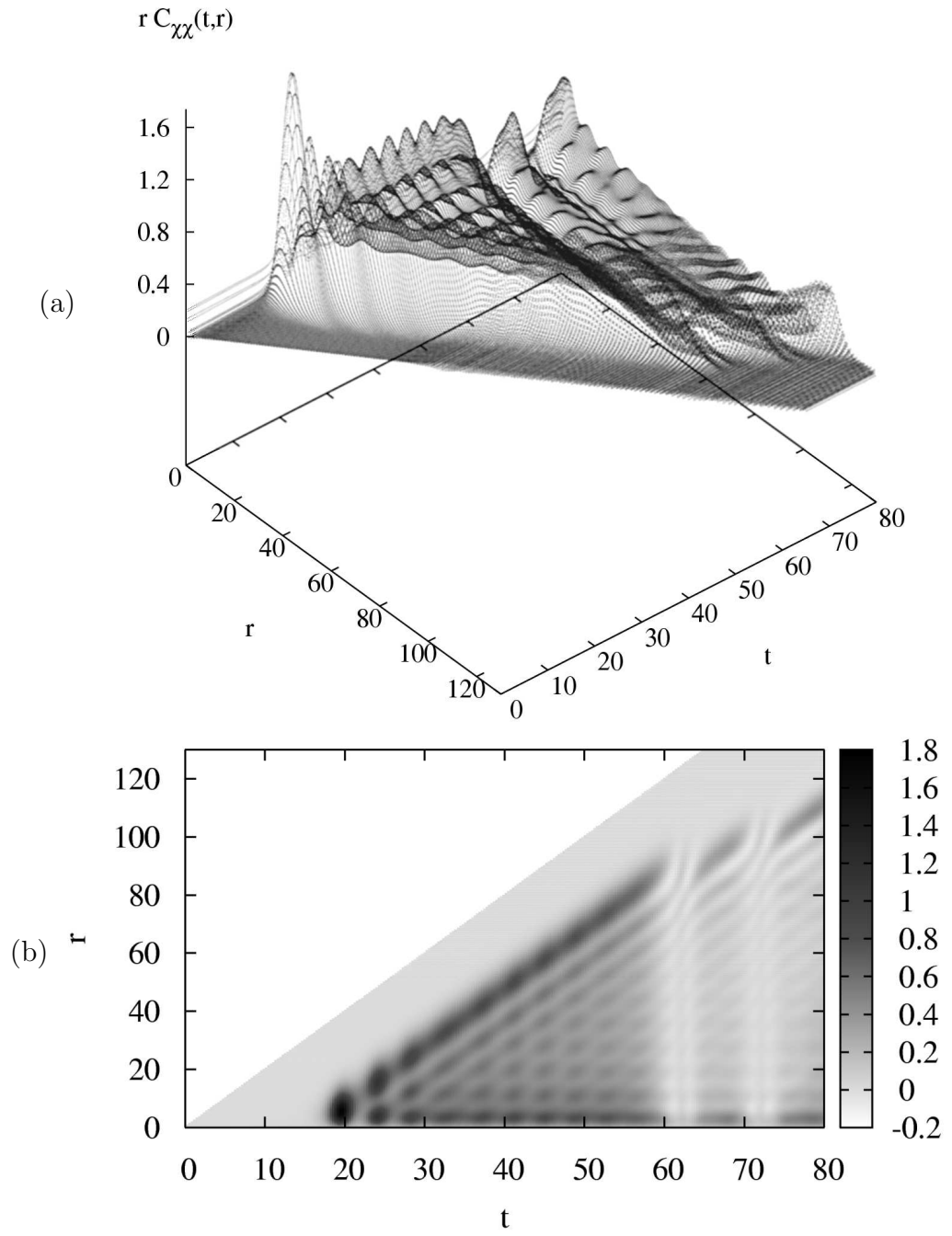

Figure 11.15: Plotted in the r-t plane is the correlation function $rC_{\chi\chi}(r,t)$; (a) 3D plot (b) 2D map in which the gray-scale coding indicates values for $rC_{\chi\chi}(r,t)$ between -0.2 (white) and 1.8 (black); the plots are cut in the r-t plane if $r > 2t$; in this particular simulation the spinodal regime is entered at $t \approx 20$ which initializes the development of spatial correlations of the Higgs field; the transition of the order parameter χ from the false vacuum to the stable vacuum is finished at $t \approx 60$ indicating the dilution of correlations; parameters as in Fig. 11.3.

definitions of Ref. [80], adapted to our normalization. The "classicality" is measured by the imaginary part $F(t, \mathbf{p})$ of a correlation function,

$$F_{ij}(t, \mathbf{p}) = \mathrm{Im}\left[\sum_{\alpha} \frac{f_i^{\alpha *}(t,p)\dot{f}_j^{\alpha}(t,p)}{2\omega_\alpha(p)}\right] . \tag{11.13}$$

The real part of the bracket is associated with the commutator. The criterion for a classical description is given by

$$|F_{ii}| \gg 1 \quad \text{(no summation over } i\text{)} . \tag{11.14}$$

We display the time for the onset of classicality ("decoherence time") as a function of momentum p for a simulation with $g^2 = 2\lambda$ in Fig. 11.16 and for a simulation with $g^2 = 0.01\lambda$ in Fig. 11.17. The time t_{dec} is implicitly defined by $|F_{ij}(t_{\mathrm{dec}}, \mathbf{p})| = 1$.

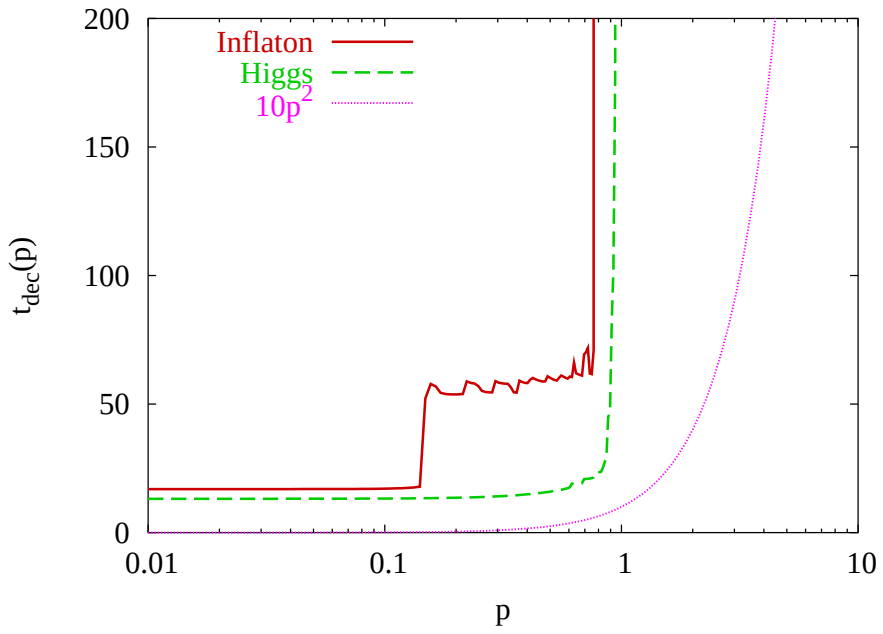

Figure 11.16: Decoherence time $t_{\mathrm{dec}}(p)$ for which a given mode p becomes "classical" ($|F_{ij}(t_{\mathrm{dec}}, \mathbf{p})| = 1$) for the simulation in Fig. 11.3 with $g^2 = 2\lambda$; the red solid line represents the inflaton ($i = j = 1$) and the green dashed line the Higgs modes ($i = j = 2$); the dotted line corresponds to $t_{\mathrm{dec}} \propto p^2$.

As far as the Higgs fluctuations ($i = j = 2$) are concerned the figures can be compared to those of Refs. [80, 84]. These authors consider the creation of quantum fluctuations via the spinodal instability. They assume for the mass of the Higgs fluctuations a behavior $\mathcal{M}^2_{\chi\chi} \propto (t_0 - t)$, where t_0 marks the onset of the spinodal regime. That way they simplify the time evolution without considering any back-reactions (see also Refs. [79, 82, 87]). In this case the mode functions become Airy functions and the results can be written in

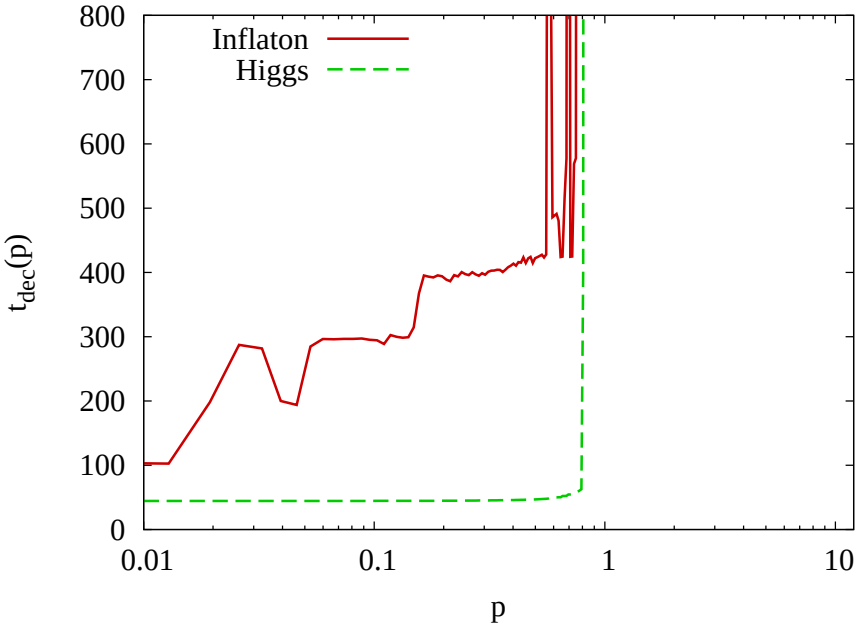

Figure 11.17: The same as Fig. 11.16 but for $g^2 = 0.01\lambda$ corresponding to the simulation in Fig. 11.5.

analytic form. The boundary $|F(t, \mathbf{p})| = 1$ between the classical and quantum regimes then behaves roughly as $t \propto \mathbf{p}^2$ [79, 80, 84]. As displayed in Fig. 11.16 and 11.17 the shape of this boundary is quite different in our simulations, the classical regime remains limited within a fixed momentum band at all times. When we include back-reaction, the behavior of the mass term is linear in time only in a very limited time interval; furthermore, due to the inflaton oscillations, the process repeats several times. The limited momentum band for which the modes can be considered as classical, can be seen as a consequence of parametric resonance. Due to the lack of strong dissipation the oscillations of the classical fields persist at late times, and therefore also the resonance band. Whether and for which time period this is physical or unphysical cannot be determined within the approximation used here, even though it is certainly more elaborate as previous approaches.

For the inflaton fluctuations, not considered in Ref. [80, 84], the structure of the curves shows that fluctuations at very small momenta become classical as early as those of the Higgs field, while those for larger momenta develop at later times. Presumably, this is due to a stronger role of parametric resonance for the evolution of inflaton fluctuations. Again the band of momenta for the classical regime remains sharply cut off even at late times. Concerning the dependence on the parameter g^2 the details of the evolution of the inflaton fluctuations can be slightly different, while the Higgs fluctuations evolve in a similar way.

Chapter 12

Conclusions of Part III

We have studied aspects of the nonequilibrium dynamics in a hybrid inflation model [73]. The hybrid model discussed here corresponds to the original proposal by Linde, using a double well potential [73].

One important result of our work is the consistent implementation of renormalized equations in the presence of quantum back-reaction for a fully coupled system of two quantum fields. We have used a one-loop bubble-resummed approximation. In the semiclassical one-loop approximation [86, 191], i.e., without quantum back-reaction, it is impossible to study the false vacuum transition, since the system becomes dynamically unstable, and the approximation breaks down. We have demonstrated that renormalization in the presence of quantum back-reaction is conceptionally not complicated, although it leads to involved calculations. We consider this as an essential achievement of our work, which will also be important when extending the model further by including the coupling to gravity and to gauge fields where proper renormalization is indispensable [205]. However, when including gauge fields, we would have to discuss gauge parameter dependences [206, 207, 208, 209] which are unavoidable in 2PI resummation schemes. We have also worked with Minkowski space-time for simplicity. There are no conceptional difficulties to extend the methods presented here to include space-time expansion via the coupling to gravity. The renormalized nonequilibrium dynamics in Friedmann-Robertson-Walker cosmologies and with simple scalar models has been investigated, e.g., in Refs. [205, 210].

In the hybrid model the inflationary stage ends with a phase transition of a symmetry breaking field that evolves from a false metastable vacuum phase to a stable vacuum. Our numerical simulations display the expected transition to a broken symmetry phase if the initial inflaton amplitude is not too large. A possible intermediate restoration of symmetry by quantum fluctuations would be followed by a later transition to the broken symmetry state after further cosmological expansion. Possible consequences like the unwanted formation of topological defects have been discussed in the literature [211, 212, 213, 214]. We found that the phase transition can happen almost instantaneously for small coupling between the fields, as observed in classical simulations using inhomogeneous fields [63], but also more slowly for larger coupling. In the latter case the evolution and back-reaction of quantum fluctuations delays the transition from the metastable vacuum to the stable

vacuum, so that neglecting space-time expansion may no longer be justified.

We have calculated the boundaries between regions where a quantum description is needed and those where one may have recurse to classical evolution equations. We find marked differences with respect to previous work in similar models [80, 84], where the production of quanta is described in a simplified way, using a squared mass of the Higgs field passing linearly through zero. We find numerically that the back-reaction limits the classical regime to a low-momentum region fixed for all times. Large excitations of quantum fluctuations seem to justify the transition to a classical description in this momentum region. However, one has to keep in mind that finally one wants to end up with an ensemble described by quantum statistics which is used in the standard thermal history of the early universe. The classical ensembles suffer from the Rayleigh-Jeans divergence, which is incompatible with the finite amount of initial energy density. This automatically forces the fluctuations back to the quantum regime.

For electroweak or GUT-scale preheating the Higgs sector is based on a symmetry group like SU(N) or SO(N) and will in general have more degrees of freedom. Near the spinodal point all masses degenerate, and this fact has been used in some studies [80] in the way of just using n_H identical copies of one and the same degree of freedom. However, once the mean value of the Higgs field departs from zero, there will be a nontrivial mass matrix for the quantum fluctuations with several massless degrees of freedom, the would-be Goldstone bosons. It can be expected that this will modify the quantum back-reaction in an essential way. While this goes beyond the scope of the present investigation, there are some studies using classical dynamics with more realistic Higgs sectors [63, 83, 215, 216]. Our formalism allows for a generalization towards more realistic Higgs sectors, albeit with the limitation of homogeneous background fields.

Though our approximation is certainly more elaborate than previous approaches [80, 84, 86], it lacks an efficient mechanism for dissipation. Once the phase transition is completed, as indicated by the mean field χ oscillating around a nonzero expectation value, the amplitude of the fields ϕ and χ, as well as of the different fluctuation integrals remains almost constant as a function of time. This is considered to be a general drawback of leading-order or mean-field approximations. Production of particles does not proceed efficiently. The situation would improve, however, even in our approximation, if Goldstone modes were included [192]. Dissipation via particle production is also found in O(N) models when using the large-N limit [59]. In more realistic models dissipation may proceed in addition via fermion and gauge fields, even for tree-level approximations in the fermionic case [195]. Strong dissipative dynamics are also expected in approximations beyond leading-order or mean-field approximations, i.e., if scattering processes between quantum fluctuations are included. Recent investigations of various authors are based on next-to-leading order approximations of the 2PI effective action approach. In Refs. [182, 185] simple 1+1 dimensional models have been investigated (see also Refs. [91, 92]). In Refs. [183, 186, 189] the unrenormalized equations of motion are solved using lattice cut-offs. In these next-to-leading-order studies the systems under investigation display dissipative dynamics for the classical fields, as well as the tendency to lose information about the initial state, which is a prerequisite for thermalization. By today, hybrid models, i.e., models with coupled scalar

fields, have not been studied at next-to-leading order. However, the general expectation is that higher order effects become effective only when quantum fluctuations have grown to sufficient size. In the earlier stages the one-loop bubble-resummed approximation, which we have used here, should be able to provide reliable information on the dynamics of the false vacuum transition.

Appendix A

Appendix to Part II

This Appendix covers some formulae for the error control function used in Chap. 5, and some comments on details of the numerical implementation (Chap. 6).

A.1 Error bounds

A key advantage of the uniform approximation presented in Ref. [42] is the uniform control over remainder terms. This control is obtained by carefully separating the dominant influence in the coefficient functions of the ordinary differential equations. Because of this uniform control, the approach is superior to the earlier results of Langer (for a good description see Ref. [217]). Additionally, Olver [42] constructs higher order approximations not present in the original work. In this Appendix we review in detail the general error formulae given by Olver. The errors in Eqs. (5.17) and (5.18) are bounded by

$$\frac{|\epsilon^{(1)}_{2n+1,\leqslant}(b,\xi)|}{M(b^{2/3}\xi)}, \frac{|\partial\epsilon^{(1)}_{2n+1,\leqslant}(b,\xi)/\partial\xi|}{b^{2/3}N(b^{2/3}\xi)} \leq 2E^{-1}(b^{2/3}\xi)\exp\left\{\frac{2\lambda\mathcal{V}_{\xi,\beta}(|\xi|^{1/2}B_0)}{b}\right\}\frac{\mathcal{V}_{\xi,\beta}(|\xi|^{1/2}B_n)}{b^{2n+1}}, \tag{A.1}$$

$$\frac{|\epsilon^{(2)}_{2n+1,\leqslant}(b,\xi)|}{M(b^{2/3}\xi)}, \frac{|\partial\epsilon^{(2)}_{2n+1,\leqslant}(b,\xi)/\partial\xi|}{u^{2/3}N(b^{2/3}\xi)} \leq 2E(b^{2/3}\xi)\exp\left\{\frac{2\lambda\mathcal{V}_{\alpha,\xi}(|\xi|^{1/2}B_0)}{b}\right\}\frac{\mathcal{V}_{\alpha,\xi}(|\xi|^{1/2}B_n)}{b^{2n+1}}, \tag{A.2}$$

where $M(x)$ and $N(x)$ are modulus functions, and $E(x)$ is a weight function defined as

$$\begin{aligned} M(x) &= \sqrt{2\mathrm{Ai}(x)\mathrm{Bi}(x)} \text{ for } x \le c, \\ M(x) &= \sqrt{\mathrm{Ai}^2(x) + \mathrm{Bi}^2(x)} \text{ for } x \ge c, \qquad \text{(A.3)} \\ N(x) &= \left\{ \frac{\mathrm{Ai}'^2(x)\mathrm{Bi}^2(x) + \mathrm{Bi}'^2(x)\mathrm{Ai}^2(x)}{\mathrm{Ai}(x)\mathrm{Bi}(x)} \right\}^{1/2} \text{ for } x \ge c, \\ N(x) &= \left\{ \mathrm{Ai}'^2(x) + \mathrm{Bi}'^2(x) \right\}^{1/2} \text{ for } x \le c, \qquad \text{(A.4)} \\ E(x) &= \sqrt{\frac{\mathrm{Bi}(x)}{\mathrm{Ai}(x)}} \text{ for } c \le x \le \infty, \\ E(x) &= 1 \quad \text{for} \quad -\infty \le x \le c\,, \qquad \text{(A.5)} \end{aligned}$$

and $c \simeq -0.36605$. Some explicit numerical values of these functions are given in Ref. [42]. The auxiliary quantity λ is defined by

$$\lambda = \sup_{(-\infty,\infty)} \left\{ \pi |x|^{1/2} M^2(x) \right\}. \qquad \text{(A.6)}$$

A numerical estimate is $\lambda \simeq 1.04$ [42]. Finally, in Eqs. (A.1) and (A.2), we introduced the total variation $\mathcal{V}_{\alpha,\beta}(f)$ of a function over the interval (α, β). The total variation of a function $f(x)$ over an interval (α, β) is the supremum

$$\mathcal{V}_{\alpha,\beta}(f) = \sup_{\{\alpha \le x_0 < \cdots < x_n < \cdots \le \beta\}} \sum_{s=0}^{n-1} |f(x_{s+1}) - f(x_s)|, \qquad \text{(A.7)}$$

for unbounded n and all possible subdivisions of the interval, $\alpha \le x_0 < \cdots < x_n \le \beta$. In case of a compact interval $[\alpha, \beta]$ one possible subdivision is given by $n = 1$, $x_0 = a$, and $x_1 = b$. Hence

$$\mathcal{V}_{\alpha,\beta}(f) \ge |f(\beta) - f(\alpha)|. \qquad \text{(A.8)}$$

Equality holds if $f(x)$ is monotonic over $[\alpha, \beta]$. When $f(x)$ is continuously differentiable in $[\alpha, \beta]$ we have

$$\mathcal{V}_{\alpha,\beta}(f) = \int_\alpha^\beta |f'(x)| dx. \qquad \text{(A.9)}$$

A.2 Numerical implementation details

A.2.1 Momentum discretization

The actual momentum discretization chosen for numerical work is arbitrary but it is a good idea to adjust the chosen values of the momenta so that the relation

$$\bar{\nu}^2(\bar{\eta}) = k^2 \bar{\eta}^2 \Rightarrow g(k, \bar{\eta}) = 0, \qquad \text{(A.10)}$$

defining the momentum-dependent turning points $\bar{\eta} = \bar{\eta}(k)$ is satisfied exactly, even though the conformal time is known only at discrete points. This can be done by locking the momentum discretization to the time discretization, i.e., by guaranteeing that if the time discretization is given, k discretization points are chosen only if they satisfy Eq. (A.10). Of course a predefined momentum discretization is unnecessary if we only wish to calculate power spectra and spectral indices in the uniform approximation; the predefined momentum discretization is used only for initializing the mode functions in the mode-by-mode approach, where we need the integrals on the left of the turning point.

A.2.2 Spectral indices in the uniform approximation

The integral for the spectral index has a square root singularity at $\eta = \bar{\eta}$ and is handled specially in the numerical routine. We split the integral appearing in the spectral index into two parts:

$$\int_{\bar{\eta}}^{\eta} \frac{d\eta'}{\sqrt{g(k,\eta')}} = \int_{\bar{\eta}}^{\bar{\eta}+\Delta\eta} \frac{d\eta'}{\sqrt{g(k,\eta')}} + \int_{\bar{\eta}+\Delta\eta}^{\eta} \frac{d\eta'}{\sqrt{g(k,\eta')}}, \tag{A.11}$$

where $\Delta\eta$ is a small quantity. Note that $\Delta\eta$ is really k-dependent, because the discretization in η is not equidistant.

In the first integral we can substitute $\nu^2(\eta)$ by $\bar{\nu}^2(\bar{\eta})$, i.e., insert the leading order of the local approximation. The first integral can then be calculated analytically and keeps track of the inverse square root singularity, while the second integral has no singularity and can be easily calculated numerically. The quantity $\Delta\eta$ is given by the actual time discretization in physical time t that we have chosen. It is further required that $-2\bar{\eta} > \Delta\eta$, i.e., $\Delta\eta$ must be sufficiently small. As $\bar{\eta}(k) \to 0^-$ in the limit $k \to \infty$, this relation also constrains the highest reliable mode for a given time discretization in the exact numerical results. The first integral gives

$$\int_{\bar{\eta}}^{\bar{\eta}+\Delta\eta} \frac{d\eta'}{\sqrt{g(k,\eta')}} \simeq \int_{\bar{\eta}}^{\bar{\eta}+\Delta\eta} \frac{d\eta'}{\sqrt{\frac{\bar{\nu}^2}{\eta'^2} - k^2}} = \frac{1}{k}\sqrt{-2\bar{\eta}\,\Delta\eta - \Delta\eta^2}. \tag{A.12}$$

In order to avoid calculating the integrals numerically up to $\eta \to 0^-$, we calculate the remainder of the integral from an asymptotic value η_a, where the integrand is sufficiently small and we can stop the numerical integration, to $\eta = 0^-$, assuming that $\nu^2(\eta) \simeq \nu^2(\eta_\mathrm{a}) + 2\nu(\eta_\mathrm{a})\nu'(\eta_\mathrm{a})(\eta - \eta_\mathrm{a})$. Then we have

$$\begin{aligned} -2k^2 \lim_{k\eta\to 0^-} \int_{\eta_\mathrm{a}}^{\eta} \frac{d\eta'}{\sqrt{\frac{\nu^2(\eta)}{\eta'^2} - k^2}} \simeq & -2\sqrt{\nu^2(\eta_\mathrm{a}) - 2\nu(\eta_\mathrm{a})\nu'(\eta_\mathrm{a})\eta_\mathrm{a}} + 2\sqrt{\nu^2(\eta_\mathrm{a}) - k^2\eta_\mathrm{a}^2} \\ & - \frac{2\nu(\eta_\mathrm{a})\nu'(\eta_\mathrm{a})}{k}\left[\arcsin\frac{2\nu(\eta_\mathrm{a})\nu'(\eta_\mathrm{a})}{\sqrt{\Delta}}\right. \\ & \left. - \arcsin\frac{2\nu(\eta_\mathrm{a})\nu'(\eta_\mathrm{a}) - 2k^2\eta_\mathrm{a}}{\sqrt{\Delta}}\right], \end{aligned} \tag{A.13}$$

with

$$\Delta = [2\nu(\eta_{\rm a})\nu'(\eta_{\rm a})]^2 + 4k^2[\nu^2(\eta_{\rm a}) - 2\nu(\eta_{\rm a})\nu'(\eta_{\rm a})\eta_{\rm a}]. \tag{A.14}$$

Alternatively, it is possible to convert the evaluation of the spectral index into the problem of solving a differential equation, rather than evaluating an integral. The limit $k\eta \to 0^-$ in Eq. (5.50) is interchangeable with a conformal time derivative, so that the physical time derivative of the spectral index reads

$$\dot{n}_S[k, \eta(t)] = -2k^2 \frac{1}{a(t)\sqrt{g_S(\eta, k)}}. \tag{A.15}$$

In order to avoid the square root singularity the integration starts at $\eta = \bar{\eta} + \Delta\eta$, so that the "initial" condition

$$n_S(k, \bar{\eta} + \Delta\eta) = 4 - 2k\sqrt{-2\bar{\eta}\,\Delta\eta - \Delta\eta^2} \tag{A.16}$$

includes the integral in Eq. (A.12). It is understood that the limit $k\eta \to 0^-$ is taken when calculating $n_S(k)$. The integration of the differential equation with a high order integrator is more precise than a standard trapezoidal rule. In contrast, as the discretization in η is not equidistant, higher order integration schemes would be somewhat more complicated to implement. However, we have verified that a standard trapezoidal integration rule already gives sufficiently precise answers. In fact, the local approximation for the spectral index at leading order is quite close to the numerical nonlocal integral in the cases where the derivative expansion is valid.

A.2.3 Conversion to physical units

For completeness, we explain here how units are handled in the numerical implementation. As always, it is convenient to work in dimensionless units, i.e., by choosing $\hbar = c = 1$. In addition, we set the factor $8\pi G$ in the Friedmann equation in the numerical code to unity. These choices lead to values for the input parameters, e.g., initial conditions and coupling constants, of order unity. This helps to prevent numerical problems arising from very large or very small numbers. In order to reconvert the dimensionless units to physical units the Hubble parameter H has to be rescaled via

$$H_{\rm phys} = \sqrt{8\pi} H_0 H, \tag{A.17}$$

where H is the dimensionless Hubble parameter used in the code and $H_0 = 100h\,\mathrm{km\,s^{-1}\,Mpc^{-1}}$. The rescaled momentum k in physical units $h\,\mathrm{Mpc}^{-1}$ is therefore given by

$$k_{\rm phys} = \sqrt{8\pi}\frac{h}{100ca(0)} k\ \mathrm{km\,s^{-1}\,Mpc^{-1}}, \tag{A.18}$$

with $c = 2.99792458 \times 10^5\,\mathrm{km\,s^{-1}}$. The initial expansion rate is $a(0)$. Throughout the paper we have dropped the suffix "phys" implying that all results are given in physical units.

Next we discuss the normalization of the amplitude of the power spectrum. The power spectra for scalar and tensor perturbations as defined in Eqs. (2.51) and (2.52) are dimensionless and therefore not sensitive to the units of k. Their amplitude is determined fully by the parameters chosen in the inflaton potential $V(\phi)$. Since parameters such as the inflaton mass m^2 in a chaotic $m^2\phi^2$ model are generally not known, we present the results for the power spectra with respect to the WMAP normalization where the amplitude of scalar perturbations is given by $|\Delta R^2| = 2.95^{-9}A$ with $A = 0.9 \pm 0.1$ (at $k_* = 0.05/\mathrm{Mpc}$), see Refs. [8, 218]. Using the fact that for a fixed number of e-folds, counted from the horizon crossing of k_*, the parameters in the monomial potentials simply lead to a global normalization factor [34] we can avoid having very small numbers in the numerical calculations and just normalize the spectra afterwards. When stating results we give the parameters in the potential corresponding to the WMAP normalization in each case.

Appendix B

Appendix to Part III

B.1 Identities for Feynman diagrams

We list some identities for Feynman diagrams which have been used in order to extract the divergences from the finite parts (see Sec. 10.28). The divergent terms have been expressed in terms of three-dimensional momentum integrals. These integrals can be converted to four-dimensional integrals and conventional regularization techniques like dimensional regularization can be used.

Within dimensional regularization ($D = 4 - \epsilon$) the following identities (no summation over Greek indices) hold

$$\int \frac{d^{D-1}p}{(2\pi)^{D-1}} \frac{1}{2\omega_\alpha \omega_\beta (\omega_\alpha + \omega_\beta)} = \int \frac{d^D p}{(2\pi)^D} \frac{1}{(p^2 - m_{0,\alpha}^2 + io)(p^2 - m_{0,\beta}^2 + io)} \tag{B.1}$$

$$= \frac{1}{16\pi^2} \left[L_\epsilon - \ln \frac{m_{0,\alpha}^2}{\mu^2} + 1 + \frac{m_{0,\beta}^2}{m_{0,\alpha}^2 - m_{0,\beta}^2} \ln \frac{m_{0,\beta}^2}{m_{0,\alpha}^2} \right], \tag{B.2}$$

and

$$\int \frac{d^{D-1}p}{(2\pi)^{D-1}} \frac{1}{2\omega_\alpha} = \int \frac{d^D p}{(2\pi)^D} \frac{i}{p^2 - m_{0,\alpha}^2 + io} \tag{B.3}$$

$$= -\frac{m_{0,\alpha}^2}{16\pi^2} \left[L_\epsilon - \ln \frac{m_{0,\alpha}^2}{\mu^2} + 1 \right], \tag{B.4}$$

with

$$\omega_\alpha = \sqrt{m_{0,\alpha}^2 + \mathbf{p}^2}, \tag{B.5}$$

$$L_\epsilon = \frac{2}{\epsilon} - \gamma + \ln 4\pi. \tag{B.6}$$

The corresponding Feynman diagrams are depicted in Fig. B.1. Note that

$$\lim_{m_{0,\beta}^2 \to m_{0,\alpha}^2} \left[-\ln \frac{m_{0,\alpha}^2}{\mu^2} + 1 + \frac{m_{0,\beta}^2}{m_{0,\alpha}^2 - m_{0,\beta}^2} \ln \frac{m_{0,\beta}^2}{m_{0,\alpha}^2} \right] = -\ln \frac{m_{0,\alpha}^2}{\mu^2}. \tag{B.7}$$

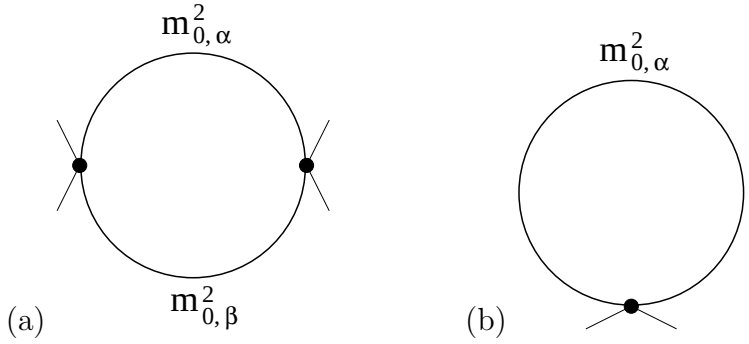

Figure B.1: (a) The Feynman diagram with a topology of a fish graph corresponding to Eq. (B.1) (b) the tadpole type graph corresponding to Eq. (B.4); in both diagrams the lines denote free propagators with the initial masses $m^2_{0,\alpha}$ and $m^2_{0,\beta}$, respectively.

An identity that is needed for the renormalization of the energy is given by

$$\int \frac{d^{D-1}p}{(2\pi)^{D-1}}\omega_\alpha = \frac{m^4_{0,\alpha}}{32\pi^2}\left[L_\epsilon - \ln\frac{m^2_{0,\alpha}}{\mu^2} + \frac{3}{2}\right] . \tag{B.8}$$

B.2 Expansion of the mode functions

In this Section we will present the isolation of the divergences via a perturbative expansion of the mode functions (see e.g. Refs. [76, 191]) for the case of a coupled system of equations.

Let us split the mode functions f^α_i into a free part containing the initial matrix O_{ij} and higher order terms represented by the reduced mode functions h^α_i, i.e.

$$f^\alpha_i(t;p) \;=\; e^{-i\omega_\alpha t}\left[O_{i\alpha} + h^\alpha_i(t;p)\right] . \tag{B.9}$$

Here and in the following no summation over Greek indices is meant if not explicitly stated.

If we define a potential

$$\mathcal{V}_{ij}(t) \;=\; \mathcal{M}^2_{ij}(t) - \mathcal{M}^2_{ij}(0) , \tag{B.10}$$

the differential equation (9.11) is equivalent to the following integral equation:

$$f^\alpha_i(t;p) \;=\; e^{-i\omega_\alpha t}O_{i\alpha} + \int_0^t dt'\, K^{\rm ret}_{ij}(t-t';p)\mathcal{V}_{jk}(t')f^\alpha_k(t';p) .$$

The retarded kernel of the free equation is given by

$$K^{\rm ret}_{ij}(t-t';p) \;=\; \sum_\beta \frac{i}{2\omega_\beta}\Theta(t-t')O_{i\beta}O_{j\beta}\left[e^{i\omega_\beta(t-t')} - e^{-i\omega_\beta(t-t')}\right] . \tag{B.11}$$

Inserting the retarded kernel in the integral equation gives

$$\begin{aligned} f_i^\alpha(t;p) &= e^{-i\omega_\alpha t}O_{i\alpha} + \int_0^t dt' \sum_\beta \frac{i}{2\omega_\beta} O_{i\beta}O_{j\beta}\left[e^{i\omega_\beta(t-t')} - e^{-i\omega_\beta(t-t')}\right] \\ &\qquad \times \mathcal{V}_{jk}(t') f_k^\alpha(t';p) \qquad \text{(B.12)} \\ &= e^{-i\omega_\alpha t}\Bigg\{O_{i\alpha} + \int_0^t dt'\, \mathcal{V}_{jk}(t') \sum_\beta \frac{i}{2\omega_\beta} O_{i\beta}O_{j\beta}O_{k\alpha} \qquad \text{(B.13)} \\ &\qquad \times \left[e^{i(\omega_\beta+\omega_\alpha)(t-t')} - e^{-i(\omega_\beta-\omega_\alpha)(t-t')}\right]\Bigg\} + \dots\,, \qquad \text{(B.14)} \end{aligned}$$

where in addition the decomposition in Eq. (B.9) has been used. The dots imply the higher order terms with h_i^α that we do not need for the analysis of the divergences here.

By partial integration the divergent contributions can be isolated in the usual way,

$$\begin{aligned} f_i^\alpha(t;\mathbf{p}) &= e^{-i\omega_\alpha t}\Bigg\{O_{i\alpha} - \sum_\beta \frac{1}{2\omega_\beta}\left[\frac{1}{\omega_\beta+\omega_\alpha} + \frac{1}{\omega_\beta-\omega_\alpha}\right] O_{i\beta}O_{j\beta}O_{k\alpha}\mathcal{V}_{jk}(t) \qquad \text{(B.15)} \\ &\quad + \sum_\beta \frac{1}{2\omega_\beta}\left[\frac{1}{\omega_\beta+\omega_\alpha}e^{i(\omega_\beta+\omega_\alpha)t} + \frac{1}{\omega_\beta-\omega_\alpha}e^{-i(\omega_\beta-\omega_\alpha)t}\right] O_{i\beta}O_{j\beta}O_{k\alpha}\mathcal{V}_{jk}(0) \\ &\quad + \sum_\beta \frac{1}{2\omega_\beta} O_{i\beta}O_{j\beta}O_{k\alpha}\int_0^t dt' \dot{\mathcal{V}}_{jk}(t') \\ &\qquad \times \left[\frac{1}{\omega_\beta+\omega_\alpha}e^{i(\omega_\beta+\omega_\alpha)(t-t')} + \frac{1}{\omega_\beta-\omega_\alpha}e^{-i(\omega_\beta-\omega_\alpha)(t-t')}\right]\Bigg\} + \dots\,. \end{aligned}$$

This expression and its complex conjugate are all that is needed to calculate the divergent contributions in $\Delta_{ij}(t)$. The divergent part of the symmetrized Green's function follows as

$$\begin{aligned} &\frac{1}{2}\Big[G_{ij}(t,t;\mathbf{p}) + G_{ji}(t,t;\mathbf{p})\Big]^{\rm div} \\ &\qquad = \sum_\alpha \frac{1}{2\omega_\alpha}{\rm Re}\Big[f_i^\alpha(t;p) f_j^{\alpha,*}(t;p)\Big]^{\rm div} \\ &\qquad = \sum_\alpha \frac{1}{2\omega_\alpha}\Bigg[O_{i\alpha}O_{j\alpha} + \sum_\beta \frac{1}{2\omega_\beta} O_{i\beta}O_{l\beta}O_{k\alpha}O_{j\alpha}\mathcal{V}_{kl}(t)\frac{-2\omega_\beta}{\omega_\beta^2-\omega_\alpha^2} \\ &\qquad\qquad + \sum_\beta \frac{1}{2\omega_\beta} O_{i\alpha}O_{l\beta}O_{k\alpha}O_{j\beta}\mathcal{V}_{kl}(t)\frac{-2\omega_\beta}{\omega_\beta^2-\omega_\alpha^2}\Bigg] \\ &\qquad = \sum_\alpha \frac{1}{2\omega_\alpha}\left[O_{i\alpha}O_{j\alpha} - \frac{1}{\omega_\beta(\omega_\alpha+\omega_\beta)} O_{i\alpha}O_{j\beta}O_{l\beta}O_{k\alpha}\mathcal{V}_{kl}(t)\right]. \qquad \text{(B.16)} \end{aligned}$$

The integral of Eq. (B.16) over d^3p becomes divergent. We will use them as subtraction terms in the fluctuation integrals in $\Delta_{ij}^{(1)}(t)$ and $E^{(1)}(t)$ [see Eqs. (9.17) and Eq. (10.54)].

The divergences in the energy can be found in an analogous way by inserting $f_i^\alpha(t,p)$ and its time derivative in the one-loop energy part $E^{(1)}(t)$ [see Eq. (10.54)]. However, we will use an alternative approach in the following.

The one-loop effective action at time t minus the one at $t=0$ is given by

$$\widetilde{\Gamma}^{(1)}[\mathcal{M}^2] = \frac{i}{2}\mathrm{tr}\ln\left\{\frac{\Box+\mathcal{M}^2(t)}{\Box+\mathcal{M}^2(0)}\right\}\ , \tag{B.17}$$

where it is understood that the numerator and denominator are 2×2 matrices. This expression can be expanded locally with respect to $\mathcal{V}(t)=\mathcal{M}^2(t)-\mathcal{M}^2(0)$ and gradients thereof. The expansion can be obtained by going to the momentum representation, i.e., by expanding with respect to insertions of $\mathcal{V}(q)$ and with respect to the external momenta $q=(q_0,\mathbf{q})$. As we do not need an infinite wave function renormalization the divergent parts are given by the terms of first and second order in $\mathcal{V}(q)$.

We introduce

$$G_{0,ij}^{-1}(p) = \left(-p_0^2+\mathbf{p}^2\right)\delta_{ij}+\mathcal{M}_{ij}^2(0)\,, \tag{B.18}$$
$$G_{ij}^{-1}(p) = \left(-p_0^2+\mathbf{p}^2\right)\delta_{ij}+\mathcal{M}_{ij}^2(t)\,. \tag{B.19}$$

G_0 is *not* the bare propagator which would be defined at the vacuum expectation values of ϕ and χ. We diagonalize the initial mass matrix by an orthogonal transformation

$$\mathcal{M}^2(0) = O\widetilde{\mathcal{M}}^2(0)O^T\,, \tag{B.20}$$

or

$$\mathcal{M}_{ij}^2(0) = O_{i\alpha}O_{j\beta}\widetilde{\mathcal{M}}_{\alpha\beta}^2(0) = O_{i\alpha}O_{j\alpha}m_{0,\alpha}^2\,. \tag{B.21}$$

Then also $G_{0,ij}^{-1}$ becomes diagonal. We likewise introduce

$$\begin{aligned} G_{ij}^{-1}(p) &= O_{i\alpha}\left(\left[-p_0^2+\mathbf{p}^2+m_{0,\alpha}^2\right]\delta_{\alpha\beta}+\widetilde{\mathcal{V}}_{\alpha\beta}(t)\right)O_{j\beta} \\ &= O_{i\alpha}\widetilde{G}_{\alpha\beta}^{-1}(p)O_{j\beta}\ , \end{aligned} \tag{B.22}$$

where of course

$$\widetilde{\mathcal{V}}_{\alpha\beta}(t) = O_{i\alpha}\mathcal{V}_{ij}(t)O_{j\beta} \tag{B.23}$$

is no longer diagonal. The effective action, in the approximation where all gradient terms are neglected, can now be rewritten as

$$\begin{aligned} \widetilde{\Gamma}^{(1)} &\simeq \frac{i}{2}\int\frac{d^4p}{(2\pi)^4}\mathrm{tr}\ln\left\{G_0G^{-1}\right\} \\ &= \int\frac{d^4p}{(2\pi)^4}\mathrm{tr}\ln\left\{1+\widetilde{G}_0\widetilde{\mathcal{V}}(t)\right\}\ . \end{aligned} \tag{B.24}$$

The first terms in the expansion are

$$\begin{aligned}\widetilde{\Gamma}^{(1)} \;\simeq\; & \frac{i}{2}\int\frac{d^4p}{(2\pi)^4}\left[\sum_\alpha \frac{1}{-p_0^2+\mathbf{p}^2+m_{0,\alpha}^2+io}\widetilde{\mathcal{V}}_{\alpha\alpha}(t)\right.\\ & \left.-\frac{1}{2}\sum_{\alpha\beta}\frac{1}{-p_0^2+\mathbf{p}^2+m_{0,\alpha}^2+io}\widetilde{\mathcal{V}}_{\alpha\beta}(t)\,\frac{1}{-p_0^2+\mathbf{p}^2+m_{0,\beta}^2+io}\widetilde{\mathcal{V}}_{\beta\alpha}(t)\right]\\ & +O(\widetilde{\mathcal{V}}^3)\end{aligned} \tag{B.25}$$

The three-dimensional reduction is obtained via Eq. (B.4) and Eq. (B.1). So we find

$$\widetilde{\Gamma}^{(1)\,\mathrm{div}} \;=\; \int\frac{d^3p}{(2\pi)^3}\left[\sum_\alpha\frac{-\widetilde{\mathcal{V}}_{\alpha\alpha}(t)}{4\omega_\alpha}-\frac{1}{2}\sum_{\alpha\beta}\frac{-\widetilde{\mathcal{V}}_{\alpha\beta}(t)\widetilde{\mathcal{V}}_{\beta\alpha}(t)}{4\omega_\alpha\omega_\beta(\omega_\alpha+\omega_\beta)}\right]. \tag{B.26}$$

The divergent parts of the fluctuation energy are, therefore,

$$E_{\mathrm{div}}^{(1)}=\int\frac{d^3p}{(2\pi)^3}\left[\sum_\alpha\frac{\widetilde{\mathcal{V}}_{\alpha\alpha}(t)}{4\omega_\alpha}-\sum_{\alpha\beta}\frac{\widetilde{\mathcal{V}}_{\alpha\beta}(t)\widetilde{\mathcal{V}}_{\beta\alpha}(t)}{8\omega_\alpha\omega_\beta(\omega_\alpha+\omega_\beta)}\right]. \tag{B.27}$$

As a cross check we may obtain the divergent terms in the fluctuation integrals Δ_{ij} which are given by

$$\frac{\Delta_{ij}^{(1)\,\mathrm{div}}}{2}=-\frac{\delta\widetilde{\Gamma}^{(1)\,\mathrm{div}}}{\delta\mathcal{M}_{ij}^2(t)}=-\frac{\delta\widetilde{\Gamma}^{(1)\,\mathrm{div}}}{\delta\mathcal{V}_{ij}(t)} \tag{B.28}$$

Using Eq. (B.23) we have

$$\frac{\delta\mathcal{V}_{\alpha\beta}(t)}{\delta\mathcal{V}_{ij}(t)}=O_{i\alpha}O_{j\beta} \tag{B.29}$$

and therefore

$$\Delta_{ij}^{(1)\,\mathrm{div}} \;=\; \int\frac{d^3p}{(2\pi)^3}\left[\sum_\alpha\frac{1}{2\omega_\alpha}O_{i\alpha}O_{j\alpha}-\sum_{\alpha\beta}\frac{O_{i\alpha}O_{j\beta}\widetilde{\mathcal{V}}_{\beta\alpha}(t)}{2\omega_\alpha\omega_\beta(\omega_\alpha+\omega_\beta)}\right]. \tag{B.30}$$

Bibliography

[1] D. W. Hogg *et al.*. *Cosmic homogeneity demonstrated with luminous red galaxies* (2004). astro-ph/0411197.

[2] M. Tegmark *et al.* (SDSS). *The 3D power spectrum of galaxies from the SDSS*. Astrophys. J., **606**, 702–740 (2004). astro-ph/0310725.

[3] J. A. Peacock. *Large-scale surveys and cosmic structure* (2003). astro-ph/0309240.

[4] http://magnum.anu.edu.au/~TDFgg/Public/Release/. Public website of the 2dF-GRS collaboration.

[5] C. L. Bennett *et al.*. *4-Year COBE DMR Cosmic Microwave Background Observations: Maps and Basic Results*. Astrophys. J., **464**, L1–L4 (1996). astro-ph/9601067.

[6] G. F. Smoot *et al.*. *Structure in the COBE DMR first year maps*. Astrophys. J., **396**, L1–L5 (1992).

[7] C. L. Bennett *et al.*. *First Year Wilkinson Microwave Anisotropy Probe (WMAP) Observations: Preliminary Maps and Basic Results*. Astrophys. J. Suppl., **148**, 1 (2003). astro-ph/0302207.

[8] D. N. Spergel *et al.* (WMAP). *First Year Wilkinson Microwave Anisotropy Probe (WMAP) Observations: Determination of Cosmological Parameters*. Astrophys. J. Suppl., **148**, 175 (2003). astro-ph/0302209.

[9] P. de Bernardis *et al.* (Boomerang). *A Flat Universe from High-Resolution Maps of the Cosmic Microwave Background Radiation*. Nature, **404**, 955–959 (2000). astro-ph/0004404.

[10] J. Kovac *et al.*. *Detection of polarization in the cosmic microwave background using DASI*. Nature, **420**, 772–787 (2002). astro-ph/0209478.

[11] W. Hu and S. Dodelson. *Cosmic Microwave Background Anisotropies*. Ann. Rev. Astron. Astrophys., **40**, 171 (2002). astro-ph/0110414.

[12] A. D. Linde. *Particle physics and inflationary cosmology* (Harwood (Contemporary concepts in physics, 5), Chur, Switzerland, 1990).

[13] E. W. Kolb and M. Turner. *The Early Universe* (Addison-Wesley, Redwood City, Calif., 1990).

[14] A. R. Liddle and D. H. Lyth. *Cosmological inflation and large-scale structure* (Cambridge Univ. Pr., Cambridge, UK, 2000).

[15] C. L. Bennett *et al.*. *First Year Wilkinson Microwave Anisotropy Probe (WMAP) Observations: Foreground Emission*. Astrophys. J. Suppl., **148**, 97 (2003). astro-ph/0302208.

[16] NASA. *Legacy Archive for Microwave Background Data Analysis (LAMBDA)*. http://lambda.gsfc.nasa.gov/.

[17] A. H. Guth. *The Inflationary Universe: A Possible Solution to the Horizon and Flatness Problems*. Phys. Rev., **D23**, 347–356 (1981).

[18] A. H. Guth and S. Y. Pi. *Fluctuations in the New Inflationary Universe*. Phys. Rev. Lett., **49**, 1110–1113 (1982).

[19] A. A. Starobinsky. *Dynamics of Phase Transitions in the New Inflationary Universe Scenario and Generation of Perturbations*. Phys. Lett., **B117**, 175–178 (1982).

[20] S. W. Hawking. *The Development of Irregularities in a Single Bubble Inflationary Universe*. Phys. Lett., **B115**, 295 (1982).

[21] J. M. Bardeen, P. J. Steinhardt, and M. S. Turner. *Spontanous Creation of Almost Scale-Free Density Perturbations in an Inflationary Universe*. Phys. Rev., **D28**, 679 (1983).

[22] L. F. Abbott and S. Y. Pi (Eds.). *Inflationary cosmology* (Singapore: World Scientific, Singapore, 1986).

[23] D. J. Fixsen *et al.*. *The Cosmic Microwave Background Spectrum from the Full COBE/FIRAS Data Set*. Astrophys. J., **473**, 576 (1996). astro-ph/9605054.

[24] http://www.rssd.esa.int/index.php?project=PLANCK. Public website of the PLANCK team.

[25] D. Barkats *et al.*. *First measurements of the polarization of the cosmic microwave background radiation at small angular scales from CAPMAP* (2004). astro-ph/0409380.

[26] http://www.astro.cf.ac.uk/groups/instrumentation/projects/quest/. (QUaD) Quest at DASI.

[27] *(BICEP) Background Imaging of Cosmic Extragalactic Polarization.* http://www.astro.caltech.edu/~lgg/bicep_front.htm.

[28] http://bolo.berkeley.edu/polarbear/index.html. (PolarBeaR) Polarization of Background Radiation.

[29] J. E. Ruhl *et al.*. *Improved measurement of the angular power spectrum of temperature anisotropy in the CMB from two new analyses of BOOMERANG observations.* Astrophys. J., **599**, 786–805 (2003). `astro-ph/0212229`.

[30] http://groups.physics.umn.edu/cosmology/maxipol/. MAXIPOL experiment.

[31] M. Colless *et al.*. *The 2dF Galaxy Redshift Survey: Final Data Release* (2003). `astro-ph/0306581`.

[32] S. Cole *et al.* (The 2dFGRS). *The 2dF Galaxy Redshift Survey: Power-spectrum analysis of the final dataset and cosmological implications* (2005). `astro-ph/0501174`.

[33] K. Abazajian *et al.*. *The Third Data Release of the Sloan Digital Sky Survey* (2004). `astro-ph/0410239`.

[34] V. F. Mukhanov, H. A. Feldman, and R. H. Brandenberger. *Theory of cosmological perturbations. Part 1. Classical perturbations. Part 2. Quantum theory of perturbations. Part 3. Extensions.* Phys. Rept., **215**, 203–333 (1992).

[35] R.E. Langer. Trans. Am. Math. Soc., **33**, 23 (1931).

[36] R.E. Langer. Trans. Am. Math. Soc., **34**, 447 (1932).

[37] R.E. Langer. Trans. Am. Math. Soc., **36**, 90 (1934).

[38] R.E. Langer. Trans. Am. Math. Soc., **37**, 397 (1935).

[39] R.E. Langer. Trans. Am. Math. Soc., **67**, 461 (1949).

[40] R.E. Langer. Phys. Rev., **51**, 669 (1937).

[41] F.W.J. Olver. Philos. Trans. R. Soc. London A, **247**, 307 (1954).

[42] F.W.J. Olver. *Asymptotics and Special Functions* (AKP Classics, Wellesley, MA, 1997).

[43] S. Habib, K. Heitmann, G. Jungman, and C. Molina-Paris. *The inflationary perturbation spectrum.* Phys. Rev. Lett., **89**, 281301 (2002). `astro-ph/0208443`.

[44] S. Habib, A. Heinen, K. Heitmann, G. Jungman, and C. Molina-Paris. *Characterizing inflationary perturbations: The uniform approximation.* Phys. Rev., **D70**, 083507 (2004). `astro-ph/0406134`.

[45] S. Habib, A. Heinen, K. Heitmann, and G. Jungman. *Inflationary Perturbations and Precision Cosmology*. Phys. Rev., **D71**, 043518 (2005). astro-ph/0501130.

[46] J.-O. Gong and E. D. Stewart. *The density perturbation power spectrum to second-order corrections in the slow-roll expansion*. Phys. Lett., **B510**, 1–9 (2001). astro-ph/0101225.

[47] U. Seljak and M. Zaldarriaga. *A Line of Sight Approach to Cosmic Microwave Background Anisotropies*. Astrophys. J., **469**, 437–444 (1996). astro-ph/9603033.

[48] http://www.cmbfast.org. Official website for the CMBFAST code, maintained by U. Seljak and M. Zaldarriaga.

[49] A. Lewis, A. Challinor, and A. Lasenby. *Efficient Computation of CMB anisotropies in closed FRW models*. Astrophys. J., **538**, 473–476 (2000). astro-ph/9911177.

[50] http://www.camb.info. Official website for the CAMB code, maintained by A. Lewis.

[51] U. Seljak, N. Sugiyama, M. J. White, and M. Zaldarriaga. *A comparison of cosmological Boltzmann codes: are we ready for high precision cosmology?* Phys. Rev., **D68**, 083507 (2003). astro-ph/0306052.

[52] N. Bartolo, E. Komatsu, S. Matarrese, and A. Riotto. *Non-Gaussianity from inflation: Theory and observations*. Phys. Rept., **402**, 103–266 (2004). astro-ph/0406398.

[53] J. A. Adams, B. Cresswell, and R. Easther. *Inflationary perturbations from a potential with a step*. Phys. Rev., **D64**, 123514 (2001). astro-ph/0102236.

[54] A. Albrecht, P. J. Steinhardt, M. S. Turner, and F. Wilczek. *Reheating an Inflationary Universe*. Phys. Rev. Lett., **48**, 1437 (1982).

[55] J. H. Traschen and R. H. Brandenberger. *Particle Production during Out-Of-Equilibrium Phase Transitions*. Phys. Rev., **D42**, 2491–2504 (1990).

[56] H. V. Peiris *et al.*. *First year Wilkinson Microwave Anisotropy Probe (WMAP) observations: Implications for inflation*. Astrophys. J. Suppl., **148**, 213 (2003). astro-ph/0302225.

[57] L. Kofman, A. D. Linde, and A. A. Starobinsky. *Reheating after inflation*. Phys. Rev. Lett., **73**, 3195–3198 (1994). hep-th/9405187.

[58] Y. Shtanov, J. H. Traschen, and R. H. Brandenberger. *Universe reheating after inflation*. Phys. Rev., **D51**, 5438–5455 (1995). hep-ph/9407247.

[59] D. Boyanovsky, H. J. de Vega, R. Holman, D. S. Lee, and A. Singh. *Dissipation via particle production in scalar field theories*. Phys. Rev., **D51**, 4419–4444 (1995). hep-ph/9408214.

[60] D. Boyanovsky, H. J. de Vega, R. Holman, and J. F. J. Salgado. *Analytic and numerical study of preheating dynamics.* Phys. Rev., **D54**, 7570–7598 (1996). hep-ph/9608205.

[61] P. B. Greene, L. Kofman, A. D. Linde, and A. A. Starobinsky. *Structure of resonance in preheating after inflation.* Phys. Rev., **D56**, 6175–6192 (1997). hep-ph/9705347.

[62] L. Kofman, A. D. Linde, and A. A. Starobinsky. *Towards the theory of reheating after inflation.* Phys. Rev., **D56**, 3258–3295 (1997). hep-ph/9704452.

[63] G. N. Felder *et al.*. *Dynamics of symmetry breaking and tachyonic preheating.* Phys. Rev. Lett., **87**, 011601 (2001). hep-ph/0012142.

[64] E. W. Kolb, A. D. Linde, and A. Riotto. *GUT baryogenesis after preheating.* Phys. Rev. Lett., **77**, 4290–4293 (1996). hep-ph/9606260.

[65] M. Kawasaki and T. Moroi. *Gravitino production in the inflationary universe and the effects on big bang nucleosynthesis.* Prog. Theor. Phys., **93**, 879–900 (1995). hep-ph/9403364.

[66] P. Ivanov. *On generation of metric perturbations during preheating.* Phys. Rev., **D61**, 023505 (2000). astro-ph/9906415.

[67] A. R. Liddle, D. H. Lyth, K. A. Malik, and D. Wands. *Super-horizon perturbations and preheating.* Phys. Rev., **D61**, 103509 (2000). hep-ph/9912473.

[68] B. A. Bassett and F. Viniegra. *Massless metric preheating.* Phys. Rev., **D62**, 043507 (2000). hep-ph/9909353.

[69] D. Wands, K. A. Malik, D. H. Lyth, and A. R. Liddle. *A new approach to the evolution of cosmological perturbations on large scales.* Phys. Rev., **D62**, 043527 (2000). astro-ph/0003278.

[70] F. Finelli and R. H. Brandenberger. *Parametric amplification of metric fluctuations during reheating in two field models.* Phys. Rev., **D62**, 083502 (2000). hep-ph/0003172.

[71] K. Enqvist, A. Jokinen, A. Mazumdar, T. Multamaki, and A. Vaihkonen. *Non-Gaussianity from Preheating* (2004). astro-ph/0411394.

[72] A. D. Linde. *Chaotic Inflation.* Phys. Lett., **B129**, 177–181 (1983).

[73] A. D. Linde. *Hybrid inflation.* Phys. Rev., **D49**, 748–754 (1994). astro-ph/9307002.

[74] J. Baacke and A. Heinen. *Out-of-equilibrium evolution of quantum fields in the hybrid model with quantum back reaction.* Phys. Rev., **D69**, 083523 (2004). hep-ph/0311282.

[75] S.-Y. Pi and M. Samiullah. *Renormalizability of the time dependent variational equations in quantum field theory.* Phys. Rev., **D36**, 3128 (1987).

[76] J. Baacke, K. Heitmann, and C. Patzold. *Nonequilibrium dynamics: A renormalized computation scheme.* Phys. Rev., **D55**, 2320–2330 (1997). `hep-th/9608006`.

[77] J. Garcia-Bellido and A. D. Linde. *Preheating in hybrid inflation.* Phys. Rev., **D57**, 6075–6088 (1998). `hep-ph/9711360`.

[78] M. Bastero-Gil, S. F. King, and J. Sanderson. *Preheating in supersymmetric hybrid inflation.* Phys. Rev., **D60**, 103517 (1999). `hep-ph/9904315`.

[79] E. J. Copeland, S. Pascoli, and A. Rajantie. *Dynamics of tachyonic preheating after hybrid inflation.* Phys. Rev., **D65**, 103517 (2002). `hep-ph/0202031`.

[80] J. Garcia-Bellido, M. Garcia Perez, and A. Gonzalez-Arroyo. *Symmetry breaking and false vacuum decay after hybrid inflation.* Phys. Rev., **D67**, 103501 (2003). `hep-ph/0208228`.

[81] D. Boyanovsky, D. Cormier, H. J. de Vega, and R. Holman. *Out of equilibrium dynamics of an inflationary phase transition.* Phys. Rev., **D55**, 3373–3388 (1997). `hep-ph/9610396`.

[82] M. J. Bowick and A. Momen. *Domain formation in finite-time quenches.* Phys. Rev., **D58**, 085014 (1998). `hep-ph/9803284`.

[83] G. N. Felder, L. Kofman, and A. D. Linde. *Tachyonic instability and dynamics of spontaneous symmetry breaking.* Phys. Rev., **D64**, 123517 (2001). `hep-th/0106179`.

[84] T. Asaka, W. Buchmuller, and L. Covi. *False vacuum decay after inflation.* Phys. Lett., **B510**, 271–276 (2001). `hep-ph/0104037`.

[85] H. Verschelde. *Summation and renormalization of bubble graphs to all orders.* Phys. Lett., **B497**, 165–171 (2001). `hep-th/0009123`.

[86] D. Cormier, K. Heitmann, and A. Mazumdar. *Dynamics of coupled bosonic systems with applications to preheating.* Phys. Rev., **D65**, 083521 (2002). `hep-ph/0105236`.

[87] A. H. Guth and S.-Y. Pi. *The Quantum Mechanics of the Scalar Field in the New Inflationary Universe.* Phys. Rev., **D32**, 1899–1920 (1985).

[88] D. Polarski and A. A. Starobinsky. *Semiclassicality and decoherence of cosmological perturbations.* Class. Quant. Grav., **13**, 377–392 (1996). `gr-qc/9504030`.

[89] F. Cooper, Y. Kluger, E. Mottola, and J. P. Paz. *Nonequilibrium quantum dynamics of disoriented chiral condensates.* Phys. Rev., **D51**, 2377–2397 (1995). `hep-ph/9404357`.

[90] D. Boyanovsky, H. J. de Vega, R. Holman, and J. Salgado. *Non-equilibrium Bose-Einstein condensates, dynamical scaling and symmetric evolution in large N Φ^4 theory.* Phys. Rev., **D59**, 125009 (1999). `hep-ph/9811273`.

[91] J. Baacke and A. Heinen. *Nonequilibrium evolution of Φ^4 theory in 1+1 dimensions in the 2PPI formalism.* Phys. Rev., **D67**, 105020 (2003). `hep-ph/0212312`.

[92] J. Baacke and A. Heinen. *Quantum dynamics of Φ^4 field theory beyond leading order in 1+1 dimensions.* Phys. Rev., **D68**, 127702 (2003). `hep-ph/0305220`.

[93] J. Baacke, A. Heinen, and S. Michalski. *The scalar O(N) model beyond the hartree approximation, in and out of equilibrium.* In *Proceedings of th XII. International Conference on Selected Problems in Modern Physics, Dubna, Russia, 8-11 Jun 2003* (2003).

[94] H. Kodama and M. Sasaki. *Cosmological perturbation theory.* Prog. Theor. Phys. Suppl., **78**, 1–166 (1984).

[95] K. A. Olive. *Inflation.* Phys. Rept., **190**, 307–403 (1990).

[96] P. J. E. Peebles and B. Ratra. *The cosmological constant and dark energy.* Rev. Mod. Phys., **75**, 559–606 (2003). `astro-ph/0207347`.

[97] A. H. Guth. *Inflation* (2004). Published in Pasadena 2002, 'Measuring and modeling the universe' 31-52, `astro-ph/0404546`.

[98] A. D. Linde. *Prospects of inflation* (2004). Extended version of the talk at the Nobel Symposium 'Cosmology and String Theory,' August 2003, `hep-th/0402051`.

[99] E. H. Hubble. Pub. Nat. Acad. Sci, **15**, 168 (1929).

[100] A. H. Guth. *Inflation and eternal inflation.* Phys. Rept., **333**, 555–574 (2000). `astro-ph/0002156`.

[101] R. J. Adler and J. M. Overduin. *The nearly flat universe* (2005). `gr-qc/0501061`.

[102] J. M. Bardeen. *Gauge Invariant Cosmological Perturbations.* Phys. Rev., **D22**, 1882–1905 (1980).

[103] D. H. Lyth. *Large scale energy density perturbations and inflation.* Phys. Rev., **D31**, 1792–1798 (1985).

[104] J. Martin and D. J. Schwarz. *The influence of cosmological transitions on the evolution of density perturbations.* Phys. Rev., **D57**, 3302–3316 (1998). `gr-qc/9704049`.

[105] D. H. Lyth and A. Riotto. *Particle physics models of inflation and the cosmological density perturbation.* Phys. Rept., **314**, 1–146 (1999). `hep-ph/9807278`.

[106] F. Lucchin and S. Matarrese. *Power law inflation.* Phys. Rev., **D32**, 1316 (1985).

[107] A. Albrecht and P. J. Steinhardt. *Cosmology for Grand Unified Theories with radiatively induced symmetry breaking.* Phys. Rev. Lett., **48**, 1220–1223 (1982).

[108] A. D. Linde. *A new inflationary universe scenario: A possible solution to the horizon, flatness, homogeneity, isotropy and primordial monopole problems.* Phys. Lett., **B108**, 389–393 (1982).

[109] K. Freese, J. A. Frieman, and A. V. Olinto. *Natural inflation with pseudo - Nambu-Goldstone bosons.* Phys. Rev. Lett., **65**, 3233–3236 (1990).

[110] F. C. Adams, J. R. Bond, K. Freese, J. A. Frieman, and A. V. Olinto. *Natural inflation: Particle physics models, power law spectra for large scale structure, and constraints from COBE.* Phys. Rev., **D47**, 426–455 (1993). `hep-ph/9207245`.

[111] S. M. Leach and A. R. Liddle. *Constraining slow-roll inflation with WMAP and 2dF.* Phys. Rev., **D68**, 123508 (2003). `astro-ph/0306305`.

[112] M. Tegmark. *What does inflation really predict?* (2004). `astro-ph/0410281`.

[113] A. D. Linde. *Eternal extended inflation and graceful exit from old inflation without Jordan-Brans-Dicke.* Phys. Lett., **B249**, 18–26 (1990).

[114] A. D. Dolgov and D. P. Kirilova. *Production of particles by a variable scalar field.* Sov. J. Nucl. Phys., **51**, 172–177 (1990).

[115] D. Boyanovsky, M. D'Attanasio, H. J. de Vega, R. Holman, and D. S. Lee. *Reheating and thermalization: Linear versus nonlinear relaxation.* Phys. Rev., **D52**, 6805–6827 (1995). `hep-ph/9507414`.

[116] E. J. Copeland, A. R. Liddle, D. H. Lyth, E. D. Stewart, and D. Wands. *False vacuum inflation with Einstein gravity.* Phys. Rev., **D49**, 6410–6433 (1994). `astro-ph/9401011`.

[117] W. Buchmuller, L. Covi, and D. Delepine. *Inflation and supersymmetry breaking.* Phys. Lett., **B491**, 183–189 (2000). `hep-ph/0006168`.

[118] R. Micha and M. G. Schmidt. *Bosonic preheating in left-right-symmetric SUSY GUTs.* Eur. Phys. J., **C14**, 547–552 (2000). `hep-ph/9908228`.

[119] L. F. Abbott and Mark B. Wise. *Constraints on generalized inflationary cosmologies.* Nucl. Phys., **B244**, 541–548 (1984).

[120] B. Ratra. *Inflation in an exponential potential scalar field model.* Phys. Rev., **D45**, 1913–1952 (1992).

[121] L.-M. Wang, V. F. Mukhanov, and P. J. Steinhardt. *On the problem of predicting inflationary perturbations.* Phys. Lett., **B414**, 18–27 (1997). astro-ph/9709032.

[122] G. R. Dvali and S. H. Henry Tye. *Brane inflation.* Phys. Lett., **B450**, 72–82 (1999). hep-ph/9812483.

[123] R. Maartens, D. Wands, B. A. Bassett, and I. Heard. *Chaotic inflation on the brane.* Phys. Rev., **D62**, 041301 (2000). hep-ph/9912464.

[124] B. Feng and X. Zhang. *Double inflation and the low CMB quadrupole.* Phys. Lett., **B570**, 145–150 (2003). astro-ph/0305020.

[125] G. Efstathiou. *Is the low CMB quadrupole a signature of spatial curvature?* Mon. Not. Roy. Astron. Soc., **343**, L95 (2003). astro-ph/0303127.

[126] J. Martin and C. Ringeval. *Superimposed Oscillations in the WMAP Data?* Phys. Rev., **D69**, 083515 (2004). astro-ph/0310382.

[127] P. Hunt and S. Sarkar. *Multiple inflation and the WMAP 'glitches'.* Phys. Rev., **D70**, 103518 (2004). astro-ph/0408138.

[128] D. Parkinson, S. Tsujikawa, B. A. Bassett, and L. Amendola. *Testing for double inflation with WMAP.* Phys. Rev., **D71**, 063524 (2005). astro-ph/0409071.

[129] D. J. Schwarz, G. D. Starkman, D. Huterer, and C. J. Copi. *Is the low-l microwave background cosmic?* Phys. Rev. Lett., **93**, 221301 (2004). astro-ph/0403353.

[130] E. D. Stewart and D. H. Lyth. *A More accurate analytic calculation of the spectrum of cosmological perturbations produced during inflation.* Phys. Lett., **B302**, 171–175 (1993). gr-qc/9302019.

[131] J. E. Lidsey *et al.*. *Reconstructing the inflaton potential: An overview.* Rev. Mod. Phys., **69**, 373–410 (1997). astro-ph/9508078.

[132] J. Martin and D. J. Schwarz. *The precision of slow-roll predictions for the CMBR anisotropies.* Phys. Rev., **D62**, 103520 (2000). astro-ph/9911225.

[133] E. D. Stewart. *The spectrum of density perturbations produced during inflation to leading order in a general slow-roll approximation.* Phys. Rev., **D65**, 103508 (2002). astro-ph/0110322.

[134] J. Choe, J.-O. Gong, and E. D. Stewart. *Second order general slow-roll power spectrum.* JCAP, **0407**, 012 (2004). hep-ph/0405155.

[135] J.-O. Gong. *General slow-roll spectrum for gravitational waves.* Class. Quant. Grav., **21**, 5555–5562 (2004). gr-qc/0408039.

[136] D. J. Schwarz, C. A. Terrero-Escalante, and A. A. Garcia. *Higher order corrections to primordial spectra from cosmological inflation.* Phys. Lett., **B517**, 243–249 (2001). astro-ph/0106020.

[137] D. J. Schwarz and C. A. Terrero-Escalante. *Primordial fluctuations and cosmological inflation after WMAP 1.0.* JCAP, **0408**, 003 (2004). hep-ph/0403129.

[138] A. R. Liddle and D. H. Lyth. *COBE, gravitational waves, inflation and extended inflation.* Phys. Lett., **B291**, 391–398 (1992). astro-ph/9208007.

[139] A. R. Liddle, P. Parsons, and J. D. Barrow. *Formalizing the slow roll approximation in inflation.* Phys. Rev., **D50**, 7222–7232 (1994). astro-ph/9408015.

[140] G. Green. Trans. Cambridge Phil. Soc., **6**, 457 (1837).

[141] J. Liouville. J. Math. Pure. Appl., **2**, 16 (1837).

[142] J. Martin and D. J. Schwarz. *WKB approximation for inflationary cosmological perturbations.* Phys. Rev., **D67**, 083512 (2003). astro-ph/0210090.

[143] R. Casadio, F. Finelli, M. Luzzi, and G. Venturi. *Improved WKB analysis of cosmological perturbations.* Phys. Rev., **D71**, 043517 (2005). gr-qc/0410092.

[144] H. Jeffreys. Proc. London Math. Soc., **23**, 428 (1924).

[145] M. Abramowitz and I. A. Stegun. *Handbook of Mathematical Functions with Formulas, Graphs, and Mathematical Tables* (Dover, New York, 1965).

[146] D. H. Lyth and E. D. Stewart. *The Curvature perturbation in power law (e.g. extended) inflation.* Phys. Lett., **B274**, 168–172 (1992).

[147] N. M. Temme. *Special functions, An introduction to the classical functions of mathematical physics* (John Wiley & Sons, New York, 1996).

[148] S. Zhang and J. Jin. *Computation of special functions* (Wiley, New York, 1996).

[149] S. Habib, K. Heitmann, and G. Jungman. *Inverse-Scattering Theory and the Density Perturbations from Inflation.* Phys. Rev. Lett., **94**, 061303 (2005). astro-ph/0409599.

[150] A. G. Riess *et al.* (Supernova Search Team). *Type Ia Supernova Discoveries at z¿1 From the Hubble Space Telescope: Evidence for Past Deceleration and Constraints on Dark Energy Evolution.* Astrophys. J., **607**, 665–687 (2004). astro-ph/0402512.

[151] E. Barausse, S. Matarrese, and A. Riotto. *The Effect of Inhomogeneities on the Luminosity Distance- Redshift Relation: is Dark Energy Necessary in a Perturbed Universe?* (2005). astro-ph/0501152.

[152] E. W. Kolb, S. Matarrese, A. Notari, and A. Riotto. *Primordial inflation explains why the universe is accelerating today* (2005). `hep-th/0503117`.

[153] C. M. Hirata and U. Seljak. *Can superhorizon cosmological perturbations explain the acceleration of the universe?* (2005). `astro-ph/0503582`.

[154] S. Rasanen. *Backreaction and spatial curvature in a dust universe* (2005). `astro-ph/0504005`.

[155] D. K. Hong, V. A. Miransky, I. A. Shovkovy, and L. C. R. Wijewardhana. *Schwinger-Dyson approach to color superconductivity in dense QCD.* Phys. Rev., **D61**, 056001 (2000). `hep-ph/9906478`.

[156] G. Baym. *Selfconsistent approximation in many body systems.* Phys. Rev., **127**, 1391–1401 (1962).

[157] H. van Hees and J. Knoll. *Renormalization in self-consistent approximations schemes at finite temperature. I: Theory.* Phys. Rev., **D65**, 025010 (2002). `hep-ph/0107200`.

[158] H. van Hees and J. Knoll. *Renormalization of self-consistent approximation schemes. II: Applications to the sunset diagram.* Phys. Rev., **D65**, 105005 (2002). `hep-ph/0111193`.

[159] H. van Hees and J. Knoll. *Renormalization in self-consistent approximation schemes at finite temperature. III: Global symmetries.* Phys. Rev., **D66**, 025028 (2002). `hep-ph/0203008`.

[160] J.-P. Blaizot, E. Iancu, and U. Reinosa. *Renormalizability of Phi-derivable approximations in scalar Φ^4 theory.* Phys. Lett., **B568**, 160–166 (2003). `hep-ph/0301201`.

[161] J.-P. Blaizot, E. Iancu, and U. Reinosa. *Renormalization of phi-derivable approximations in scalar field theories.* Nucl. Phys., **A736**, 149–200 (2004). `hep-ph/0312085`.

[162] D. Boyanovsky, H. J. de Vega, R. Holman, and M. Simionato. *Dynamical renormalization group resummation of finite temperature infrared divergences.* Phys. Rev., **D60**, 065003 (1999). `hep-ph/9809346`.

[163] D. Boyanovsky, H. J. de Vega, and S. Y. Wang. *Dynamical renormalization group approach to quantum kinetics in scalar and gauge theories.* Phys. Rev., **D61**, 065006 (2000). `hep-ph/9909369`.

[164] J. S. Schwinger. *Brownian motion of a quantum oscillator.* J. Math. Phys., **2**, 407–432 (1961).

[165] L. V. Keldysh. *Diagram technique for nonequilibrium processes.* Zh. Eksp. Teor. Fiz., **47**, 1515–1527 (1964).

[166] R. D. Jordan. *Effective field equations for expectation values.* Phys. Rev., **D33**, 444–454 (1986).

[167] E. Calzetta and B. L. Hu. *Nonequilibrium quantum fields: closed time path effective action, Wigner function and Boltzmann equation.* Phys. Rev., **D37**, 2878 (1988).

[168] K.-c. Chou, Z.-b. Su, B.-l. Hao, and L. Yu. *Equilibrium and nonequilibrium formalisms made unified.* Phys. Rept., **118**, 1 (1985).

[169] F. Cooper, S.-Y. Pi, and P. N. Stancioff. *Quantum dynamics in a time dependent variational approximation.* Phys. Rev., **D34**, 3831 (1986).

[170] O. J. P. Eboli, R. Jackiw, and S.-Y. Pi. *Quantum fields out of thermal equilibrium.* Phys. Rev., **D37**, 3557 (1988).

[171] D. Boyanovsky, D.-S. Lee, and A. Singh. *Phase transitions out-of-equilibrium: Domain formation and growth.* Phys. Rev., **D48**, 800–815 (1993). `hep-th/9212083`.

[172] D. Boyanovsky, C. Destri, H. J. de Vega, R. Holman, and J. Salgado. *Asymptotic dynamics in scalar field theory: Anomalous relaxation.* Phys. Rev., **D57**, 7388–7415 (1998). `hep-ph/9711384`.

[173] D. Boyanovsky *et al.*. *Scalar field dynamics in Friedman Robertson Walker spacetimes.* Phys. Rev., **D56**, 1939–1957 (1997). `hep-ph/9703327`.

[174] F. Cooper *et al.*. *Nonequilibrium quantum fields in the large N expansion.* Phys. Rev., **D50**, 2848–2869 (1994). `hep-ph/9405352`.

[175] F. Cooper, S. Habib, Y. Kluger, and E. Mottola. *Nonequilibrium dynamics of symmetry breaking in lambda Φ^4 field theory.* Phys. Rev., **D55**, 6471–6503 (1997). `hep-ph/9610345`.

[176] J. Baacke, K. Heitmann, and C. Patzold. *Nonequilibrium dynamics of fermions in a spatially homogeneous scalar background field.* Phys. Rev., **D58**, 125013 (1998). `hep-ph/9806205`.

[177] J. Baacke and K. Heitmann. *Nonequilibrium evolution and symmetry structure of the large-N Φ^4 model at finite temperature.* Phys. Rev., **D62**, 105022 (2000). `hep-ph/0003317`.

[178] J. M. Luttinger and J. C. Ward. *Ground state energy of a many fermion system. 2.* Phys. Rev., **118**, 1417–1427 (1960).

[179] C. de Dominicis and P. Martin. J. Math. Phys., **5**, 14 (1964).

[180] J. M. Cornwall, R. Jackiw, and E. Tomboulis. *Effective action for composite operators.* Phys. Rev., **D10**, 2428–2445 (1974).

[181] J. Berges and J. Cox. *Thermalization of quantum fields from time-reversal invariant evolution equations.* Phys. Lett., **B517**, 369–374 (2001). hep-ph/0006160.

[182] J. Berges. *Controlled nonperturbative dynamics of quantum fields out of equilibrium.* Nucl. Phys., **A699**, 847–886 (2002). hep-ph/0105311.

[183] J. Berges and J. Serreau. *Parametric resonance in quantum field theory.* Phys. Rev. Lett., **91**, 111601 (2003). hep-ph/0208070.

[184] G. Aarts, D. Ahrensmeier, R. Baier, J. Berges, and J. Serreau. *Far-from-equilibrium dynamics with broken symmetries from the 2PI-1/N expansion.* Phys. Rev., **D66**, 045008 (2002). hep-ph/0201308.

[185] F. Cooper, J. F. Dawson, and B. Mihaila. *Quantum dynamics of phase transitions in broken symmetry lambda ϕ^4 field theory.* Phys. Rev., **D67**, 056003 (2003). hep-ph/0209051.

[186] A. Arrizabalaga, J. Smit, and A. Tranberg. *Tachyonic preheating using 2PI - 1/N dynamics and the classical approximation.* JHEP, **10**, 017 (2004). hep-ph/0409177.

[187] H. Verschelde and M. Coppens. *A Variational approach to quantum field theory.* Phys. Lett., **B287**, 133–137 (1992).

[188] M. Coppens and H. Verschelde. *General analysis of n loop corrections in the 2 P PI variational approach to lambda Φ^4.* Z. Phys., **C58**, 319–323 (1993).

[189] J. Berges, S. Borsanyi, and J. Serreau. *Thermalization of fermionic quantum fields.* Nucl. Phys., **B660**, 51–80 (2003). hep-ph/0212404.

[190] M. Salle, J. Smit, and J. C. Vink. *Thermalization in a Hartree ensemble approximation to quantum field dynamics.* Phys. Rev., **D64**, 025016 (2001). hep-ph/0012346.

[191] J. Baacke, K. Heitmann, and C. Patzold. *Nonequilibrium dynamics: Preheating in the SU(2) Higgs model.* Phys. Rev., **D55**, 7815–7825 (1997). hep-ph/9612264.

[192] J. Baacke and S. Michalski. *Nonequilibrium evolution in scalar O(N) models with spontaneous symmetry breaking.* Phys. Rev., **D65**, 065019 (2002). hep-ph/0109137.

[193] H. Verschelde and J. De Pessemier. *Study of the O(N) linear sigma model at finite temperature using the 2PPI expansion.* Eur. Phys. J., **C22**, 771–779 (2002). hep-th/0009241.

[194] G. Smet, T. Vanzielighem, K. Van Acoleyen, and H. Verschelde. *A 2 loop 2PPI analysis of lambda Φ^4 at finite temperature.* Phys. Rev., **D65**, 045015 (2002). hep-th/0108163.

[195] H. P. Nilles, M. Peloso, and L. Sorbo. *Coupled fields in external background with application to nonthermal production of gravitinos.* JHEP, **04**, 004 (2001). hep-th/0103202.

[196] J. Baacke, D. Boyanovsky, and H. J. de Vega. *Initial time singularities in non-equilibrium evolution of condensates and their resolution in the linearized approximation.* Phys. Rev., **D63**, 045023 (2001). hep-ph/9907337.

[197] W. H. Kinney, E. W. Kolb, A. Melchiorri, and A. Riotto. *WMAPping inflationary physics.* Phys. Rev., **D69**, 103516 (2004). hep-ph/0305130.

[198] V. Barger, H.-S. Lee, and D. Marfatia. *WMAP and inflation.* Phys. Lett., **B565**, 33–41 (2003). hep-ph/0302150.

[199] J. Garcia-Bellido, D. Y. Grigoriev, A. Kusenko, and M. E. Shaposhnikov. *Non-equilibrium electroweak baryogenesis from preheating after inflation.* Phys. Rev., **D60**, 123504 (1999). hep-ph/9902449.

[200] L. M. Krauss and M. Trodden. *Baryogenesis below the electroweak scale.* Phys. Rev. Lett., **83**, 1502–1505 (1999). hep-ph/9902420.

[201] E. J. Copeland, D. Lyth, A. Rajantie, and M. Trodden. *Hybrid inflation and baryogenesis at the TeV scale.* Phys. Rev., **D64**, 043506 (2001). hep-ph/0103231.

[202] R. Easther and K.-i. Maeda. *Chaotic dynamics and two-field inflation.* Class. Quant. Grav., **16**, 1637–1652 (1999). gr-qc/9711035.

[203] Y. Jin and S. Tsujikawa. *Chaotic dynamics in preheating after inflation* (2004). hep-ph/0411164.

[204] S. Yu. Khlebnikov and I. I. Tkachev. *Classical decay of inflaton.* Phys. Rev. Lett., **77**, 219–222 (1996). hep-ph/9603378.

[205] J. Baacke and C. Patzold. *Out-of-equilibrium evolution of scalar fields in FRW cosmology: Renormalization and numerical simulations.* Phys. Rev., **D61**, 024016 (2000). hep-ph/9906417.

[206] K. Heitmann. *Gauge fields out-of-equilibrium: A gauge invariant formulation and the Coulomb gauge.* Phys. Rev., **D64**, 045003 (2001). hep-ph/0101281.

[207] A. Arrizabalaga and J. Smit. *Gauge-fixing dependence of Phi-derivable approximations.* Phys. Rev., **D66**, 065014 (2002). hep-ph/0207044.

[208] E. Mottola. *Gauge invariance in 2PI effective actions.* In *Proceedings of the 5th Workshop on Strong and Electroweak Matter (SEWM 2002)* (World Scientific Publ. Co, 2003). hep-ph/0304279.

[209] E. A. Calzetta. *The 2-particle irreducible effective action in gauge theories.* Int. J. Theor. Phys., **43**, 767–799 (2004). `hep-ph/0402196`.

[210] J. Baacke, K. Heitmann, and C. Patzold. *Renormalization of nonequilibrium dynamics in FRW cosmology.* Phys. Rev., **D56**, 6556–6565 (1997). `hep-ph/9706274`.

[211] S. Khlebnikov, L. Kofman, A. D. Linde, and I. Tkachev. *First-order nonthermal phase transition after preheating.* Phys. Rev. Lett., **81**, 2012–2015 (1998). `hep-ph/9804425`.

[212] L. A. Kofman and A. D. Linde. *Generation of density perturbations in the inflationary cosmology.* Nucl. Phys., **B282**, 555 (1987).

[213] M. F. Parry and A. T. Sornborger. *Domain wall production during inflationary reheating.* Phys. Rev., **D60**, 103504 (1999). `hep-ph/9805211`.

[214] M. Broadhead and J. McDonald. *Simulations of the end of supersymmetric hybrid inflation and non-topological soliton formation* (2005). `hep-ph/0503081`.

[215] S. Borsanyi, A. Patkos, and D. Sexty. *Goldstone excitations from spinodal instability.* Phys. Rev., **D66**, 025014 (2002). `hep-ph/0203133`.

[216] S. Borsanyi, A. Patkos, and D. Sexty. *Non-equilibrium Goldstone phenomenon in tachyonic preheating.* Phys. Rev., **D68**, 063512 (2003). `hep-ph/0303147`.

[217] C. M. Bender and S. A. Orszag. *Advanced Mathematical Methods for Scientists and Engineers* (McGraw-Hill, New York, NY, 1978).

[218] L. Verde *et al.*. *First Year Wilkinson Microwave Anisotropy Probe (WMAP) Observations: Parameter Estimation Methodology.* Astrophys. J. Suppl., **148**, 195 (2003). `astro-ph/0302218`.

Acknowledgments

It is a great pleasure to thank the people who have contributed to the realization of this work.

At first, I am deeply indebted to Prof. Dr. Jürgen Baacke for his continuous support over the last years. He has been an exquisite advisor and I have learned a lot from him. I never took it for granted that he left me the freedom to follow my own path while he was always helpful when help was needed. The collaboration with him during our research and teaching activities has always been very efficient. Life is too short to drink bad coffee. Drinking fine teas has improved my performance.

In the second half of my PhD I had the chance to start collaborating with people from Los Alamos National Laboratory (LANL). I am grateful to the people who helped initiating this, in particular Prof. Dr. Jürgen Baacke, Dr. Salman Habib, and Dr. Katrin Heitmann. The collaboration with Dr. Salman Habib, Dr. Katrin Heitmann, Dr. Gerard Jungman, and Dr. Carmen Molina-Paris has been extremely inspiring and highly productive. During my stay at LANL (and also beyond it) Salman and Katrin have provided a lot of help and advice. Both stays at LANL have been very intense. I have to thank them for inviting me for lunch and dinner so many times. I deeply acknowledge their confidence in me, no matter whether it was physics, numerics, programming, climbing, running or driving. Katrin even gave me her Subaru® for the entire second stay. We also have to thank Jerry for being so pedantic with respect to the content of our papers. While sometimes exhausting, his criticism has improved the presentation. Dr. Matthew Martin has been a very kind office mate. I also thank Dr. Kevork Abazajian for leaving me his office space equipped with two 20" Apple® wide-screen plasma displays.

Many discussions have improved my understanding of physics. In particular I thank Prof. Dr. Dominik Schwarz, who has also been so kind to take the part of the second referee, Dr. Alejandro Arrizabalaga, Dr. Jürgen Berges, Dr. Szabolcz Borsanyi, Dr. Fred Cooper, Paul Hunt, Dr. Andreas Ipp, Dr. Bogdan Mihaila, Prof. Dr. András Patkós, Prof. Dr. Jan Smit, Dr. Urko Reinosa, Dr. Paul Romatschke, Dr. Mischa Sallé, Dr. Julien Serreau, Prof. Dr. Hector de Vega, Prof. Dr. Henri Verschelde, Harmen Warringa, and certainly many more.

A warm thanks to all present and former members of T III and T IV for a friendly atmosphere. I acknowledge Jens Noritzsch for being an excellent master of the computer universe. Although there is no official record it is not unlikely that I took a fairly large amount of computer time. Thanks to all people for being patient while my programs were

running. I thank Stefan Michalski for computer administration and for being a nice office mate, providing continuous mineral water supply and drinking tea with me. We had many interesting discussion on physics and non-physics topics in the last four years. Thanks! Our secretary Susanne Laurent is acknowledged for administrative help.

In 2003, 2004 and 2005 I had the chance to give exercises for the newly invented course "Computational Physics". As a side effect of this interesting and instructive course I have benefitted from using an IBM® Think-pad® which has been a typesetting and programming slave at day, night, work, home, or airports.

The quality of this thesis improved by proof-reading of several people, most notably Dr. Katrin Heitmann, Dr. Salman Habib, and Christoph Schuck. I thank Katrin for very valuable suggestions and many comments at various stages of the completion of this thesis.

I acknowledge the *Deutsche Forschungsgemeinschaft* (DFG) for providing financial support in the first five month of my PhD through grant Ba703/6-1 and the University of Dortmund for the remainder of my PhD. I thank the *Deutscher Akademischer Austauschdienst* (DAAD) for awarding me a two-month fellowship for graduate students which rendered possible my second stay at LANL. Several travel grants from the DFG-*Graduiertenkolleg* "Physics of Elementary Particles at Accelerators and in the Universe" have allowed me to visit conferences, workshops and meetings so that I could interact actively with other people of the community.

My billiard friends Christian Beisenherz, Dennis Bullmann, Dominic Grzbielok, Björn Schuster, and Alexander Sprack are acknowledged for improving the work-life balance on a couple of Saturday evenings.

Last but not least I deeply thank my wonderful wife Claudia for all her love, encouragement and patience over the years and I thank my whole family for continuous support.